BEYOND THE NOISE - HIGH FIDELITY MR SIGNAL PROCESSING

A DISSERTATION SUBMITTED

BY

REIKA MASUDA

IN FULFILMENT OF THE REQUIREMENTS
FOR THE DEGREE OF

DOCTOR OF PHILOSOPHY

NANOSCALE ORGANISATION AND DYNAMICS GROUP
SCHOOL OF SCIENCE AND HEALTH
WESTERN SYDNEY UNIVERSITY
AUSTRALIA
2018

BEYOND THE NOISE - HIGH FIDELITY MR SIGNAL PROCESSING

A DISSERTATION SUBMITTED
BY

REIKA MASUDA

IN THE FULFILMENT OF THE REQUIREMENTS
FOR THE DEGREE OF
DOCTOR OF PHILOSOPHY (Ph.D.)

NANOSCALE ORGANISATION AND DYNAMICS GROUP
SCHOOL OF SCIENCE AND HEALTH
WESTERN SYDNEY UNIVERSITY
AUSTRALIA

SUPERVISOR

PROF. WILLIAM S. PRICE
NANOSCALE ORGANISATION AND DYNAMICS GROUP
WESTERN SYDNEY UNIVERSITY
AUSTRALIA

CO-SUPERVISORS

DR GANG ZHENG
NANOSCALE ORGANISATION AND DYNAMICS GROUP
WESTERN SYDNEY UNIVERSITY
AUSTRALIA

DR TIM STAIT-GARDNER
NANOSCALE ORGANISATION AND DYNAMICS GROUP
WESTERN SYDNEY UNIVERSITY
AUSTRALIA

DR ALLAN M. TORRES
NANOSCALE ORGANISATION AND DYNAMICS GROUP
WESTERN SYDNEY UNIVERSITY
AUSTRALIA

Acknowledgements

Completion of this doctoral dissertation became possible only because of the support of many people around me. First and foremost I wish to thank my principal advisor, Professor William S. Price who has been supportive since I was an undergraduate project student never heard of NMR. Thank you for providing me with an exciting topic, ideas and guidance throughout my candidature.

I thank all my supervisors Dr Gang Zheng, Dr Tim Stait-Gardner, Dr Allen M Torres for sharing your knowledge and inspirational ideas. Thanks to Dr Bahman Ghadirian for helping me patiently to build the foundation of NMR signal processing. All other former and present members of WSU Nanoscale Organization and Dynamics Group: Dr Batchimeg Ganbold, Dr Amninder Virk, Dr James Stranger, Dr Mikhail Zubkov, Dr Ryan Dean, Dr Dale Codling, Dr Scott Willis, Dr Abhishek Gupta, Mr Ben Moroney, Mr Mark Donohoe, Ms Yanurita Dwhapsari, Ms Cynthia Khan, Ms Azy Panah, Mr Dj Wijesekera for kindly providing me one of the NMR experimental data set, Mr Johnny Chen, and Ms Robyn Grey for your support in both time when I ask and before I ask for help.

Back in my days at the University of Utah, Dr Robert Easton taught me that Mathematics is fun, thank you, I still enjoy solving the mathematical problem and helped me throughout the candidature going through textbooks and literature with all the complex equations.

To my work colleagues and friends Ms Stacy Paris, Mr Jason Denis, and Ms Julia Taylor, your angelic kindness and constant encouragement made waitressing much more enjoyable to endure and helped me balanced study/work/life altogether.

Statement of Authentication

I, Reika Masuda, declare that this thesis contains no material that has been accepted for the award of any other degree or diploma and that, to the best of my knowledge and belief, this thesis contains no material previously published or written by another person, except when due reference has been made in the text of this thesis.

Date: 31/08/2018

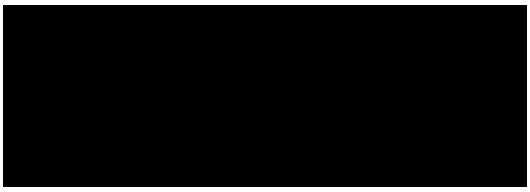

Reika Masuda

List of publications

1. Willis S. A, Stait-Gardner T, Virk A. S, Masuda R, Zubkov M, Zheng G, et al. Diffusion: Definition, Description and Measurement. In: Fisher J, editor. Modern NMR Techniques for Synthetic Chemistry. 1 ed. Boca Raton: CRC Press; 2014. pp. 125-75.

2. Masuda R, Gupta A, Stait-Gardner T, Zheng G, Torres AM, Price WS. Shortening NMR Experimental Times. *Magn. Reson. Chem*., 2018;56(9):847-51.

3. Masuda R, Gupta A, Stait-Gardner T, Zheng G, Torres AM, Price WS. Improved processing of low signal-to-noise NMR diffusion experiments. *J. Magn. Reson.*, **In Preparation from Chapters 5**.

Table of Contents

List of Tables

List of Figures

List of Abbreviations and Symbols

ADC: analogue-to-digital converter

AQ: acquisition time

b: diffusion weighting factor

$\mathbf{B}_0$: static magnetic field

CW: Continuous wave

D: diffusion coefficient

dB: decibel

DFT: discrete Fourier transform

DS: number of dummy scans

DW: dwell time

EM: exponential multiplication

f: friction coefficient

FT: Fourier transform

FID: free induction decay

FFT: fast Fourier transform

g: applied gradient strength

HSVD: Hankel singular value decomposition

h: Planck's constant

I: nuclear spin quantum number

$\mathbf{I}$: spin quantum angular momentum

IFT: inverse Fourier transform

k_B: Boltzmann's constant

LP: linear prediction

LB: line broadening

m: spin quantum state/number

MRI: magnetic resonance imaging

$\mathbf{M}$: net magnetization

M_x: x-component of net magnetization

M_y: y-component of net magnetization

M_z: z-component of net magnetization

M_{eq}: net magnetisation observed at thermal equilibrium

N_α, N_β: spin populations

NMR: nuclear magnetic resonance

NP: number of data points

NS: number of scans

NUS: non-uniform sampling

PGSE: Pulsed gradient spin echo

PGSTE: Pulsed gradient stimulated echo

ppm: parts per million

Q: quadrupole moment

r_s: Stokes radius of spherical particles

RF: radio frequency

RMS: root-mean-squared

RG: receiver gain

SNR: signal-to-noise ratio

SVD: singular value decomposition

SI: size of the real spectrum

T_1: spin-lattice relaxation time

T_2: spin-spin relaxation time

TD: size of FID

US: uniform sampling

WT: wavelet transform

γ: gyromagnetic ratio

δ: duration of the pulsed gradient

η: viscosity

ϕ: phase

κ: wavenumber

λ: eigenvalue

μ: magnitude of intrinsic magnetic moment

$\boldsymbol{\mu}$: intrinsic magnetic moment

ρ_w: noise variance

σ: singular value

τ_c: rotational correlation time

τ: delay time

φ: phase angle

ψ: mother wavelet

ω_0: Larmor frequency

$\hbar$: Planck's constant/2π

Δ: diffusion time

Δf: frequency bandwidth

$\|\cdot\|_F$: Frobenius norm

Abstract

This thesis describes a variety of methods developed to increase the sensitivity and resolution of liquid state nuclear magnetic resonance (NMR) experiments. NMR is known as one of the most versatile non-invasive analytical techniques yet often suffers from low sensitivity. The main contribution to this low sensitivity issue is a presence of noise and level of noise in the spectrum is expressed numerically as "signal-to-noise ratio".

NMR signal processing involves sensitivity and resolution enhancement achieved by noise reduction using mathematical algorithms. A singular value decomposition based reduced rank matrix method, composite property mapping, in particular is studied extensively in this thesis to present its advantages, limitations, and applications. In theory, when the sum of k noiseless sinusoidal decays is formatted into a specific matrix form (i.e., Toeplitz), the matrix is known to possess k linearly independent columns. This information becomes apparent only after a singular value decomposition of the matrix. Singular value decomposition factorises the large matrix into three smaller submatrices: right and left singular vector matrices, and one diagonal matrix containing singular values. Were k noiseless sinusoidal decays involved, there would be only k nonzero singular values appearing in the diagonal matrix in descending order providing the information of the amplitude of each sinusoidal decay. The number of non-zero singular values or the number of linearly independent columns is known as the rank of the matrix. With real NMR data none of the singular values equals zero and the matrix has full rank. The reduction of the rank of the matrix and thus the noise in the reconstructed NMR data can be achieved by replacing all the singular values except the first k values with zeroes. This noise reduction process becomes difficult when biomolecular NMR data is to be processed due to the number of resonances being unknown and the presence of a large solvent peak.

There are seven chapters in this thesis. The first three chapters are dedicated to the introduction to scientific problems addressed in this PhD research, the NMR theory relevant to this study, and the introduction to NMR signal processing including detailed discussion on the types and origin of noise commonly encountered in NMR experiments; different signal processing strategies to shorten experimental time and enhance signal to noise ratio are presented in Chapters 4 to 7.

Chapter 4 focuses on reinvigorating the conventional method by implementing normalisation to the diffusion NMR study. Conventionally, arrayed NMR experiments, such as diffusion and relaxation, are performed with the same number of scans at each iteration despite the signal-to-noise ratio being more than sufficient for many of the iterations. Here, we propose a simple yet effective approach that significantly shortens experimental times by varying number of scans through the arrayed experiments while keeping the signal-to-noise ratio essentially the same and retaining experimental accuracy. This normalisation approach was tested with ^{23}Na NMR diffusion and relaxation studies; accurate diffusion and relaxation measurements were achieved with less than one third of the conventional experimental time being consumed for both.

Chapter 5 focuses on the noise reduction in quadrupolar diffusion NMR using composite property mapping algorithm. The composite property mapping algorithm was applied to a set of ^{23}Na NMR diffusion data. ^{23}Na nuclei being observed as a single resonance in liquid state NMR simplified the determination of the pre-specified rank dramatically due to the prior knowledge of the rank of the noiseless data matrix (corresponding to the ^{23}Na data) being equal to one. In spite of knowing the pre-specified matrix rank, the composite property mapping algorithm has a limitation due to the residual noise property hidden within the noise reduced data. With array experiment such as diffusion NMR, the acquired data sees a range of SNR values due to signal attenuation. To obtain accurate and precise results, the minimum SNR required for each array signal was determined through simulation study. Successful noise reduction lead to accurate and precise diffusion measurements in spite of using only 3% of the total experimental time required by the reference experiment array.

Chapter 6 focuses on the application of composite mapping algorithm to the noise reduction in the diffusion NMR experiments on a ligand-protein system. In this study, the signal of interest was well-resolved from the remainder of the spectrum and therefore the remaining spectrum was replaced by the baseline extracted from the original full spectrum so as to eliminate the process of determining the pre-specified rank corresponding to the original full spectrum. The extracted spectrum containing only the resonance of interest was inverse Fourier transformed and then processed in the same way as the ^{23}Na data was. Significant improvement on the accuracy and precision of the diffusion measurement was achieved without complicated iterative processes of finding the pre-specified ranks corresponding to the original full spectra obtained with different gradient amplitudes.

Chapter 7 focuses on the development of a method for the determination of the minimum rank needed for the noise reduction in biomolecular NMR using composite property mapping algorithm. In biomolecular NMR, it is often impossible to completely resolve a ^{1}H spectrum into its constituting resonances and thus to know the exact number of sinusoidal decays within the free induction decay, which makes it extremely difficult to determine the pre-specified rank corresponding to the full spectrum. Traditionally, the pre-specified rank is determined by observing the difference between each pair of consecutive singular values to find the cut-off singular value supposedly existing right before a sharp drop. This method can provide misleading rank determination when a typical biomolecular ^{1}H NMR spectrum is processed because of the existence of multiple steep descending regions observed when plotting the singular values in a descending order. Instead of directly examining the singular values, the first/largest singular value was divided by itself and all the other singular values, respectively, to generate the singular value ratios which were used to determine the initial minimum matrix rank to be fed into the iteration process for further rank reduction. This new method was applied to a ^{1}H 400 MHz NMR spectrum containing a partially suppressed water peak obtained on an aqueous lysozyme solution using the WATERGATE pulse sequence. After the determination of the initial minimum matrix rank, the final minimum matrix rank was found with only 15 iterations. A distinct feature of the new method is that it avoids underdetermining the matrix rank and thus avoids eliminating the signals of interest in the noise reduction process. Moreover, all the spectral features were well preserved after the noise reduction. As a comparison, a commercially available signal processing method based on wavelet transform was also tested on the same data. Efficient noise reduction was achieved by the use of the wavelet based method, however, signal amplitude distortion and line broadening were observed in the noise reduced spectrum.

CHAPTER 1. INTRODUCTION

Nuclear magnetic resonance (NMR) in its various guises including magnetic resonance imaging (MRI) provides a suite of techniques, which can be used to provide a wealth of information across many of the sciences and clinical medicine [1-3]. NMR spectroscopy can be applied to a broad range of systems ranging from solid matter [4, 5] to biological tissue, from small molecules at low concentration to polymers [6], from frozen materials [7] to inorganic compounds at high temperature [8], and anywhere between [9]. The technology is capable of providing information unobtainable by other means and it can do so non-invasively. A major weakness of magnetic resonance compared to other techniques is that it suffers from an inherently low signal-to-noise ratio (SNR). In this thesis, some new and improved methods of enhancing SNR by using mathematical signal processing or alternatively shortening the overall NMR experimental time are presented. These new approaches are illustrated with applications to quadrupolar nuclei (i.e. nuclei with spin quantum number $I > 1/2$), non-quadrupolar nuclei (i.e. nuclei with spin quantum number $I = 1/2$), and NMR diffusion measurements. This chapter provides the context and a roadmap to the content of this thesis. In particular, it provides a brief introduction to NMR, the reasons for its inherently low SNR including the origins of the noise and the experimental and practical means to acquire NMR data more efficiently to obviate the noise limitations. It also includes a succinct introduction to the types of experiment used to demonstrate the new approaches developed in this thesis. The concepts will be elaborated on in subsequent chapters.

1.1 NMR SIGNAL

The major reason for the low sensitivity of NMR is the source of the NMR signal and how it is acquired. The signal originates from quantum properties of atomic nuclei. In particular, NMR is concerned with the magnetic properties of atomic nuclei, sometimes referred to as 'spins'. Not all elements (or isotopes) have NMR sensitive nuclei, but of those that do (i.e., those with $I > 0$) the spins behave like microscopic bar magnets. In the simple case of a spin-1/2 nucleus (i.e., $I = 1/2$) such as ^{1}H there are two possible spin states: up or down. In the absence of an external magnetic field, these spin states are degenerate. However, in the presence of an external static magnetic field, $\mathbf{B}_0$, these spin states become non-degenerate with the energy difference

between the two states proportional to $\mathbf{B}_0$ – hence the need for a magnet when conducting NMR experiments. The population of spins in each state is governed by the Boltzmann distribution. The population difference between the two states is extremely small but increases with $\mathbf{B}_0$. The vector sum of all of the nuclear magnetisation is termed the net magnetisation, **M**. The magnitude of the thermal equilibrium value of **M** is denoted by M_0 which prior to any perturbation is initially oriented parallel to $\mathbf{B}_0$. In addition to non-degeneracy, the magnetic field also causes the spins (and thus **M**) to precess around $\mathbf{B}_0$ at a frequency termed the Larmor frequency. This Larmor (or resonance) frequency is isotope-dependent (i.e., it depends on the gyromagnetic ratio, γ, specific to each isotope) and proportional to $\mathbf{B}_0$ and is normally in the MHz range (i.e., a radio frequency; RF). The actual value of the magnetic field sensed by the nucleus is modulated by the local environment of the nucleus. Specifically, the electron shells of the atom shield the nucleus from $\mathbf{B}_0$. Thus, the same nucleus but in a different chemical environment has a very slightly different resonance frequency (i.e. experiencing a 'chemical shift'). These chemical shifts are very small and are consequently normally expressed in terms of parts per million (ppm) from the base Larmor frequency of bare nuclei.

A short burst ('pulse') of electromagnetic radiation at the Larmor frequency (often referred to as an RF pulse) oriented perpendicular to $\mathbf{B}_0$ has the effect of nutating **M** away from $\mathbf{B}_0$ into the transverse plane. The duration and amplitude of the RF pulse determine the angle that **M** is nutated away from $\mathbf{B}_0$. The magnetisation then precesses as described above. Ultimately it is this precessing nuclear magnetisation that is the source of the detected NMR signal. A coil located perpendicular to $\mathbf{B}_0$ detects the transverse component of this precessing magnetisation as an oscillating voltage. Spin magnetisation which is not at thermal equilibrium returns to thermal equilibrium via a process known as spin relaxation. Spin relaxation can be separated into two concurrent processes: (i) Longitudinal (or spin-lattice) relaxation in which energy absorbed by the spins is lost to the surroundings (i.e., the lattice) and (ii) transverse (or spin-spin) relaxation in which involves the loss of phase coherence of the spins. Consequently, the detected oscillating voltage decays and thus the detected signal is often referred to as a free induction decay (FID). Since the relaxation process is normally governed by an exponential time constant the FID appears as an exponentially decaying sinusoid as shown in Figure 1. In reality, and as depicted in Figure 1, the NMR signal inherently

contains noise. The spectral linewidth is related to the transverse relaxation rate, with rapidly relaxing spin systems having broad resonances.

As shown in Figure 1, the Fourier Transform (FT) is the most common signal processing technique in NMR and has traditionally been used to transform the (time domain) FID into a spectrum (i.e., the frequency domain). However, the noise in the FID is also transferred into the frequency domain resulting in a noisy spectrum. This noise distorts the baseline but also degrades the resonance lineshape and its amplitude.

NMR experiments generally involve a sequence of RF pulses interspersed by delays and sometimes magnetic gradient pulses (i.e., a pulse sequence). As an analogy, the pulse sequence to an NMR spectrometer is like a music score to an orchestra. The choice of pulse sequence determines what information can be obtained in the experiment.

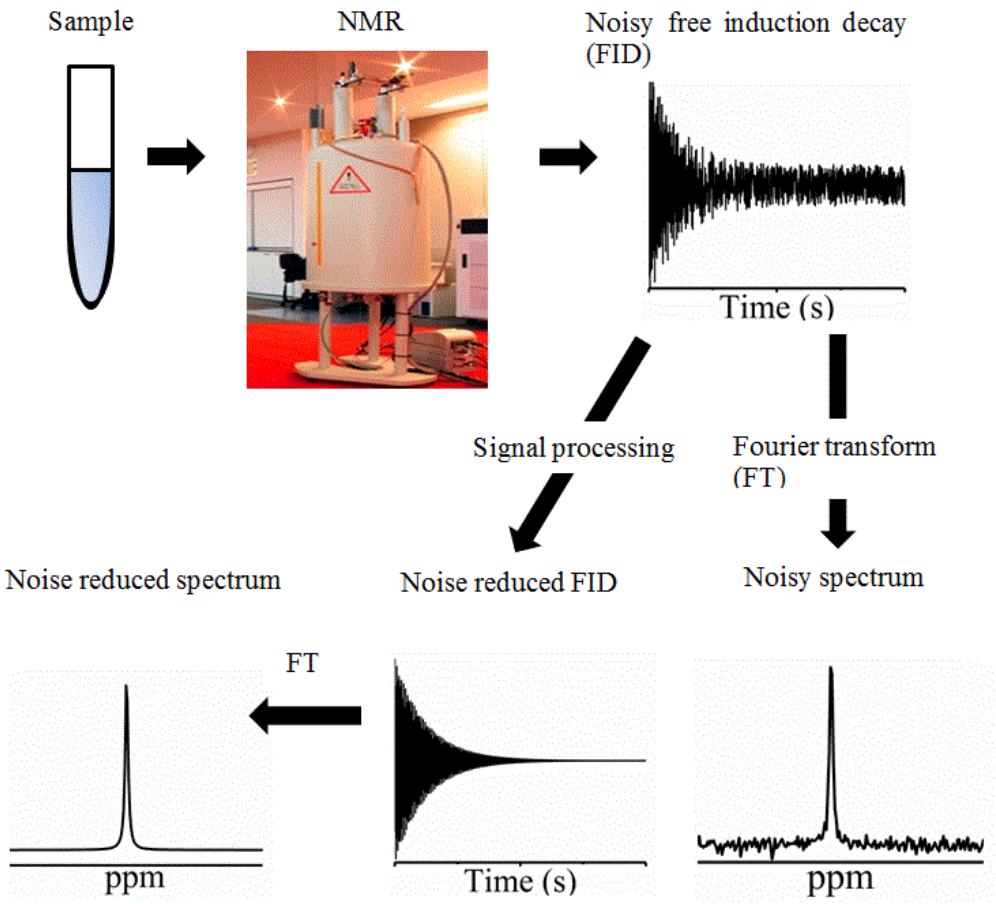

Figure 1. Flowchart of NMR signal acquisition and signal processing. The chemical and physical information possessed by the sample is first collected as a time domain free induction decay (FID), which is then transformed into the frequency domain via

Fourier transformation (FT). The frequency of the resonance is normally given in terms of parts per million (ppm) of the centre frequency. All experimentally acquired FIDs inherently contain noise. By applying appropriate signal processing it is possible to reduce this noise.

1.2 NUCLEI AND SENSITIVITY

Most elements in the periodic table contain at least one NMR sensitive isotope. The sensitivity of an isotope varies according to its natural abundance and its specific value of γ. The Larmor frequency and the sense of spin precession are determined by γ and $\mathbf{B}_0$. A higher γ and thus Larmor frequency leads to greater sensitivity.

Of all NMR active nuclei, the proton (i.e., ^{1}H) is the most commonly probed nucleus in NMR studies. ^{1}H is the second to the most NMR sensitive nuclei with a very high natural abundance of 99.98% (i.e., ^{3}H has the highest sensitivity yet its natural abundance is 10^{-18} of ^{1}H [10, 11]). Molecules, especially biomolecules, containing protons are ubiquitous. Many other nuclei such as ^{13}C, ^{23}Na, ^{43}Ca are also commonly used. After ^{1}H, the next commonly probed nucleus is ^{13}C. Most carbon exists as the NMR inert isotope ^{12}C (i.e., $I = 0$) with the only NMR sensitive carbon isotope being ^{13}C (i.e., $I = 1/2$) and having a natural abundance of only 1.1 %. Further, the γ of ^{13}C is only quarter that of ^{1}H. The low γ and low natural abundance result in ^{13}C having only 10^{-4} the sensitivity of ^{1}H.

Despite this lower sensitivity, ^{13}C has its own advantages [12]. ^{13}C NMR can provide structural information of carbon atoms that are not bonded to hydrogen. This feature is ideally suited for studying the structure of organic molecules. Another advantage is having a larger chemical shift range than protons. This wider chemical shift range provides a more sensitive probe of structural changes. Finally, ^{13}C nuclei typically have longer relaxation times than ^{1}H nuclei which influences the line widths [13]. Longer relaxation times result in narrower linewidths. The combination of a larger chemical shift range and narrower line widths reduces the likelihood of spectral overlap.

More than 70% of active nuclei have the spin property of $I > 1/2$. Such nuclei are specifically called “Quadrupolar nuclei”. Many biologically important nuclei are quadrupolar including ^{7}Li, ^{23}Na, ^{43}Ca, ^{39}K [14-16].

1.3 SOME NMR STUDIES LIMITED BY NOISE

Due to SNR limitations, many experiments that are in theory possible are in practice not practicable since they would take too long or, even worse, the signal would be too low to be detectable. Further, speeding up NMR experiments expands the horizons of NMR experiments, for example, to time-sensitive samples including the measurement of reaction kinetics. Below we give a brief introduction to the problems facing the measurement of quadrupolar nuclei and of molecular diffusion.

1.3.1 Quadrupolar nuclei

In general, quadrupolar nuclei possess much faster spin relaxation times compared to $I = 1/2$ nuclei [17]. Rapidly relaxing nuclei complicate NMR measurements in two ways: broader lines and low sensitivity. Faster transverse magnetisation decay leads to broader spectral peaks and, consequently, lower spectral resolution. The other issue is the signal loss during the period when the electromagnetic radiation is removed and the signal detection starts. This period of time is called "dead time" which is often measured in μs (e.g. 10 μs). Since the electromagnetic radiation emits from the same coils where the signal is detected, complete cut off of the voltage before the signal detection is mandatory. This duration does not cause a crucial signal loss to the nuclei with long relaxation time. However, with fast relaxation, the quadrupolar nuclei such as ^{23}Na (an important indicator of human cellular membrane function, especially sodium and potassium exchange [1]). Other nuclei such as: ^{39}K, ^{35}Cl, ^{33}S, and ^{17}O can lose sensitivity due to this delay [18].

Some quadrupolar nuclei are known to have very long relaxation time. ^{7}Li and ^{6}Li, for example, take up to few minutes to fully relax [19]. Signal averaging and detection in another one or two dimensions (e.g., 2D and 3D NMR experiments) for these nuclei can lengthen the experimental time enormously.

One of the major differences between non-quadrupolar and quadrupolar nuclei in a liquid state is the number of resonance. The number of resonance in the quadrupolar nuclei NMR measurements is always one. Knowing the number of resonance is such a significant prior knowledge in signal processing. One resonance frequency means the measured FID only contains one exponentially decayed

oscillating sinusoid function with the addition of noise. Further details of the quadrupolar nucleus is found in Section 2.7.

1.3.2 Diffusion and Multidimensional NMR Experiments

Reducing the required number of scans is extremely important in advanced NMR applications such as NMR diffusion study and multidimensional NMR experiments. NMR diffusion measurements can provide detailed information on molecular organisation [20, 21], pore structure of porous media [22, 23], molecular aggregation [24] and more [25, 26].

Diffusion NMR measurements of translational motion are performed using the pulse gradient spin-echo (PGSE) sequence as an arrayed experiment in which an experimental parameter (e.g., the applied gradient strength) is altered with each increment [27, 28]. Thus, the echo signal attenuates with each arrayed experiment (i.e., with increasing applied gradient strength).

In theory, the diffusion coefficient could be obtained from experiments conducted at only two different gradient strengths. However, in practice the majority of measurements are conducted as an array of eight to sixteen experiments. The gradient strength is usually increased linearly to a maximum strength which results in an attenuation of the echo signal to 10 to 20 % of its original intensity [27]. As the signal attenuates, the SNR decreases. Thus, with the conventional method, numerous signal averaging is performed consecutively at each gradient strength to ensure the sufficient spectral sensitivity throughout the experimental measurements.

Not only to consider the number of scans required for the most attenuated signal but also each scan requires at least five times the spin-lattice relaxation time to ensure the nuclear spins fully relax back to its equilibrium state before the next pulse sequence cycle begins. The majority of pulse sequences have a specific number of scans per one phase cycle. The PGSE sequence used in this thesis has a phase cycle of 8 scans. Considering the matters listed above and additional matters such as measuring a mixed sample containing macromolecules where a wide range of SNR values are found within the spectrum, a nucleus with long relaxation time, and/or simply samples with low concentrations, very long experimental time is often encountered.

There are many other complex NMR experiments which are known to require long machine time. For example, while using the 3D gradient enhanced HCCH-

TOCSY sequence to study protein amino acid side chain [29], the total acquisition time was up to 65 hours per spectrum. Adding one more dimension to the HCCH-TOCSY experiment, a 4D-HCCH-TOCSY experiment by Olejniczak took up to 6.4 days [30].

1.3.3 Incredible Natural Abundance Double Quantum Transfer Experiment (INADEQUATE) NMR Sequence

Most organic molecules contain a large number of protons and carbons. A measurement of the coupling constants in both ^{1}H-^{1}H and ^{13}C-^{13}C can provide a lot of information about the molecular structure using ^{1}H and ^{13}C NMR respectively [31]. The main difference between ^{1}H and ^{13}C NMR is sensitivity. In order to measure the coupling constant of two ^{13}C nuclei, the satellite signals with very small intensity (i.e., 0.5% of the main signal each) must be well-separated from the main peak, otherwise it is almost impossible to measure them. For ^{1}H NMR on the other hand, ^{13}C-^{1}H couplings are much larger that the satellite signals and can be measured easily compared to ^{13}C NMR [32]. In order to measure the ^{13}C-^{13}C coupling constant as easily as ^{13}C-^{1}H coupling in ^{1}H NMR, the 1D-INADEQUATE sequence was introduced which eliminates the main-carbon signal so the satellite signals can be observed[33].

Development of the INADEQUATE NMR sequence enables the study of very weak ^{13}C-^{13}C spin-spin couplings for structural elucidation in organic molecules [33-35]. Apart from the obvious sensitivity issues, identification of these carbon satellites (i.e., ^{13}C-^{13}C spin-spin coupling) is particularly difficult due to the presence of incomplete proton decoupling, weak spinning sideband lines (from the rate of spin of an NMR tube) and unavoidable signals due to impurities [36]. The INADEQUATE sequence can be applied to both 1D and 2D NMR experiments, although, in practice, the 2D version is more commonly used to obviate the problems of spectral crowding in the 1D experiment [35-37].

It is very time-consuming to acquire high-quality spectral data. Thus, numerical signal processing is strongly beneficial not only to reduce the experimental time but also for signal enhancement purpose. As an example, Lambert proposed a numerical post signal processing method [38]. In his method prior knowledge about the -CH multiplicities was required. In fact, many NMR signal processing techniques

strongly benefit from prior knowledge of the NMR data to be processed (e.g., number of peaks, size of coupling constant. However, in the general case no such prior knowledge is available. Indeed, in the ideal case to facilitate general applicability such processing techniques would not require such information.

1.4 OVERCOMING SOME SIGNAL-TO-NOISE LIMITATIONS

There are numerous ways to overcome SNR limitations: (i) using higher $\mathbf{B}_0$ and/or making the hardware more sensitive [39-44], (ii) improved implementation of pulse sequences to more efficiently use the available experimental time [45-48] and (iii) signal processing approaches which extract information from the acquired NMR signal more efficiently [49-64].

Numerous hardware and signal processing (i.e., software) approaches have been developed to reduce noise and improve NMR sensitivity. Signal processing approaches cannot truly remove all noise and come with caveats (e.g., requiring 'prior' knowledge on the content of the spectrum or increase the SNR at the expense of spectral resolution). However, under specific conditions sophisticated signal processing algorithms can dramatically reduce the noise components of NMR signals. Some of the major signal processing algorithms are summarised in Section 3.4.

Signal processing

Signal processing, more specifically, post signal processing is a signal enhancement method which does not interfere with NMR signal acquisition process nor equipment itself. The signal processing utilises mathematical theory applied directly to experimentally measured FID data, manipulated in such a way as to enhance resonance sensitivity. The signal processing not only enhances the sensitivity of experimentally measured data but also lowers the required signal sensitivity before signal processing, leading to reducing the total experimental time from excessive signal averaging [60, 65].

There are a number of signal processing software packages included in modern standard NMR spectrometer software environments. Additional signal processing techniques can be performed externally using a standard programming language. Many of the signal processing methods are considered to be optimisation processes which often require iteration to generate optimised FIDs with reduced noise. For every optimisation method, some form of information about the raw data is required to set the initial parameter values [52, 64, 66-68]. Information such as the number of summed exponentially decaying sinusoids within the FID is crucial for successful post signal processing. Other methods include the Harmonic Inversion method (HI) [65, 69-73] (Section 3.7.2), the wavelet shrinkage method [74] (Section 3.4.4), the maximum entropy reconstruction method [75], and composite property mapping based methods [52] which are described in Section 3.4. Other non-iterative/ non-optimisation procedures such as the Linear Prediction Singular Value Decomposition (LPSVD) [76, 77] (Section 3.6.1), the Hankel Singular Value Decomposition (HSVD) [78, 79] (Section 3.6.2), the Matrix Pencil (MP) [80-82] (Section 3.6.3), and the Filter Diagonalisation Method (FDM) [73] (Section 3.6.4) are also briefly described in Chapter 3.

1.5 AIMS AND OVERVIEW OF THE THESIS

This thesis focuses its discussion on an NMR signal normalisation approach developed to accelerate NMR relaxation and diffusion measurements and a signal processing method based on composite property mapping developed to achieve efficient noise reduction in a variety of NMR experiments. The development of both the experimental approach and the signal processing method was aimed at obtaining superior signal sensitivity and/or accuracy and/or shortening overall experimental time compared to the conventional/existing methods. The basic NMR theory and signal acquisition procedure are explained in Chapter 2. Information on the basic NMR signal, noise, and signal enhancement techniques are given in the following Chapter 3. The contents of the signal enhancement techniques in Chapter 3 include both hardware developments and numerical signal processing methods. The composite property mapping algorithm which is the foundation of the signal processing method developed in this thesis will be found in Section 3.7. The rest of this thesis from Chapter 4 onward

presents the simulation and experimental results obtained in the development and application of the NMR signal normalisation approach and the noise reduction method based on composite property mapping.

1.5.1 Shortening NMR experimental times with Normalisation

As previously discussed, most of the array experiments suffer from the extensive experimental time due to having a same number of scans for each array experiment. The number of scans is set in such a way that the most attenuated signal has sufficient SNR. The number of scans required for acquiring the most attenuated signal is excessive for acquiring the least attenuated signal. With a rough estimate of the signal attenuation rate against the attenuation factor used in the experiment, the number of scans required for each array experiment can be estimated. The overall experimental time can be reduced enormously by tailoring the number of scans for each arrayed signal. Each collected array signal is normalised by its corresponding number of scans and then fed into the relaxation/diffusion data analysis. This approach was applied to ^{23}Na T_1 and PGSE NMR study which theory and results can be found in Chapter 4.

1.5.2 Noise reduction in quadrupolar nuclei diffusion NMR using composite property mapping algorithm

The application of signal processing, especially the methods based on composite property mapping algorithm, can dramatically reduce total NMR scanning time of array experiments such as diffusion and relaxation studies. To demonstrate the effect of composite property mapping signal processing, the diffusion measurement of 10 mM NaCl was first performed using the conventional method with a large number of scans. The same experiment with considerably fewer scans (lower SNR) was also performed and then the acquired NMR data was processed using the composite property mapping algorithm. Since ^{23}Na is a quadrupolar nucleus which exhibits a single resonance in liquid state NMR experiments. This prior knowledge becomes a great advantage when using composite property mapping algorithm because the pre-specified matrix rank is already known as one. In Chapter 5, the limitations faced by the composite property mapping based noise reduction method is also presented.

1.5.3 Frequency selective signal processing

A simple spectrum containing only one resonance as observed for quadrupolar nuclei is rarely seen in biomolecular NMR where numerous resonances with various intensities and line shapes can be found in one spectrum. In protein structure analysis, for example, the one-dimensional spectrum of a protein sample is often containing clusters of overlapped resonances that create broad baseline-like features. If one resonance out of many was the signal of interest it would be wise to only select and process the region of interest. This idea was applied to ^{1}H PGSTE NMR diffusion experiments on a diluted solution containing 5 mM 2-nitroimidazole and 38 mM bovine serum albumin (BSA) dissolved in D_2O. A single resonance at around 8.4 ppm was selected and then the rest of the spectrum was replaced with baseline values so that the modified spectrum shared the single resonance feature with the liquid state quadrupolar nuclei dataset. This approach can eliminate the minimum matrix rank determination and iteration process altogether which is very difficult when a biomolecular NMR spectrum is processed. The development and application of the frequency selective signal processing method are presented in Chapter 6.

1.5.4 Singular value ratio method for noise reduction in biomolecular NMR

When applying composite property mapping based noise reduction to biomolecular NMR spectra, the noise reduction method requires so-called threshold matrix rank determination before matrix rank reduction. This threshold matrix rank is used to estimate the pre-specified matrix rank which is associated with the number of sinusoids representing the signals. With heavily overlapping resonances, it is tremendously difficult to determine the minimum matrix rank that separate signals from the noise. To make the matter worse, biomolecular solutions often contain a far larger amount of water molecules than their solutes, which result in a deleteriously strong water peak in the ^{1}H NMR spectra. The intense water sinusoid in the FID can mislead the threshold matrix rank determination process due to the significant magnitude difference between the singular values corresponding to the water resonance and the ones corresponding to the solute resonances.

With incorrect threshold matrix rank determination, the processed data may have some important solute signals missing or some ghost signals originating from imperfect noise reduction. A new method (i.e. singular value ratio method) for more accurately determining the threshold matrix rank was proposed in Chapter 7. The proposed method was applied to the one-dimensional lysozyme ^{1}H NMR spectrum with the water signal partially suppressed by using WATERGATE. With the proposed method, efficient matrix rank determination was achieved in spite of the problems caused by strong residual water resonance, heavily overlapping lysozyme resonances, and non-Lorentzian line shape.

CHAPTER 2. NMR THEORY

2.1 NUCLEAR SPIN

Each atomic nucleus contains a specific number of protons and neutrons which are known comprised of quarks and gluons [83]. As an example, a deuterium nucleus which has one neutron (purple dash circle) and one proton (red dash circle) are depicted in Figure 2. In fact, ^{2}H is one of only four (i.e., ^{2}H, ^{6}Li, ^{10}B, and ^{14}N) stable bosons (i.e., nuclei having integer spin).

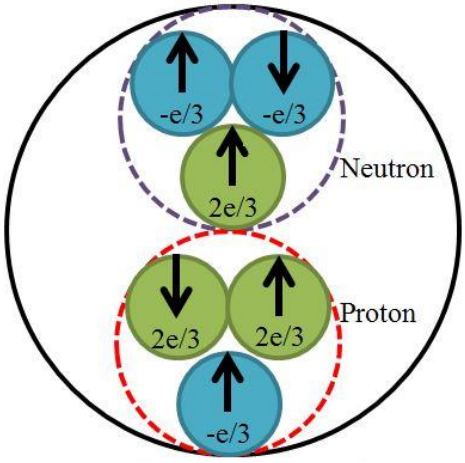

Figure 2. A deuterium atomic nucleus (black solid circle). Each neutron (purple dash circle) or proton (red dash circle) contains quarks (green and blue circles) with positive or negative charge and the quark spin is depicted with an arrow.

Each neutron or proton consists of three quarks that are connected to each other by gluons. There are six known flavours of quarks available in nature, a quark has an electric charge of either + 2e/3 or - e/3. The quarks that determine the spin quantum number of the nuclei are specifically called valence quarks. Valence quarks have spin-1/2 and exist either as "up" or "down" quarks as indicated by the arrows in Figure 2.

The neutron has one + 2e/3 charged quark and two – e/3 charged quarks, which gives an overall charge of zero. Since each quark has spin-1/2 and the sum of two up-quarks and one down-quark results in a neutron spin quantum number, $I_{n,}$ of 1/2. The proton has two + 2e/3 charged quarks and one – e/3 charged quark, which gives an overall charge of one. In a proton, there is one up-quark and two down-quarks, which

gives the total proton spin quantum number, I_p, of 1/2. The nuclear spin quantum number, I,is determined as follows [83]:

$$I = \begin{cases} \left|I_n - I_p\right| \\ \left|I_n - I_p\right| + 1 \\ \vdots \\ \left|I_n + I_p\right| \end{cases}, \tag{1}$$

I can be zero, a positive integer (i.e., boson), or a half-integer (i.e., fermion). Following Eq. (1), ^{2}H with one neutron and one proton both having spin-1/2 (i.e., $I_n = I_p = 1/2$), I will have a two possible values of 0 and 1, corresponding to the proton and neutron spins being the antiparallel and parallel position, respectively. I determine the number of spin quantum states experienced by each nucleus and these spin quantum states are associated with the quantum number m calculated by

$$m = -I, -I+1, ..., +I \ . \tag{2}$$

Following Eq. (2), each value of I will be associated with a total of $2I$ +1 degenerate spin quantum states in the absence of $\mathbf{B}_0$. For deuterium, only the spin state with $I = 1$, which is the lowest energy state, is directly observable in NMR and it is associated with three spin quantum states (m = -1, 0, +1).

Table 1 summarises the relationship between the number of nucleons and the spin quantum number [84].

Table 1. Using the number of protons and the number of neutrons to predict the spin quantum number of an atomic nucleus.

Number of protons	**Number of neutrons**	**Spin quantum number (*I*)**	**Examples**
Even	Even	Zero	^{12}C, ^{16}O, ^{32}S
Odd/Even	Even/Odd	Half Integer	^{1}H, ^{13}C, ^{31}P, ^{35}Cl
Odd	Odd	Integer	^{2}H, ^{14}N

Protons, the most commonly observed nuclei, have a spin of 1/2. Each ^{1}H nucleus can experience one of or a weighted sum of the two spin quantum states (i.e., eigenstates) associated with m = +1/2 and -1/2 respectively. Any nucleus with a non-zero I possess a spin angular momentum (**I**) and thus a magnetic moment (**μ**) which can be calculated by

$$\boldsymbol{\mu} = \gamma \mathbf{I} \tag{3}$$

where γ is the gyromagnetic ratio. In the presence of $\mathbf{B}_0$, the energy (E) associated with a particular spin quantum state can be calculated by [83]:

$$\begin{aligned} E &= -\boldsymbol{\mu} \cdot \mathbf{B}_0 \\ &= -\gamma \hbar m B_0 \end{aligned} \tag{4}$$

where $\hbar$ is the Planck's constant divided by 2π. According to the Eq. (4), spins with different m values will stay at different energy levels on the application of $\mathbf{B}_0$, which is so-called Zeeman effect illustrated in Figure 3.

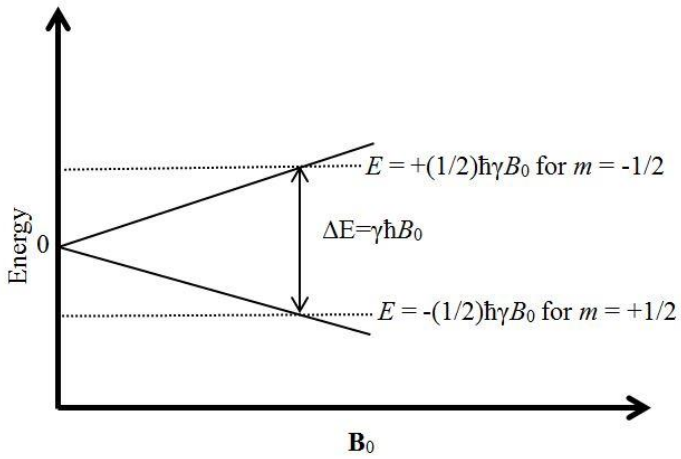

Figure 3. The Zeeman effect on I = 1/2 nuclei creating an energy difference (ΔE).

As shown in Figure 3, there are two energy levels associated with the two eigenstates, a higher energy level for the β or m = -1/2 eigenstate and a lower energy level for the

α or m = +1/2 eigenstate. The ratio of nuclei at each eigenstate can be described by the Boltzmann distribution [85, 86]:

$$\frac{N_\alpha}{N_\beta} = e^{\frac{\Delta E}{kT}} \tag{5}$$

where N is the population of the spins/nuclei at particular eigenstate, k is the Boltzmann's constant (1.3805×10^{-23} J K^{-1}) and T is the temperature in Kelvin (K). At room temperature, the spins in the α state outnumber slightly the spins in the β state. The population difference between the spin states is calculated by:

$$\frac{N_\alpha - N_\beta}{N_\alpha + N_\beta} = \frac{\exp\left(-E_a / kT\right) - \exp\left(-E_\beta / kT\right)}{\exp\left(-E_a / kT\right) + \exp\left(-E_\beta / kT\right)} \approx \frac{\hbar \gamma B_0}{2kT} \ . \tag{6}$$

From Eqs. (4) and (6), a stronger $\mathbf{B}_0$ will result in a higher ΔE, a higher population differences, and thus a higher NMR sensitivity. The NMR sensitivity of a particular isotopic species can also be affected by the gyromagnetic ratio and the natural abundance of the isotope as shown in Table 2 [83].

Table 2. NMR sensitivity of commonly observed nuclei.

Nucleus	**Spin Quantum Number (*I*)**	**Gyromagnetic Ratio (10^7 rad T^{-1} s^{-1})**	**Natural Abundance (%)**	**Sensitivity compared to ^{1}H (%)**
^{1}H	1/2	26.7520	99.984	100.00
^{2}H	1	4.1067	0.0156	0.965
^{7}Li	3/2	10.3962	92.58	0.29
^{13}C	1/2	6.7265	1.108	1.59
^{15}N	1/2	-2.7108	0.365	0.104
^{23}Na	3/2	7.0761	100.00	0.093
^{43}Ca	7/2	-1.8025	0.135	8.68×10^{-4}

2.2 LARMOR FREQUENCY

The magnetic moment associated with each spin precesses around the applied external field at the Larmor frequency ω_0 (rad s^{-1}) determined by [87]:

$$\omega_0 = -\gamma B_0 \tag{7}$$

or expressing the frequency in Hz is given by

$$\nu_0 = \frac{-1}{2\pi}\gamma B_0 \ . \tag{8}$$

Each isotopic species has a unique gyromagnetic ratio and thus a unique Larmor frequency for a given B_0. If the gyromagnetic ratio has a positive value (e.g., for ^{1}H), the precession occurs in the clockwise direction while anti-clockwise precession is observed for a negative gyromagnetic ratio (e.g., for ^{15}N) [83, 84]. As an example, a Larmor frequency of a proton ($\gamma = 267.513\times10^{6}$ rad $s^{-1}T^{-1}$) in an external magnetic field of 9.4 T, is 25.13×10^{8} rad s^{-1} (400 MHz).

2.3 MAGNETISATION

The sum of the individual magnetic moments exposed to the applied magnetic field would form a net magnetisation vector **M** as shown in Figure 4. This vector is associated with the population differences of the spins occupying different eigenstates. Thus, the net magnetisation vector at the thermal equilibrium state (i.e., $\mathbf{M}_0$), will be pointing along the direction of the applied field (i.e., $+z$ direction).

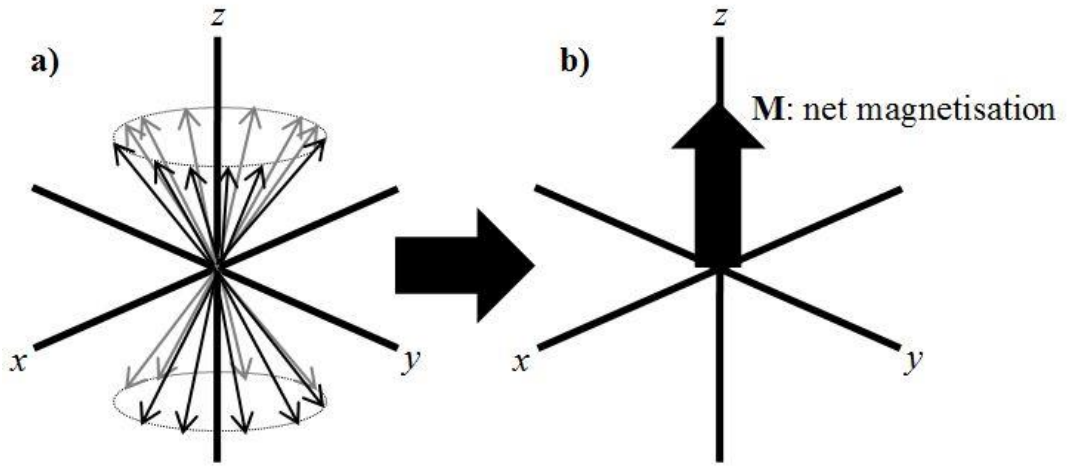

Figure 4. a) The individual magnetic moments precessing around the *z*-axis, illustrating the slight excess of magnetic moments aligned with the applied field ($\mathbf{B}_0$) which is aligned along *z*. b) The net magnetisation (**M**) is the sum of all the magnetic moment vectors exposed to the applied field [88].

At the thermal equilibrium state, no NMR signal can be obtained since the spin ensemble is fully relaxed. In order to detect the precessing spins, the system has to be perturbed by the application of radiofrequency radiation.

2.4 RADIO FREQUENCY PULSE

It does seem impossible to pull the magnetisation vector away from its equilibrium states at first, since the external magnetic field ($\mathbf{B}_0$) is so strong. However, with this applied external magnetic field, the Larmor frequency of any active nuclei falls in the range of the radiofrequency. When there is an application of a very small magnetic field ($\mathbf{B}_1$) oscillating at the Larmor frequency along the *x*-axis, this small magnetic field can pull the net magnetisation away from the equilibrium state [88].

This oscillating magnetic field, $\mathbf{B}_1$, is applied as an RF pulse and its duration and the amplitude can manipulate the nuclear polarization between $+z$ –axis to the $-z$-axis. Typical RF pulses have durations of the order of 10 μs. This transition can be illustrated in two different frames of reference: laboratory/stationary and rotating frame as shown in Figure 5.

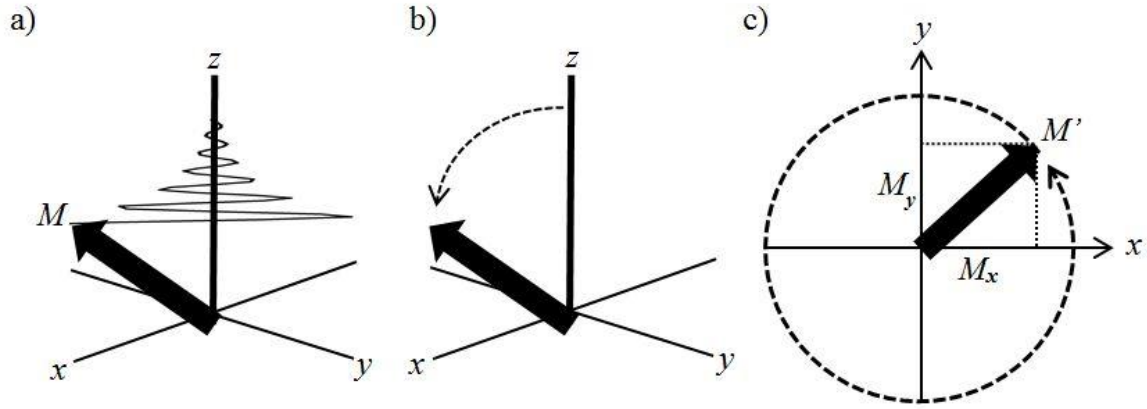

Figure 5. During the application of an RF pulse along the *x*-axis, the net magnetisation (*M*) experiences a combination of the rotations around the *x*- and *z*-axes in the laboratory frame a) or an apparent rotation around the *x*-axis in the rotating frame b). Immediately after the application of the RF pulse, the transverse component of the net magnetisation (*M'*) precesses around the *z*-axis c).

Using the rotating frame of reference, the vector length of the net magnetisation with duration of the RF pulse at each axis can be calculated by:

$$\begin{aligned} M_x(t) &= M_0 \sin(\theta)\cos(\omega_0 t) \\ M_y(t) &= -M_0 \sin(\theta)\sin(\omega_0 t) \\ M_z(t) &= M_0 \cos(\theta) \end{aligned} . \qquad (9)$$

Once the *M* reaches the *y*-axis, the voltage recorded from a coil at the *x*-axis would measure a maximum voltage. A pulse that causes *M* to tilt orthogonal to $\mathbf{B}_0$ is called a 90º ($\pi/2$) pulse. The $\mathbf{B}_1$ field also creates coherence within the spins, meaning the phases of the spins are partially correlated. When the spins are correlated, the transverse vector becomes measurable.

2.5 PULSE ACQUIRE EXPERIMENT

The most basic NMR experiment is called a pulse and collect or pulse-acquire experiment [88], illustrated in Figure 6. The first two periods have been mentioned in the previous two sections. At the end of the period (2) in Figure 6, as the RF pulse is

switched off, the spins are coherently precessing in the transverse *xy*-plane at the Larmor frequency.

The third period is known as the 'dead time' and lasts for approximately 10 μs. This delay time is important due to the coil geometry having the RF pulse emission and the signal detector located on the same axis. If any residual voltage from the RF pulse remained within the circuitry during the signal detection, the signal would be destroyed and the detection circuitry might be damaged.

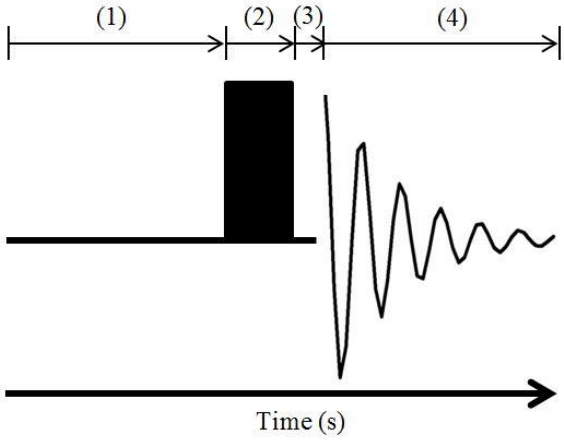

Figure 6. The pulse-acquire experiment. (1) This delay, which is typically of the order of seconds, allows the nuclear spins to reach the thermal equilibrium state. (2) A π/2 RF pulse is applied to the magnetisation. (3) The dead time delay between the end of the RF pulse and the opening of the receiver. (4) The signal detection/acquisition period, typically of the order of a second, in which the FID is collected.

When the RF pulse has switched off, the net magnetisation is free from external RF radiation, it starts to precess back to its thermal equilibrium state. This process is called "spin relaxation". The precession induces an oscillating electric current by Faraday induction. The current is detected by the receiver on the same axis along which the RF pulse was applied. The collected voltage is then amplified and digitised through an analogue-to-digital converter (ADC) forming the FID.

2.6 RELAXATION

There are two types of relaxation processes observed after the RF pulse has removed. One involves the restoration of the spin population back to its thermal equilibrium

state (i.e., Boltzmann distribution). The second is the process in which the coherence of the transverse magnetisation decays back to zero. Those two relaxation processes are often denoted as T_1 and T_2 relaxation, respectively [89].

T_1 (Longitudinal) relaxation: Longitudinal relaxation refers to the return of the longitudinal component of the magnetisation (i.e., **M**) back to its thermal equilibrium state after it has been excited (e.g., by the application of a π/2 RF pulse as in Figure 5. During this process, the spin states and the corresponding energy states will be flipping up and down changing their energy levels different to its surrounding (the "lattice"). The maximum energy difference occurs when the bulk magnetization is on the *xy*-plane. The minimum energy difference will be obtained once the bulk magnetization returns to its thermal equilibrium state along the *z*-axis. The return of thermal equilibrium generally follows an exponential time course characterised by a time constant T_1 also known as *spin-lattice* relaxation time.

T_2 (Transverse or spin-spin) relaxation: T_2 relaxation represents the loss of phase coherence due to the energy exchange between the spin states. Specifically it reflects the loss of the net transverse magnetisation (i.e., in the *xy*-plane) as it returns to its thermal equilibrium state of zero transverse magnetisation. Similar to longitudinal relaxation, this process is also described by any exponential time course, but in this case it is characterised by a time constant T_2. The transverse magnetization at time *t* after an RF pulse is defined by [90-93]:

$$M_{xy}(t) = M_{xy0} \exp\left(\frac{-t}{T_2}\right) . \tag{10}$$

T_2 is always shorter or equal to T_1. Although for a single resonance the spectral line width at half maximum intensity is given by $1/\pi T_2$, accurate measurements of T_2 are normally performed with a spin echo sequence (π/2 - τ - π - τ – acquisition) [94].

The majority of NMR experimental time is occupied by the recovery delay time (e.g., period (1) in Figure 6) where spin relaxation (mainly the longitudinal relaxation) takes its place. For some nuclei such as ^{29}Si and ^{13}C NMR which are known for their long relaxation times this can greatly affect total experimental time [95, 96].

Inversion recovery

The inversion recovery experiment is used to determine T_1 relaxation time. The standard inversion recovery experiment [92, 93, 97, 98] illustrated in Figure 7.

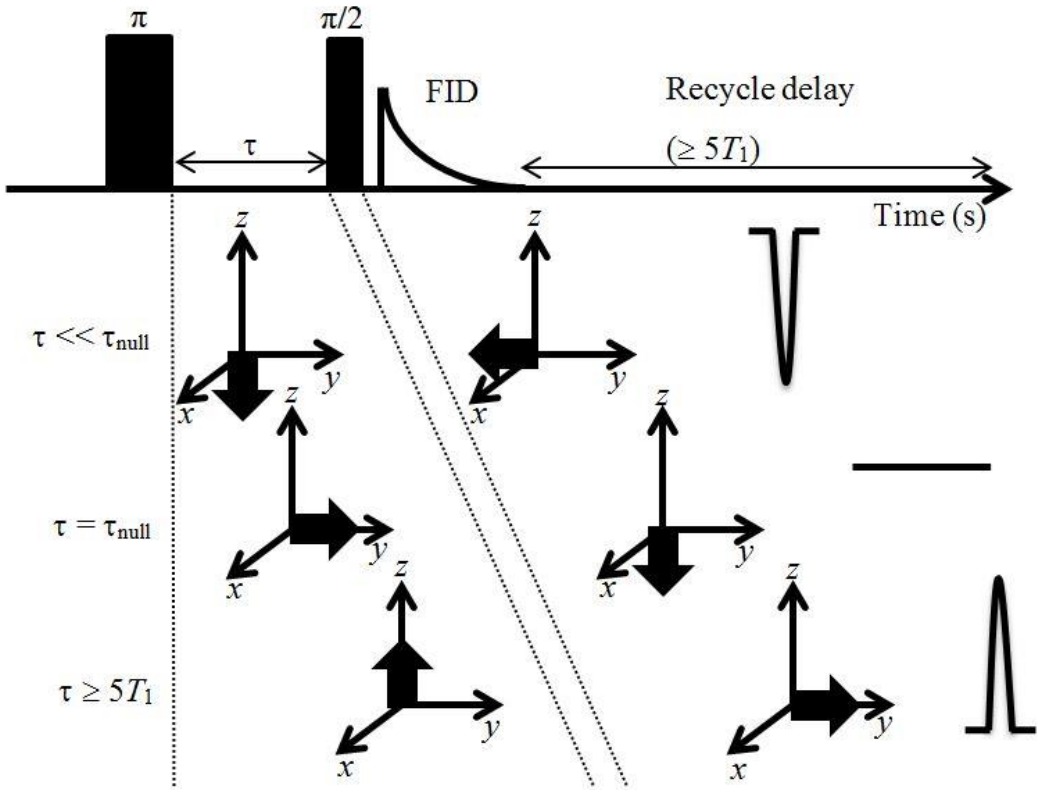

Figure 7. The inversion recovery experiment. The signal intensity changes when τ is varied.

In this sequence the π RF pulse pushes the net magnetisation vector to the –*z*-axis. If the following π/2 RF pulse is applied immediately after, then the net magnetisation vector will then be oriented along the –y-axis giving a maximum negative intensity. By acquiring a series of spectra with different τ, a plot of signal intensity versus τ will reveal an exponential profile as shown in Figure 8.

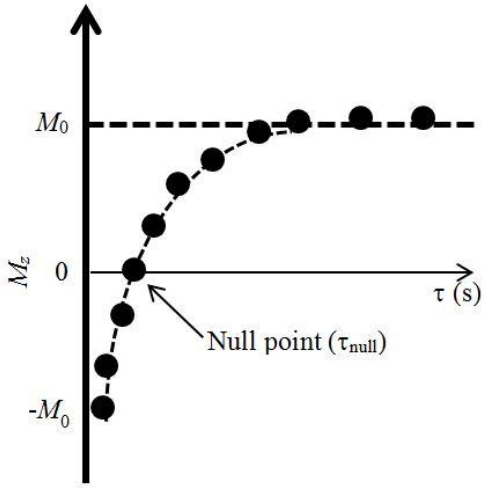

Figure 8. A plot of exponential recovery of M_z versus τ in the inversion recovery sequence.

The signal intensity in the inversion recovery sequence is described

$$M(\tau) = M_0\left(1 - 2\exp\left(-\tau/T_1\right)\right) \tag{11}$$

After one T_1, the net magnetisation relaxes back to 63% of its thermal equilibrium value. For the net magnetisation to relax back to 99% of its thermal equilibrium value, a delay equal to five times T_1 is required [88]. Thus, knowledge of T_1 values is important for conducting many NMR experiments where quantitative results are required.

The τ value when the signal intensity reaches zero (i.e., the "null point"), termed "τ_{null}" is the point at which the longitudinal relaxation has relaxed back to the point M_z = 0. Thus, a rough estimate of T_1 can be obtained from experimentally determining τ_{null} and noting from Eq. (11) that:

$$T_1 = \tau_{null}/\ln(2) \ . \tag{12}$$

More generally, accurate estimates of T_1 require a series of measurements with a range of τ delays as depicted in Figure 8, Eq. (11) is then regressed on to the data to provide the T_1 estimate.

2.7 QUADRUPOLAR NUCLEI

Quadrupolar nuclei (I >1/2) have a non-spherical distribution of electric charge, characterised by a constant called the quadrupole moment, Q [99]. The higher the quadrupole moment is, the more asymmetrical (e.g. ellipsoidal) the charge distribution is.

The spectral line width of a particular quadrupolar nucleus is heavily dependent on the magnitude of its quadrupole moment. For example, ^{2}H nuclei with a relatively low Q = 0.0028 give a reasonably sharp spectral line. In contrast, $^{125}I^{-}$ nuclei with a relatively high Q = 0.6 give a broad spectral line (i.e., $^{125}I^{-}$, half height spectral width ≈ 1800 Hz) [100]. In solid-state NMR, quadrupolar nuclei are well known for showing multiplets with broad line shape [101]. This is due to the fact that quadrupolar interactions are usually stronger than chemical shift effects and/or dipole-dipole couplings [4]. In liquid-state NMR, on the other hand, quadrupolar nuclei are observed as single resonances [102].

The difficulty in measuring quadrupolar nuclei is that some of the quadrupolar nuclei (e.g., ^{23}Na, Q = 0.1) have very short T_1 and T_2 relaxation times [17] by virtue of the efficiency of the quadrupolar relaxation mechanism – especially when subject to a large electric field gradient as, for example, when a quadrupolar ion is bound to a protein binding site [103-105]. As opposed to ^{23}Na nuclei, ^{7}Li ($Q = -4\times10^{-2}$) and ^{6}Li ($Q = -8\times10^{-4}$) have relatively slow relaxation [106-108]. In addition, many quadrupolar nuclei have an inherently low receptivity which is sometimes exacerbated by low natural abundance (e.g., ^{43}Ca has a natural abundance of 0.145%, and an absolute sensitivity of $\sim 9.27\times10^{-6}$ compared to ^{1}H) [105]. Observation of such nuclei often suffers from low sensitivity. Generally, the quadrupolar NMR line shape is distorted due to the first, second and above orders quadrupolar couplings corresponding to I =1, I = 3/2 and above respectively [109, 110].

2.8 DIFFUSION NMR

The random thermal motion of a molecule, also known as Brownian motion [111-113], is one of the most fundamental forms of molecular transport. Brownian motion is the underlying mechanism behind all chemical reactions and binding and aggregation

processes [111, 114, 115]. Self-diffusion, also known as translational diffusion, characterised by a diffusion coefficient D (m^2 s^{-1}), is the measure of Brownian motion in a solution at thermal equilibrium. The diffusion coefficient of a species depends on many factors such as concentration, temperature, and viscosity. As such, diffusion coefficient can provide information on the molecular size [116] and shape [117], reaction kinetics [118], aggregation processes [119], and even the surrounding boundary structures such as cell walls [120].

Diffusion coefficient can be experimentally measured using a range of techniques [121], including pressure decay method [122], capillary methods [123] and fluorescence spectroscopy [124]. However, most of the methods have a very limited sensitivity range. NMR, on the other hand, can measure diffusion coefficients in the range of 10^{-6} to 10^{-15} m^2 s^{-1} [121]. In NMR, there are two methods of measuring diffusion based: relaxation-based [125-129] and PGSE NMR [130]. The two methods are discussed briefly below.

Relaxation-based method

The self-diffusion of a molecule in solution state can be characterised by a specific time constant called rotational correlation time (τ_c). The rotational correlation time is the average time that a molecule requires to rotate by one radian (typically in the range of picoseconds to nanoseconds [91, 128]). The rotational correlation time is determined from T_1 relaxation measurements [27, 34, 126, 131-134]. Once the rotational correlation time is known, the viscosity η of the solution can then be calculated using the Debye equation [135]

$$\begin{aligned} \tau_c &= \frac{4\pi\eta r_s^3}{3kT} \\ \eta &= \frac{3kT\tau_c}{4\pi r_s^3} \end{aligned}, \qquad (13)$$

where r_s is the Stokes radius of the spherical particle. This viscosity parameter can then be used to estimate the friction coefficient f, which in turn provide the diffusion coefficient using the Stokes-Einstein-Sutherland equation [136-138]

$$D = \frac{kT}{f}$$
$$f = 6\pi\eta r_s. \tag{14}$$

Combining Eqns. (13) and Eq. (14) gives

$$D = \frac{kT\,4\pi r_s^3}{6\pi r_s\,3kT\tau_c} = \frac{2r_s^2}{9\tau_c}. \tag{15}$$

Note however, that in the above equations, the observed molecules are assumed to be spherical. Prior knowledge (estimate) of the Stokes radius is also required. In reality, very few molecules, especially macromolecules are even close to spherical in structure. Thus, estimation of the diffusion coefficient using the relaxation method will have limitations, leading to the prevalence of the PGSE method, discussed below.

Pulse gradient spin-echo

The PGSE NMR technique measures the diffusion coefficient from the spin-echo signal attenuation process [28, 139, 140]. A typical PGSE experiment, illustrated in Figure 9, starts with the application of a π/2 RF pulse, reorientating the magnetisation into the transverse plane. A pulsed magnetic field gradient of amplitude *g* and duration δ is applied to spatially encode the spins, thereby forming a magnetisation helix. At the end of the first τ period a π RF pulse is then applied to change the chirality of the helix.

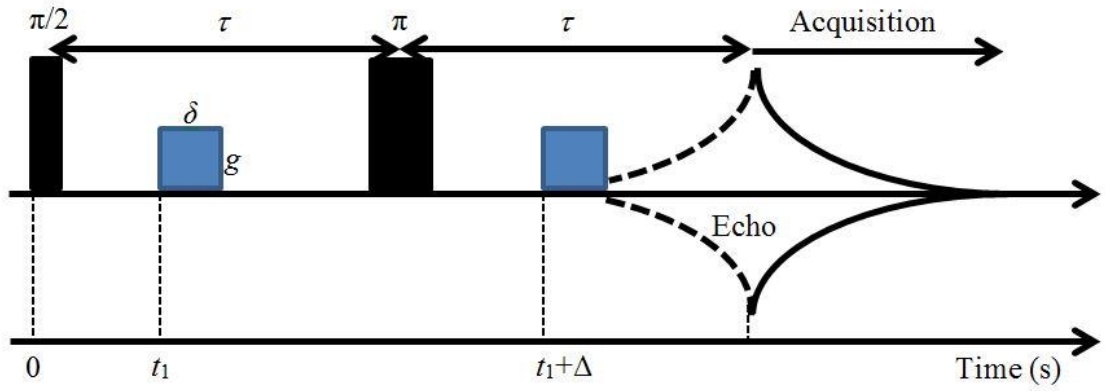

Figure 9. The Hahn-spin echo based PGSE sequence. The black rectangles are RF pulses. The blue rectangles are the (identical) applied magnetic gradient pulses of duration δ and amplitude g. The echo maximum occurs at 2τ and the second half of the echo (denoted by the solid line) is collected as the FID.

During the second τ period second gradient pulse (of the same magnitude and duration) is applied to unwind the helix and decode the spins. This second gradient pulse occurs after a delay Δ after the first gradient pulse. Δ defines the timescale of the diffusion measurement. If there is no diffusion of spins along the direction of the gradient pulses during Δ, complete decoding of the helix will be observed leading to a maximum of the spin-echo signal. However, in reality, self-diffusion results in degraded decoding and consequently an attenuated NMR signal. In a typical diffusion experiment, the PGSE sequence is repeated numerous times with different gradient strengths, and a profile of echo attenuation is obtained. Provided all other parameters are the same, the diffusion coefficient can be estimated by regressing the Stejkal and Tanner equation [28],

$$\begin{aligned} E &= \frac{S(g)}{S(0)} = \exp\left(-\gamma^2 g^2 D\delta^2\left(\Delta - \frac{\delta}{3}\right)\right) \\ &= \exp(-bD) \end{aligned} \tag{16}$$

onto the diffusion data. In the second line of the Eq. (16), all the experimental parameters are combined into the so-called diffusion weighting factor b (also simply known as the b value). Note that in diffusion experiments, as the signal attenuates, so

does the NMR sensitivity. Therefore, a large number of scans are often required to obtain accurate results. A commonly used variant of the PGSE sequence is the pulsed gradient stimulated echo sequence (PGSTE) [141]. It is particularly useful for measuring the diffusion of larger molecules. The important aspects of how it measures diffusion and the analysis of the resulting data are essentially the same as the PGSE.

2.9 SOLVENT SIGNAL SUPPRESSION

With a biological sample, it is common to have a significantly high proportion of H_2O as solvent compared to the solute. For example, in protein structure analysis using ^1H NMR, a protonated solvent is required to observe exchangeable protons within proteins [142, 143]. Thus, a buffer containing 90% H_2O and 10% D_2O (v/v) is commonly used to dissolve biomolecules [144]. In ^1H NMR, the resonance of H_2O appears at ~4.8 ppm and often overlaps with solute resonances of interest. A large solvent signal requires a relatively low RG to avoid receiver saturation [145]. This often leaves the sensitivity enhancement entirely to signal averaging [146]. Other complications such as radiation damping, the demagnetizing field effect, and baseline distortion are commonly observed in the presence of a large solvent peak [147, 148].

The suppression of solvent resonance can be achieved by using pulse sequence based methods (e.g., PURGE [149], WET [150], WATERGATE [151, 152]) and post-processing methods (e.g., [153-156]). As an example, the WATERGATE pulse sequence is discussed in the next subsection. One example of post-processing-based solvent suppression is discussed in Section 3.7.1.

WATERGATE

The WATERGATE pulse sequence [151] (Figure 10) is one of the most robust solvent suppression techniques and it can be combined with PGSE NMR diffusion experiments [157, 158]. Within the WATERGATE sequence, the first $\pi/2$ RF pulse bring the magnetisation to the *y*-axis on the *xy*-plane which is then de-phased by the application of a shaped magnetic gradient pulse with strength *g*, then a selective π pulse inverts all except the solvent magnetisation, and finally the last gradient pulse de-phases the solvent magnetisation further due to the accumulation of the dephasing effect, leaving only the solute magnetisations detectable.

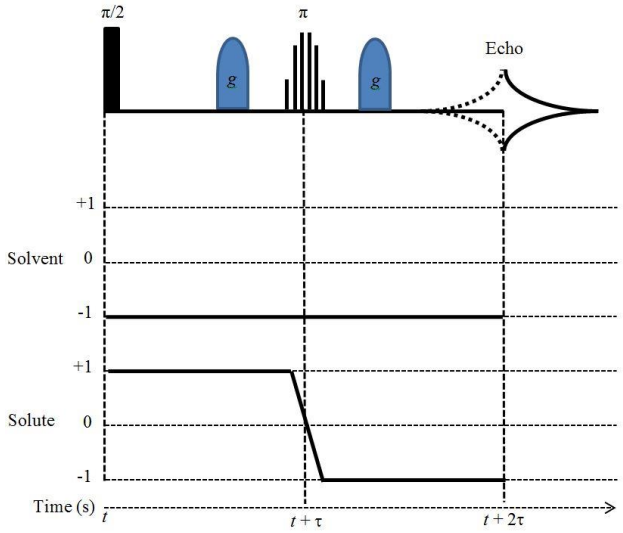

Figure 10. A standard WATERGATE sequence: a selective binomial π pulse (represented by a bar grouping) sandwiched by two identical shaped gradients (*g*). The coherence transfer pathways of the solvent and solute resonances are also shown underneath the pulse sequence by solid black lines. Illustration adapted from [158].

A standard pulse sequence parameter settings for a WATERGATE experiments are: g = 0.1 T m^{-1} for a duration of 1 ms, and τ = 2 ms [158]. Water suppression for PGSE (PGSE-WATERGATE) was also developed (see Price [157]). The application of WATERGATE or the like allows observation of the resonances of dilute solutes and exchangeable protons.

CHAPTER 3. NMR SIGNAL ACQUISITION AND PROCESSING

3.1 NMR SIGNAL

During the signal acquisition, the oscillating voltage which decays exponentially over time is then amplified and demodulated to baseband. Which then digitized through an ADC converter to store the FID numerically. With signal averaging the digitised FIDs are added coherently before visually presented as the FID and later as the spectrum via time to frequency domain transform (e.g., Fourier transform).

3.1.1 Signal amplification and digitisation

As shown in Figure 11, the weak NMR signal is amplified and demodulated by a receiver system containing a preamplifier, an intermediate frequency (IF) amplifier, mixers, and two low pass filters [159]. Without folding of signals, the process signals guarantees "clean" spectra and removal of noise signal folding can improve SNR [160]. The total gain in such a system is typically between 60 – 100 dB.

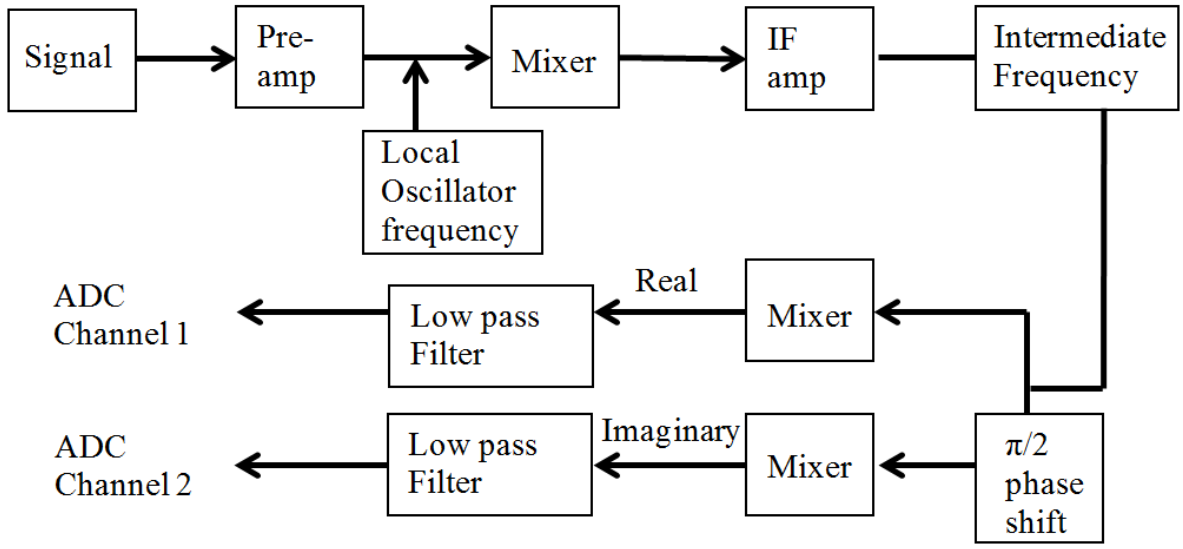

Figure 11. Flow diagram of a quadrature detection receiver system.

If the receiver gain is low, the SNR is often poor; on the other hand, artefacts can be observed when high receiver gain is used in the presence of strong resonances. For example, if there is a strong solvent or solute signal present, a low receiver gain is

usually required to avoid FID being clipped (Figure 12). The spectrum obtained from a clipped FID suffers from both intense baseline and lineshape distortions [161, 162].

There is a very short delay between the last RF pulse application and the beginning of the signal acquisition. This delay called the *group delay* or *dead time* is used to allow the diplexer, which separates the receiver and transmitter, to prevent the current generated by the preamplifier from flowing to the (sensitive) receiver.

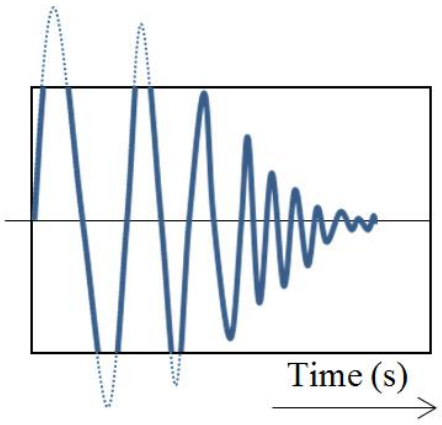

Figure 12. An FID is clipped when a high receiver gain is applied. The dotted line is used to indicate the clipped part of the FID. The height of the box represents the dynamic range of the digitiser and the length of the box represents the effective acquisition time.

The duration of the group delay takes about 60 to 80 data points before the observable FID starts. Meaning the first 60 to 80 data points of the FID signal will be eliminated and so the acquired FID does not start at time = 0 s. Without proper treatment, Fourier transformation of such an FID results in severe spectral artefacts including baseline artefacts especially at the outer region of the spectrum. Commercially available software such as Topspin, MestReNova, Chenomx and other open source such as PepsNMR [163] have algorithms that attempt to remove such artefacts. The lost data during this group delay can also be estimated by backward Linear Prediction method [164-166].

As shown in Figure 13, the relationship between receiver gain (RG) and SNR was studied experimentally. A ^{23}Na 105.8 MHz NMR spectrum of 100 mM NaCl in D_2O was obtained in a pulse acquire experiment. Each measurement was made with one scan and with various receiver gain values (i.e., RG = 2^k, where k = 0, 1, 2… 14).

As shown in Figure 13a and b, the spectral amplitude increases linearly with RG while the SNR experiences a sharp rise when RG ≤ 32 and then levels off. Therefore, the RG level is not necessarily required to be set to its maximum value to yield high SNR. More details of the receiver gain function are studied diligently by Hoult [159, 167] and Mo [145, 168, 169].

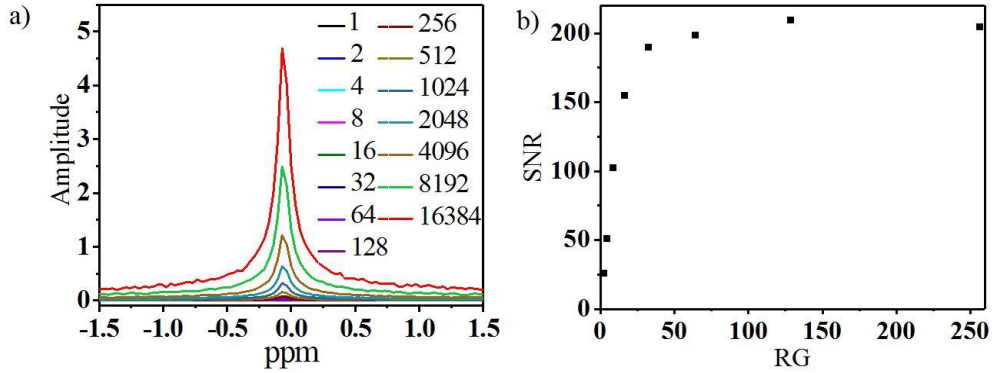

Figure 13. a) The stacked ^{23}Na spectra of 100 mM NaCl in D_2O with various RG values. b) The SNR values calculated for the spectra shown in a).

3.1.2 Free induction decay

Without the spin relaxation process, the free evolution of the transverse components of the magnetisation is given by,

$$\begin{aligned} M_x(t) &= M\cos(\omega_0 t+\phi) \\ M_y(t) &= M\sin(\omega_0 t+\phi) \end{aligned} \quad . \tag{17}$$

where M is the magnitude of the magnetisation, ϕ denotes the initial phase and ω_0 is the Larmor frequency (see Chapter 2). The acquired signal is then given by,

$$\begin{aligned} S(t) &= S_x(t)+iS_y(t) \\ &= S_0\cos\omega_0 t+iS_0\sin\omega_0 t \\ &= S_0\exp(i\omega_0 t) \end{aligned} \tag{18}$$

where, without loss of generality $\phi = 0$, and $S_x(t)$ being defined by the first term on line two of Eq. (18) and $S_y(t)$ by the second. S_0 is simply proportional to M, its actual magnitude being unimportant. Adding the effects of transverse relaxation T_2 (see Section 2.6) to Eq. (18) gives,

$$S(t) = S_0 \exp(i\omega_0 t) \exp\left(\frac{-t}{T_2}\right) . \tag{19}$$

Both Eqs. (18) and (19) assume that signal at $t = 0$, the S_x (t) components have its maximum magnitude and S_y (t) has zero magnitudes (i.e. $\phi = 0$ as above). With experimentally collected data, this is often not the case and the phase ϕ may be unknown. The phase shift parameter ϕ can be included in the complex signal as followings,

$$S(t) = S_0 \exp(i\phi) \exp(i\omega_0 t) \exp\left(\frac{-t}{T_2}\right) \tag{20}$$

As discussed before, every experimentally measured signal (i.e., FID) contains noise. Since the noise comes from multiple sources, its distribution cannot be expressed by a simple formula. Here it is simply defined as w_t and added to the Eq. (20)

$$S(t) = S_0 \exp(i\phi) \exp(i\omega_0 t) \exp\left(\frac{-t}{T_2}\right) + w_t . \tag{21}$$

Eq. (21) represents the mathematical formula for the signal obtained from liquid state spin-l/2 nuclei. Most samples are composed of many nuclei in different chemical environments and thus possessing different Larmor frequencies. The signals from such samples are thus summations over the signals from all the individual nuclei. The nuclei can be divided into classes with each class being composed of nuclei in the same chemical environment. Nuclei in different chemical environments will have different

Larmor frequencies and relaxation times, giving a signal that is a summation over these different classes,

$$S(t) = \sum_k S_0^k \exp\left(i\phi^k\right)\exp\left(i\omega_0^k t\right)\exp\left(\frac{-t}{T_2^k}\right) \tag{22}$$

where the superscript k's denote variables that now depend on the class of nuclei. As an example water has one class of hydrogen nuclei (all the protons are in the same chemical environment) giving one peak but ethanol has multiple classes (CH_3 hydrogens, CH_2 hydrogens and OH hydrogens) giving more than one peak. When the acquired signal is digitised – $S(t)$ becomes x_n with $x_n = S(n\Delta t)$, i.e. the signal is sampled at time intervals of Δt. Taking account of multi-resonance and digitisation, the FID signal $S(t)$ is rewritten as x_n, the sum of K exponential decay sinusoids plus the noise w_n as,

$$x_n = \sum_{k=1}^{K} A_k \exp\left(i\phi_k\right)\exp\left(\left(-d_k + i2\pi f_k\right)n\Delta t\right) + w_n . \tag{23}$$

The acquired signal can be thought of as a vector, each component (n = 0, 1,.., N-1) being given by Eq. (23). The n^{th} component of the vector is the signal at time $n\Delta t$. The relaxation parameter (t/T_2) is replaced by damping factor d. Other parameters A_k, ϕ_k, and f_k represents the signal amplitude, the phase and the frequency of the k^{th} exponentials (i.e. there are K classes of nuclei).

3.1.3 Fourier transform

With the introduction of Fourier transform NMR, the Fourier transform became the fundamental method of choice for domain transformation between time and frequency [170]. Let $x(t)$ to denote a time domain function (i.e., x_n in Eq. (23)), Fourier Transformation of $x(t)$ [170, 171] is given by:

$$X(f) = \int_{-\infty}^{\infty} x(t)\exp\left(-2\pi i f t\right)dt , \tag{24}$$

where $X(f)$ represent the frequency-domain data and its inverse Fourier Transformation (IFT) is given by:

$$x(t) = \int_{-\infty}^{\infty} X(f) \exp(2\pi i f t)\, df \,. \tag{25}$$

Eq.(24) is also known as continuous time Fourier transform (CTFT). However, since the FID starts at time $t = 0$, integration in Eq. (24) goes from $0 < t < \infty$ when converting FID from the time to the frequency domain. Since the signal has been digitised to transform from the time to the frequency domain requires the "*Discrete Fourier Transform"* to be applied instead.

Discrete Fourier transform

The discrete Fourier transform (DFT) is slightly different from CTFT, the formula is given by [171]:

$$X_n = \sum_{k=0}^{N-1} x_k \exp\left((-2\pi i n k)/N\right) \tag{26}$$

and its inverse is

$$x_k = \frac{1}{N} \sum_{n=0}^{N-1} X_n \exp\left((2\pi i n k)/N\right), \tag{27}$$

for $n = 0, 1, \ldots, N\text{-}1$ and $k = 0, 1, \ldots, N\text{-}1$. Explaining a little further on Eq. (26), if

$$b_n = \frac{2\pi n k}{N}$$

then, Eq. (26) can be simplified into

$$X_n = \left[x_0 \exp\left(-b_0 i\right) + x_1 \exp\left(-b_1 i\right) + \cdots + x_{N-1} \exp\left(-b_{N-1} i\right) \right], \quad (28)$$

where the exponential part of this equation can be expanded into sine and cosine function following Euler's formula [172]

$$X_n = \left\{ \begin{array}{l} x_0 \left[\cos\left(-b_0\right) + i \sin\left(-b_0\right) \right] + x_1 \left[\cos\left(-b_1\right) + i \sin\left(-b_1\right) \right] + \cdots \\ + x_{N-1} \left[\cos\left(-b_{N-1}\right) + i \sin\left(-b_{N-1}\right) \right] \end{array} \right\} \quad (29)$$

which leads to the sum of real and imaginary parts,

$$X_n = \left(\mathrm{Re}_j + \mathrm{Im}_j \, i \right). \quad (30)$$

Just like the time-domain data, the spectral domain is also complex valued.

3.1.4 Other spectral properties

Nyquist theorem

It is important for the FID to be collected at a Nyquist sampling rate in order to represent the resonances at the accurate frequency after FT. This basically states that if the highest frequency present is f then the sampling period must be $1/(2f)$. That is, two data points must be collected per one sinusoidal period [173]. The time interval of this sampling rate in the time domain is called dwell time (DW). The range of frequencies is called the spectral width (SW). The relationships between the SW and DW at Nyquist theorem is represented as:

$$SW = \frac{1}{2DW} \quad (31)$$

Nyquist sampling method only applies to the FID measured at the constant DW which then transferred to the frequency domain by FT.

Uniform and non-uniform sampling

Traditionally, all FIDs are collected with uniformly spaced consecutive time increments (i.e., uniform sampling US). If the sample rate satisfyies the Nyquist theorem, the resonance frequency can be obtained accurately after Fourier transformation. This simplicity and accuracy have made US followed by FT the standard signal processing procedure in NMR [174]. However, concerns over the trade-off between NMR resolution and sensitivity versus the length of the acquisition time lead to the development of the non-uniform sampling (NUS) approach [175]. In NUS the FID is sampled at unequal periods. NUS schemes are often designed to collect more data at the beginning of the signal decay with shorter time intervals than in the US approach, and the time interval increase as the acquisition time prolong [176]. In practice, the US FID is normally collected with an acquisition time~$3T_2$ in order to avoid FID truncation - which would result in baseline distortion and loss of spectral resolution. However, after 1.26 times T_2 the SNR decreases with increase in total acquisition time [175, 177-179].

NUS has now been widely adopted in multidimensional NMR experiments [175, 176, 180-183] and imaging [184]. In multidimensional NMR experiments, long experimental time is one of the concerns along with sensitivity and resolution [185]. Application of NUS can allow for dramatically shortened experimental times without loss of either sensitivity or resolution [175]. The conventional FT (including DFT and FFT) of an NUS dataset often yields non-lorentzian distorted resonances unless the NUS data is carefully supplemented with zeroes [186]. NUS is performed using either an on- or off-grid scheme where "on-grid" is simply a subset of the normal Nyquist US scheme [187] whilst an off-grid scheme (i.e., radical sampling) does not follow a Cartesian grid [187, 188]. A radical sampling method is often applied to nD NMR with narrow peak width [189]. To successfully reconstruct frequency domain from UNS FID data without major artefacts, a modified FT based algorithm such as nonuniform discrete Fourier transform (NDFT), Maximum-Entropy [190], and Iterative Soft Threshold (IST) [191, 192] reconstruction methods can be applied.

Spectral line shape

The real and imaginary part (when $\phi = 0$) of the frequency data is depicted as the absorption spectrum (Figure 14 a) and the dispersion spectrum (Figure 14 b) respectively.

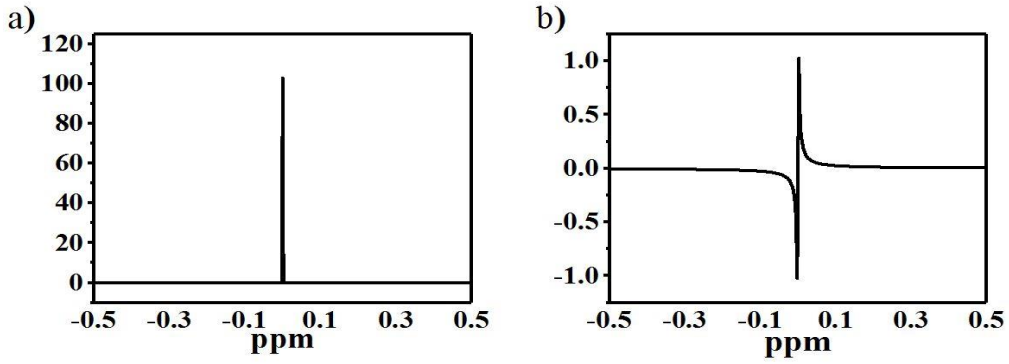

Figure 14. The frequency domain a) real spectra (absorption) and b) imaginary spectra (dispersion).

If the magnetisation at the time of acquisition was not initially aligned along x then the spectrum will need to be phased by multiplying it by a phase factor; this is a relatively minor processing step described in more detail in the next section. As Figure 14 shows, not only the spectral shape but also the spectral width and amplitude are significantly different between the absorption and dispersion spectrum. Only the real part of the frequency data illustrated in the absorption spectrum is used for the NMR analysis. The noiseless absorption spectral line shape is called the Lorentzian function. Figure 15 is presented to clarify the differences between Lorentzian and Gaussian, which is another major function often used for spectral line fitting.

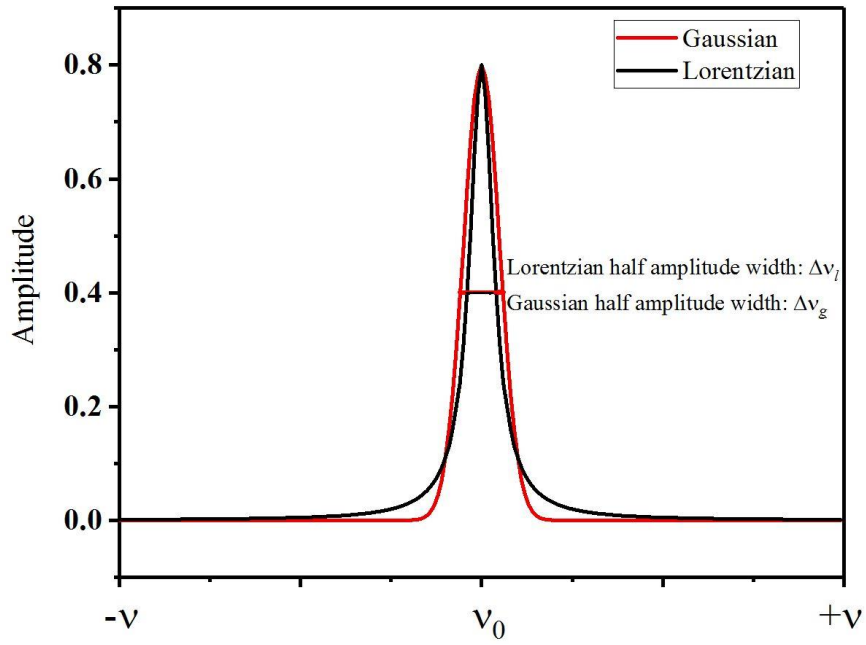

Figure 15. Lorentzian (black line) and Gaussian (red line) spectral line shape and its difference.

The obvious difference between a Lorentzian and Gaussian line shape is the rate of the transition from the baseline to the peak maximum amplitude. The Gaussian and Lorentzian line shape are given mathematically [193] by

Gaussian

$$A_g = \frac{2\sqrt{\ln 2}}{\sqrt{\pi}\Delta\nu_g}\exp\left[-\left(\frac{2\sqrt{\ln 2}}{\sqrt{\pi}\Delta\nu_g}(\nu-\nu_0)\right)^2\right], \tag{32}$$

Lorentzian

$$A_l = \frac{1}{\pi}\frac{\Delta\nu_l/2}{(\nu-\nu_0)^2+(\Delta\nu_l/2)^2}. \tag{33}$$

Theoretically, all real resonances would have a Lorentzian line shape. However, spectral line shape deviation may be observed as a result of the presence of eddy currents, magnetic inhomogeneity and other deviations from the ideal situation described in the foregoing. There are many line shape correction methods available that are both general and specific to the origin of lineshape distortion [194-196].

Phase correction

The phase parameter ϕ is often ignored, and it is assumed that the signal at time zero has maximum amplitude along the *x*-axis (and zero along the *y*-axis). With experimentally collected data the phase of the signal is most likely shifted such that the Fourier transformed spectrum has somewhere between the absorption and dispersion line shapes along both the real and imaginary axes. The majority of the NMR processing software has its own automatic and manual phase correction modules embedded. However, when the measured signal goes through signal processing, the phase parameter often requires readjustment. The basic phase correction formula has two orders of phase correction (i.e., zeroth and first order). Zeroth order phase correction is performed by the multiplication of the FID in Eq. (23) by $\exp(i\phi_{\text{corr}})$:

$$\begin{aligned}\exp\left(i\phi_{\text{corr}}\right)x(n) &= \exp\left(i\phi_{\text{corr}}\right)\left[\sum_{k=1}^{K} A_k \exp\left(i\phi_k\right)\exp\left(\left(-d_k + i2\pi f_k\right)n\Delta t\right)\right] \\ &= \sum_{k=1}^{K}\exp\left(i\left(\phi_{\text{corr}} + \phi_k\right)\right)\sum_{k=1}^{K} A_k \exp\left(\left(-d_k + i2\pi f_k\right)n\Delta t\right)\end{aligned} \tag{34}$$

The zero order phase correction parameters are often found by a trial and error process until the spectrum obtains the absorption line shape (this is often done dynamically and visually). Another major phase error is known as a frequency dependent phase shift [88]. In most cases, the phase correction required is proportional to the resonance offset and the parameter used to correct it is known as *first-order* phase correction. This is essentially a multiplication of the spectrum by a factor $\exp(i\phi_1\omega)$. A combination of both first and the second phase correction is often required and is an iterative process, although there are some automated methods are available from various references [197-202].

There are a few spectral distortions that cannot be corrected by phase correction. The origin of these spectral distortions are different from those that cause phase errors. An example is the Fourier ripples that appear on either side of the peak in Figure 16b inset. These are due to extensive FID truncation (Figure 16a**).** Essentially, there is a convolution of the Lorentzian and Sinc functions.

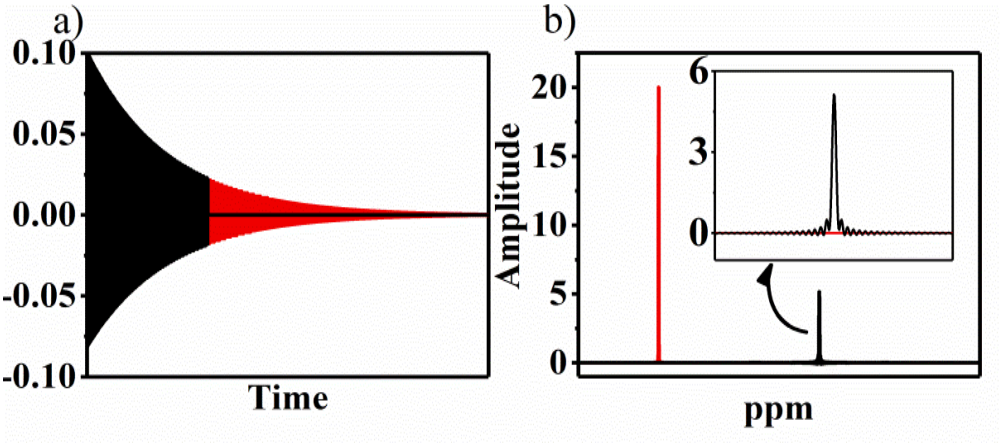

Figure 16. The effect of FID truncation in spectral sensitivity and resolution. a) overlapped comparison of full FID (red) and heavily truncated FID (black). b) Spectra of FT full FID (red) and FT of truncated FID (black)

Figure 16 shows the Fourier ripples due to the heavy FID truncation. Since the lost part of the decaying sinusoid signal also possess the resonance property (e.g., amplitude, phase, frequency, and damping factors). A window function (See Section 3.4.2) can be applied to remove such artifacts.

Another common spectral line shape distortion may be observed due to poor shimming [203]. Shimming is a part of the signal acquisition preparation process. Even with the high field superconductor magnet, inhomogeneity of the magnetic field is inevitable [203]. Inhomogeneity issue of the B_0 field arises from multiple sources such as the magnet, probe or even the sample itself [204]. Figure 17 shows the example of the FID and its spectra of the good shim and bad shim (off z shim). Bad shimming can lead to incorrect, broad, and asymmetrical spectral line shape, wrong spectral and FID intensities are observed. Such measurements are often not able to be used for analysis.

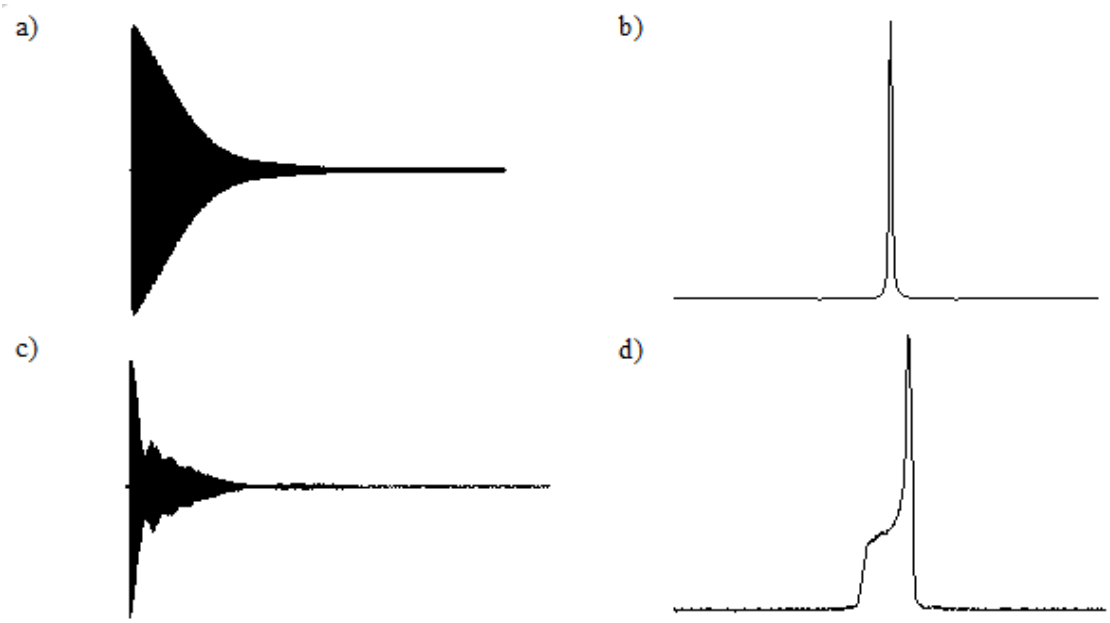

Figure 17. Example of good shimming and bad shimming – how the FID and spectrum appear. a) FID of the good shim FID. b) The spectrum of good shim FID. c) FID collected where z-direction of the static magnetic field is not homogeneous. d) The spectrum of the badly shimmed FID.

A set of shim coils that are wrapped very close to the sample are the key to minimise the overall static magnetic field inhomogeneity by the generation of compensating magnetic fields. On some occasions, the shimming process can be a time-consuming task due to the fact that the current going through each of the shim coils are changing the B_0 field individually such that constant readjustment is required. To shorten the shimming process, automatic gradient shimming algorithms [205] were developed. Poorly shimmed spectra not only lose their Lorentzian line shapes but also lose their spectral sensitivity. These two sources of spectral line distortion (along with other sources) introduce distortions that cannot be solved by phase correction. Much attention is required during the pre-acquisition preparation period to ensure such distortions are at acceptable levels.

Baseline distortion artefacts can also often be found due to instrumental field drift or presence of macromolecule signals or large solvent signals [206, 207]. The three steps baseline correction algorithm by Pearson [208] for an example, can correct for these effects. Those three steps are: the spectral baseline is first corrected starting from a determination of signal and baseline noise within the frequency domain; this is

followed by smooth baseline modelling using a function such as cubic spline which is completed by subtracting the baseline model from the original signal.

Wavelet transform

Wavelet transform (WT) is another mathematical function which translates between the time and the frequency domain by using a function called mother wavelet ψ. Similar to FT, WT also has continuous wavelet transform (CWT) and discrete wavelet transform (DWT). While the FT has one formula for domain transform, there is an infinite number of mother wavelet functions that can be applied [209]. Each mother wavelet function has a specific boundary called compact support. Within the compact support region, the sum of the area underneath every wavelet function must be equal to zero [210]. Chosen mother wavelet function is then two parameters dilation (s) and translation (u) used to fit the FID data $x(t)$ as follows:

$$\begin{aligned} W(u,s) &= \int_{-\infty}^{\infty} x(t)\psi_{u,s}(t)\,dt \\ &= \left\langle x, \psi_{u,s} \right\rangle \end{aligned}, \tag{35}$$

where

$$\psi_{(u,s)}(t) = \frac{1}{\sqrt{s}}\psi\left(\frac{t-u}{s}\right). \tag{36}$$

The function $\psi_{(u,s)}(t)$ is called daughter wavelet and the ψ itself is the original function which known as the mother wavelet. The factor $(1/\sqrt{s})$ in Eq. (36) is a weighting function and the whole translation process is done by computing the inner product of $x(t)$ and $\psi_{u,s}$. Translation parameter determines the location of the wavelet function along the x-axis, and the dilation parameter defines the size of the wavelet function thus the parameter must be positive ($s > 0$). When the dilation parameter increases, the wavelet function stretches having wider compact support region. The stretched wavelet will be beneficial in analysing coarse features and gain superior frequency precision.

3.2 NOISE

3.2.1 Introduction

The presence of noise in the measured signal is an inevitable problem in NMR studies. The noise sources can be varied: the currents that run through the spectrometer, within the sample itself, and also influenced by other external factors [167, 211-218]. From the similarity of the numerical signal presentation between acoustic and NMR measurements, many NMR signal processing theories and algorithms are adapted from acoustic signal processing methods [219].

3.2.2 Types of noise

Majority of the noise behaves randomly within the constant amplitude range. When the noise is independent of the frequency and possesses a constant spectral power density, such noise form is called white noise. When the noise is frequency dependent and has a specific noise power pattern then it is called non-white noise [220].

White Gaussian noise

In simulation studies, especially to test signal processing methods, white Gaussian noise is often added to a noiseless FID [221]. As the name suggested, white Gaussian noise follows the Gaussian probability density and being frequency independent:

$$f(x) = \frac{1}{\sqrt{2\pi\sigma}} \exp\left[-\frac{(x-\mu)^2}{2\sigma^2} \right] \tag{37}$$

where $-\infty < x < \infty$, μ is the mean and σ^2 is the variance (σ is the standard deviation). The term "white" signifies that the noise distribution is independent of frequency. Alternatively, it can be characterised as noise such that all sample points are drawn from the same distribution independently. Figure 18 The distribution pattern and the spectral presentation of three major noise types: uniform, white Gaussian and flicker noise are presented in Figure 18 as examples.

In Figure 18, both the white Gaussian noise and flicker noise histograms show a Gaussian distribution whereas the uniform noise histogram is clearly non-Gaussian. While the flicker noise has a Gaussian distribution it is not white noise as the probability distribution for each data point is influenced by its immediate predecessor. Flicker noise is often referred to as pink noise. In NMR thermal noise and shot noise (which are both described later in this section) both follow this white Gaussian noise pattern. Gaussian white noise theory in NMR spectroscopy in details can be found in [222].

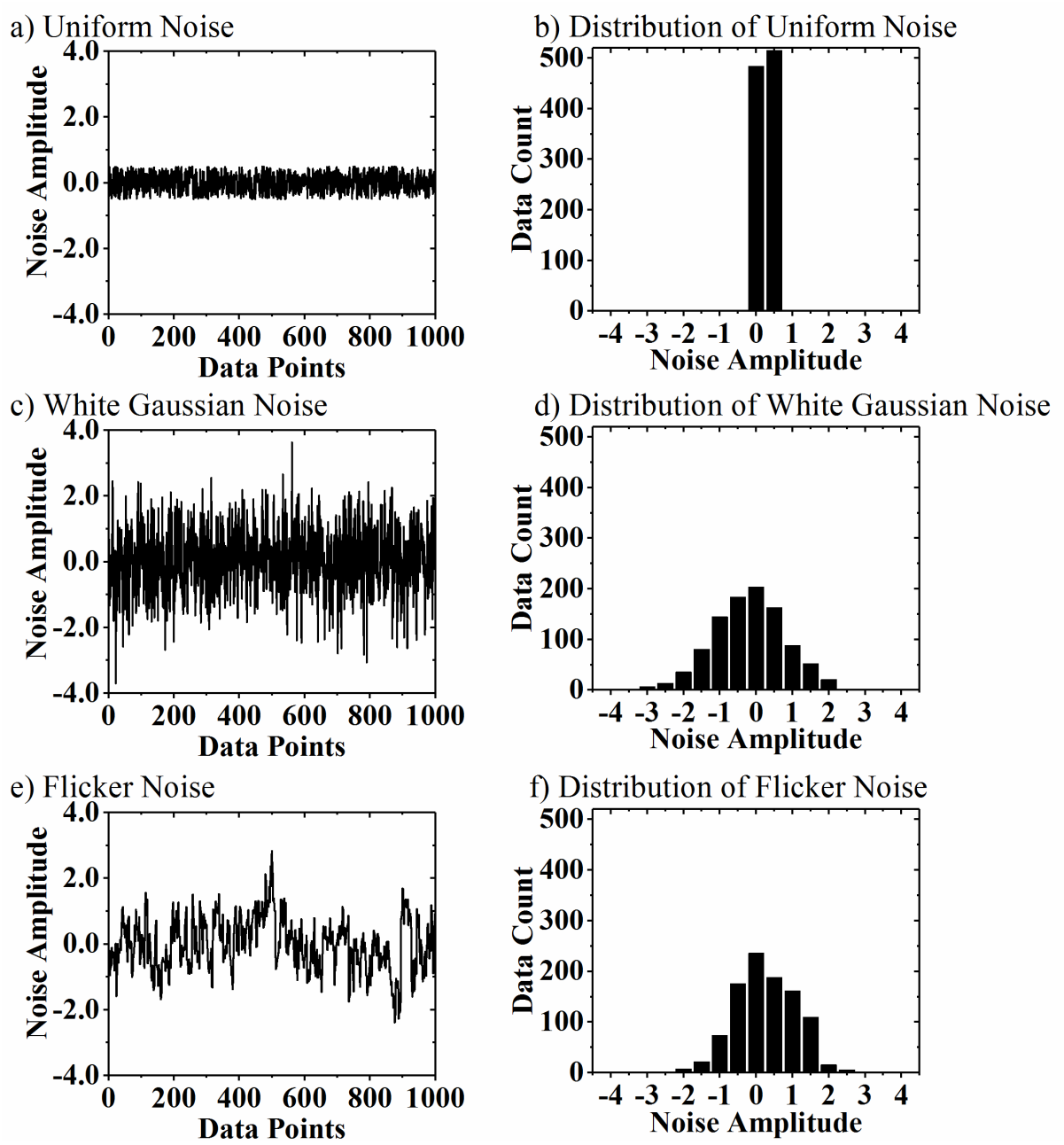

Figure 18. Comparison of three different simulated noise patterns and their distributions: a) uniform noise spectrum of amplitude range between -0.5 to 0.5; b) histogram of the uniform noise amplitude; c) white Gaussian noise spectrum; d) histogram of white Gaussian noise amplitude distribution; e) flicker noise spectrum; f) histogram of flicker noise amplitude distribution.

Non-white noise

Flicker noise as shown in Figure 18 c) and d) is a good example of non-white noise. The flicker noise spectrum and the distribution plot shows randomness. With sampling

and filter frequency not following the symmetrical spectral density and/or band-width being less than its cut-off frequency, the real and imaginary noise sinusoids will not have a π/2 phase difference and the signal exhibit correlations in noise signal [223]. The collected noise signal such as environmental, flicker noise is then considered to be non-white noise.

3.2.3 Origin of noise in NMR

Thermal noise

Majority of the noise collected during the signal acquisition is thermal noise. Thermal noise is also known as Johnson noise [224], Nyquist noise [225], and white Gaussian noise [223]. The power spectral density of thermal noise is near constant throughout both time and frequency domains. As a result, the amplitude of thermal noise in the frequency domain follows a Gaussian distribution and being frequency independent means the thermal noise is a white noise. Thermal noise is the mean-squared value of the electromagnetic force found in the circuit due to the thermal fluctuation of the electromagnetic modes coupled to the charged carriers [223-225]. Thermal noise is depending on the resistance and temperature of the detection coil, sample, and the temperature of the amplifier within the circuit. As Figure 19 shows, there is no external voltage input, yet thermal agitations arise due to a stochastic motion of electrons in the conductor [225]. The root mean squared voltage of this thermal agitation in a narrow frequency band is given by

$$V_N = \sqrt{4k_B TR\Delta f}\ , \tag{38}$$

where R is a resistance in ohms, Δf is the frequency bandwidth. As Eq. (38) suggested, the thermal noise reduction is highly dependent on the temperature within the circuit and also the frequency bandwidth. The temperature change leads to experimental condition changes that may not be suitable for the study. Also shortening the spectral bandwidth would lead to much longer acquisition time. For further information, the derivation of the thermal noise equation is presented in the following context.

Derivation of thermal noise

Let us assume there are two resistors with the equal resistance R located within the circuit at L distance apart from each other in the loop as shown in Figure 19. Both of the resistors are at the equal temperature T which generates the thermal fluctuation voltage (V). This voltage travel down the circuit to the other resistor, leading to a current (I) and measured as a power (P) in a relation of $P = IV = I^2R$.

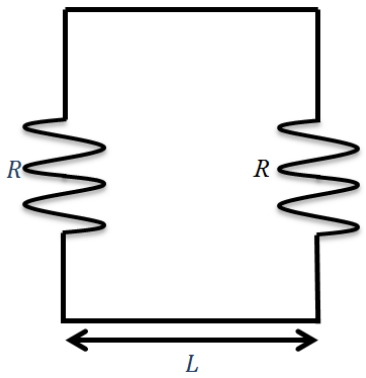

Figure 19. Circuit diagram for thermal noise. Two equal resistors R are placed in the loop with L distance apart from its both edges.

The thermal fluctuation voltage involves transferring of electromagnetic energy which can be viewed as the light wave travelling L distance at the velocity of c' and the angular frequency of ω [223-225]. The voltage of the wave function travelling to the right (positive) direction V_R is given by

$$V_R = V_{R0} \exp i(\kappa x - \omega t), \tag{39}$$

and the voltage of the wave function travelling to the left direction V_L

$$V_L = V_{L0} \exp i(-\kappa x - \omega t) \tag{40}$$

where V_{R0} and V_{L0} are the original amplitude of the voltage travelling to the right and left direction respectively, the $\kappa = \omega/c'$ is the wavenumber, the x is the distance

$(0 \leq x \leq L)$ and t as the time that wave travelling. If the direction of the wave is omitted from the Eq. (39) and Eq. (40), the standing waves $V(x, t)$, or the normal modes can be calculated by assuming the $V_{R0} = V_{L0} = V_0$:

$$\begin{aligned} V(x,t) &= V_0 \exp i(\kappa x - \omega t) + V_0 \exp i(-\kappa x - \omega t) \\ &= 2V_0 \exp(-i\omega t)\cos(\kappa x) \end{aligned} . \tag{41}$$

This standing wave function is true only if the following condition is satisfied

$$\begin{aligned} & L = m\frac{\lambda}{2}, \\ & \text{or} \\ & \kappa = \frac{m\pi}{L} \end{aligned} \tag{42}$$

Where m is simply an integer and the λ is a wavelength. The interval between the standing waves in terms of the wavenumber κ is equal to π / L. The number of standing wave (modes) from κ to $\kappa + d\kappa$ denoted as $N_\kappa d\kappa$ is

$$N_\kappa d\kappa = \frac{L}{\pi} d\kappa \ . \tag{43}$$

The Eq. (43) is true only if the distance L is greater than the wavelength λ. Since the frequency f is equal to the velocity divided by the wavelength, it leads to $f = c' \kappa / 2\pi$. Thus the frequency interval $df = c' \, d\kappa / 2\pi$ and the Eq. (43) can be rewritten in frequency range from f to $f + df$, with the same number of standing wave $N_f df$

$$N_f df = \frac{2L}{c'} df \ . \tag{44}$$

The density of standing wave per unit length per unit frequency interval (ρ_f) is then defined by dividing the Eq. (44) by unit length and frequency interval (Ldf):

$$\rho_f = \frac{N_f df}{Ldf} = \frac{2}{c'} \tag{45}$$

If there are voltage and movement through thermal fluctuation, there will be energy involved. The simplest form of explaining the thermal fluctuations travelling through the circuit is as the energy in the form of photons travelling in wave function from one resistor to another. If N number of photons is found in each standing wave, then the energy state (E_N) will be

$$E_N = Nhf\,, \tag{46}$$

where h is Planck's constant. If the E_N follows Boltzmann distribution at the constant temperature T, then the energy state at thermal equilibrium state, $p(E_N)$, is proportional to:

$$p\left(E_N\right) \propto \exp\left(-E_N / k_B T\right) \tag{47}$$

If the number of photons is infinite ($0 < N < \infty$), the probability distribution of the photon $p(N)$ is

$$p\left(N\right) = \left[1 - \exp\left(-hf / k_B T\right)\right] \exp\left(-Nhf / k_B T\right). \tag{48}$$

Then the average number of photons in the standing wave $\bar{N}$ is given by

$$\bar{N} = \sum_{N=0}^{\infty} Np\left(N\right) = \left[1 - \exp\left(-x\right)\right] \sum_{N=0}^{\infty} N \exp(-Nx) \tag{49}$$

which can simplify to

$$\begin{aligned}\bar{N} &= \left[1-\exp(-x)\right]\sum_{N=0}^{\infty} N\exp(-Nx) \\ &= -\left[1-\exp(-x)\right]\frac{\partial}{\partial x}\sum_{N=0}^{\infty}\exp(-Nx) \quad \because N\exp(-Nx) = \exp(-Nx)\frac{\partial}{\partial x} \\ &= -\left[1-\exp(-x)\right]\frac{\partial}{\partial x}\frac{1}{\left[1-\exp(-x)\right]} \\ &= \left[1-\exp(-x)\right]\frac{\exp(-x)}{\left[1-\exp(-x)\right]^2} = \frac{1}{\exp(x)-1} \\ &= \frac{1}{\exp(hf/k_BT)-1} \quad \because x \equiv hf/k_BT .\end{aligned} \tag{50}$$

Now combining Eq. (45) and Eq. (46) using the average number of protons in the standing wave obtained from the Eq. (50) which will give the average energy per unit length and bandwidth $\bar{E}_{lf}$:

$$\bar{E}_{lf} = \rho_f \bar{N} hf = \frac{2}{c'}\frac{1}{\exp(hf/k_BT)-1}hf = \frac{2hf}{c'\left[\exp(hf/k_BT)-1\right]}. \tag{51}$$

Recalling that there are two identical resistors that each resistor carries half of the energy per unit length, bandwidth, times the velocity c'. The averaged power per bandwidth $\bar{P}_f$ is given by

$$\bar{P}_f = \frac{1}{2}E_{lf}c' = \frac{hf}{\exp(hf/k_BT)-1}, \tag{52}$$

and multiplying the bandwidth Δf to the $\bar{P}_f$ to estimate the total averaged power $\bar{P}$

$$\bar{P} = \bar{P}_f \Delta f = \frac{hf\,\Delta f}{\exp\left(hf/k_B T\right) - 1}. \tag{53}$$

Now recalling the basic Ohm's law

$$\begin{aligned} P &= V^2/R \\ V &= IR \end{aligned}. \tag{54}$$

Reformatting the Eq. (54) by replacing the R by $2R_0$ since the current run through both resistors, and similar changes to V with V_0, I with I_0, and P with P_0. The current I_0 with the amplitude of V_0 is

$$I_0 = V_0/2R_0 . \tag{55}$$

Remembering from the Eq. (52) and Eq. (53) that the power P_0 is thus

$$\begin{aligned} P_0 &= I_0^2 R = V_0^2/4R \\ V_0^2 &= 4RP_0 \end{aligned} \tag{56}$$

and knowing there is no outsourced applied voltage in the circuit, the averaged outsourced voltage is $\bar{V} = 0$. The mean squared voltage at each resistor $\overline{V^2}$ is

$$\overline{V^2} = 4R\bar{P} = \frac{4Rhf\,\Delta f}{\exp\left(hf/k_B T\right) - 1} . \tag{57}$$

Therefore, the mean squared voltage difference $\overline{(\Delta V)^2}$ is

$$\overline{(\Delta V)^2} = \overline{V^2} - \bar{V}^2 = \overline{V^2} = \frac{4Rhf\,\Delta f}{\exp(hf/k_BT)-1} \ . \tag{58}$$

Since the $hf << k_BT$, the exponential in the Eq. (58) is then

$$\exp(hf/k_BT) \cong 1 + \frac{hf}{k_BT} \ , \tag{59}$$

applying the Eq. (59) to the Eq. (50) simplify $\bar{N}$ to

$$\overline{N} = \frac{1}{\exp(hf/k_BT)-1} \cong \frac{1}{1+\frac{hf}{k_BT}-1} = \frac{k_BT}{hf} \ , \tag{60}$$

and applying the Eq. (60) to the Eq. (53) will lead to the averaged power per standard wave measured at each resistor

$$\bar{P} = k_BT\Delta f \ . \tag{61}$$

Finally, combining Eq. (58) and Eq. (60) to simplify the thermal fluctuation voltage mean square V_N^2 and its root mean squares V_N becomes

$$\begin{aligned} V_N^2 &\equiv \overline{(\Delta V)^2} = 4Rk_BT\Delta f \\ V_N &\equiv (\Delta V)_{rms} = \sqrt{4Rk_BT\Delta f} \end{aligned} \tag{62}$$

■

Shot noise

Shot noise may also know as photon noise, contact junction noise and Schottky noise. Shot noise first discovered its origin from the vacuum tube circuits in 1918 [226]. Unlike thermal noise, shot noise is independent of temperature which measures the

current running through at the certain point of the circuit [227]. However, the electron which carries the current colliding at the random point of the circuit thus the collected shot noise follows the white Gaussian distribution. Since the electrons activities are completely random on the circuit, the averaged value of the current $\bar{N}$ is collected many times over the time intervals at length Δt with consideration of a finite electron charge q = -1.60×10^{-19} coulombs:

$$\bar{N} = \frac{I\Delta t}{q} \tag{63}$$

To increase the accuracy on the probability that N electrons are observed at the certain point A in Figure 20 during the time interval Δt the averaged value is then divided by a large number of counted charges n. The probability of an electron passing through the point A within the one time segmented is equal to $(\bar{N}/n) \ll 1$ and it opposes that the probability of and electron *not* passing through the point A during the time segment is $1 - (\bar{N}/n)$.

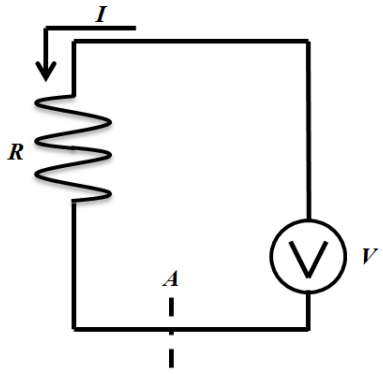

Figure 20. Shot noise current circuit.

The probability of the electron passing through the point A within the N time segments is $(\bar{N}/n)^N$ thus the probability for electrons not passing through the point A during the remaining $n - N$ segments is $(1 - \bar{N}/n)^{n-N}$. One problem in this probability is that the fact you cannot distinguish one electron from another. Including this issue, the probability of the exact N electrons passing through within the time interval Δt is given by following binomial distribution

$$P_n(N) = \frac{n!}{N!(n-N)!}\left(\frac{\bar{N}}{n}\right)^N \left(1-\frac{\bar{N}}{n}\right)^{n-N}. \tag{64}$$

The proof of the sum of the probability to be equal to one is stated as follows:

$$\begin{aligned}
\sum_{N=0}^{n} P_n(N) &= \sum_{N=0}^{n} \frac{n!}{N!(n-N)!}\left(\frac{\bar{N}}{n}\right)^N \left(1-\frac{\bar{N}}{n}\right)^{n-N} \\
&= \left(1-\frac{\bar{N}}{n}\right)^n \sum_{N=0}^{n} \frac{n!}{N!(n-N)!}\left(\frac{\bar{N}}{n}\right)^N \left(1-\frac{\bar{N}}{n}\right)^{-N} \\
&= \left(1-\frac{\bar{N}}{n}\right)^n \left[1+\left(\frac{\bar{N}}{n}\right)\left(1-\frac{\bar{N}}{n}\right)^{-1}\right]^n \\
&= \left[\left(1-\frac{\bar{N}}{n}\right)+\left(\frac{\bar{N}}{n}\right)\right]^n \\
&= 1.
\end{aligned} \tag{65}$$

Since the probability has been proving, the fluctuation of the noise current I_N is:

$$\begin{aligned}
I_N^2 &= \overline{(\Delta I)^2} \\
&= \frac{q^2}{\Delta t^2}\overline{\left(N-\bar{N}\right)^2} = \frac{q^2\bar{N}}{\Delta t^2} \\
&= \frac{qI}{\Delta t} \\
&\left(\because I = \bar{I} = q\bar{N}/\Delta t\right)
\end{aligned} \tag{66}$$

and recalling the Nyquist sampling rate theorem, $\Delta t = 1/(2\Delta f)$, the root-mean-square of the noise current is given by

$$I_N = \sqrt{2qI\Delta f}\,. \tag{67}$$

To reduce the shot noise, the structural circuit is often used aluminium for its light weight and nonmagnetic nature.

Flicker noise

Flicker noise is a unique noise that found only at low frequency [226] often called pink, 1/f noise. The cause of this noise is not well understood or known however it is found specifically in the frequency range lower than 100 Hz. The first spectral density measurement of a flicker noise was measured by Johnson in 1925 [228] while he was studying shot noise. While Johnson studying the shot noise the excess spectral density was found at the lower frequency despite the fact the shot noise does not have a frequency dependency. The name "flicker effect" was given by Schottky in the following year with brief theoretical explanation [226]. Unlike other spectral property, the flicker noise does not have a Lorentzian structure but the distribution of flicker noise falls into the Gaussian.

As for mathematical modelling, McWhorter Model describes the flicker noise as the fluctuation of the charge trapped in the surface area [229], which later studied further by Reimbold [230] and Ghibaudo [231] separately to define the spectral density of the drain current. The Brophy's experiment raises the issue of large fluctuation in the variance; however, this issue was reinvestigated by Hooge and Hoppenbrouwers that the flicker noise variance is constant. His argument was supported experimentally [214] and theoretically [232]. Flicker noise is inversely proportional to the total number of free electron charges within the sample volume and also as long as the current level is low the power of flicker noise is negligible since the thermal noise will dominate [233].

Environmental noise

To measure the signal accurately and highest sensitivity as possible, the external magnetic field homogeneity holds a very important role. Anything that disturbs the condition such as the electric current from the surrounding apart from the appropriate RF circuit, temperature differences, even floor vibration can affect the magnetic field homogeneity a risk [234, 235]. Environmental noise affects more on the lower field such as Earth's field NMR. Each noise source and the measuring condition affect the overall signal differently, which therefore there is no specific mathematical model to

express environmental noise. Majority of the environmental noise is collected at the conductor of an instrument itself as an antenna. The environmental noise sources can be a power line (60 to 240 Hz), radio (just below 10^6 Hz) and TV (around 10^7 Hz) signal with narrow frequency bandwidths [211], or even by lightning that occurs close to the facility. Since environmental noise has a variety of sources it does not always classify as white or Gaussian noise.

Floor vibration

Due to the presence of floor vibration, where the NMR spectrometer located can be crucial to the NMR spectrum [234, 235]. The study concluded that the sensitivity strongly varies with frequency and similar to flicker noise, the noise becomes more significant below 10 Hz. The direction of vibrations also affects differently toward the sensitivity where horizontal vibrations are ten times more likely to affect sensitivity than vertical direction [236]. In the frequency domain, unlike white Gaussian noise, the environmental noise often selectively appears where the signal is and distorts Lorentzian spectral line shape. As a solution, the vibration isolation system is often installed to reduce the effect of floor vibration noise [236].

Nuclear spin noise

The nuclear spin noise was first predicted by Bloch in 1946 [237], observed by Sleator et al. in 1985 [238]. Bloch stated that there is a weak residual of spin states due to the incomplete cancellation of magnetic fluctuations are to be observed as a noise. To experimentally measure nuclear spin noise, long consistent FID without any RF pulse or gradients are first collected. The collected time domain data were then divided into a segment with the length equal to the T_2 relaxation time. Each segmented FIDs are then Fourier transform into the spectral data and accumulation of the data just like the time averaging of the signal are observed as nuclear spin noise spectra. It was truly difficult to measure the nuclear spin noise until recently. Since the first successful spin noise measurement was taken, more researchers such as Hoult and Bhakar [239] discover the truth of the nuclear spin noise of the different nuclei.

There are two major factors that considered as the origin of this particular noise. The first is the quantum fluctuation of the transverse magnetisation and the other is incoherence in RF excitation which produces the Nyquist noise at the detection circuit

[240]. It is also known that the nuclear spin noise has a strong correlation to radiation damping which induced by the precessing transverse magnetisation current in the detection coil. Theoretically speaking, the nuclear spin noise shape is considered Lorentzian however it is often highly distorted.

The total spin-noise power $W(\omega)$ that Sleator et al., and McCoy and Ernst have derived is following:

$$W(\omega) = q\frac{1+a(\Delta\omega)\alpha_r^0}{\left[1+a(\Delta\omega)\alpha_r\right]^2+\left[d(\Delta\omega)\alpha_r+2Q\Delta\omega_c/\omega_c\right]^2} \tag{68}$$

where $\Delta\omega$ is the resonance offset which is between the Larmor frequency and the circuit resonance frequency, α is the damping factor and $a(\Delta\omega)$ and $d(\Delta\omega)$ are absorptive and dispersive spectral components respectively. The spectral line shapes of both absorptive and dispersive nuclear spin noise are:

$$\begin{aligned} a(\Delta\omega) &= \frac{1/T_2^*}{\left(1/T_2^*\right)^2+(\Delta\omega)^2} \\ d(\Delta\omega) &= \frac{\Delta\omega}{\left(1/T_2^*\right)^2+(\Delta\omega)^2} \end{aligned} \tag{69}$$

The actual study and observation begin much later in the NMR history. In 1985 the first nuclear spin noise observed by Sleator at liquid helium temperature [238], followed by McCoy and Ernest [240], Gueron and Leroy [241] independently in 1989 at ambient sample temperature. The interests in spin noise increase rapidly recently for the probe tuning optimisation technique [242-244].

t_1 Noise

In multidimensional spectra, there are streaks along the indirect (t_1) direction is often found randomly and this type of noise is specifically called "t_1 noise" which considered due to the instrumental instabilities collected during signal acquisition [245]. The source of t_1 noise includes a variation of the rotation angle and the phase of the RF

pulse, difference in the intervals between the operation, sample spinning (which cause amplitude and phase shift), receiver gain instability and magnetic field inhomogeneity [245, 246]. There are few post-processing methods such as reference deconvolution method [247], and Cadzow procedure (i.e., based on composite property mapping algorithm, see Section 3.7) [49] have been developed to reduce t_1 noise.

3.3 NMR SENSITIVITY

The low sensitivity of NMR in comparison to other techniques such as mass spectroscopy and electron spin resonance has been mentioned previously as a key disadvantage. Sensitivity fundamentally comes down to the SNR, and NMR sensitivity can, therefore, be improved either by increasing the NMR signal or reducing of the noise. In this section, the calculation of SNR is briefly described followed by various approaches and key features that relate to NMR sensitivity and which are presented in the subsections below.

3.3.1 Signal to noise ratio

In NMR, there are a number of different equations for determining SNR values [167, 248-250]. Some of these are described below.

Theoretical SNR calculation

Previously, major noise types and their origins were presented and there were several SNR studies in the early days of NMR development [159, 167, 251] using those information. A comprehensive expression for SNR giving the contributions from current and resistance in the receiver coils (see Hoult [167]) is given by:

$$\Psi_{\mathrm{rms}} = \frac{K\left(B_1\right)_{xy} V_{\mathrm{s}} N_{\mathrm{spin}} \gamma \hbar^2 I\left(I+1\right)}{7.12 k T_{\mathrm{s}}} \cdot \left(\frac{\rho_{\mathrm{c}}}{F k T_{\mathrm{c}} l_{\mathrm{c}} \varsigma \Delta f} \right)^{1/2} \cdot \frac{\omega_0^{\,7/4}}{\left[\varsigma \varsigma_0 \rho\left(T_{\mathrm{c}}\right) \right]^{1/4}} \qquad (70)$$

Where the SNR Ψ_{rms} is estimated from many factors: $K(B_1)_{xy}$ is the inhomogeneity factor and depends on the coil geometry, V_{s} is the volume of the sample and N_{spin} is the number of spins at resonance per unit volume, T_{s} is the temperature of the sample,

ρ_c is the perimeter of the conductor, F is the noise figure of preamplifiers, T_c the temperature of the coil, l_c the length of conductor, ζ the proximity factor which replaces the filling factor and quality factor of the coil, Δf is the bandwidth (Hz) of the receiver, ω_0 the Larmor angular frequency, ς the permeability of the wire, ς_0 the permeability of free space, and the $\rho(T_c)$ the resistivity of the conductor. In this equation, there are many factors that cannot be defined or calculated accurately and the equation is not generally applicable to the every coil geometry.

Even though the SNR formula above cannot provide an accurate figure for the SNR for many situations it does emphasize the relationships between SNR and the RF coil and informs avenues for improvement. For example, to reduce the sensitivity issue due to the interaction of the coil, a cryoprobe [252-254] and dielectric insert [43] were invented to enhance sensitivity for such matter.

Bruker Topspin "SINO" command

With the development of processing systems, there is software embedded SNR calculation tools that allow real-time sensitivity analysis. One of these is called the *"SINO"* command and is an SNR calculator embedded in Bruker's Topspin software. It returns a value for SNR from,

$$SINO = \frac{maxval}{2 \cdot noise} \tag{71}$$

Without any specification, the *sino* command will calculate *maxval* as the highest intensity of the signal region (i.e., the entire spectral range minus the *noise* region). Unless manually specified, the noise region is automatically selected as the first 1/16th of the spectral data set where known signals apart from the noise are assumed to be present. The *noise* component of Eq. (71) is defined by,

$$noise = \sqrt{\frac{\sum_{i=-n}^{n} y(i)^2 - \frac{1}{N}\left(\left(\sum_{i=-n}^{n} y(i)\right)^2 + \frac{3\left(\sum_{i=1}^{n} i\left(y(i) - y(-i)\right)\right)^2}{N^2 - 1}\right)}{N - 1}} \tag{72}$$

where $y(i)$ is the frequency data of the noise region with total N data points ($-n < i < n$). Taking the advantage of instant SNR calculation, the *sino* command was used in NMR diffusion study using Normalisation scheme (Chapter 4). The origin of Eq. (72) is hard to determine.

General SNR formula

In every other SNR calculation used throughout this thesis, the SNR is defined by [255],

$$\mathrm{SNR} = \frac{\max(\text{Signal Intensity})}{\mathrm{stdev(noise)}} \tag{73}$$

where the 'stdev' refers to the standard deviation of the noise region. This expression is intuitively clearer than the definition used in Eq. (72). The standard deviation of noise is calculated from the edge of the spectrum data (five to ten percent of the entire frequency range) where there is no signal observed.

SNR and optimal acquisition time

The study from Hoult mentioned that the RMS noise of the spectral baseline increases as the time increases [256]. Ultimately, an acquisition time equal to 1.26 T_2 should yield the maximum SNR. However, such short truncated data often results in a low-resolution spectrum after Fourier transformation. When the FID is collected at 1.26 T_2 acquisition time, it is often smoothed-out by multiplying by exponential decay function. This procedure is called applying a window function and it is explained further in Section 3.4.2. Such alteration of the FID, while reducing the noise signal, can broaden the spectral line and lowers the peak amplitude.

3.3.2 Signal averaging

As a conventional NMR signal enhancement procedure, signal averaging is often performed. Recalling the noiseless FID signal x_n from Eq.(23) and adding the noise signal as e_n, and presenting the experimentally measured FID y_n as,

$$y_n = x_n + e_n \quad n = 1, \ldots, N \tag{74}$$

If the signal is repeatedly obtained perfectly aligned then as the number of scans (NS) increases, the signal increases periodically. However, the noise, specifically white Gaussian noise has characteristics of zero mean and a standard deviation of σ_n. The noise level after NS signal averaging will be,

$$\sum_{i=1}^{NS} e_n^i = \sqrt{(NS)\sigma_n^2} = \sqrt{(NS)}\sigma_n \ . \tag{75}$$

Comparing with the signal property, the SNR of FID after NS signal averaging will be

$$SNR_{(NS)} = \frac{(NS)x_n}{\sqrt{(NS)}\sigma_n} = \sqrt{(NS)} \times SNR_1 \ . \tag{76}$$

Thus, the SNR increases as the square root of the number of scans. It is important to remember that even though signal averaging can increase the sensitivity, yet it does not mean that the noise becomes zero, in fact, the noise always increases but the signal increases faster [216].

3.3.3 Increasing signal strength

Concentration

The majority of NMR studies are conducted with samples having a concentration range of 100 µM to 10 mM. The number of spins found within the signal detection range that gives the energy differences after the Zeeman splitting is very limited. Since increasing the concentration does not increase the noise, the concentration of the sample has a linear relationship with the SNR. In many cases, available sample quantity may be limited. In such cases, the sample is often diluted to meet the volume

requirement in order to be measured. When the sample is diluted, the population of spins located within the detection area decreases and leading to lower signal sensitivity. It is highly recommended not to dilute the sample any more than necessity dictates. Thus for every NMR experiment, it is important to measure the highest concentration that is available/allowed and avoid unnecessary dilution. In saying so, concentration changes can highly influence molecular behaviour within the solution (such as diffusion [257, 258] and reaction study [259]). Also, peptides and large proteins tend to aggregate forming new chemical structures as the concentration increases which sets an upper limit on the concentrations [260]. In many biological samples, for example, one cannot simply change the concentration since it may defeat the purpose of the measurements and study.

Sample volume

In general, the standard 5 mm NMR tube requires 0.4 to 0.6 ml of the sample solution, where limited regions are measured. To avoid unnecessary dilution, when a very little amount of sample is available, it is often placed and/or stored in a special tube called capillary tube. The capillary tube is designed to carry a smaller amount of sample by having a specific separate insert within the 5 mm conventional NMR tube [261]. This capillary tube allows the limited amount of the sample to be located directly at the hight of the active coil volume. There is various volume sizes available, and they can be small as 30 µl of the sample stored within a 1.7 mm diameter insert tube which can increase the sensitivity by five-fold compared to the conventional 5 mm NMR tube [262, 263].

Susceptibility match

Magnetic field homogeneity is known to be adversely affected by magnetic susceptibility differences in the NMR tube materials, possible air bubbles and by the sample itself. A specially crafted susceptibility matched NMR tube (i.e., a Shigemi tube) has a known capability of solving lineshape defects matter [264] while enhancing the signal sensitivity significantly [265].

Filling factor

With a standard 5 mm NMR tube and an appropriately sized probe, an RF active coil only covers about a 10 to 20 mm height at 50 to 70 mm above the bottom of the NMR tube. The higher the RF active coil volume with a homogeneous sample the higher NMR sensitivity becomes [266]. The ratio of the total sample volume to the RF active coil volume is commonly referred to as filling factor [267]. In other words, a higher filling factor is better NMR sensitivity received.

Coil geometry

The filling factor is predominantly influenced by the coil geometry within the probe [39]. Standard NMR probes contain two saddle coils aiming to match with two different nuclei [268]. Since two coils cannot be overlapped, one will be the inner coil and the other the outer coil. This small diameter difference between the inner and outer coil can largely influence the filling factor and thus the NMR sensitivity [42]. During the signal detection process, the same RF coil is used as a receiver. The closer the RF coil to the sample is, the stronger signal to be recorded.

Magnetic field

A stronger magnetic field does increase the spin polarisation, leading to an increase in both the NMR sensitivity by $\mathbf{B}_0^{3/2}$ and resolution due to high homogeneity [269]. For example, comparing spectra measured at 300 MHz and at 600 MHz, the SNR increment can be expected to be 2.83 times, following the equations here,

$$\begin{aligned} &SNR \propto B_0^{3/2} \\ &\left(\frac{600\ \text{MHz}}{300\ \text{MHz}}\right)^{3/2} = \left(\frac{14.16\ \text{T}}{7.08\ \text{T}}\right)^{3/2} \approx 2.83 \end{aligned} . \tag{77}$$

In the early days of NMR spectroscopy, iron electromagnets were used to provide the magnetic field. These magnets required constant electrical supplies to reach the range of 20-60 MHz and often suffered from poor homogeneity [270]. The first superconducting magnet was introduced in 1966 by Varian Instruments [271]. Ever since the trend of going to the higher field has led to the current commercially

available NMR magnetic field strength of 23 T (1 GHz) [272]. Since the cost of the instrument increases dramatically with the field strength and the installation procedure is time-consuming this trend of going higher field NMR is not always practical. The modern superconducting magnet consists of a superconducting solenoid magnet immersed in low-temperature liquid helium as Figure 21 shows. This liquid helium bath is to keep the magnet temperature below 4.2 K. Having such low temperature brings near zero resistance in the magnet creating superconductivity where the current loss is at its minimum which eventually eliminates the need for constant external power sources.

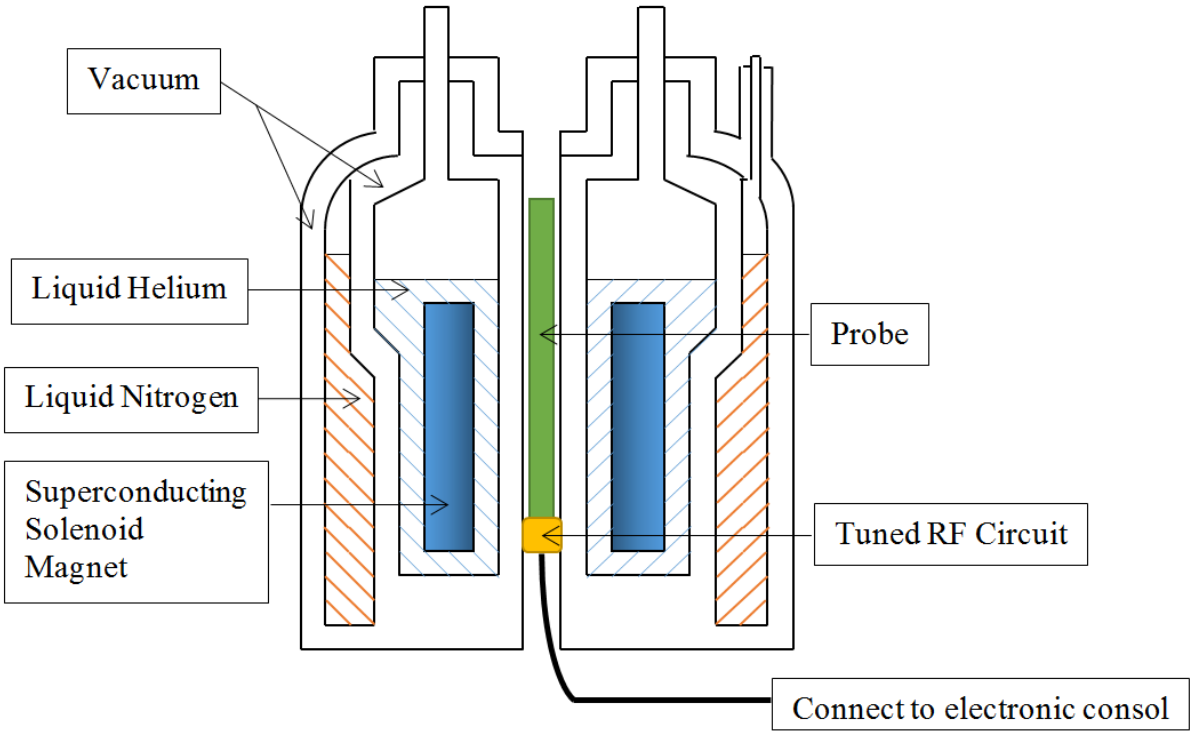

Figure 21. Simplified cut off the image of NMR spectrometer and major components.

Even with this very high magnetic field, there are many areas of study that require extensive signal averaging due to the low sensitivity of the nuclei.

Polarisation transfer

Apart from the magnetic field strength, there is a method which can increase the spin polarisation even further by a technique called polarisation transfer [85, 273]. Polarisation transfer which widely appreciated in solid-state NMR [274, 275] also

share the beneficial signal enhancement effect in liquid-state NMR [276, 277]. The method increases the signal intensity by transferring larger polarisation of higher-γ spin onto the lower-γ spin by inverting spin polarisation [278]. This application enables to lower the NMR experimental limit on biomolecule complex mixtures with low natural abundance such as ^{13}C and ^{15}N NMR studies [279, 280]. There are many applications using polarisation transfer. For example, heteronuclear nuclear Overhauser effect (NOE) [281], dynamic nuclear polarisation (DNP) [282], insensitive nuclei enhanced by polarisation transfer (INEPT) [283, 284], and optical pumping [2, 285] are the major techniques associated with polarisation transfer.

As a short summary, polarisation transfer technique has a potential to increase resonance sensitivity significantly for those nuclei with a low gyromagnetic ratio and slow relaxation time. For this reasons, nuclei with very low gyromagnetic ratio and sensitivity (but high in natural abundance) such as ^{57}Fe [283], ^{109}Ag [286] in solid state have a great advantage in applying polarisation method. For some liquid state quadrupole nuclei such as ^{23}Na on the other hand, due to the fast relaxation rate polarisation technique is considered the non-suitable option.

Dynamic nuclear polarization

The Dynamic Nuclear Polarization (DNP) technique transfers the high spin polarization effects observed from the electrons of paramagnetic impurities which caused by microwave irradiation into the nuclei of interests [2, 282, 287]. The Theoretical idea of hyperpolarization was proposed way back in 1953 [288], noting that it was possible saturation of electron transition can increase the polarization of the nuclei. Soon after, this was experimentally performed on lithium metal by Caver and Slichter [289].

A detailed description of a theoretical Overhauser DNP in the liquid state NMR can be found in [281] along with the Solomon equation, the overall signal enhancement ε after the DNP procedure can be calculated by Overhauser enhancement formula [290],

$$\varepsilon = 1 - \xi ls \frac{|\gamma_e|}{\gamma_n} \tag{78}$$

where ξ is called the coupling factor, l is the leakage factor (i.e., $0 < l < 1$), s is the saturation factor of the electron spins (i.e., $0 < s < 1$), γ_e is the gyromagnetic ratio of the electron, and the γ_n is the gyromagnetic ratio of the nuclei. Basically, the factor of signal enhancement by DNP is given by the electron to nuclear gyromagnetic ratios. For example, the proton will theoretically experience the maximum signal enhancement by a factor of 658, and 2618 for the ^{13}C. The DNP has been applied to ^{1}H [291], ^{13}C, ^{15}N, ^{19}F, ^{31}P and more [292, 293].

Various methods to increase the nuclear spin polarization over the thermal equilibrium state have been proposed. Such techniques include chemically induced dynamic polarization [294], parahydrogen induced polarization [295], techniques also studied in all three physical states liquid state [296], noble gas [297], and solid state [298]. After a long silence, the DNP-NMR was reinvestigated recently with a development of terahertz range microwave source to suit higher magnetic field [299, 300].

3.3.4 Reducing noise

Since thermal noise takes the majority of the noise input, reducing the temperature within the circuit become a primary target for reducing noise.

Probe

The probe where all the RF circuit and receiver embedded is the major source of the NMR noise, especially the thermal noise [301].

The NMR probe is arguably the most important and also the most delicate part of the NMR spectrometer. Unlike the magnet, the NMR probe is more application [302, 303] and nuclei specific [304]. Almost all of the NMR phenomena explained before occurs within the probe. At advanced NMR facilities, it is often found more than one probe per spectrometer to suit their experimental requirements. Each probe has several RF circuits embedded into two layers: The innermost layer of the coil known as the observe coil is the most sensitive for given nuclei to be locked. The outer layer coil which will be less sensitive since it is slightly away from the sample is to decouple the signal arise from other nuclei within the sample. As the RF coil geometry

was discussed previously as the factor of increasing signal, the Probe design indeed influence largely in noise reduction [266]

Cryogenically cooled probe

Another instrumental application for sensitivity increment is the use of the cryogenically cooled probe and its special NMR tube [39] in some cases, the application is known to enhance ^{1}H NMR SNR up to 400 fold [305].

The concept of the cryogenic probe is to keep a temperature of rf coil and preamplifier below 20K to reduce the thermal noise arise from the resister of the coil and temperature of the coil and the preamplifier [41, 252]. The cryogenic probe was first demonstrated in 1984 improving the ^{13}C signal by a factor of eight [41]. The commercially available cryogenic probe normally uses the closed-loop cooling system with a compressed helium gas [306]. There are much application for the cryogenic probe to be used to enhance signal sensitivity, such as large protein analysis [307], small molecules analysis [44, 308] and more [253, 306, 309-312]. The cryogenic probe can indeed increase the NMR sensitivity, however, it will be a lot of expenses to spend for such an application.

Oversampling

The Nyquist sampling theorem as discussed is indeed important to present the observed signal accurately on the frequency range after FT. However, Nyquist sampling theorem can be a limiting factor in NMR sensitivity [175, 313]. Measuring the continuous sinusoidal signal in the discrete time scale can create the quantisation error which observed as digitization noise. Data sampling at a much faster rate known as the oversampling can reduce such noise. The sensitivity gain can be estimated by [160, 314]:

$$gain = \log_2 \frac{SW_{oversampling}}{SW_{Nyquist}} \tag{79}$$

The oversampling is known to benefit the multiple-resonance spectrum [315]. As in the multiple-resonance spectrum, there will be a wide range of the signal strength. If the study is to focus on small signals of the minor components, then the heavy

application of receiver gain can worsen the sensitivity of those weak signals. Yet, low receiver gain does not improve any sensitivity of those weak signals either. Thus, application of oversampling to lower the digitization noise can improve the overall sensitivity [315] without changing any experimental time.

3.4 NMR SIGNAL PROCESSING

Signal processing methods, which are applied to time domain data [60, 316], can be categorised into two streams: parametric and nonparametric which pertains, respectively, to whether they can be used with or without prior knowledge [317, 318]. The prior knowledge can include the number of exponentially decaying signals, their frequencies, amplitudes and decay rates. In NMR study, there are different aims and purposes for signal processing depending on its application. For example, high-resolution NMR is widely used for large biomolecule analysis in a liquid state. Majority of biomolecule experiment does not have prior knowledge of the sample thus expected NMR spectrum is often unknown. In such an environment, a complex experimental technique such as multidimensional measurements are often applied and signal processing is aim to assist in obtaining maximum information (e.g., chemical shift and structure) from the experiment. Knowing the number of exponentials representing the signal within the FID is one of the most beneficial pieces of prior knowledge in the majority of signal processing approaches. Hence, signal processing approaches are suited to the analysis of most liquid state NMR spectra of quadrupolar nuclei, since such spectra typically have only one single peak. NMR diffusion measurements are performed by acquiring a series of echo attenuations at various magnetic gradient pulse amplitudes. Thus, each spectrum and the FID in the series differ only by peak amplitude with all other signal parameters remaining the same.

In vivo quantitative analysis, signal processing is focused on both sensitivity and resolution to measure the area underneath the resonance correctly. For both fast and long relaxation nuclei, the severe truncation of the FID may be observed. For one of many applications, some signal processing methods are designed to estimate those missing data points to recover information which could not be measured during the experiment [319, 320]. In this section, only the major signal processing methods that are used regularly in modern days NMR study are presented. Towards the end of this

chapter, the foundation for this thesis “composite property mapping algorithm” is discussed in depth.

3.4.1 Zero-filling

As discussed above, the measured FID contains real and imaginary parts. If a total of *N* data points were collected during the acquisition time, there are only *N*/2 independent complex Fourier coefficients representing the absorption and dispersion mode signals each. The sensitivity and resolution of such a signal is significantly less than optimal but this can be improved by appending *N* zero amplitude data to the end of the FID prior to Fourier transformation [321]. This simple preprocessing is called zero-filling. Zero-filling is capable of enhancing both sensitivity and digital resolution [60, 174, 321, 322]. When the same number of data points with zeroes are added to the tail of the FID, the Fourier transformed spectrum increases the SNR by a factor of $\sqrt{2}$ [174, 321]. However, zero-filling beyond twice the number of the original FID data points provides no further enhancement of sensitivity or resolution [174].

3.4.2 Window function

A window function involves multiplying the FID by a function, typically to shorten the FID. The weighting function can be linear, sine bells, exponentially decay or more specialized form to fit the FID data [323].

As an example, Figure 22 shows the application process and the outcome results of multiplication by an exponential weighting function (the EM function is displayed in Figure 22b). The rate of the decay is strongly associated with the line broadening parameter. It is evident from Figure 22 that the application of a window function can lead to inaccuracy in spectral parameters such as resonance amplitude, linewidth [324]. Thus in some signal processing techniques, use of the window function is only to assist further signal processing and the weighting function is multiplied back to cancel the effect applied to the FID before Fourier transformation [325]. An example situation where a window function is useful would be a truncated FID. Multiplying such an FID by an exponential function can effectively remove the Sinc wiggles from the spectrum at the expense of broadening the spectral lines.

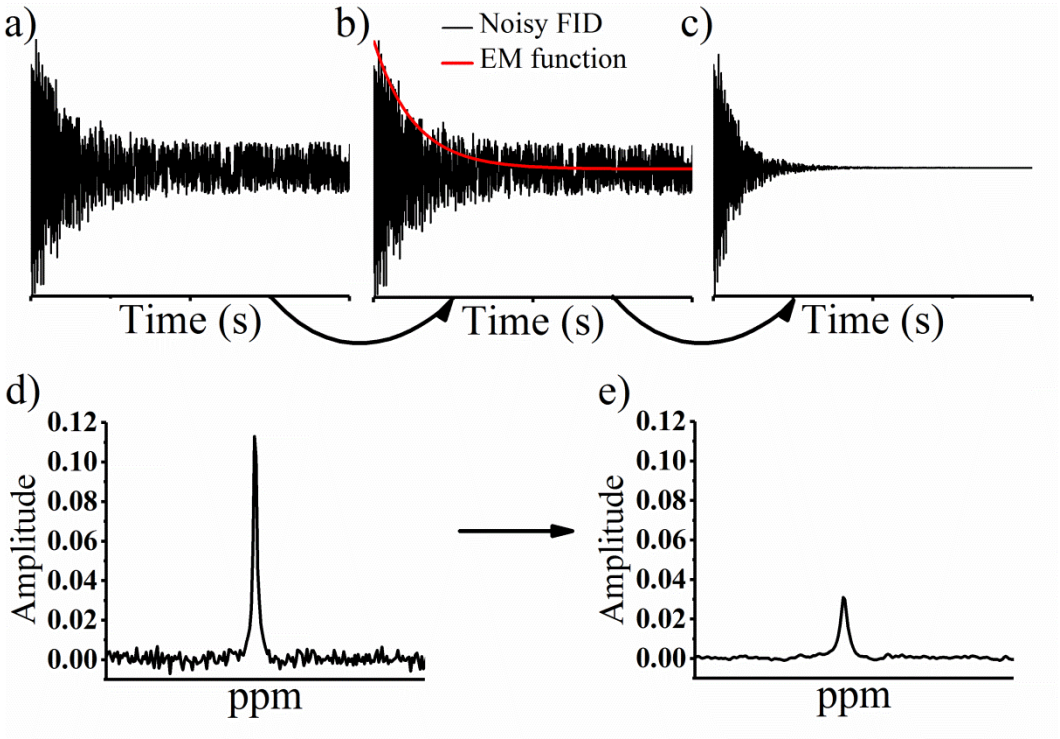

Figure 22. Effects of EM function application in both FID and spectrum. a) Simulated FID with one exponential with additive random noise. b) Exponential multiplication line in red overlapped with noisy FID. c) FID after multiplied by the EM function. d) The spectrum of a). e) The spectrum of c).

The window function is known to have a trade-off between resolution and sensitivity. For example, the matched filter, which for a Lorentzian peak amounts to line broadening by an amount that doubles the peak width, will yield a spectrum with grater SNR than other window functions. It will also reduce resolution as nearby peaks will overlap due to their increased peak widths. Even so, adapted window functions such as Transform of Reverse Added FIDs [323, 326] and the Matched Filter [327] are known to successfully improve sensitivity by applying line broadening that matches the original linewidth which results in the optimal SNR. Many argue that the trade-off between resolution and sensitivity is due to the FID structure where resolution resides in the tail of the FID as opposed to the sensitivity and SNR residing at the beginning of the FID [328].

For the resolution enhancement, the Gaussian multiplication (GM) can be applied to convert the Lorentzian spectral line shape into a Gaussian spectral line shape. As previously mentioned in Section 0, Gaussian line shape has a much narrower base.

Application of appropriate GM function can increase spectral resolution while reducing the sensitivity due to deemphasising the effect at the beginning of the FID [305]. Thus, the GM function is often aimed at resolving the small coupling that may not be obvious at first. The further application and comparison of different types of window functions can be found in Ref. [323, 328, 329].

3.4.3 Reference deconvolution

Similar to window function, reference deconvolution is a simple yet robust data processing method. The method can be used as a preparation step for other signal processing methods such as linear prediction and the maximum entropy method [53]. The idea of using experimental singlet resonance as a reference to analyse overlapping multiplets were first introduced by Keller et al, in 1966 [330]. The same principle was applied to enhance spectral resolution by Ernst et al., [331]. The most significant feature of reference deconvolution method is that the resonance artefacts such as noise distortion, poor shimming effect and truncation artefact can be smoothed out from this application [332, 333]. The basic concept is explained in the flowchart (Figure 23) and the supporting literature can be found in Ref [53, 333-336].

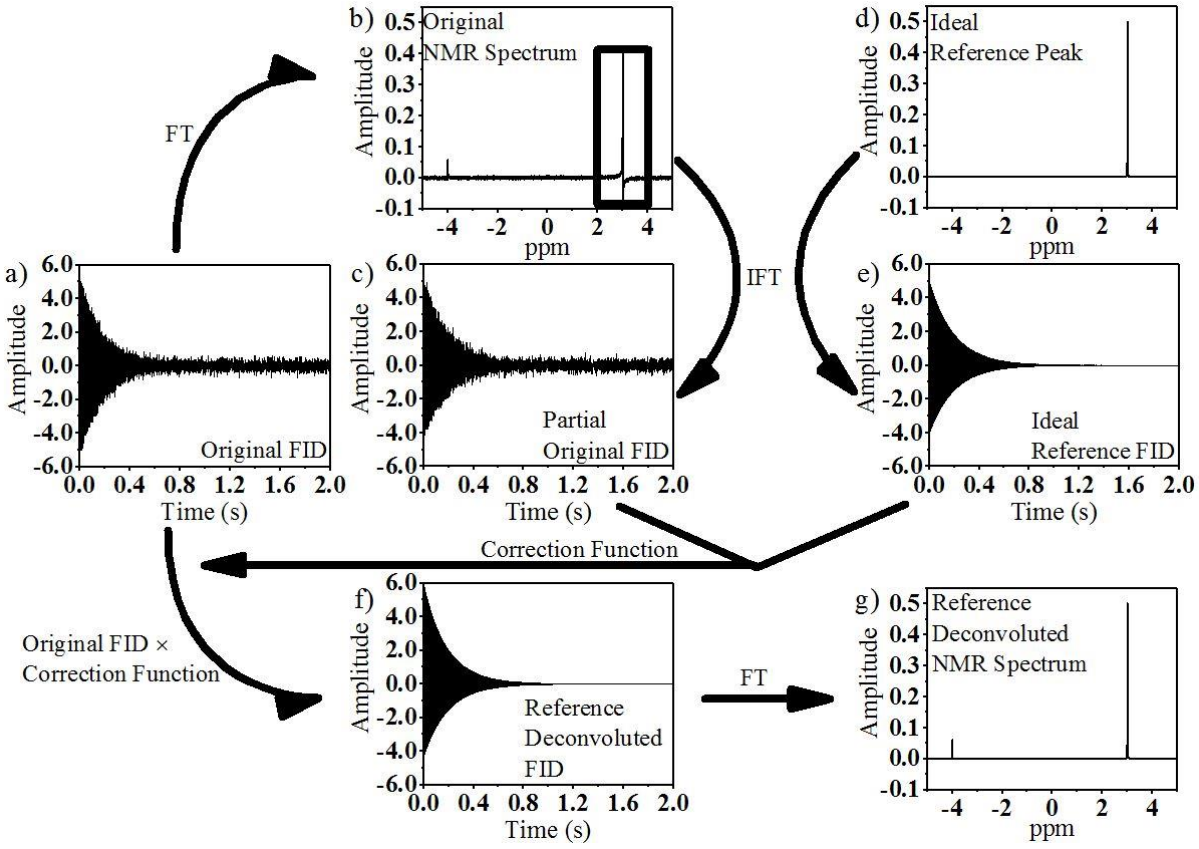

Figure 23. A flowchart of the reference deconvolution method. a) A phase distorted FID. b) The phase distorted spectrum which was Fourier transformed from the data a). c) IFT of the phase distorted spectral range in the rectangular region found in b). d) An ideal resonance of the selected range in b). e) IFT of d). f) correction function formed from data c) and e) is multiplied to the original FID a). g) FT of f) as the reference deconvoluted NMR spectrum.

To follow the flowchart, first, the experimental FID is collected (Figure 23a) which is then Fourier transformed into a spectrum (Figure 23b). A reference peak is chosen which is ideally the singlet resonance with the largest amplitude. A reference spectrum is created (Figure 23d) by applying an appropriate window function (Figure 23c) to suppress all unrelated components including noise. The IFT of the reference spectrum is then performed (Figure 23d) to obtain the reference FID of the peak (Figure 23e). The correlation function is then made, applied to the original FID data to produce the reference deconvoluted FID (Figure 23f). The FT of this treated FID to produce a spectrum with each resonance having a Lorentzian lineshape.

The method was developed to correct imperfect spectral shapes due to poor shimming. The corrected spectral data often requires further signal processing for

sensitivity enhancement. The majority of spectra that reference deconvolution is applied to contain multiple-resonances that are overlapped and/or have a baseline error. It is important to mention that the blind application of the reference deconvolution method can create further signal artifacts without Hilbert Transformation. For example, if the reference resonance is overlapped with other resonance (e.g., Section 6.3.1) and the zeroing window function is applied, there can be a drop between the reference signal region and the zeroed baseline (e.g., Chapter 6 Figure 38b). When this type of modified spectrum is transformed into a time-domain signal by IFT, additional incorrect information is added to the exponential decay function. A FT of such an FID can cause major truncation artifacts [53, 337].

3.4.4 Wavelet shrinkage

Wavelet transform described in Section 0 as the domain transformation method. Wavelet theory, in fact, can be developed into many signal processing methods such as solvent suppression [153], denoising [338, 339] and more [209, 340]. Wavelet shrinkage (see Donoho [74, 341]) is a nonparametric wavelet-based signal denoising method which is available through major programming software such as Mathcad (i.e., waveshrink) and Matlab (i.e., wdenoise). This wavelet shrinkage denoising method is composed of three major steps:

1. Chose the appropriate wavelet base and perform a discrete wavelet transform to the measured data
2. Apply soft coefficient thresholding and shrink the wavelet coefficients to zero
3. Take an inverse discrete wavelet transform to reconstruct denoised data

First of all, there are many types of wavelet forms (e.g., Harr, Coiflets, Symmlets, and Daubechies) available. When the appropriate wavelet form and its vanishing moment are chosen, then a square orthogonal finite wavelet transform matrix is constructed. This wavelet matrix is then multiplied by the measured signal vector yielding the wavelet coefficient vector.

As a second step, the soft threshold value for the wavelet coefficient is defined through estimated noise level. The soft threshold is known to provide better smoothing than a hard threshold while preserving the spectral details [74]. By shrinking the

wavelet coefficients that are below the threshold to zero, noise properties related to those eliminated wavelet coefficients are also removed from the measurements. At the last steps, the inverse discrete wavelet transform is applied to transform the data to its original domain.

This method is applied to one of the ^{1}H 1-dimensional multiple-resonance NMR spectra in Chapter 7. The result of this denoising method is then compared with the newly proposed method (see Section 7.3) for its spectral accuracy and computational time.

3.4.5 Iterative thresholding and minimum l1-norm reconstruction method

Throughout the history of NMR signal processing, a number of methods have been dedicated specifically to process multiexponential decay signals and also diffusion measurements (e.g., GANT [342], ITAMeD [343], IQML [344]). As an example, iterative thresholding and the minimum l_1 norm reconstruction method by Stern [57] is presented here.

The iterative thresholding approach is a fixed-point technique where an operation is applied repeatedly until the output does not show any changes. Iterative thresholding and the minimum *l*1-norm reconstruction method both utilise the fact that the majority of the signal is at the beginning of the decay and the rest the decay mostly corresponds to the noise. The basic methodology of the thresholding and iteration process of this method is illustrated in the diagram in Figure 24.

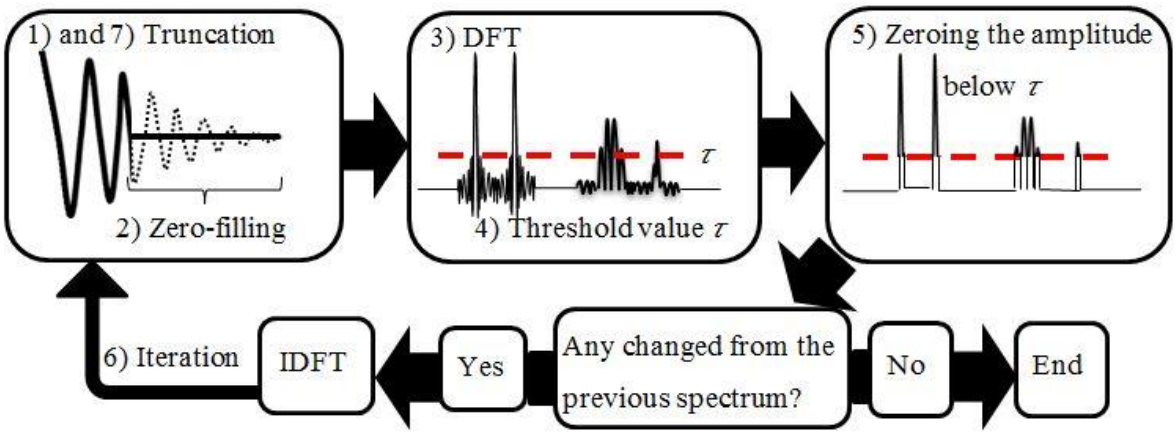

Figure 24. Flow diagram of iterative thresholding and minimum l_1-norm reconstruction method.

The diagram in Figure 24 has seven cycle steps to follow: 1) The initial FID data for this method is collected from the Inverse Discrete Fourier Transform (IDFT, i.e. the inverse fast Fourier transform) of the spectrum which is then heavily truncated before it fully decays; 2) zero-filling is then applied to this truncated FID data; 3) take the Discrete Fourier Transform (DFT) of the zero-filled FID into the frequency domain; 4) choose the amplitude threshold value τ to be such that it is smaller than the true peaks' maxima but also greater than the artefacts caused by truncation (i.e. Sinc side lobes); 5) set any spectral amplitude below the threshold τ to zero and take the IDFT; 6) truncate the tail of the FID the same amount as in the step 1) and 7) repeat the process until no change is observed in the spectrum.

If the threshold value τ decreases at each iteration, the method is categorised as a soft thresholding method unlike hard thresholding where the value τ is stationary. There are similarities among the fixed point iterative process, minimal l_1-norm reconstruction method [57], maximum entropy reconstruction (MaxEnt) [345], and minimum area reconstruction [59]. Those similarities are explained in the ref [57].

3.4.6 Continuous Diffusion Coefficients (CONTIN)

When studying the aggregation process, polymers and complex mixture analysis, a two dimensional NMR experiment called diffusion-ordered spectroscopy (DOSY)

NMR is often performed [346-349]. DOSY experiment can express both physical and chemical information in two dimensions: one dimension for self-diffusion behavior while others inform its chemical shift [350, 351]. DOSY is such a versatile approach yet limited by required spectral sensitivity, low concentrations, long relaxation time, and available data processing techniques [347]. There are two classes of data processing techniques that can be applied to DOSY NMR data sets: single channel methods and multivariate methods.

A continuous diffusion coefficient (CONTIN) is one of the single channel methods available as a constrained regularisation program [352, 353]. To determine distributions of translational diffusion coefficients, DOSY experiments require the inverse Laplace transformation (ILT) [349, 351]. CONTIN can solve the ILT problem and provide the Laplace spectrum of the diffusion coefficients as well as smoothing the spectrum data by using a constrained regularisation to fit experimental data [351]. However, the method assume the noise is in random Gaussian which leads tosystematic errors and artifacts when SNR is low. As a limitation, due to smoothing and broadening features that CONTIN possess, the diffusion coefficient is often smaller than the true values [346, 347, 352, 353]. More details of the theory and applications of the CONTIN method can be found in Ref ([116, 352, 353]). For spectra with overlapping resonances, a multivariate methods called DECRA (Section 3.4.7) would be much more suitable for signal processing.

3.4.7 Direct Exponential Curve Resolution Algorithm (DECRA)

Direct exponential curve resolution algorithm (DECRA) is a multivariate method that can resolve self-diffusion coefficients as well as spectral components [354-357]. DECRA is an extension of the generalized rank annihilation method (GRAM) which is an eigenvalue problem using two data matrices [358]. Compared to GRAM, it can process noisy data with much lower SNR and severe spectral overlap and is able to distinguish small differences in diffusion coefficient [359]. Previously, CONTIN has an assumption of the noise being random Gaussian, while a DECRA assumes each pure spectrum is formed by a pure exponential decay function [356]. This assumption

of the algorithm leads to inevitable error in NMR diffusion and relaxation analysis after processing NMR data with a non-single exponential decay function [140, 360].

3.5 LINEAR ALGEBRA IN SIGNAL PROCESSING

In this section, the matrix terminology and the basic matrix linear algebra used in composite property mapping algorithm is summarised. This is needed to understand the composite property mapping algorithm presented at the end of this chapter. For readers with the basic mathematical background can skip this section and move to Section 3.7 where the composite property mapping theory is discussed.

3.5.1 Matrix terminology and operations

The rest of this chapter is an introduction to the signal processing methods based on linear algebra and matrix decomposition. This section explains the major matrix terminologies used in the eigen (Section 3.5.3) and singular value decomposition (Section 3.5.4). The reader is assumed to be familiar with basic vector and matrix terminology, however, a brief review follows concentrating on those parts of matrix algebra that are important in the forthcoming sections.

Transpose

Transpose of a matrix is often denoted by superscripted ^{T}. Transport of a matrix can be done by converting rows element into columns element and vice versa. For example, if

$$A = \begin{bmatrix} a_1 & a_2 & a_3 \\ a_4 & a_5 & a_6 \end{bmatrix} \tag{80}$$

then, A^T is

$$A^T = \begin{bmatrix} a_1 & a_4 \\ a_2 & a_5 \\ a_3 & a_6 \end{bmatrix}. \tag{81}$$

Conjugate transpose

The term conjugate transpose also known as Hermitian transpose is the transpose of the matrix along with taking the complex conjugate of each element within. The conjugate transpose may denote by many alternate symbols such as *, ^{H}, and †. As an example, if

$$A = \begin{bmatrix} 1 & 1-2i \\ i & 2+i \end{bmatrix} \tag{82}$$

then

$$A^* = \begin{bmatrix} 1 & -i \\ 1+2i & 2-i \end{bmatrix}. \tag{83}$$

Note that for matrices possessing only real elements, the conjugate transpose is identical to the transpose.

Identity matrix

A square matrix with principal diagonal elements equal to 1 and non-diagonal elements being zero is called an identity matrix (*I*). The principal diagonal runs from the top left to the bottom right of the matrix. One significant property of the identity matrix is that a matrix *A* multiplied by *I* is equal to *A*. For example,

$$A=\begin{bmatrix}1 & 2\\ 3 & 4\end{bmatrix}, I=\begin{bmatrix}1 & 0\\ 0 & 1\end{bmatrix}$$
$$AI=\begin{bmatrix}1 & 2\\ 3 & 4\end{bmatrix}\begin{bmatrix}1 & 0\\ 0 & 1\end{bmatrix}=\begin{bmatrix}1 & 2\\ 3 & 4\end{bmatrix}=A=\begin{bmatrix}1 & 0\\ 0 & 1\end{bmatrix}\begin{bmatrix}1 & 2\\ 3 & 4\end{bmatrix}=IA \quad . \tag{84}$$

Orthogonal matrix

When multiplication of a matrix A by its transpose A^T gives an identity matrix, then the matrix A is called an orthogonal matrix. For example, if

$$A=\begin{bmatrix}3/5 & -4/5\\ 4/5 & 3/5\end{bmatrix} \tag{85}$$

then

$$AA^T=\begin{bmatrix}3/5 & -4/5\\ 4/5 & 3/5\end{bmatrix}\begin{bmatrix}3/5 & 4/5\\ -4/5 & 3/5\end{bmatrix}=\begin{bmatrix}1 & 0\\ 0 & 1\end{bmatrix}, \tag{86}$$

and also

$$A^TA=\begin{bmatrix}3/5 & 4/5\\ -4/5 & 3/5\end{bmatrix}\begin{bmatrix}3/5 & -4/5\\ 4/5 & 3/5\end{bmatrix}=\begin{bmatrix}1 & 0\\ 0 & 1\end{bmatrix}. \tag{87}$$

That is, $A^{-1}=A^T$.

Unitary matrix

Unitary matrices generalise the concept of orthogonality to complex-valued matrices. A matrix with complex numbers as elements that when multiplied by its conjugate transpose gives the identity matrix is called a unitary matrix, i.e. $A^{-1}=A^*$.

Determinant

A determinant simplifies a large square matrix data into a single value. It is often denoted as $|A|$ or det(A). Both eigen and singular value decomposition require taking a determinant of a matrix to find the matrix eigen and singular value respectively. For example, if

$$A = \begin{bmatrix} a_{1,1} & a_{1,2} \\ a_{2,1} & a_{2,2} \end{bmatrix} \tag{88}$$

then, the determinant of A, det(A) is

$$\det(A) = |A| = \begin{vmatrix} a_{1,1} & a_{1,2} \\ a_{2,1} & a_{2,2} \end{vmatrix} = a_{1,1} \cdot a_{2,2} - a_{1,2} \cdot a_{2,1} \tag{89}$$

With non-square matrix A, a matrix A is multiplied by its transpose (AA^T) or A^TA before taking the determinant.

Matrix norm

To compare the differences or distance between two matrices, the matrix norm is often quantified. The most commonly used matrix norm in signal processing is called Frobenius norm (i.e., $\| A \|_F$ or $\| A \|^2$). The Frobenius norm calculates the sum of the squares of all the matrix elements:

$$\|A\|_F = \sqrt{\sum_{i,j} |A_{ij}|^2} = \sqrt{\mathrm{tr}\left(A^T A\right)} \tag{90}$$

When measuring the distance between two vectors or matrices A and B of the same dimension, then Frobenius norm is defined as

$$\|A - B\|_F = \sqrt{\sum_{i,j} |A_{ij} - B_{ij}|^2} \,. \tag{91}$$

Matrix structure

There are two types of matrix structure; Hankel and Toeplitz [361-365] are often used in NMR signal processing. Both matrix structures arrange each column elements in a way that creating a trend of signal rich and noise rich corner using FID signals (e.g., $x_0, x_1, \ldots, x_{n-l}$) as shown below.

Hankel Toeplitz

$$\begin{bmatrix} x_0 & x_1 & \cdots & x_{m-1} \\ x_1 & x_2 & \cdots & \vdots \\ \vdots & \vdots & \ddots & x_{n-2} \\ x_{l-1} & x_l & \cdots & x_{n-1} \end{bmatrix}, \begin{bmatrix} x_{m-1} & \cdots & x_1 & x_0 \\ x_m & \cdots & x_2 & x_1 \\ \vdots & \ddots & \vdots & \vdots \\ x_{n-1} & \cdots & x_l & x_{l-1} \end{bmatrix}$$

n : total data points

l : number of rows

m : number of columns

3.5.2 Matrix subspaces, range, null space, and rank

Let A be the l by m matrix where $l > m$. Writing $A\mathbf{x} = \mathbf{b}$ for some $\mathbf{b}$ gives an overdetermined system of equations,

$$A\mathbf{x} = \mathbf{b}$$

$$\begin{bmatrix} a_{1,1} & \cdots & a_{1,m} \\ a_{2,1} & \ddots & a_{2,m} \\ \vdots & \ddots & \vdots \\ a_{l,1} & \cdots & a_{l,m} \end{bmatrix} \begin{bmatrix} x_1 \\ \vdots \\ x_{m-1} \\ x_m \end{bmatrix} = \begin{bmatrix} b_1 \\ \vdots \\ b_{l-1} \\ b_l \end{bmatrix} \tag{91}$$

where the matrix A becomes the linear transformation of the vector $\mathbf{x}$ in R^m to the vector $\mathbf{b}$ in R^l.

There are two subspaces associated with the matrix A. The first subspace is called range. The range of the matrix A is equal to the number of the column that satisfy $A\mathbf{x} = \mathbf{b} \neq 0$, which means the maximum number of linearly independent

column/row vectors found within the matrix. The range of the matrix A is often denoted as $R(A)$. The second subspace called null space of A is equal to the number of the column that leads non-zero vectors $\mathbf{x}$ mapped to zero by A (i.e., $A\mathbf{x} = 0$), denoted as $N(A)$. The dimension of the range $R(A)$ is called the 'rank' of the matrix and the dimension of the null space $N(A)$ is called the 'nullity' of the matrix A. In another word, the sum of the range and null space dimension is equal to the length of column A.

When the matrix A filled with randomly generated numbers, then all column and row vectors are linearly independent. Therefore, the rank of the matrix $A = \min(l, m)$, since $l > m$ then the matrix rank of A is expressed a full rank which is equal to m. Each of the vectors $\mathbf{x}$ and $\mathbf{b}$ will be separated into two subspaces in respect to the matrix A as shown in Figure 25. Row space is a subspace of A^T, has the range of A^T: $R(A^T)$ with the same dimension of r. Null space of A^T: $N(A^T)$ is a subspace of A^T with dimension $m - r$.

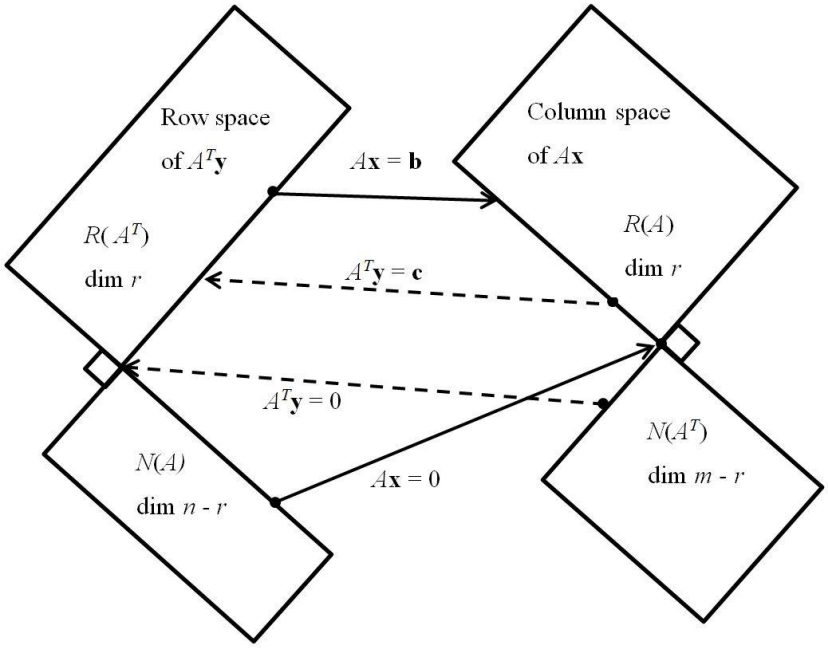

Figure 25. Linear relationships of four subspaces to the matrix A: Row to column space and null space to zero.

These subspaces notations will become much clearer in the Section 3.5.4 with singular value decomposition.

3.5.3 *Eigenvectors and eigenvalues*

To solve matrix algebra, a matrix is often decomposed into simpler matrices. In particular matrix decomposition called eigendecomposition applies only to a square matrix though does not exist for all square matrices. A principal component analysis (PCA), for an example, utilises eigendecomposition of a covariance or correlation matrix to provide the least squared estimate of the matrix. A factorisation of a square matrix A by eigendecomposition produces a set of eigenvalues and eigenvectors. For a square matrix A, there is a set of eigenvalues λ and a corresponding eigenvectors $\mathbf{v}$ that satisfy the following linear relationships:

$$A\mathbf{v} = \lambda\mathbf{v} \tag{92}$$

For example, if

$$A = \begin{bmatrix} 0 & 1 \\ -2 & -3 \end{bmatrix} \tag{93}$$

then to find the eigenvectors $\mathbf{v}$ of a matrix A, the Eq. (92)

$$\begin{aligned} A\mathbf{v} - \lambda I\mathbf{v} &= 0 \\ \left(A - \lambda I\right)\mathbf{v} &= 0 \end{aligned} \tag{94}$$

where I is the identity matrix and the Eq. (94) is equivalent to:

$$\det\left(A - \lambda I\right) = 0 \tag{95}$$

The determinant of a matrix $(A - \lambda I)$ is equal to:

$$
\begin{aligned}
\det\left(\begin{bmatrix} -\lambda & 1 \\ -2 & -3-\lambda \end{bmatrix}\right) &= 0 \\
(-\lambda)(-3-\lambda)-1(-2) &= 0 \\
\lambda^2+3\lambda+2 &= 0 \\
(\lambda+1)(\lambda+2) &= 0
\end{aligned}
\tag{96}
$$

which lead directly to the eigenvalues $\lambda_1 = -1$ and $\lambda_1 = -2$. Since eigenvalues are known, plugging the eigenvalues one at the time can find the corresponding eigenvectors. Starting from $\lambda_1 = -1$:

$$
\begin{aligned}
A\mathbf{v} &= \begin{bmatrix} 0 & 1 \\ -2 & -3 \end{bmatrix}\begin{bmatrix} v_{11} \\ v_{12} \end{bmatrix} = \lambda_1 \begin{bmatrix} v_{11} \\ v_{12} \end{bmatrix} \\
0(v_{11})+1(v_{12}) &= -1(v_{11}) \\
-2(v_{11})-3(v_{12}) &= -1(v_{12})
\end{aligned}
\tag{97}
$$

where eigenvectors $v_{11} = -v_{12}$ and for the $\lambda_2 = -2$:

$$
\begin{aligned}
A\mathbf{v} &= \begin{bmatrix} 0 & 1 \\ -2 & -3 \end{bmatrix}\begin{bmatrix} v_{21} \\ v_{22} \end{bmatrix} = \lambda_2 \begin{bmatrix} v_{21} \\ v_{22} \end{bmatrix} \\
0(v_{21})+1(v_{22}) &= -2(v_{21}) \\
-2(v_{21})+-3(v_{22}) &= -2(v_{22})
\end{aligned}
\tag{98}
$$

where eigenvectors $v_{21} = -2v_{22}$ and finally, combining all those component into the original Eq. (92):

$$
\begin{aligned}
A\mathbf{v} &= \lambda\mathbf{v} \\
\begin{bmatrix} 0 & 1 \\ -2 & -3 \end{bmatrix}\begin{bmatrix} v_{11} & v_{21} \\ v_{12} & v_{22} \end{bmatrix} &= \begin{bmatrix} \lambda_1 & 0 \\ 0 & \lambda_2 \end{bmatrix}\begin{bmatrix} v_{11} & v_{21} \\ v_{12} & v_{22} \end{bmatrix} \\
A\begin{bmatrix} \mathbf{v}_1 & \mathbf{v}_2 \end{bmatrix} &= \begin{bmatrix} \lambda_1 & 0 \\ 0 & \lambda_2 \end{bmatrix}\begin{bmatrix} \mathbf{v}_1 & \mathbf{v}_2 \end{bmatrix}
\end{aligned}
\tag{99}
$$

can be simplified to:

$$\begin{aligned} AV &= V\Lambda \\ A &= V\Lambda V^{-1} \end{aligned} \tag{100}$$

The eigendecomposition can only be performed if a matrix A is a square diagnosable.

3.5.4 Singular value decomposition

Singular value decomposition, on the other hand, can be applied to every type of matrix [366, 367]. It can provide robust solutions to many problems: such as over/under-determined least squared problem [50, 366], matrix approximation [368] and optimisation of ill-conditioned systems [369]. The SVD method has such diverse applications such as system recognition [370, 371], filtering system [372], data compression [373] and more [374]. As in NMR signal processing, SVD-based methods can provide spectral analysis [375], parameter estimation [320, 376] and signal enhancement by noise reduction [51, 52, 64]. There is no specific origin of who concreated the theory, however, it can be traced down to five mathematicians solving linear algebra problems treating the number of linear equations as a matrix and vectors [377]. The fundamental of the SVD can factorise any form of a matrix $A \in \mathbb{C}^{L\times M}$ into three submatrices:

$$A = U\Sigma V^{T} \tag{101}$$

where $U \in \mathbb{C}^{L\times L}$ and $V \in \mathbb{C}^{M\times M}$ are both unitary and $\Sigma \in \mathbb{C}^{L\times M}$ is a diagonal matrix. The Σ matrix has the form:

$$\Sigma_{L\times M} = \mathrm{diag}\left(\sigma_1, \sigma_2, \ldots, \sigma_p\right), \tag{102}$$

where $p = \min(L, M)$. The diagonal elements of Σ (i.e., $\sigma_1,\sigma_2,\ldots,\sigma_p$) are called the singular values of A which are in descending order

$$\sigma_1 \geq \sigma_2 \geq \cdots \geq \sigma_p \geq 0. \tag{103}$$

With matrix size of A being $L > M$, then the system is called overdetermined thus the $p = M$, while the matrix size of A being $L < M$, the system is called underdetermined and the $p = L$. Since both U and V being unitary matrices, the following properties of the SVD are established.

$$\begin{aligned} A^T A &= V\Sigma^T U^T U \Sigma V^T \\ &= V\Sigma^T \Sigma V^T \end{aligned} \tag{104}$$

Let $\Lambda \in \mathbb{C}^{M\times M}$ be defined by

$$\begin{aligned} \Lambda &= \Sigma^T \Sigma \\ &= \operatorname{diag}\left(\sigma_1^2, \sigma_2^2, \ldots, \sigma_n^2\right) \\ &= \operatorname{diag}\left(\lambda_1, \lambda_2, \ldots, \lambda_n\right) \end{aligned} \tag{105}$$

The Eq. (104) can be rewritten as

$$A^T A = V\Sigma^T \Sigma V^T = V\Lambda V^T \tag{106}$$

This format looks somewhat similar to the eigendecomposition. Multiplying by V on both sides of Eq. (106) is then,

$$\left(A^T A\right)V = V\Lambda V^T V = V\Lambda \tag{107}$$

Which indicates that the diagonal elements in the matrix Λ, (i.e., $\lambda_1, \lambda_2, \ldots, \lambda_n$) are the eigenvalues of $A^T A$. Thus the columns of the matrix V are the eigenvectors of $A^T A$, or more specifically, the right eigenvector of $A^T A$. Similarly, computing the AA^T:

$$\begin{aligned} AA^T &= U\Sigma V^T V\Sigma^T U^T \\ &= U\Sigma\Sigma^T U^T \\ &= U\Lambda U^T \end{aligned}, \tag{108}$$

and multiplying both sides by U gives

$$\begin{aligned} AA^T U &= U\Lambda U^T U \\ &= U\Lambda \end{aligned}. \tag{109}$$

leading to the columns of the matrix U being the left eigenvectors of AA^T. In a similar manner to Figure 25, Figure 26 visualise the linear relationships between subspaces fond in SVD.

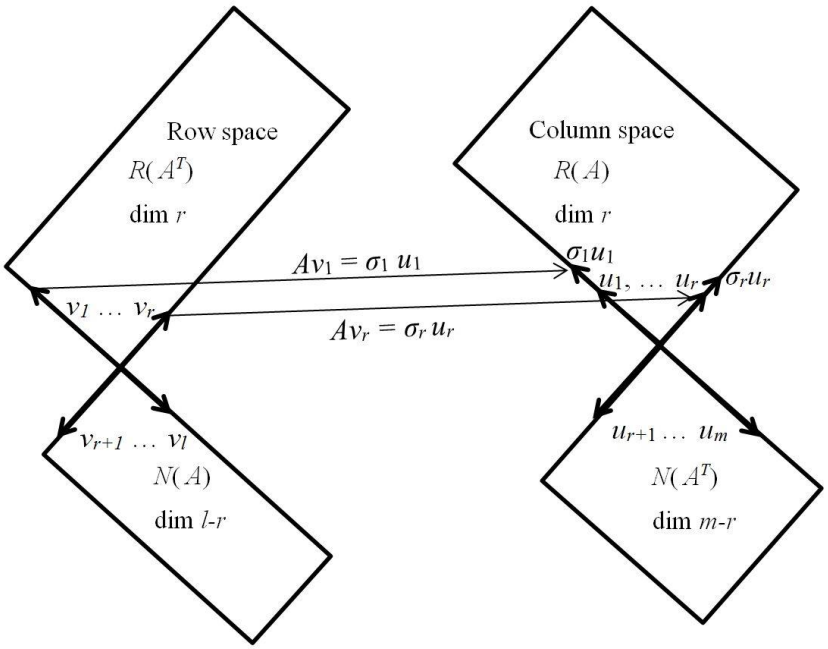

Figure 26. Linear relationships between subspaces representing a property of singular values and left and right singular vectors. With r linearly independent column within the matrix A, the range of the matrix A; $R(A)$ is represented by singular values σ multiplied by the right singular vectors u with the rank of r. Corresponding left singular vectors v of the rank r is represented by the range of A^T.

As Figure 26 shows, the column space of A, which is the range of A (i.e., $R(A)$) is spanned by the first r columns of U. the null space of A (i.e., $N(A)$) is spanned by the last $l - r$ columns of V. The row space (i.e., range of $R(A^T)$) is spanned by the first r column of V. Finally, the null spacer of A^T (i.e., $N(A^T)$) is spanned by the last $m - r$ columns of U.

3.6 NMR SPECTRAL PARAMETER ESTIMATION USING SVD

Next two subsections present well-known NMR spectral parameter estimation using SVD. By presenting these two methods, the relationships between the NMR spectral parameter in FID and the property of each submatrix after SVD should be clarified.

3.6.1 Linear prediction singular value decomposition (LPSVD)

The linear prediction singular value decomposition method was introduced to solve the NMR parameter estimation problem [76, 77, 165, 378]. Recalling the FID signal from Eq. (23), the time-domain signal can also be expressed as,

$$\begin{aligned} x_n &= \sum_{k=1}^{K} A_k \exp(i\phi_k) \exp\left(\left(-d_k + i2\pi f_k\right) n\Delta t\right) + w_n \\ &= \sum_{k=1}^{K} c_k z_k^n + w_n \\ c_k &= A_k \exp(i\phi_k) \\ z_k^n &= \exp\left(\left(-d_k + i2\pi f_k\right) n\Delta t\right) \end{aligned} \tag{110}$$

where $n = 0, 1, \ldots, N\text{-}1$ and c_k is often called "complex amplitude" and the z_k as the "signal pole". The Eq. (110) can be further simplified as

$$x_n = s_n + w_n \tag{111}$$

separating the FID x_n into noiseless FID s_n and the additive noise w_n. Let T be an N-M by M Toeplitz matrix filled with x_n excluding the first data point (x_0):

$$\mathrm{T}_{(N-M)\times M} = \begin{bmatrix} x_M & x_{M-1} & \cdots & x_1 \\ x_{M+1} & x_M & \cdots & x_2 \\ \vdots & \vdots & \ddots & \vdots \\ x_{N-1} & x_{N-2} & \cdots & x_{N-M} \end{bmatrix} \tag{112}$$

The dimension of the matrix should satisfy ($K \leq M \leq N$-$M < N$). Multiplying the linear prediction coefficient vector $\mathbf{p}$ to predict a signal vector $\hat{\mathrm{x}}$ of N-M-1 length, the Eq. (112) can then written as

$$\begin{aligned} \hat{\mathrm{x}} &= \mathrm{T}\mathbf{p} \\ \begin{bmatrix} x_0 \\ x_1 \\ \vdots \\ x_{N-M-1} \end{bmatrix} &= \begin{bmatrix} x_M & x_{M-1} & \cdots & x_1 \\ x_{M+1} & x_M & \cdots & x_2 \\ \vdots & \vdots & \ddots & \vdots \\ x_{N-1} & x_{N-2} & \cdots & x_{N-M} \end{bmatrix} \begin{bmatrix} p_1 \\ p_2 \\ \vdots \\ p_M \end{bmatrix}. \end{aligned} \tag{113}$$

The linear prediction coefficients vector can be obtained by solving Eq. (113) using a linear least square approach. One obstacle in finding the linear prediction coefficient vector is that the matrix cannot do division. Instead, an inverse of the matrix T in the form of submatrices after singular value decomposition is used as

$$\begin{aligned} \mathbf{p} &= \mathrm{T}^{-1}\hat{\mathrm{x}} \\ &= V\Sigma^{-1}U^T\hat{\mathrm{x}} \end{aligned}. \tag{114}$$

Once the linear prediction coefficient vector $\mathbf{p}$ is defined then Eq. (110) can define the signal pole by solving

$$z^M + p_1 z^{M-1} + p_2 z^{M-2} + \cdots + p_{M-1} z^1 + p_M = 0 \tag{115}$$

leading to estimation of spectral parameters in the signal pole, such as damping factor

$$d_k = \frac{-1}{\Delta t}\ln\left|z_k\right|, \tag{116}$$

and the frequency

$$f_k = \frac{1}{2\pi\Delta t}\tan^{-1}\frac{\mathrm{Im}\left(z_k\right)}{\mathrm{Re}\left(z_k\right)}\ . \tag{117}$$

Once the damping factors and the frequencies are estimated, the rest of the parameters amplitude and phase can also be estimated by solving the least square problem from Eq. (110).

3.6.2 Hankel singular value decomposition (HSVD)

Hankel SVD [379] has a similar concept to LPSVD. Recalling the FID from Eq. (110), arranging the time domain vector x_n into L by M Hankel matrix H

$$\mathrm{H} = \begin{bmatrix} x_0 & x_1 & \cdots & x_{M-1} \\ x_1 & x_2 & \cdots & x_M \\ \vdots & \vdots & \ddots & \vdots \\ x_{L-2} & x_{L-1} & \cdots & x_{N-2} \\ x_{L-1} & x_L & \cdots & x_{N-1} \end{bmatrix}. \tag{118}$$

The same condition in LPSVD applies to HSVD, both rows and columns number must be greater than K. The characteristic of HSVD is that the Vandermonde decomposition of H leads to three submatrices just like the SVD method. However, the factorised submatrices have special features and structure,

$$\mathrm{H} = \begin{bmatrix} 1 & \cdots & 1 \\ z_1^1 & \cdots & z_K^1 \\ \vdots & \ddots & \vdots \\ z_1^{L-1} & \cdots & z_K^{L-1} \end{bmatrix} \begin{bmatrix} c_1 & \cdots & 0 \\ \vdots & \ddots & \vdots \\ 0 & \cdots & c_K \end{bmatrix} \begin{bmatrix} 1 & z_1^1 & \cdots & z_1^{M-1} \\ \vdots & \vdots & \ddots & \vdots \\ 1 & z_K^1 & \cdots & z_K^{M-1} \end{bmatrix} \tag{119}$$
$$= \zeta_{L\times K} C_{K\times K} \zeta^T{}_{K\times M}$$

where z_k and c_k, $k = 1,..,K$ represent the signal pole and the complex amplitude of the FID respectively. The format of a matrix $\zeta_{L\times K}$ and $\zeta^T_{K\times M}$ is called Vandermonde where each row are represented by the signal pole of the FID and its exponents of the row numbers (i.e., 0,1, …, L-1). Giving this information, the following statement must be true.

$$\begin{bmatrix} z_1^1 & \cdots & z_K^1 \\ \vdots & \ddots & \vdots \\ z_1^{L-2} & \ddots & z_K^{L-2} \\ z_1^{L-1} & \cdots & z_K^{L-1} \end{bmatrix} = \left[\begin{bmatrix} 1 & \cdots & 1 \\ z_1^1 & \ddots & z_K^1 \\ \vdots & \ddots & \vdots \\ z_1^{L-2} & \cdots & z_K^{L-2} \end{bmatrix} \right] \begin{bmatrix} z_1 & \cdots & 0 \\ \vdots & \ddots & \vdots \\ 0 & \cdots & z_K \end{bmatrix} \tag{120}$$
$$\zeta_t = \zeta_b diag\left(z_K\right)$$

where ζ_t is equal to the $\zeta_{L\times K}$ entries without the top row, and ζ_b is missing the bottom row of the $\zeta_{L\times K}$. The submatrices of Vandermonde and singular value decomposition share similarity that the $\zeta_{L\times K}$ can be replaced by $\widehat{U}_t, \widehat{U}_b$ which equivalent to the right singular vector submatrices without the first and the last rows respectively and Z' as the diagonal matrix of z_k notation and the Eq. (120) becomes

$$\hat{U}_t = \hat{U}_b Z' \tag{121}$$

The Eq. (121) is now in the same condition as the linear prediction format that previously described in Section 3.6.1. To find the entries of Z', use the orthogonality of the matrix $\widehat{U}_b$ and multiply both sides of the Eq. (121) by $\widehat{U}_b^T$

$$\hat{U}_b^T \hat{U}_t = \hat{U}_b^T \hat{U}_b Z', \tag{122}$$

then take the inverse of $\widehat{U}_b^T \widehat{U}_b$ which allow eliminating $\widehat{U}_b^T \widehat{U}_b$ from the right side of the equation by multiplying the matrices on the left side

$$\left(\hat{U}_b^T \hat{U}_b\right)^{-1} \hat{U}_b^T \hat{U}_t = Z' \tag{123}$$

The matrix property $\widehat{U}_b^T \widehat{U}_b$ can be rewritten as

$$\hat{U}_b^T \hat{U}_b = \left(I - \hat{\mathbf{u}}_b^T \hat{\mathbf{u}}_b\right) \tag{124}$$

where I is the unit matrix and where $\hat{\mathbf{u}}_b$ is the last row vector of $\widehat{U}_b$. Applying the Sherman-Morrison matrix inversion formula [380, 381] to the Eq. (123) with Eq. (124):

$$Z' = \left(I + \frac{\hat{\mathbf{u}}_b \hat{\mathbf{u}}_b^T}{1 - \hat{\mathbf{u}}_b^T \hat{\mathbf{u}}_b} \right) \hat{U}_b^T \hat{U}_b . \tag{125}$$

The Z' matrix is diagonal and from this the signal pole elements including the damping factors and frequencies can be obtained first then amplitudes and phases can be calculated from Eq. (110).

When performance is compared between LPSVD and HSVD, HSVD is known to process much faster and provide more precise results than LPSVD since there is no polynomial rooting is required [79].

3.6.3 Matrix Pencil Method (MPM)

Unlike the LPSVD method, the Matrix Pencil method finds the signal pole property by determining an eigenvalue. LetX_0 and X_1 be (*N-M*) by *M* matrices filled with noiseless FID data

$x_n = \sum_{k=1}^{K} A_k \exp(i\phi_k) \exp\left(\left(-d_k + i2\pi f_k\right) n\Delta t\right) = \sum_{k=1}^{K} c_k z_k^n, (n = 0,1,...,N-1)$ as shown

$$X_0 = \begin{bmatrix} x_{M-1} & x_{M-2} & \cdots & x_0 \\ x_M & x_{M-1} & \cdots & x_1 \\ \vdots & \vdots & \ddots & \vdots \\ x_{N-2} & x_{N-3} & \cdots & x_{N-M-1} \end{bmatrix}, X_1 = \begin{bmatrix} x_M & x_{M-1} & \cdots & x_1 \\ x_{M+1} & x_M & \cdots & x_2 \\ \vdots & \vdots & \ddots & \vdots \\ x_{N-1} & x_{N-2} & \cdots & x_{N-M} \end{bmatrix} \quad (125)$$

where the length of column M is called the pencil parameter that is equal to or larger than the true minimum rank (i.e., K) of the matrix. Similar to HSVD, these two matrices can be decomposed as

$$X_0 = Z_L C Z_R, X_1 = Z_L C Z Z_R \quad (126)$$

where submatrices Z_L, C, Z_R, and Z are

$$Z_L = \begin{bmatrix} 1 & \cdots & 1 \\ z_1^1 & \cdots & z_K^1 \\ \vdots & \ddots & \vdots \\ z_1^{N-M-1} & \cdots & z_K^{N-M-1} \end{bmatrix}, C = \begin{bmatrix} c_1 & \cdots & 0 \\ \vdots & \ddots & \vdots \\ 0 & \cdots & c_K \end{bmatrix}$$
$$Z_R = \begin{bmatrix} z_1^{M-1} & z_1^{M-2} & \cdots & 1 \\ \vdots & \vdots & \ddots & \vdots \\ z_K^{M-1} & z_K^{M-2} & \cdots & 1 \end{bmatrix}, Z = \begin{bmatrix} z_1 & \cdots & 0 \\ \vdots & \ddots & \vdots \\ 0 & \cdots & z_K \end{bmatrix} \quad (127)$$

This method shares many similarities with HSVD such as Vandermonde matrix structures in the Z_L and Z_R matrices, diagonal matrix forms found in both C and Z that contain the complex amplitude and signal poles properties respectively. Creating the matrix pencil $X_1 - \lambda X_0$ to compare the linear combination of two matrices X_0 and X_1 can be done by finding its eigenvalues λ.

$$
\begin{aligned}
X_1 - \lambda X_0 &= Z_L C Z Z_R - \lambda \left(Z_L C Z_R \right) \\
&= Z_L C \left(Z - \lambda I_K \right) Z_R \\
&= Z_L C \begin{bmatrix} z_1 - \lambda & 0 & 0 \\ 0 & z_2 - \lambda & \\ & & 0 \\ 0 & 0 & z_K - \lambda \end{bmatrix} Z_R
\end{aligned} \tag{128}
$$

Eq. (128) shows that the set of signal poles can be found by generalising the eigenvalues of these two matrices X_0 and X_1. For each eigenvalue, there will also be an eigenvector $\boldsymbol{\xi}_k$,

$$
X_1 \boldsymbol{\xi}_k = z_k X_0 \boldsymbol{\xi}_k \tag{128}
$$

Multiplying both sides of the equation with the Moore-Penrose pseudo-inverse of X_0, X_0^*, gives,

$$
X_0^* X_1 \boldsymbol{\xi}_k = z_k \boldsymbol{\xi}_k . \tag{128}
$$

Since the matrix elements are noiseless, solving for the eigenvectors $\boldsymbol{\xi}_k$ leads to finding the signal pole property z_k of the matrices X_0, X_1 and their complex amplitude c_k. The MPM approach has been included as part of a novel detection-estimation scheme [76] as well as other applications [81, 382].

3.6.4 Filter Diagonalization Method

The Filter Diagonalization Method (FDM) is a nonlinear parametric method originally designed by Neuhauser and Wall to solve quantum dynamics problem. This method was subsequently introduced to NMR as parameter estimation and spectral resolution enhancement method [73, 383, 384]. The term "filter" refers to the segmentation of the spectrum into small sections in order to reduce the computational burden. The FDM is designed to solve the HI problem [383, 385]. With 1D NMR data sets, FDM is used

to fit the time-domain complex signal x_n to a Hamiltonian operator function with complex eigenvalues [386],

$$\begin{aligned} x_n &= \sum_{k=1}^{K} A_k \exp\left(i\phi_k\right)\exp\left(\left(-d_k + i2\pi f_k\right)n\Delta t\right) \\ &= \sum_{k=1}^{K} c_k u_k^n \\ &= \left\langle \Phi_0 \middle| \hat{U}^n \Phi_0 \right\rangle \end{aligned} \tag{129}$$

where Φ_0 is often stated as some "initial state" and $\hat{U}$ is a Hamiltonian operator. If the Hamiltonian operator $\hat{U}$ is diagonalized and normalised by a set of orthogonal eigenvectors E_k, then the operator $\hat{U}$ can be written in spectral representation using eigenvalues u_k and normalised eigenvectors

$$\begin{aligned} \hat{U} &= \sum_{k=1}^{K} \left| E_k \right\rangle u_k \left\langle E_k \right| \\ \hat{U}^n &= \left(\sum_{k=1}^{K} \left| E_k \right\rangle u_k \left\langle E_k \right| \right)^n . \end{aligned} \tag{130}$$

Applying Eq. (130) into Eq. (129) leads to

$$\begin{aligned} x_k &= \left\langle \Phi_0 \middle| \hat{U}^n \Phi_0 \right\rangle \\ &= \left\langle \Phi_0 \middle| \left(\sum_{k=1}^{K} \left| E_k \right\rangle u_k \left\langle E_k \right| \right)^n \Phi_0 \right\rangle \\ &= \sum_{k=1}^{K} \left\langle \Phi_0 \middle| E_k \right\rangle \left\langle E_k \middle| \Phi_0 \right\rangle u_k^n \\ &= \sum_{k=1}^{K} \left\langle \Phi_0 \middle| E_k \right\rangle^2 u_k^n \\ &\equiv \sum_{k=1}^{K} c_k u_k^n \end{aligned} \tag{131}$$

shows that eigenvectors can determine the amplitude and phase of the exponential decay signal while the eigenvalues determine its frequency and widths. Unlike other similar methods such as LP, the operator $\hat{U}$ in FDM does not require to be full rank. The FDM method can also be applied to multidimensional NMR data sets for both

parameter estimations and signal processing purposes [72, 73, 383, 385, 387]. Two well known limitations of FDM in NMR signal processing is that the method does not perform well with low SNR nor overlapping spectral data.

3.7 COMPOSITE PROPERTY MAPPING ALGORITHM (CADZOW'S METHOD)

Introduction

The composite property mapping algorithm proposed by Cadzow has become one of the fundamental NMR signal processing technique since when published in 1988 [52]. The general concept of the composite property mapping algorithm is that if the set of the measured signal is known to possess certain well-defined properties then the solution set can be optimised to find the new signal set with elements that lie closest to the noiseless composite property set in the minimum Frobenius norm sense [366, 388]. The method represents a series of discrete time data into a structured matrix form. The structured matrix form possesses three properties: Toeplitz structure, positive semi-definite and pre-specified rank. By reducing the rank of the matrix, it minimizes the root mean square error (RMSE) between the original and the reduced rank approximation. In the past, the relation between the Eigen polynomials and the Toeplitz matrix representation in the spectral analysis has been studied by various researchers [362, 389-391], yet it was often criticized for its computational load [78, 79, 318]. This is perhaps a reason for its limited use when first introduced. However, with modern technology and improvements in computer processing capabilities, it is very much worth revisiting and studying for possible applications and improvements.

3.7.1 Signal processing with composite property mapping theorem

There are four major steps involve in the composite property mapping theory which are illustrated in Figure 27. Let the measured FID data set (x_n) from Eq. (23) be the sum of two (i.e., $K = 2$) exponential decay signals (s_n) and the noise (w_n) with total N

data points (n = 0,1,…, N-1). When the x_n is formed into the L by M overdetermined Toeplitz matrix structure, it can be assumed that the matrix structure of the noiseless signal s_n and the noise w_n also follow as

$$\begin{bmatrix} x_{M-1} & \cdots & x_0 \\ \vdots & \ddots & \vdots \\ x_{N-1} & \cdots & x_{L-1} \end{bmatrix} = \begin{bmatrix} s_{M-1} & \cdots & s_0 \\ \vdots & \ddots & \vdots \\ s_{N-1} & \cdots & s_{L-1} \end{bmatrix} + \begin{bmatrix} w_{M-1} & \cdots & w_0 \\ \vdots & \ddots & \vdots \\ w_{N-1} & \cdots & w_{L-1} \end{bmatrix}, \quad (132)$$
$$X = S + W$$

where Toeplitz matrix X which can be written as the sum of two matrices S + W: noiseless FIDs (S) and the noise properties matrix (W). The three properties: Toeplitz structure, positive semi-definite and pre-specified rank only (and always) applies to the noiseless matrix S; while the noise properties matrix does not hold any of these eigencharacteristics. The Toeplitz matrix of W has full rank while the Toeplitz matrix S have prespecified rank (i.e., k = 2) after SVD. Recalling the definition of the matrix rank, which is equal to the maximum number of linearly independent column and row vectors, if the sums of two sinusoidal signals formatted into Toeplitz or Hankel structure, there will be only two linearly independent column vectors that exist in the matrix S. Therefore, pre-specified matrix rank is equal to the number of summed sinusoids in the noiseless FID. By preserving the properties equal to the prespecified rank and removing the others, the processed matrix X'' holds the minimum error to the noiseless data set S.

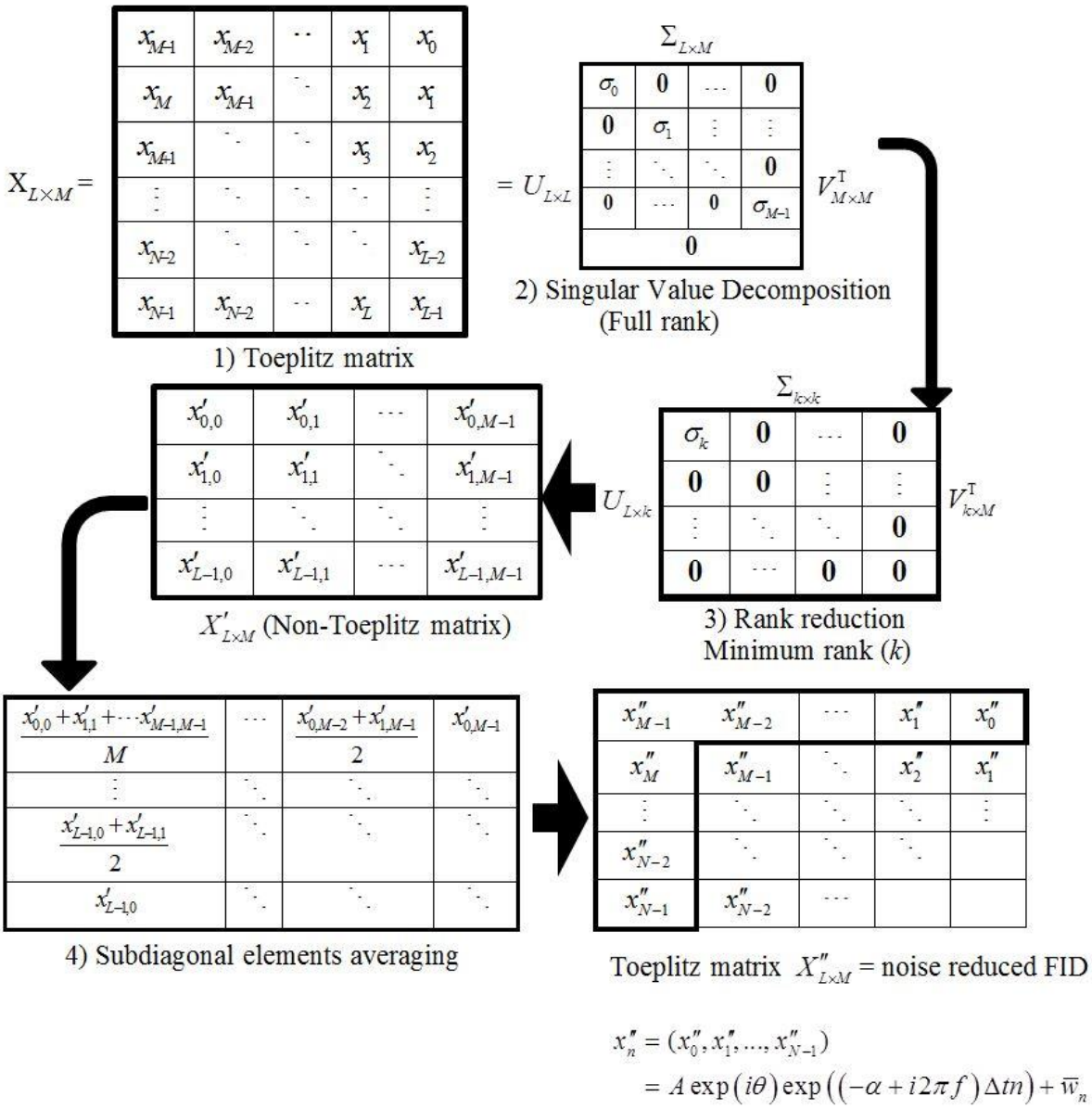

Figure 27. A conceptual view of Cadzow's composite property mapping algorithm. The method contains four fundamental steps: 1) Arrangement of the measured FID into Toeplitz matrix, 2) Factorise the matrix X by SVD. 3) Reduce the matrix rank to its prespecified minimum rank. 4) Take the average of sub-diagonal elements to reconstruct Toeplitz structure.

To explain further, in the first step, the dimension of the Toeplitz matrix L by M must be greater than the number of exponentials ($K \leq \min(L, M)$), where $N = L + M - 1$. The number of rows L is greater than the number of columns M. For faster computation ($O(LM^2)$ for $M < L$) and also creating the overdetermined matrix algebra environment, the column number M was set to 1/10th of the N (Rows L: Column M)

throughout this thesis. This large Toeplitz matrix is then decomposed into three submatrices U, Σ and V^T by the singular value decomposition method,

$$X_{L\times M} = U_{L\times L} \times \Sigma_{L\times M} \times V^T_{M\times M} \tag{133}$$

where U and V are column orthogonal matrices containing right and left singular vectors, respectively. The Σ matrix is a diagonal matrix with positive real values called singular values (σ), which, in descending order, determine the rank of the overall matrix X, $r = M$ (in $L > M$). After the SVD, the three decomposed submatrices for both the signal and noise properties are represented separately as

$$\begin{aligned} X &= \tilde{U}_r \tilde{\Sigma}_r \tilde{V}_r^T + U_o \Sigma_o V_o^T \\ &= \tilde{X}_r + X_o \\ &= S + W \end{aligned} \quad . \tag{134}$$

With eigencharacteristics of the noiseless Toeplitz matrix, the number of the prespecified rank of the matrix S is equal to the number of non-zero singular values in the Σ matrix after factorisation. As Eq. (129) states, the noiseless data can be reconstructed by multiplying r columns of the submatrix U by an r by r diagonal matrix Σ, and by r rows of the submatrix V^T,

$$\begin{aligned} S &= \left[\tilde{U}_r \middle| \quad \tilde{U}_o\right] \begin{bmatrix} \tilde{\Sigma}_r & 0 \\ 0 & 0 \end{bmatrix} \begin{bmatrix} \tilde{V}_r^T \\ \hline \tilde{V}_o^T \end{bmatrix} \\ &= \tilde{U}_r \tilde{\Sigma}_r \tilde{V}_r^T + \tilde{U}_o 0 \tilde{V}_o^T \\ &= \tilde{U}_r \tilde{\Sigma}_r \tilde{V}_r^T \end{aligned} \tag{135}$$

Each singular value corresponds to the magnitude of the FID amplitude or spectral amplitude (including noise) of each contributing resonance. As the noise amplitude increases, the singular values of the noise increase while the signal singular values stay the same. This leads to difficulties in determining the minimal matrix rank to extract the signal since the gap between the singular values of the signal and noise

become smaller and harder to differentiate [52]. By removing the noise related singular value elements Eq. (128) becomes,

$$\begin{aligned} X_r &= \tilde{U}_r \tilde{\Sigma}_r \tilde{V}_r^T + U_{or} \Sigma_{or} V_{or}^T \\ &= S + E \\ &= U_r \Sigma_r V_r^T \end{aligned} \tag{136}$$

where S still continues to be a Toeplitz matrix filled with signal only elements, while the E is a non-Toeplitz matrix filled with error values that arise from the original noise elements w_n of the minimal rank $r = k$. After the multiplication of the three submatrices with the reduced rank Σ_r matrix, the average of the sub-diagonal elements are taken to reconstruct not only the Toeplitz matrix form but also the estimated reduced noise FID $x''(t)$ vector form,

$$x''(t) = \begin{bmatrix} x''(0) & x''(1) & \cdots & x''(N-1) \end{bmatrix}^T \tag{137}$$

The mathematical proof of how the sub-diagonal averaging leads back to the FID vector form is found in [392].

In general, increasing noise levels complicates the determination of the minimum rank. Even if the correct minimum rank is known, if the noise level is large then the residual noise may affect the minimum rank singular values, and thus, the estimated optimal data set. The minimum rank determination process becomes even harder with complex data with multiple resonances and highly noise distorted data.

Proof of reducing rank and optimisation

Replacing the tail singular values (those related or coming from the noise) by zeros would reduce the dimension of the overall matrix. This is called the reduced rank matrix [393]. By reducing the rank of the matrix, the RMS error between the original and the reduced rank approximation is minimised. Let A be the original matrix and A' the approximated matrix (i.e., the reduced rank matrix)

$$
\begin{aligned}
&A = U\Sigma V^T \\
&a_{ij} = \sum_k \sum_l u_{ik}\sigma_{kl}v_{lj}^T \\
&\|A\|^2 = \sum_i \sum_j \left(a_{ij}\right)^2 = \sum_i \sum_j \left(\sum_k \sum_l u_{ik}\sigma_{kl}v_{lj}^T\right)^2 \\
&\left(\sum_k \sum_l u_{ik}\sigma_{kl}v_{lj}^T\right)^2 = \sum_k \sum_l \sum_m \sum_n u_{ik}\sigma_{kl}v_{lj}^T u_{in}\sigma_{nm}v_{mj}^T \\
&\|A\|^2 = \sum_i \sum_j \sum_k \sum_l \sum_m \sum_n u_{ik}\sigma_{kl}v_{lj}^T u_{in}\sigma_{nm}v_{mj}^T
\end{aligned} \quad . \tag{138}
$$

Since the Σ matrix is known as diagonal square matrix it can be simplified by replacing *l* by *k* and *m* by *n,* then Eq. (132) can be rewritten as,

$$
\|A\|^2 = \sum_i \sum_j \sum_k \sum_n u_{ik}\sigma_{kk}v_{kj}^T u_{in}\sigma_{nn}v_{mj}^T \quad . \tag{139}
$$

Eq. (133) shows that if $k = n$ then $\sum_i u_{ik}u_{in} = 1$ since the vector u is column-orthonormal. The same rule applies to vector v which is row orthonormal (i.e., $\sum_j v_{kj}^T v_{mj}^T = 1$), and as result, only the singular value components remain,

$$
\|A\|^2 = \sum_k \sigma_{kk}\sigma_{kk} = \sum_k \left(\sigma_{kk}\right)^2 \quad . \tag{140}
$$

Let us assume that the rank of the matrix is reduced from *k* to *t* and new singular value matrix is denoted as Σ′, the reconstructed matrix A' is then,

$$
\begin{aligned}
&A' = U\Sigma' V^T \\
&A - A' = U(\Sigma - \Sigma')V^T \\
&\|A - A'\|^2 = \sum(\Sigma - \Sigma')
\end{aligned} \tag{141}
$$

To minimize $\|A - A'\|^2$, requires keeping the large singular values and replacing the smaller singular values with zero and as results, the rank of the matrix is reduced.

Solvent suppression with Cadzow's method

As previously mentioned, singular values yielded through the composite property mapping algorithm are proportional to the amplitude of the sinusoidal components of

the FID. Resonance manipulation apart from noise reduction, such as solvent resonance suppression can also be applied by adjustment of the singular values in a similar manner [154, 156]. In solution state ^{1}H NMR studies, processing FID data is often dominated by the large solvent signal. This amplitude difference also shows in the singular values, leaving solute and noise singular values significantly small. Thus the determination of the minimum rank separating signal from noise becomes difficult.

The elimination of the solvent signal can be easily performed by replacing the first singular value with zero and reconstructing using the same procedure taken for noise reduction. This approach is only applicable if the resonance lineshape is Lorentzian. When the solvent resonance is somehow distorted (e.g., Figure 41 in Chapter 7), more than one singular value may require to be replaced with zeros to eliminate the solvent resonance from the FID.

3.7.2 Other Signal Processing Methods similar to Cadzow's method

Harmonic Inversion (HI)

The harmonic inversion noise reduction (HINR) method was developed by Taylor et al, to improve spectral sensitivity to facilitate the detection of weak NMR signals [69, 71]. There are four steps in the method: 1) Transform the original FID into a spectrum via FT. 2) Segment the spectrum into a smaller window of approximately 300 Fourier grid points and take the inverse FT of each spectral segment. 3) A Hermitian correlation matrix is then constructed from the segmented FID. 4) Perform SVD to clean the FID by discarding small (i.e., noise) singular values. Step 4 is performed in the same manner as Cadzow's rank determination process. A detailed mathematical explanation for HINR method is found in Ref [65, 69, 394]. HINR method has been tested in ^{13}C [65], ^{15}N [69], ^{17}O, and ^{31}P [70].

Singular Spectrum Analysis (SSA)

"Singular Spectrum Analysis (SSA)" also known as "Structured Total Least Squares (STLS)" is a time series analysis and noise filtering technique using a rank reduced Hankel matrix method [395]. The method is constructed by two complementary

stages: decomposition and reconstruction with two steps each within. The first step "embedding" maps the 1D time series (i.e., FID) data into a Hankel matrix *H*. The characteristics of the Hankel matrix include both the rows and columns which are subseries of the original time series resulting in anti-diagonal elements (see Eq.(118)). The number of rows is specifically called window length in the SSA method. The second step of the Decomposition stage is computing the SVD of this Hankel matrix. The Hankel matrix is first multiplied by its transpose matrix (viz., HH^{T}) to create a covariance matrix which then decomposed into submatrices containing eigenvalues and its corresponding eigenvectors. The first reconstruction step is so-called Eigen-triple grouping [396]. This grouping step chooses the set of Eigen-triple which refers to the signal component of the eigenvalues. This and the following last steps "diagonal averaging" follow the same procedure as other SVD-based signal processing methods to reform the matrix data back into 1D time series vector.

There are two key parameters that the SSA method's outcome are highly dependents on; the window length of the embedding, and the number of eigenvalues that separate the signal from the noise. These two parameters must be chosenand if an unsuitable choice is made for one parameter the outcome of the noise reduced spectrum may not be the optimum [397]. The SSA method is designed to overcome the heavy computational load in SVD without any compensation on the accuracy of the results [398, 399]. To reduce the SVD computational time, extensions of the SSA method such as QR factorisation [400] and the Lanczos method [401] were also developed, however, both methods have limited outcome accuracy and reliability which depend on the smoothness and/or the decay rate of the original singular spectrum [402]. Under certain conditions, the SSA method can be viewed as one iteration of Cadzow's basic algorithm [52, 395]. Meaning that One iteration of Cadzow's basic algorithm will yield the same results obtained from the SSA method if the window length and the Eigen-Triple grouping chosen are the same values in both methods. There is some discussion about the superiority of the methods between SSA and Cadzow's [403]. Even with such similarity found in the procedure, both methods are still studied, improved and applied to many studies not only for NMR but also for other fields. For this thesis, Cadzow's composite property mapping algorithm was chosen to be studied, applied and utilised to improve existing NMR signal processing methods.

CHAPTER 4. SHORTENING NMR EXPERIMENTAL TIMES WITH NORMALISATION

4.1 INTRODUCTION

Some NMR experiments are typically run as an array in which one experimental parameter (EP) is iteratively varied to modulate the signal amplitude. Two common examples being NMR relaxation [93, 404] and NMR diffusion [27, 28] measurements. When measuring longitudinal relaxation using the inversion recovery sequence [93], the parameter being varied is the τ delay between the π and $\pi/2$ RF pulses. For diffusion measurements, the varied parameter is the magnitude of the dephasing effects of the diffusion encoding gradients normally proportional to the magnitude g of the gradient pulses [111]. In either case, the result is ultimately a change in the magnitude of the acquired signal. Due to low SNR and phase cycling considerations, a considerable number of scans may be required for each value of the varied experimental parameter. Both types of measurements have traditionally, and possibly out of early computational limitations, been conducted with the same number of scans for each iteration. Consequently, the SNR changes significantly from one spectrum to the next, in a generally defined manner, due to signal attenuation depending upon the experimental parameter whilst the noise component of the signal is constant. In general, approximate values for the diffusion coefficient or relaxation times are known beforehand. Quite often there is more than sufficient SNR at some values of the experimental parameter (e.g., at long or very short τ values or at low gradient values) but insufficient at others (e.g., τ values near the null point or at high gradient values) in conventionally performed experiments.

Without additional hardware or complicated pulse sequences, much simpler and time efficient array experiments can be performed using the 'normalisation technique' presented here. Unlike the conventional signal collection scheme with a constant number of scans throughout the experiment, the number of scans is tailored for each value of the experimental parameter to optimise the SNR. In the normalisation approach, a target SNR (SNR_{required}) is chosen and a sufficient number of scans is calculated for each value of the experimental parameter, NS(EP), so that (ideally) the acquired signal, S(EP), exceeds SNR_{required}. Importantly, NS is now a function of EP, and the signal acquired for each EP value is then normalised according to the total number of averages that were used to acquire it. This is done independently for each EP value. This time efficient 'scan number normalisation' approach to acquiring

arrayed NMR experiments is quite general and is readily applicable beyond relaxation and diffusion measurements.

The utility of this approach is demonstrated with ^{23}Na NMR diffusion and spin-lattice relaxation measurements on an aqueous l0 mM NaCl sample. As will be shown, this approach leads to a significant reduction in experimental time and increased experimental precision yet requires only a trivial change to the acquisition protocol and analysis.

4.2 THEORY

4.2.1 Practical implementation of the normalisation approach

T_1 measurement

The signal intensity $M(\tau)$ resulting from the standard inversion recovery sequence (see Figure 7 from Section 2.6) was previously given at Eq. (11). An initial measurement $M(0)$ and $NS_{initial}$ scans is used to determine $SNR_{initial}$. Hence, the number of scans required at $\tau = 0$, ($NS(0)$), to obtain a spectrum with at least $SNR_{required}$ is given by

$$NS(0) = NS_{cycle} \times max\left(1,\ floor\left(\frac{NS_{initial}\left(\frac{SNR_{required}}{SNR_{initial}}\right)^2}{NS_{cycle}}\right)\right) \tag{142}$$

where NS_{cycle} is the number of scans required for one phase cycle and the *floor* function ensures an integer value. Including the effects of relaxation using Eq. (11), the number of scans required ($NS(\tau)$) for $\tau > 0$ can be estimated from

$$NS(\tau) = NS_{cycle} \times max\left(1,\ floor\left(\frac{NS(0)\left(\frac{M(0)}{M(\tau)}\right)^2}{NS_{cycle}}\right)\right) \tag{143}$$

In practice, an upper limit of $NS(\tau)$ would be set to prevent impracticably large values near the null point (i.e., $\tau_{null} = T_1 \ln(2)$), or, alternatively, the null point could be skipped.

Since, $M(\tau)$ was acquired with $NS(\tau)$, prior to regression of Eq. (11) onto the relaxation data, the individual $M(\tau)$ values must be normalised according to

$$M_{normalised}(\tau) = \frac{M(\tau)}{NS(\tau)} \ . \tag{144}$$

Eq. (11) is then regressed onto the $M_{normalised}(\tau)$ values to obtain the T_1 relaxation time.

Diffusion measurement

The NMR signal attenuation resulting from a standard PGSE sequence (see Figure 9 in Section 2.8) for a freely diffusing species is given at the Eq. (16). The diffusion coefficient D is determined by regressing Eq. (16) onto the $E(g)$ values. A typical PGSE measurement begins by a rough determination of the maximum b value, corresponding to the values of the PGSE parameters (i.e., δ, g, Δ) required to attenuate the echo signal by at least 90% (i.e., $E(g) \leq 0.1$). This also provides an approximate value of D. In a conventional measurement, the same value of NS is used for all gradient strengths. Similar to the relaxation measurements, in the normalisation approach the number of scans required for each gradient strength, $NS(g)$, can be estimated and tailored.

Using Eq. (136) and including the effects of the PGSE attenuation from Eq. (16), the number of scans required for $g > 0$ spectra, ($NS(g)$), can be estimated by

$$NS(g) = NS_{cycle} \times max\left(1,\ floor\left(\frac{NS(0)\left(\frac{1}{E(g)}\right)^2}{NS_{cycle}}\right)\right) \tag{145}$$

where $NS(0)$ is now the number of scans required to obtain $SNR_{required}$ at $g = 0$. However, blind use of Eq. (139) could lead to a very large number of scans at high attenuations. In practice, an upper limit of $NS(g)$ should be set.

Since, $S(0)$ was acquired with $NS(0)$, prior to regression of Eq. (16) onto the PGSE data, the individual $E(g)$ values must be normalised according to

$$E_{normalised}(g) = \frac{\left(\frac{S(g)}{NS(g)}\right)}{\left(\frac{S(0)}{NS(0)}\right)} = \frac{S(g)}{S(0)}\frac{NS(0)}{NS(g)} \ . \tag{146}$$

4.3 MATERIALS AND METHODS

4.3.1 Sample preparation

A 0.5 ml aliquot of a 10 mM NaCl solution in D_2O was dispensed into a 5 mm NMR tube (Wilmad, USA). The sample was bringing to the room temperature (298K) at the time of the experiment.

4.3.2 NMR Experiments

All ^{23}Na NMR measurements were performed at 298 K and 105.8 MHz on a 400 MHz Bruker Avance NMR spectrometer (Bruker Biospin, Karlsruhe, Germany) using a 5 mm BBFO probe equipped with a *z*-gradient coil. A typical $\pi/2$ pulse length as 9.8 μs. A spectral width of 847 Hz was digitised into 32,768 points with an acquisition time of 0.3 s and a recycle delay of 0.3 s sufficient for full thermal relaxation. A line broadening of 0.5 Hz was applied prior to Fourier transformation. Spectral intensities were determined by integration of the region from -0.2 to 0.2 ppm. SNR values were calculated using the Bruker Topspin command 'SINO'. Inversion recovery and PGSE

measurements were performed using the standard sequences [28, 93]. NS_{cycle} = 8 for both inversion recovery and PGSE NMR sequences, respectively. The ^{23}Na diffusion measurements were conducted with Δ = 60 ms, δ = 4 ms and g increased from 0.006 to 0.503 T m^{-1} in increments of 0.050 T m^{-1}. Data fitting was performed using OriginPro 9.1 (OriginLab, Massachusetts, USA).

4.4 RESULTS AND DISCUSSION

4.4.1 T_1 measurement

The ^{23}Na T_1 was roughly estimated from the null point to be 47.0 ms. Twelve different τ values ranging from 0.001 to 0.8 s were then selected to accurately measure the T_1. As a reference, a conventionally acquired T_1 relaxation measurement with NS = 80 yielded T_1 = 49 ± 1 ms (Figure 28a and b). The SNR for these reference spectra ranged from 45 (τ = 0.02 s) to 174 (τ = 0.8 s) as shown in Table 3.

Table 3. The τ values used in the ^{23}Na inversion recovery experiments and the measured SNR from the NS = 80 'reference' inversion recovery experiment. Also shown are the estimated number of scans, $NS(\tau)$, required to achieve SNR ~ 40 and the measured SNR(τ) values. The NS value for τ = 0.001 s was used as $NS(0)$.

τ (s)	**SNR of NS = 80**	**Normalisation Approach**	
		NS(τ)	**SNR(τ)**
0.001	102	8	43
0.003	112	8	34
0.005	115	8	39
0.01	90	16	36
0.02	45	80	45
0.05	57	80	57
0.06	88	40	49
0.07	90	24	58
0.08	118	16	45
0.2	103	8	49
0.5	138	8	55
0.8	174	8	54

The T_1 measurement was then performed using the normalisation approach using the same τ values, but with the $NS(\tau)$ values are chosen to achieve an SNR of ~ 40. The $NS(\tau)$ values together with the corresponding experimentally measured SNR values are tabulated in Table 3. The corresponding spectra and analysis are plotted in Figure 28c and d, respectively, giving $T_1 = 49 \pm 1$ ms, which is in perfect agreement with the reference dataset but with a 68% reduction in experimental time.

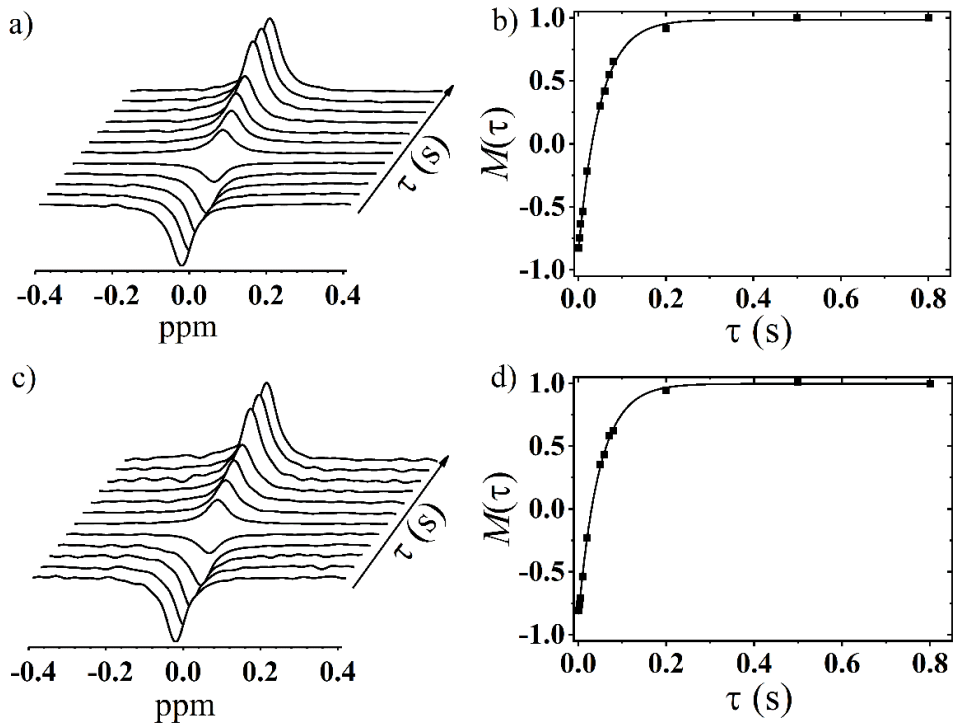

Figure 28. ^{23}Na inversion recovery measurements of 10 mM NaCl in D_2O at 298 K a) Reference spectra acquired with $NS = 80$ and c) spectra acquired with $NS(\tau)$ as defined in Table 1. The corresponding T_1 relaxation time estimation plots are shown in b) and d), respectively.

4.4.2 Diffusion measurement

The number of scans required at the highest gradient strength (g = 0.503 T m^{-1}) to satisfy $SNR_{required} = 40$ was first calculated to be $NS = 1440$. A conventionally acquired reference NMR diffusion dataset acquired with $NS = 1440$ at every gradient strength

gave the sodium diffusion coefficient to be $D = (1.27 \pm 0.02)\times10^{-9}$ m^2 s^{-1}. The SNR for these reference spectra is tabulated in Table 4. To utilise the normalisation approach, a spectrum was first collected with the lowest gradient strength ($g = 0.006$ T m^{-1}) with $NS = 8$, which gave $SNR_{initial} = 13$. Thus, according to Eq. (136), 72 scans (i.e., $NS(0)$) were required to achieve $SNR_{required} = 40$. The $NS(g)$ values estimated from Eq. (139) are tabulated in Table 4 together with the corresponding experimental SNR(g) values. The spectral data set after normalisation according to Eq. (140) and its analysis using Eq. (16) is presented in Figure 29 giving $D = (1.26 \pm 0.03)\times10^{-9}$ m^2 s^{-1}, which is within experimental error of the estimate from the reference dataset but with a 75% reduction in experimental time.

Table 4. The SNR of the $NS = 1440$ reference ^{23}Na NMR diffusion experiment. Also shown are the estimated number of scans ($NS(g)$) required to achieve an SNR = 40 and the corresponding measured SNR(g) values. The NS value for $g = 0.006$ T m^{-1} was used as $NS(0)$.

***g* (T m^{-1})**	**SNR of NS = 1440**	**Normalisation Approach**	
		NS(g)	**SNR(*g*)**
0.006	135	72	40
0.055	171	72	45
0.105	126	80	35
0.155	142	96	39
0.205	161	120	44
0.254	97	160	33
0.304	67	216	29
0.354	87	320	37
0.404	67	496	37
0.453	63	824	36
0.503	43	1440	43

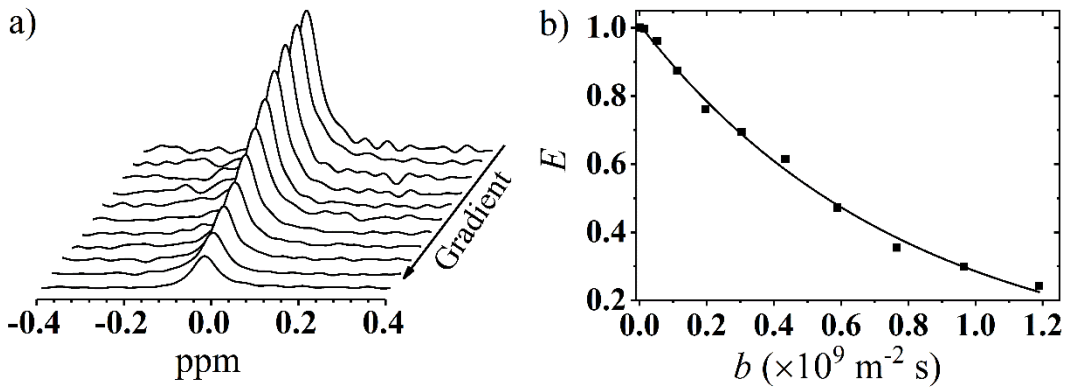

Figure 29. a) ^{23}Na PGSE NMR spectra of 10 mM NaCl in D_2O at 298 K obtained with NS(g) as defined in Table 2 and b) non-linear regression of Eq. (5) onto the data set gave $D = (1.26 \pm 0.03)\times10^{-9}$ m^2 s^{-1}.

4.5 CONCLUDING REMARKS

The normalisation approach, in conjunction with a simple calculation preparation, can significantly reduce the overall experimental time in diffusion and T_1 (or similarly T_2) measurements with essentially no loss in accuracy. Both of the above examples involved some elements of prior knowledge in choosing the experimental parameters (i.e., an estimate of the diffusion coefficient and the relaxation time) and the functional form of the signal amplitude dependence on the experimental parameter (i.e., Eqs. (11) and Eq. (16)). In general, the functional form will be known and in most cases it is possible to obtain some pertinent estimate of T_1 or D. Less accurate estimates of T_1 or D will still lead to parameters resulting in a considerable reduction in overall experimental time compared to merely using the same number of scans for each element of the experimental array. In contrast to other approaches for speeding up NMR experiments, the normalisation approach can be rather generally applied and in principle, could be largely or totally automated.

CHAPTER 5. NOISE REDUCTION IN QUADRUPOLAR NUCLEI DIFFUSION NMR USING COMPOSITE PROPERTY MAPPING ALGORITHM

5.1 INTRODUCTION

As discussed in Section 1.3.1 and Section 2.7, quadrupolar nuclei are ubiquitous and thus extremely important in biology and chemistry. Rapid quadrupolar relaxation can further exacerbate signal-to-noise issues [89, 108]. For example, ^{23}Na relaxes rapidly (e.g., T_1 = 49 ms in D_2O at 298K measured in Chapter 4) and the SNR can easily become a limiting factor in the practicality of an experiment when there is a significant duration in the pulse sequence between excitation and acquisition as in a diffusion experiment.

Quadrupolar nuclei often have a significant advantage in NMR post-signal processing. Specifically, solution state spectra of quadrupolar nuclei NMR generally have only one resonance thus allow the rank of the Toeplitz matrix into which the FID is formatted to be pre-specified as one. Therefore, no matrix rank investigation is required during the signal processing procedure. What is more, there will be no false rank determination which could lead to inaccurate results.

Here we apply 'Composite property mapping' method [52] for the analysis of quadrupolar nuclei NMR diffusion measurements. The theory and methodology of the composite property mapping algorithm are previously provided in Section 3.7. ^{23}Na nuclei was used as an example for quadrupolar nuclei NMR diffusion experiment.

This simple application of a composite property mapping method is believed to provide superior SNR with very short processing time. The effect of noise reduction was compared with the usual direct Fourier transformation approach and the Savitzky-Golay (SG) filtering method. The SG filtering method is a well-known NMR denoising technique using polynomial function fitting and windowing [405-407]. The only concern for applying composite property mapping algorithm is the sensitivity limitation. When the noise level increases, the residual noise error within the processed data also increases, thus the accuracy and precision of the diffusion coefficient estimation decrease. The sensitivity limitation of composite property mapping was investigated further by using simulated diffusion data.

5.2 MATERIALS AND METHODS

5.2.1 Sample preparation and NMR measurements

NaCl (99.0%, Chem-supply, AU) was dissolved in D_2O and diluted to 10 mM. Aliquots (0.5 ml) were dispensed into 5 mm NMR tubes (Wilmad, USA).

5.2.2 NMR diffusion measurements

^{23}Na PGSE NMR diffusion experiments were performed at 105.8 MHz, on a 400 MHz Bruker Avance NMR spectrometer using a 5 mm BBFO probe at 298 K. The parameters for the standard PGSE sequence (see Figure 9) are: δ = 5 ms, Δ = 60 ms, g from 0.005 to 0.503 T m^{-1} in increments of 0.045 T m^{-1}, an acquisition time of 0.2 s and a recycle delay of 0.3 s (i.e., total recycle delay = 0.5 s). Each spectrum was originally digitised into 32 K data points from 24K data points collected as the FID. The narrow frequency region (i.e., 423.36 Hz) containing the sodium signal was extracted and inverse Fourier transformed for processing. The size of the dataset was reduced to 926 data points. The processing of each spectrum took less than half a second on a PC (CPU of 3.40 GHz and RAM of 16.0 GB) to enhance the SNR of each spectrum using Cadzow's method (see Section 3.7.1) code written in MathCad 15. With prior knowledge of the resonance being a single peak, the minimum rank for the matrix was set equal to one for each dataset.

5.2.3 Savitzky-Golay Filtering Method

The effectiveness and efficiency of Cadzow's technique were compared with the nonparametric SG filtering method [51, 407]. The SG method shares similarities with other methods such as the moving average method, Whittaker smoother [405, 408] and the low pass filter method. As the term "filtering" suggests, the SG method is not designed to estimate parameters, but to smooth the data directly from the time-domain signal [409]. The SG filtering method uses least squares polynomial fitting with small moving windows. To obtain optimal output, two key parameters; the degree of the polynomials and the size of the moving window must be chosen adequately [410, 411]. For example, if the spectrum contains narrow peaks represented by 10 data points, and the moving window size must be chosen with more than 10 data points, the resulting

filtered spectrum contains broadened peaks with much lower amplitudes. The degree of the polynomial function is also important for data smoothing and fitting. A polynomial of degree one will give a linear fit to the data values within the window and thus only a very small smoothing effect. The basic theory, methodology, and applications of SG filters can be found in the following references ([406, 407, 410-412]). Due to the accessibility and adaptability of this method, the SG filtering method was written in many processing programming languages such as Matlab [413] and Mathcad [414]. Following the steps in ref [414], the experimental ^{23}Na NMR diffusion data acquired with NS = 64 was treated with a 4th degree polynomial with 15 and 25 moving window data points, and fitted with an 8th degree polynomial also with 15 and 25 moving window data points as presented in the next section.

5.3 RESULTS AND DISCUSSION

5.3.1 Diffusion coefficient estimation of Na^+ in aqueous solution

The 10 mM NaCl sample was measured with RG = 16384 with NS = 2048 ("reference" dataset), 128 or 64 ("noisy" datasets). All datasets were processed using standard FT processing followed by diffusion coefficient determination. The 'noisy' datasets were also processed with Cadzow's method followed by diffusion coefficient determination. The analysis for the NS = 64 datasets is shown in Figure 30 and the results for all three datasets are summarized in Table 5.

Table 5. SNR and results of the diffusion coefficient determination for the ^{23}Na resonance of the reference and noisy datasets after processing using FT and with Cadzow's method.

NS	**SNR after FT[1]**		***D* after FT ($\times10^{-9}$ m^{2}s^{-1})**	**SNR after Cadzow[1]**		***D* after Cadzow ($\times10^{-9}$ m^{2}s^{-1})**
	g = 0.005 (T m^{-1})	**g = 0.503 (T m^{-1})**		**g = 0.005 (T m^{-1})**	**g = 0.503 (T m^{-1})**	
2048	453	35	1.24 ± 0.02	298100	204000	1.24 ± 0.01
128	107	11	1.21 ± 0.05	21970	9288	1.23 ± 0.04
64	61	6	1.27 ± 0.05	53000	3000	1.23 ± 0.04

[1]with increasing gradient strength.

As can be seen in Figure 30, the application of Cadzow's method results in significant noise reduction, providing cleaner spectra and more accurate diffusion coefficient values with far fewer scans. In the present case, this results in a 32-fold reduction in experimental time.

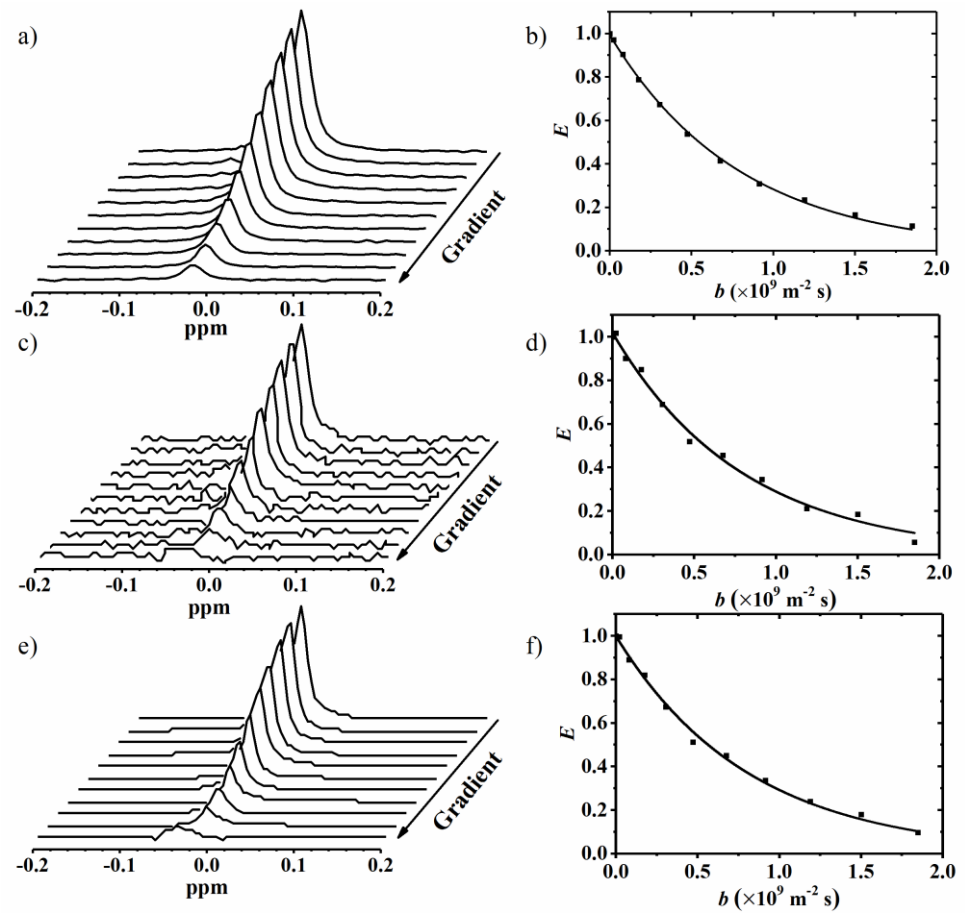

Figure 30 ^{23}Na PGSE NMR spectra of NaCl in D_2O at 298 K obtained with a) NS = 2048, c) NS = 64 and the diffusion attenuation analysis of the data using Eq. (16) are shown in panels b) and d), respectively. For the same dataset with NS = 64, but after signal processing with Cadzow's method, the spectra and diffusion attenuation analysis are shown in e) and f), respectively.

The spectrum with the lowest SNR in Figure 30e shows Cadzow's method is unable to recover the correct line shape below a certain SNR threshold. To investigate the SNR threshold above which the SNR of raw diffusion NMR data has to be kept in order to obtain valid denoised results, the following simulation study with different additive Gaussian noise level was conducted.

5.3.2 SNR threshold for Cadzow's method studied by simulation

The key to the successful application of Cadzow's method lies in the determination of the minimum matrix rank when the number of resonances is unknown. Even with the prespecified minimum rank (i.e., the number of resonances is known), the reconstructed matrix still contains noise components (see Eq. (131)). This residual noise embedded within the singular values of minimal rank can affect spectral amplitude even after signal processing.

The reference diffusion coefficient value was determined to be $D = (1.24 \pm 0.01)\times10^{-9}$ m^2 s^{-1}. The amplitudes of the simulated FIDs were determined at eleven equally incremented gradient strengths and each FID was constructed with 2048 data points. Additive white Gaussian noise was generated using signal processing command 'gaussn(n)' in Mathcad and added to the simulated FIDs. The Mathcad command, gaussn(n), act as a simulated noise generator which returns an n element vector of noise in Gaussian distribution of mean 0 and standard deviation of 1. Series of additive white Gaussian noise were tested to find the SNR threshold for the raw diffusion NMR data to be processed by using the composite property mapping algorithm. The diffusion coefficient values obtained before and after the noise reduction are summarised in Table 6 indicating the highest and the lowest SNR values obtained from each simulated data before and after signal processing. This tabulated data is then visually summarised in Figure 31 a) and b) as before and after noise reduction respectively.

Table 6. SNR values and results of the diffusion attenuation analysis for the simulated ^{23}Na spectra of the reference and the spectra with added noise after processing using FT and with Cadzow's method.

Dataset	**Noisy data**			**Processed Data**		
	SNR		**Diffusion coefficient ($\times 10^9$ m^2 s^{-1})**	**SNR**		**Diffusion coefficient ($\times 10^9$ m^2 s^{-1})**
	g = 0.005 (T m^{-1})	**g = 0.503 (T m^{-1})**		**g = 0.005 (T m^{-1})**	**g = 0.503 (T m^{-1})**	
1	295.6	24.4	0.98 ± 0.07	8.5 ×10^5	8.2 × 10^4	1.24 ± 0.01
2	143.7	11.8	0.76 ± 0.08	1.1 × 10^6	6.7 × 10^4	1.24 ± 0.01
3	112.4	9.2	0.59 ± 0.08	1.0 × 10^6	9.6 × 10^4	1.25 ± 0.02
4	65.9	7.6	0.45 ± 0.07	1.1 × 10^6	3.6 × 10^4	1.22 ± 0.02
5	59.2	6.2	0.36 ± 0.07	4.7 × 10^5	2.9 × 10^4	1.21 ± 0.03

These simulations show that highly accurate diffusion coefficient determination (e.g., 1% error) can be achieved by the application of Cadzow's method to the dataset having the lowest SNR of 11.8 at applied gradient strength g = 0.503 T m^{-1} (corresponding to dataset_2). This SNR value is about three times lower than the experimentally measured dataset's lowest SNR of 35 (NS = 2048 in Table 5). The diffusion coefficients obtained from the processed datasets_3 to 5 listed in Table 6 are in agreement with the reference diffusion coefficient value of 1.24 × 10^9 m^2 s^{-1} however the error range is more than 1%. This slight shift in the diffusion coefficient after processing are also visualised in Figure 31b). Figure 32a) shows the echo attenuation plot of the simulated dataset_5 with SNR ranging from 6.2 to 59.2 listed in Table 6. This dataset is similar to the experimental dataset collected with NS = 64 in terms of SNR range.

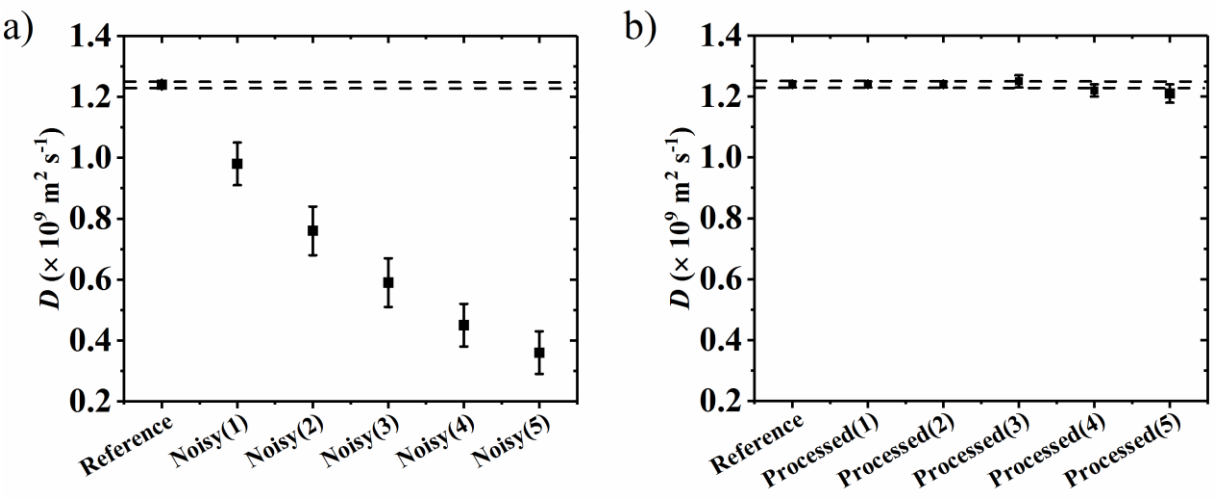

Figure 31. Diffusion coefficient estimates obtained from simulated datasets before and after composite property mapping signal processing. The weight of additive white Gaussian noise increased from noisy 1 to 5 datasets as indicated in Table 6. a) The accuracy and precision of estimated diffusion coefficient estimation from those noisy datasets are compared with the simulated reference diffusion coefficient and its error range indicated with a dotted line. b) Diffusion coefficients and its errors after application of composite property mapping signal processing to the corresponding noisy datasets are represented as processed data sets.

It can be seen in Figure 31 that a remarkable improvement in diffusion coefficient estimation was achieved by the application of Cadzow's method to all the simulated datasets. To have a closer look at the improved diffusion estimation, we turned to the dataset_5 with the lowest SNRs. Figure 32 shows the fitting of Eq. (16) to the original and processed dataset_5; the processed dataset_5 clearly follows the pattern of a single exponential decay in contrast with the highly distorted decay pattern of the original.

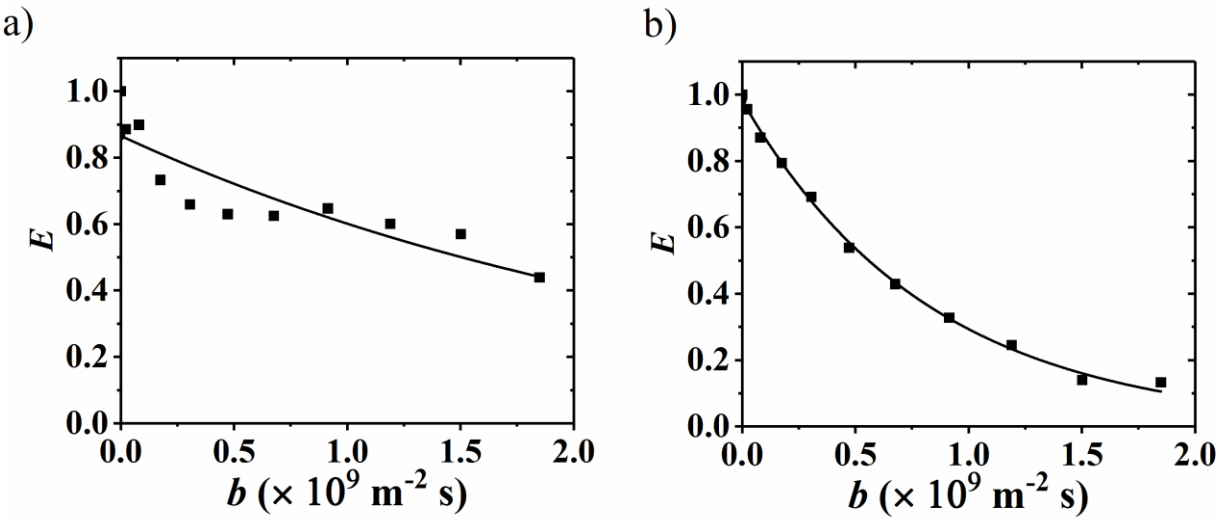

Figure 32. The illustration comparing the accuracy of the signal attenuation rate and its exponential curve fitting precision of the simulated diffusion experiments dataset_5 before a) and after b) applying composite property mapping signal processing.

The results in Figure 31 clearly highlight the strength of Cadzow's method. These simulated results have revealed that in order to successfully reduce the noise and obtain accurate diffusion coefficient estimation a certain level of SNR is required in the original dataset. As mentioned previously in Section 3.7, there is always a residual noise $\overline{w}_n$ remained within the processed dataset. This inevitable fact leads to the limitation of the Cadzow's method yet; promising sensitivity enhancement was evidently demonstrated in this study. From both experimental and simulated studies, acquiring an accurate and precise diffusion coefficient by Cadzow's signal processing method require the minimum SNR of 11.8. Each processing only took less than a second of computational time which is almost negligible compared to the experimental time taken for signal averaging.

5.3.3 Savitzky-Golay Filtering method post-signal processing

The SG filtering method was applied to ^{23}Na PGSE NMR spectra of NaCl in D_2O at 298 K obtained with NS = 64. The effect of the parameters k = "degree of polynomial" and w = "moving window data points" on the SG filtering is illustrated in Figure 33. The effect of the SG filtering method was compared with the original noisy spectrum

(Figure 33a) on the ^{23}Na PGSE NMR spectra of NaCl with the lowest applied gradient strength (g = 0.05 Tm^{-1}) acquired with NS = 64.

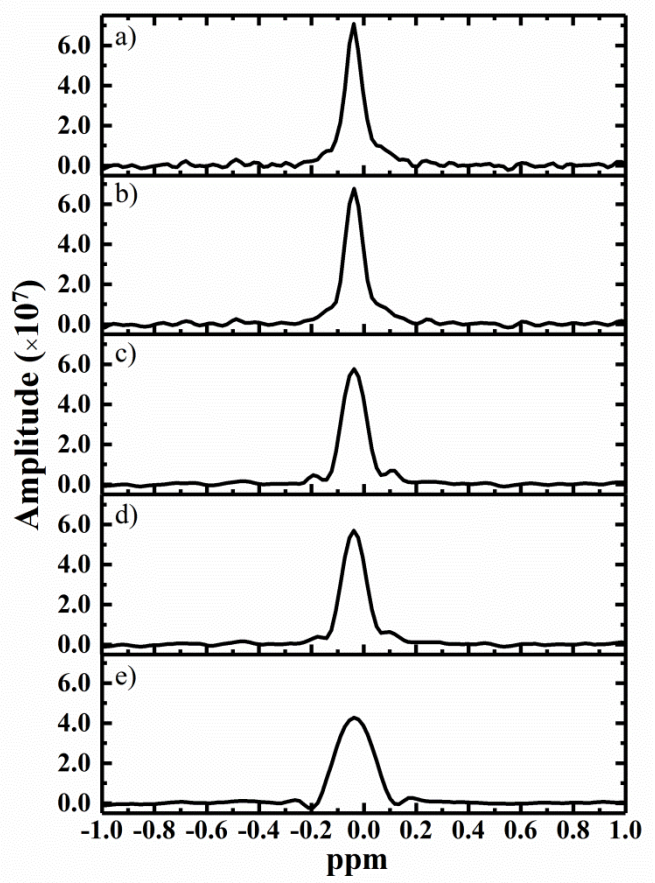

Figure 33. The stacked plot of the ^{23}Na NMR spectrum (NS = 64) with and without SG filtering. a) Original spectrum. b) to e) SG filtered spectra. The values of the key parameters *k* = "degree of polynomial" and *w* = "moving window data points" used for each SG filtering process were b) *k* = 8, *w* = 25; c) *k* = 8 and *w* = 25; d) *k* = 4 and *w* = 15, and e) *k* = 4 and *w* = 25.

Figure 33 shows that higher the degree of polynomial chosen for the fitting, fewer changes to its spectral width and less noise removal is observed especially on the baseline. Applying lower degrees of polynomial, on the other hand, can smooth out baseline noise with the cost of broadening of the spectral width. The same degrees of a polynomial function with moving window size was applied to the rest of the attenuation spectrum to estimate its diffusion coefficient. The waterfall spectrum of the ^{23}Na NMR PGSE data with SG filter of 8th polynomial function with 25 moving

window size is provided at Figure 34 a) and the corresponding diffusion attenuation plot is found in Figure 34 b).

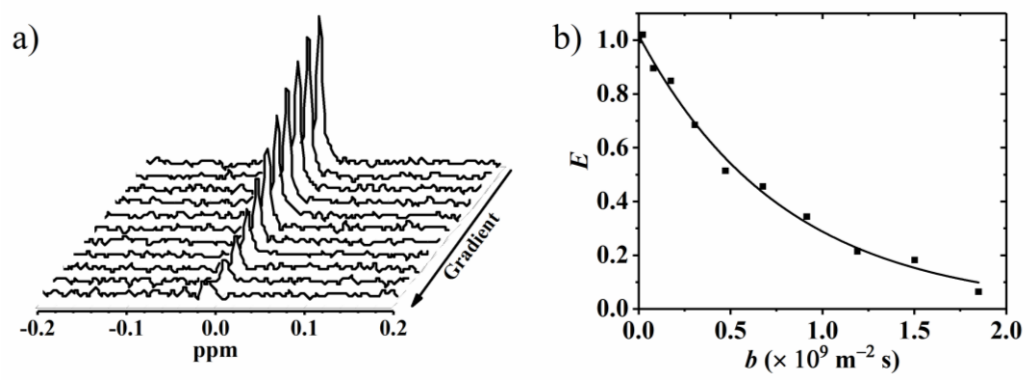

Figure 34. a) ^{23}Na PGSE NMR spectra of NaCl in D_2O at 298 K acquired with NS = 64, processed with Savitzky-Golay filter parameter of 8th polynomial function and 25 moving window size. b) Diffusion attenuation analysis of the data a) giving the diffusion coefficient of 1.26 ± 0.05 ×10^9 m^2 s^{-1}.

Interestingly, all of the processed data presented the diffusion coefficients of 1.26 ± 0.05 ×10^9 m^2 s^{-1}. As the reference diffusion coefficient acquired with NS = 2048 being 1.24 ± 0.02 ×10^9 m^2 s^{-1} and the original diffusion coefficient acquired with NS = 64 being 1.27 ± 0.05 ×10^9 m^2 s^{-1}, it is appropriate to say that the SG filtering method did smooth out the noise spectrum. However, the method did not achieve sufficient signal enhancement to obtain accurate and precise diffusion coefficient after processing compared to Cadzow's method processing the same dataset giving a diffusion coefficient of 1.23 ± 0.04 ×10^9 m^2 s^{-1}.

5.4 CONCLUSIONS

Cadzow's method can improve the SNR of the noisy NMR data under certain conditions and do so much more efficiently than merely acquiring more signal averages. It is suited to experiments such as NMR diffusion measurements were all of the spectra in a series differ only by an attenuation factor. Solution-state spectra of quadrupolar nuclei are especially suited as there is generally only a single peak in the

spectrum. It is possible to process one NMR diffusion dataset using Cadzow's method in only a few seconds.

As the noise level exceeds a certain threshold, the noise properties found within the singular values and corresponding singular vectors of the minimal rank can affect the estimated signal and its amplitude. To determine diffusion coefficients with sufficient accuracy all spectra in a dataset should have SNR > 11.8. A spectrum acquired with a low gradient value combined with a rough estimate of the diffusion coefficient is sufficient to allow cogent settings of gradient parameters and NS value to achieve the SNR threshold.

Compared to the SG filtering method, Cadzow's method provides far superior noise removal providing accurate and precise spectral information which, in turn, allows accurate estimation of the diffusion coefficient. Cadzow's method does not require any pre-calculation for method optimisation in contrast to the SG filtering method in which the optimal degrees of a polynomial function and window size for spectral data smoothing must be determined.

CHAPTER 6. FREQUENCY SELECTIVE SIGNAL PROCESSING FOR MULTIEXPONENTIAL DECAYS

6.1 INTRODUCTION

^{1}H and ^{13}C NMR are often used as quantitative analytical tools to study macromolecules such as proteins in biological samples [115, 312, 415]. Almost all biological molecules contain hydrogen and carbon as their major constituents, indeed carbon atoms form the backbone of most organic molecules. Both ^{1}H and ^{13}C nuclei are spin 1/2, and the nuclei are often spin-coupled, consequently, the measured signals have multiple resonances. Each resonance's frequency, signal intensity, and splitting pattern provide a lot of molecular level information. This is why the NMR technique is highly regarded in many areas of study including protein/ligand binding [416] and biofluid analysis [417]. In real-life NMR diffusion study of the biomedical and synthetic sample, and protein analysis often presented in a crowded spectrum heavily distorted by noise obtaining an accurate measurement of diffusion difficult.

A complex mixture analysis, affinit NMR approach [416], and the purity assay of nanoparticles often face difficulty analysing due to the presence of proteins, biofluids, macromolecules and other impurity contents that measured altogether creating heavily overlapped resonance with broad baseline [418-420]. Although these problems are most commonly observed when acquiring ^{1}H spectra, the issues are general and can occur with any nucleus.

The difficulties often arise due to the existence of a large solvent signal that is non-deuterated, specific measuring temperature requirement, and/or simply having low solute concentrations. Having a large solvent signal can lead to radiation damping due to the strong net magnetisation which resulted in inefficient solvent suppression and creating artifacts. Solvent signal suppression pulse sequences have been studied and introduced yet not many can be applied to PGSTE or PGSE NMR sequence. To remove such a hurdle, a number of experimental approaches including advanced pulse sequences such as PGSE WATERGATE [157, 158, 421], and the T_2 filtration method [419, 422] were previously proposed. The WATERGATE pulse sequence, which was briefly summarised in Section 2.9, is a commonly used solvent suppression pulse sequence that can be incorporated into the PGSTE NMR sequence without generating any phase distortions [421]. The T_2 filtering method based on the Carr-Purcell-Meiboom-Gill (CPMG) sequence can be used to detect the resonances of small molecules which are often hidden under broad macromolecular resonances [419, 423].

The total relaxation delay time in the pulse sequence can be set so that there is a large loss of transverse magnetisation from the large molecules and solvent signals compared to other smaller molecules within the mixture leading to sufficient filtration of the rapidly relaxing macromolecule resonances [419, 422].

These experimental signal suppression approaches provide superior acquisition of weak signals in the presence of a solvent than standard pulse and acquire. However, the acquired spectral data still contains noise and post-signal processing is often required for further signal enhancement and accurate diffusion measurement. Further, large differences in amplitudes between signals can also frustrate the application of the composite property mapping algorithm since the processing procedure is strongly influenced by the amplitude of the signals (Section 3.7). The challenges involved with post-signal processing exist irrespective of the advanced suppression technique, unless, the signal of interest can be extracted from the crowded multiple-resonance spectra.

Most signal processing methods are designed to be applied to the entire FID. As noted in Chapter 5, signal processing of liquid state quadrupolar nuclei using the composite property mapping algorithm was simplified by the prior knowledge of there being only a single resonance in the spectrum thus making the denoising process almost autonomous with none or only a few iterations being required. However, with a multiple-resonance dataset, even with prior knowledge such as the number of exponentially decaying signals within the FID, denoising the entire dataset without loss of sensitivity or resolution can be very difficult. Especially in diffusion NMR measurement, each molecule within a mixture has an individual signal attenuation rate thus diffusion coefficient. If any resonance attenuates fully during the diffusion NMR experiment, the minimum rank of the matrix will change through each element of the arrayed experiment.

The signal processing of biomolecular NMR often requires some form of starting values/conditions such as the model spectrum and noise level. In the composite property mapping algorithm, the starting condition is the threshold matrix rank, where the rank of the matrix is the number of singular values which are strongly correlated with the resonance amplitudes. The threshold matrix rank can be roughly estimated by knowing the number of resonance in the data or using so-called hard/soft

thresholding estimation [424]; however, it is often manually determined from the singular value plot.

In this chapter, the new composite property mapping algorithm-based signal processing approach is applied to NMR diffusion measurements involving spectra containing multiple resonances. Specifically to diffusion NMR data sets containing resonances from each component that are moderately well separated from each other. This new signal processing approach reduces the number of iterations required and prevents processing errors that are often encountered in the matrix rank determination process when multiple resonances are involved.

In the previous subsections (Sections 3.7.2 and 3.4.3), a brief summary of harmonic inversion and reference deconvolution method was presented respectively. The efficiency and the accuracy of both harmonic inversion and reference deconvolution methods increase significantly when the data contains only a single resonance compared to a multi-resonance spectrum [53, 69, 425]. Knowing the advantage of processing only a single resonance, a new signal processing approach for multiple-resonance diffusion measurement was proposed. The idea of this new signal processing approach started with "What if" question. What if the measured signal is segmented with a small window that covers only the signal of interest and possibly a few overlapped baseline just like choosing the reference signal in reference deconvolution method. If such data set is then processed as a singlet resonance using Cadzow's method would be a segment of a Harmonic Inversion scheme, would this outcome be similar to signal processing a liquid state quadrupolar nuclei data presented in Chapter 5. If this frequency selective signal processing can yield accurate diffusion estimates from data sets containing multiple-resonance almost autonomously then the method may able to assist and provide signal enhancement of the small signals hiding beneath the large solvent resonance that originaly required complex pulse sequences such as WATERGATE and T_2 filtration. The aim of this study is to develop a much simpler signal processing approach without requiring the estimation of the minimum matrix rank and or iteration processes. Here this approach is applied to NMR diffusion measurements in order to obtain accurate diffusion estimates but with fewer scans. This new approach named “frequency selective signal processing” involves the application of the composite property mapping algorithm to a single signal in a selected frequency range. Hence, this approach reduces the problem

of dealing with a spectrum containing multiple resonances into dealing with a spectrum containing only a single resonance akin to the study in Chapter 5 on the diffusion of quadrupolar nuclei.

6.2 MATERIALS AND METHODS

6.2.1 Experimental details

The experimental NMR diffusion dataset was kindly provided by Mr Wijesekera. The dataset was of a sample containing 38 mM BSA (heat shock fraction, pH 7, ≥ 98%) and 5 mM 2-nitroimidazole (98%) both purchased from Sigma-Aldrich (Australia) diluted in deuterium oxide (99.8% D) and sodium deuteroxide (99.5% D, 40% in D_2O) purchased from Cambridge Isotope Laboratories Inc. (USA) in a 5 mm NMR tube (535-PP-7 Wilmad, USA).

^{1}H NMR diffusion measurements were measured at 500 MHz on a 500 MHz Bruker Avance III (Bruker Biospin, Karlsruhe, Germany) using a 5 mm PABBI-Z inverse probe at 298 K using the standard PGSTE sequence (see Section 2.8). Typical experimental parameters were a $\pi/2$ RF pulse length of 8.25 μs, δ = 1 ms, Δ = 70 ms, g from 0.001 to 0.509 T m^{-1} in increments of 0.027 T m^{-1}, a spectral width of 12500 Hz, an acquisition time of 1.49 s and a recycle delay was 25.3 s (i.e., total recycle delay of 26.79 s). The reference experimental data was acquired with NS = 64, RG = 80.6, collected with 37 K data points digitised into a 4096 point spectral domain. The total number of data points were reduced to 4096 due to matrix size limitations in the subsequent signal processing. The total acquisition time for the reference dataset was just over 9 hours. The noisy data set to be processed, the same experiment was conducted with NS = 8 but RG = 256, and only the diffusion time was changed from 70 to 30 ms. The total acquisition time for the noisy data set was just over an hour.

6.2.2 Frequency selective signal processing

At first, a single resonance of interest and its surrounding frequency range were defined in the experimentally measured diffusion NMR spectrum. Secondly, the mean value of the noisy spectral baseline where no signal resonances to be found was calculated. This calculated mean value of the noisy spectral baseline replaced the

experimentally measured spectrum apart from the previously selected signal frequency range of interest.

The modified spectrum should contain only resonance of interest similar to the liquid state quadrupolar nuclei NMR spectra in Chapter 5. Inverse Fourier transform of this modified spectrum is then noise reduced in the exact same manner as Chapter 5. This modified FID is then formatted into a Toeplitz matrix where the column length is equal to $1/10^{th}$ of the number of FID data points. This Toeplitz matrix is then factorised through SVD, the matrix rank reduced to one and reconstructed accordingly. Unlike other signal processing methods developed for multiexponentially decaying signals, the SVD of such discrete time domain data with Toeplitz properties is able to determine the minimum rank of the matrix without any iterative process

6.3 RESULTS AND DISCUSSION

6.3.1 Choosing a signal of interest

Figure 35 shows the 1D ^{1}H NMR noisy spectrum of 2-nitroimidazole and BSA from the NMR diffusion data set acquired with NS = 8 at g = 0.001 T m^{-1} (i.e., the lowest applied gradient strength). The well-defined singlet resonance at 8.4 ppm was chosen to be the signal of interest.

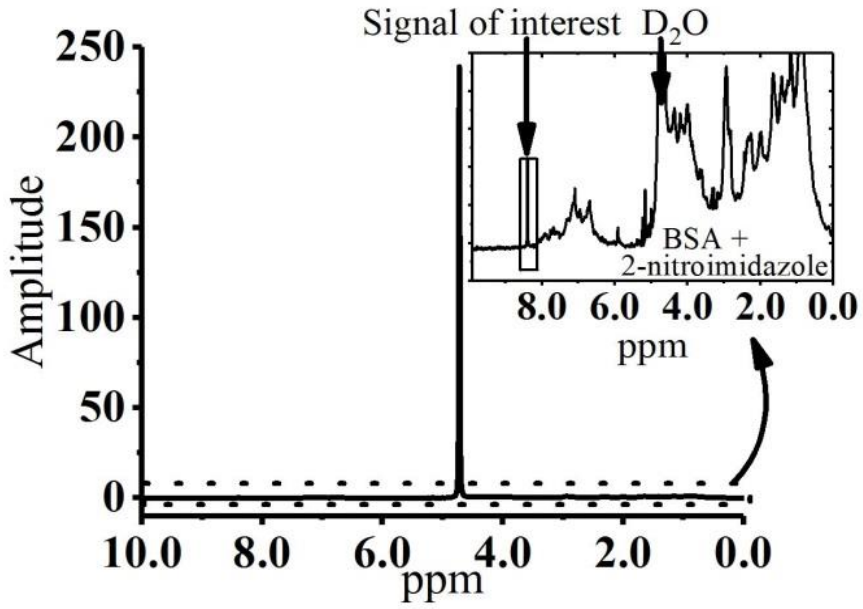

Figure 35. Noisy 1D ^{1}H NMR spectrum of 2-nitroimidazole and BSA in D_2O acquired with NS = 8 at g = 0.001 T m^{-1}. The inset is an expansion of the spectrum to allow the resonances of the interest, 2-nitroimidazole and BSA to be clearly seen. The large peak at 4.8 ppm is the residual HDO of the solvent. The signal of interest is a single resonance at 8.4 ppm.

6.3.2 Signal attenuation rate differences in biological sample

Two diffusion NMR spectra acquired with different applied gradient strengths are presented in Figure 36. The difference in attenuation of the peaks according to the individual diffusion coefficient leads to the difference in theordering of the singular values representing specific resonances between the two spectra and also changes the minimum matrix rank for the noise reduced spectrum reconstruction.

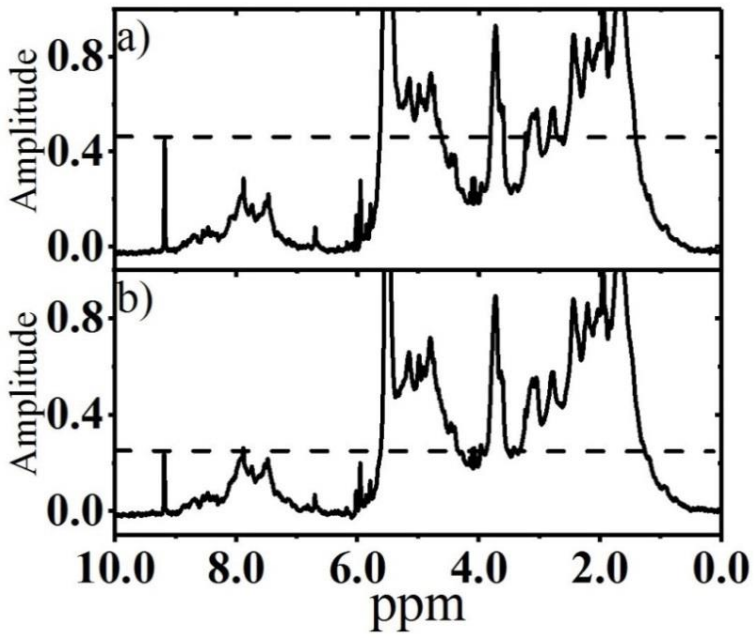

Figure 36. 1D ^{1}H PGSTE NMR spectrum of 2-nitroimidazole and BSA in D_2O acquired with a) 0.001 T m^{-1} and b) 0.509 T m^{-1} applied diffusion gradients. The dashed lines highlight the different signal attenuation of the signal of interest.

Some resonances may attenuate fully during the diffusion NMR experiment and thus the application of a conventional signal processing approach of denoising the entire spectrum would require numerous iterations to find the minimum matrix rank for each spectrum in the dataset leading to a long processing time.

6.3.3 Singular value plot of biological NMR data

Figure 37 shows the singular value plot of the whole spectrum of 2-nitroimidazole and BSA in D_2O acquired with 0.001 T m^{-1} applied diffusion gradient (Figure 36a).

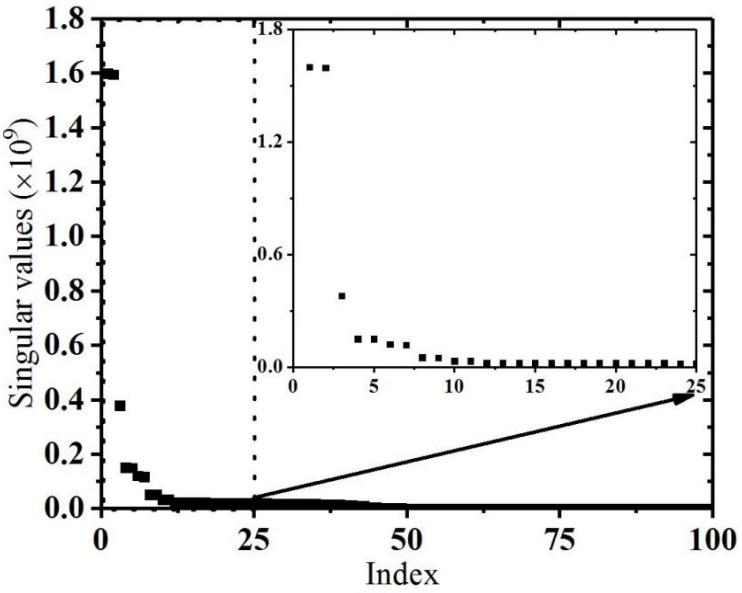

Figure 37. Singular value plot of the noisy 500 MHz ^{1}H PGSTE NMR spectrum of 2-nitroimidazole and BSA in D_2O acquired with a 0.001 T m^{-1} applied diffusion gradient. The inset is an expansion of the first 25 singular values.

Visual inspection of the singular value plot in Figure 37 suggests the minimum matrix rank to be either seven or nine. However, it is obvious from the whole spectrum shown in Figure 36 that the measured spectrum contains more than seven or nine resonances.

6.3.4 Spectrum modification for frequency selective signal processing

As the first step of frequency selective noise reduction the signal frequency region (i.e., 7.92 to 8.72 ppm) which includes the resonance of interest (i.e., 8.4 ppm) was defined. The mean value of the baseline was calculated from the frequency region containing no signals (i.e., 9.0 to 10.0 ppm). The whole noisy spectrum (Figure 38a), apart from the previously selected signal frequency range was replaced by this mean value of the baseline as shown in Figure 38b.

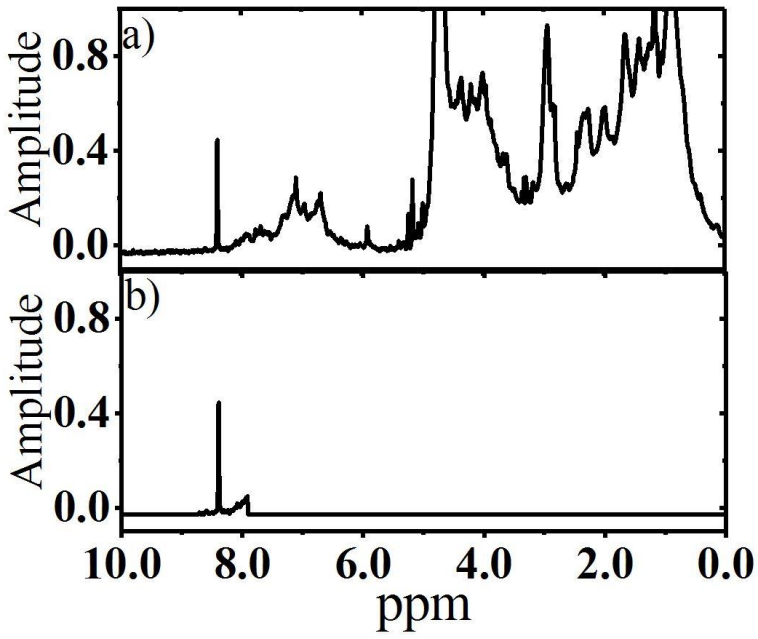

Figure 38. The noisy spectrum of BSA and 2-nitroimidazole in D_2O from 0.0 to 10.0 ppm region a) before data modification. b) Same spectral data as a) where everything except the range 7.92 to 8.72 ppm was replaced with the mean value of the baseline.

The modified spectrum in Figure 38b shows only one resonance creating and is thus similar to the liquid state quadrupolar nuclei NMR spectra in Chapter 5. The FID generated by taking the inverse Fourier transform predominantly contains information on the signal of interest. SVD of such discrete time domain data with Toeplitz properties was known to have the minimum rank of the matrix as being equal to one and no iteration process was required during the noise reduced spectral reconstruction.

The computational time for processing a single spectrum using frequency selective signal processing only required less than two seconds to process 4096 data points including the spectral data modification process.

6.3.5 Diffusion coefficient estimation

The diffusion coefficient value of the signal of interest was accurately determined from the reference data set giving $D = (0.18 \pm 0.01) \times 10^{-9}$ m^2 s^{-1} as shown in Figure 39a. Direct analysis of the noisy dataset resulted in a much poorer estimate of the diffusion coefficient with $D = (0.10 \pm 0.05) \times 10^{-9}$ m^2 s^{-1} as shown in Figure 39b. However, after processing the noisy dataset, the diffusion coefficient was able to be accurately and precisely determined as shown in Figure 39c. The waterfall plot of the

processed spectra are shown in Figure 39d and the resonance of interest is show to be free of other spectral interference.

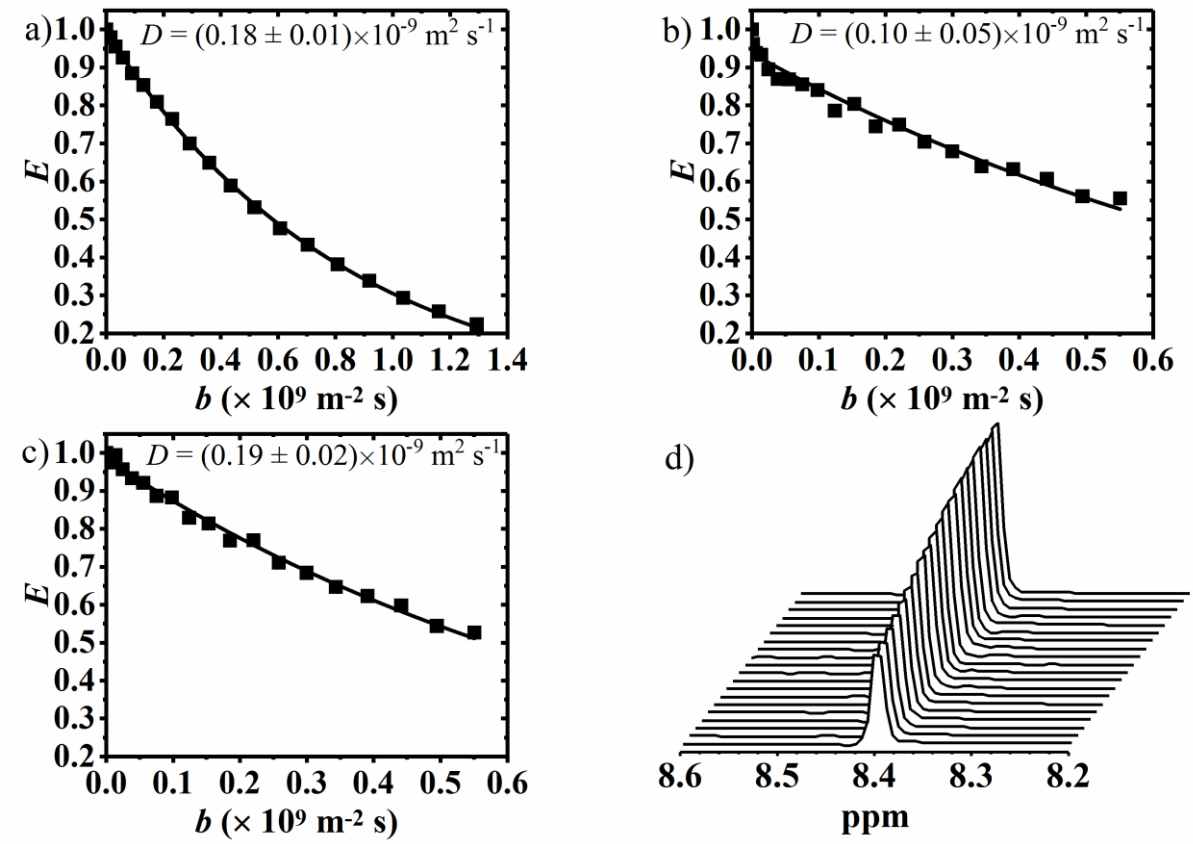

Figure 39. Diffusion coefficient estimation of the resonance of interest. a) PGSTE attenuation plot from the reference PGSTE NMR dataset acquired with NS = 64. b) PGSTE attenuation plot from the noisy PGSTE NMR dataset acquired with NS = 8 without signal processing and c) after processing, d) a waterfall plot of the processed noisy PGSTE NMR spectra of interest.

The *b* value scale and the attenuation range difference between the reference data (Figure 39a) and the fewer scanned data (Figure 39b and c) were due to the changes in the experimental parameter as mentioned. This change in parameters decreased the maximum signal attenuation at the highest *b* value to 50% instead of the 80% observed in the reference data set. This parameter change in the noisy data set (Figure 38b) allowed the signal of interest to have a higher SNR of 49.5 at the higher applied diffusion gradient strength (i.e., 0509 T m^{-1}) with NS = 8. The results show that application of frequency selective minimum rank signal processing allows the total experimental time reduced to one eighth.

6.4 CONCLUSION

The frequency selective composite property mapping algorithm successfully reconstructed a resonance of the interest from noisy spectra in a biomolecular ^{1}H NMR diffusion data set without any matrix rank determination and iteration process. This allowed an accurate and precise diffusion coefficient to be determined. This diffusion coefficient was within experimental error and similar precision to that obtained from a conventional 'reference' NMR diffusion data set collected with eight times more scans and thus an SNR of about 2.8 times better. Thus, in just a few seconds the signal processing makes up for the shortfall in SNR in going from 64 to 8 scans.

The frequency selective approach transformed the biomolecular NMR spectrum containing multiple resonances into a spectrum containing only a single resonance of interest. As long as the resonance of interest was a well-defined resonance and the number of data points kept the same, the composite property mapping algorithm treated the inverse Fourier transformed FID data of the modified spectrum similar to the FID of a liquid state quadrupolar nucleus. Spectral modification provided the prior knowledge of the modified FID containing information of only one resonance, the processing matrix rank was known to be one. This process completely eliminated the possibility of erasing the solute signal from the whole spectrum during the matrix rank determination.

CHAPTER 7. SINGULAR VALUE RATIO METHOD FOR NOISE REDUCTION IN BIOMOLECULAR NMR

7.1 INTRODUCTION

Previously, the strength of the composite property mapping algorithm [52] in noise reduction was demonstrated by its application to the quadrupolar nuclei NMR diffusion experiment (see Chapter 5). The application was also extended to ^{1}H biomolecular NMR diffusion measurements with frequency selective approach (see Chapter 6). By selecting the frequency range, noise reduction for the resonance of interest was easily performed. Both studies confirmed that effective noise and experimental time reduction can be achieved with prior knowledge of the matrix rank.

In this final chapter of the thesis, the singular value ratio method was applied to the determination of the matrix rank in biomolecular NMR signal processing. Biomolecules are often studied using ^{1}H and ^{13}C NMR [426]. Their chemical structures are often represented by heavily overlapped resonances [427]. Processing and analysing such data requires high resolution and sensitivity and generally, the experiments require considerable signal averaging. Prior knowledge of the original spectrum such as the number of resonances and the noise level makes the application of a noise reduction process much faster and more accurate [428-431].

The composite property mapping algorithm stated that the noiseless FID holds three theoretical properties when the data is represented in the form of a matrix: a Toeplitz matrix structure, being positive semidefinite, and having a prespecified rank. The factorisation of a Toeplitz matrix containing the noiseless FID data via SVD resulted in two groups of singular values: non-zero singular values in descending order, and zero value singular values. Each non-zero singular value correspond to the strength of the resonance amplitude only when the resonance holds Lorentzian lineshape. The number of the singular values corresponding to the number of resonances becomes the prespecified rank.

In reality, experimentally measured data does not possess exactly Lorentzian lineshapes and is often distorted due to the presence of noise and by large solvent signal(s). As a result, the number of resonances observed in the frequency range would not match with the number of the prespecified rank of the matrix. For such reasons, the determination of the prespecified rank becomes challenging for noisy biomolecular NMR data. Thus a soft threshold matrix rank is defined first by examining the plot of the singular values and then it will be gradually reduced through iteration to the

minimum matrix rank (i.e., prespecified matrix rank) [52]. This soft threshold matrix rank must not be lower than the prespecified matrix rank. Otherwise, the composite property mapping algorithm could recognise a signal as noise and eliminate the signal erroneously.

With the composite property mapping, the soft threshold matrix rank is often determined by spotting a sharp decline in the magnitude of the singular values as illustrated in Figure 40. However, this method often leads to unreliable results. For example, the spectrum of a low concentration biomolecular sample often contains a large solvent resonance and its singular value plot would look similar to Figure 40a. Without any prior knowledge the singular values corresponding to the biomolecular resonances would be falsely recognised as corresponding to noise and thus be mistakenly eliminated due to the extremely large singular value of the solvent resonance. Figure 40b illustrates another case of biomolecular NMR data in which there are multiple prospective minimum ranks.

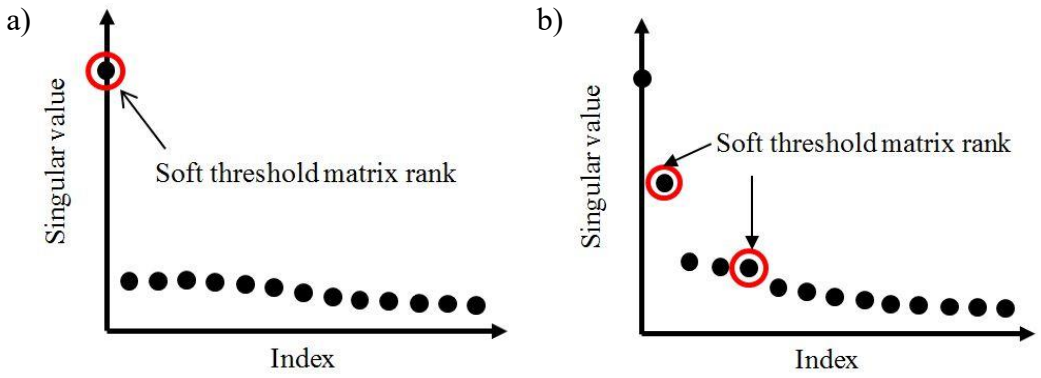

Figure 40. Examples of singular value magnitude versus index plot for a biomolecular sample containing a large solvent resonance and much smaller resonances. a) Obvious cut-off singular value before a sharp descent highlighted with a red circle. b) Two possible cut-off singular values corresponding to two possible soft threshold matrix ranks also indicated with red circles.

The singular value ratio method presented here can be used to estimate the soft threshold matrix rank of a real experimental dataset, which is never less than, but very close to, the prespecified rank. Once the optimal soft threshold matrix rank is defined and the Σ matrix (see Section 3.7.1) is processed accordingly, the noise reduced spectrum should contain some residual noise represented by dispersion peaks. The

observation of dispersion peaks indicates the matrix rank should be reduced closer to the minimum matrix rank through iteration. Since it is not practical to obtain noiseless experimentally measured FIDs, the term prespecified rank only remains valid theoretically and the minimum matrix rank is used instead in processing experimental data.

The utility of the singular value ratio method was demonstrated on a ^{1}H NMR spectrum of lysozyme. To highlight the strength of this singular value ratio method, partial solvent suppression was performed using the WATERGATE sequence (see Section 2.9) and the residual water resonance appeared as a dispersion peak. Some signal processing methods such as MEM are not capable of processing dispersion peaks because of the undesirable conversion into magnitude mode [66, 68]. The overall effect of signal enhancement by the singular value ratio method was compared with another widely used NMR signal processing method: Wavelet shrinkage (see Section 3.4.4).

In this chapter, the rank determination process was tested with simulated overlapped multiplet spectral data with various SNR levels and compared with the MDL method as described in Section 7.2.5. Unlike the wavelet shrinkage method, the SVD-based signal processing method is often criticised for it being limited to processing only very small data sets (1~ 2K) and its heavy computational load. To overcome this limitation, localisation approaches, such as LocCapE which utilises the MDL and the MP-based methods, have been developed to reduce the overall computational time [432]. All of the signal processing and analysis performed in this chapter used 4K data sets. This larger data set size were able to be successfully processed in a reasonable processing time by changing the matrix size to a much narrower column matrix instead of the square matrix which is typically used in the SVD-based signal processing method.

7.2 MATERIALS AND METHODS

7.2.1 Sample preparation

A 0.5 ml aliquot of a 2 mM lysozyme (Sigma-Aldrich, Australia) solution in 90% H_2O and 10% D_2O was dispensed into a 5 mm standard NMR tube (Wilmad, USA).

7.2.2 WATERGATE parameter

^{1}H NMR measurements were performed at 298 K on a 400 MHz Bruker Avance NMR spectrometer (Bruker Biospin, Karlsruhe, Germany) using a 5 mm BBFO probe equipped with triple-axis gradients. Typical acquisition parameters for the WATERGATE experiments were: NS = 256, DS = 4, spectral width = 8012.82 Hz, acquisition time = 1.2 s, T_1 relaxation delay = 3.0 s, gradient recovery delay = 250 μs, inter-pulse delay = 208 μs, FID recorded with 19228 data points, π/2 RF pulse length was 15.50 μs, g = 0.106 T m^{-1}, and δ = 2 ms. The measured FID was Fourier transformed into a spectrum containing 4096 data points.

7.2.3 Singular value ratio method

Following the first step of the composite property mapping previously illustrated in Figure 27, the experimentally measured FID (x_n) with the total number of data points, N = 4096, was converted into a 3689 × 408 Toeplitz matrix $X_{L\times M}$. The size of the matrix was selected to ensure the number of columns was larger than the minimum matrix rank and much smaller than the number of rows. Having such a structure creates an overdetermined environment for SVD. It also leads to shorter computational times as the matrix becomes a skinnier rectangle.

In the second step, this Toeplitz matrix was then factorised through SVD giving three submatrices: U, Σ, and V^T. Due to the presence of noise, the rank (p) of the matrix was full (i.e., p = min(L, M)). The singular values (σ: $\sigma_0 \geq \sigma_1 \geq \cdots \geq \sigma_{p-1} \geq 0$) are the diagonal elements of the matrix Σ which hold the key to successful noise reduction with the composite property mapping algorithm.

This new approach, the singular value ratio method, calculates the singular value ratio by dividing the first/largest singular value ($\sigma_{0,0}$) by itself and all the other singular values ($\sigma_{i,i}$ $i = 0,1, \ldots, p-1$). The plot of singular value ratio against its index number is illustrated in Figure 41 and shows a more characteristic sigmoidal pattern than the plot of singular values itself (Figure 40).

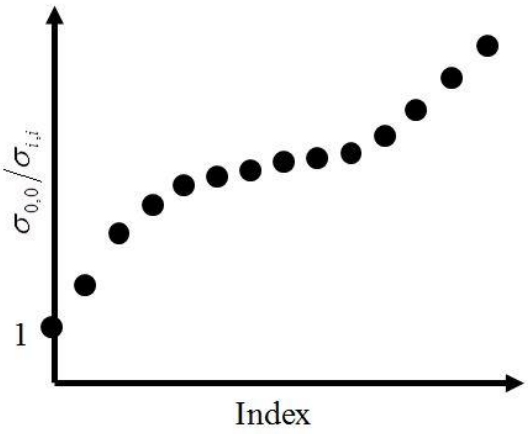

Figure 41. The sigmoidal-shaped plot of the singular value ratio calculated by dividing the first/largest singular value by itself and all the other singular values, respectively.

To define the soft threshold matrix rank (r), a linear function is fitted to the first two distinctive slopes separately. The index value corresponding to the intercept of two lines of best fit becomes the soft threshold matrix rank, r, as shown in Figure 42.

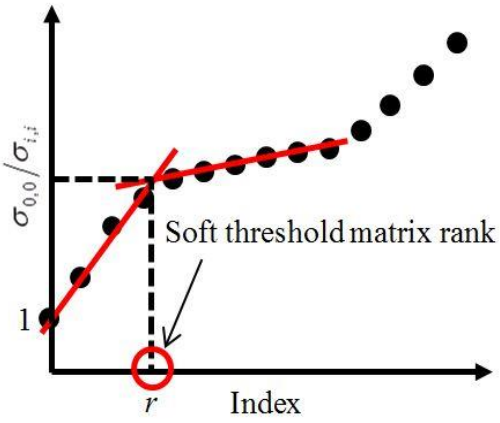

Figure 42. Soft threshold matrix rank (r) determination. Application of linear fitting (red line) to the first two slopes of the singular value ratio plot. The index value corresponding to the intercept of the two lines of best fit becomes the soft threshold matrix rank.

Once the threshold rank was determined, the reduced rank matrix X' was calculated by:

$$X'_{L\times M} = \left(U_{L\times r} \middle| U_{L\times L-r}\right)\begin{pmatrix}\Sigma_{r\times r} & 0\\ 0 & 0\end{pmatrix}\begin{pmatrix}V^T_{r\times M}\\ \hline V^T_{M-r\times M}\end{pmatrix}. \approx U_{L\times r}\Sigma_{r\times r}V^T_{r\times M} \tag{147}$$

As described in Section 3.7, the reduced rank matrix X' no longer holds a Toeplitz form which violates the characteristics of the matrix formed from the noiseless FID. Thus, an average of the sub-diagonal elements is taken to reconstruct the non-Toeplitz X' into Toeplitz form. The first column and the first row of these Toeplitz matrix elements are then reformatted into a single column vector as the noise reduced FID.

The noise reduced FID is then Fourier transformed into a spectrum. If the noise reduced data contains any dispersion peaks, further matrix rank reduction will be iteratively performed to remove these peaks.

7.2.4 Simulation studies

To study the capability of this Singular value ratio method, an FID model including a total of thirty resonances with different amplitudes and frequencies creating overlapped multiplets was simulated as a reference. Two hundred additive Gaussian noise 4K vectors were generated for each of thirteen different strengths of applied noise amplitude leading to an SNR range of 37.88 to 106.24 and added to the reference to create a collection of noisy FID data sets. The SNR calculation was performed using Eq. (73). The processing data size limitation in the SVD-based advanced signal processing methods is a well-known issue [432]. To enable processing to proceed in a reasonable time-frame (e.g., at most 10 seconds per data set) in the simulation study using singular value ratio method, the FIDs were constructed with 4K vectors each. Simulated FID data sets were processed with the singular value ratio method found in Section 7.2.3 to find the threshold matrix rank of the noisy data sets. To compare the efficiency and accuracy of the study outcome, the results were compared with the MDL method (see Section 7.3.6).

7.2.5 Minimum Description Length (MDL) Method

The MDL method is an information theory-based method used for Matrix rank determination in NMR signal processing [76, 433, 434]. The MDL method is often

compared with other information theoretical methods such as the Akaike Information Criterion (AIC) [435]. The AIC method is known to perform well with low SNR signals provided that the number of data points is limited (<4K) since the accuracy of the rank determination deteriorates as the number of data points increases [436]. The main difference between these information theory methods when compared to the majority of reduced rank signal processing methods is that both the MDL and AIC methods do not require any prior threshold settings nor human observations for rank determination.

Application of MDL in the matrix rank determination process starts with fitting noisy FID data into an L by M Toeplitz matrix followed by the basic Matrix Pencil Method (Section 3.6.3) of decomposing a matrix by performing SVD. For each rank r of the matrix, the minimum description length is calculated using the equation ,

$$MDL(r) = -\log\left[\frac{\left(\prod_{i=r+1}^{L}\sigma_i\right)^{N}}{\left(\frac{1}{L-r}\sum_{i=r+1}^{L}\sigma_i\right)^{(L-r)N}}\right] + \frac{1}{2}r\left(2L-r\right)\log\left(N\right) \qquad (147)$$

where N is the total number of data points and σ_i are the singular values. The MDL is plotted as a function of r in Figure 43.

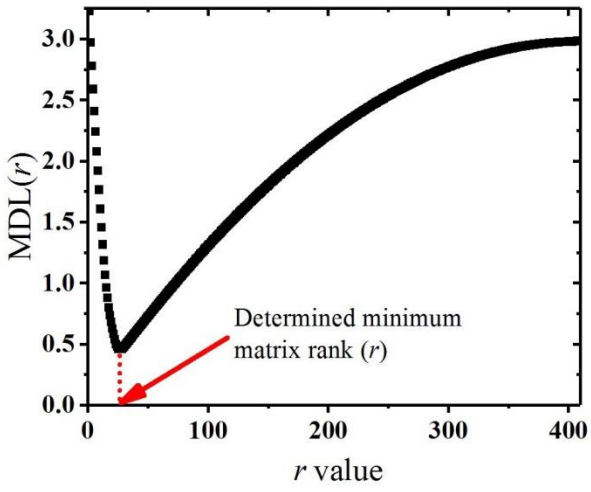

Figure 43. A plot of MDL as a function of r. The value of r giving the minimum MDL value leads to the minimum matrix rank of the processed data.

The minimum matrix rank is defined by the value *r* at which the MDL value is a minimum. Figure 43 illustrates the effortless determination of the matrix rank.

7.3 RESULTS AND DISCUSSION

7.3.1 SNR calculation

In order to compare the sensitivity before and after the signal processing, one resonance well resolved from the remainder of the spectrum was selected to calculate its SNR. This signal of interest, which did not overlap with any other resonances was selected from the chemical shift range -0.6 to -0.8 ppm as shown in the inset to Figure 44. The maximum amplitude of this peak was measured and then divided by the standard deviation of the baseline noise (14.6 to 12.1 ppm) following Eq. (72), providing an SNR of 15.58, which is greater than the minimum SNR (i.e. SNR = 11.80 given in Chapter 5) required for highly accurate signal reconstruction.

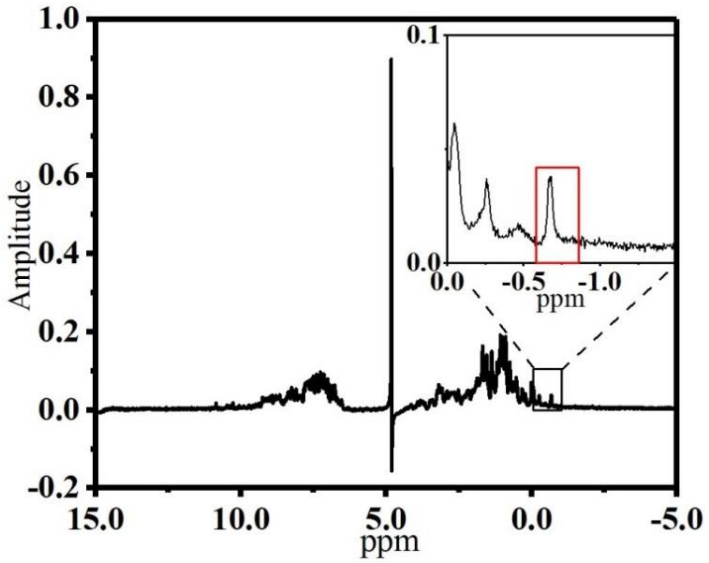

Figure 44. ^{1}H 400 MHz spectrum of 2 mM lysozyme in 90% H_2O and 10% D_2O obtained at 298 K using the WATERGATE sequence. The resonance in the red box (-0.6 to -0.8 ppm) within the inset was used to calculate SNR.

7.3.2 Conventional threshold determination process

A plot of the full rank singular values obtained after SVD is shown in Figure 45. The plot shows a sharp decline in magnitude between the first two singular values followed by a smoothly decaying curve.

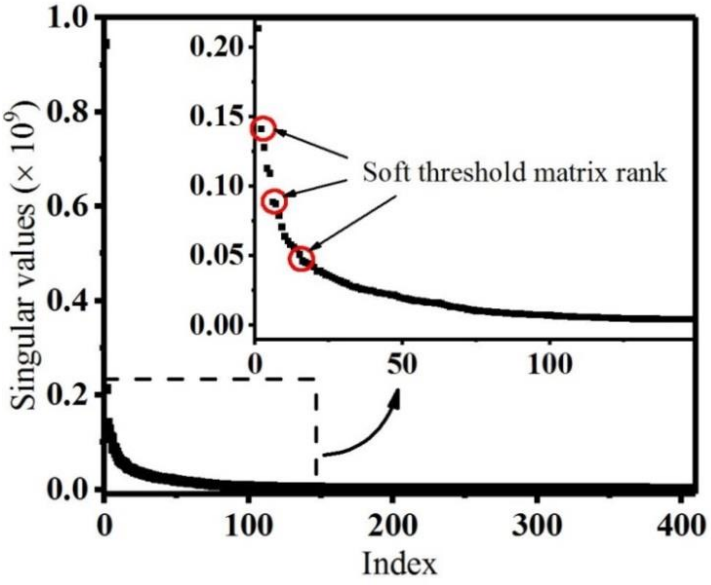

Figure 45. Singular value plot obtained from the SVD of the FID acquired of the 2 mM lysozyme sample. An expansion of the singular values corresponding to the majority of the solute signals and also the noise is presented in the inset. The red circles within the inset indicate the cut-off singular values corresponding to possible soft threshold matrix ranks.

The singular value plot in Figure 45 is a good example of why the conventional soft threshold matrix rank determination process can be a difficult task. Through visual inspection, there are three potential soft threshold matrix ranks circled in red illustrated in Figure 45. In fact, none of these three potential soft threshold matrix ranks lies close to the optimal minimum matrix rank. Had any one of those red circled potential soft threshold matrix ranks been used in noise reduction, an underdetermined minimum matrix rank would have been obtained. Therefore, the utilisation of the singular value ratio method is necessary.

7.3.3 Singular value ratio method

The new threshold determination method which uses the singular value ratios and two linear fitting functions is illustrated in Figure 46. The first linear function was fitted to the initial steepest linear region on the singular value ratio plot, in this case, the singular values corresponding to the index number 65 to 120 and contained singular values relating to solute resonances. The second linear function was fitted to the linear region immediately following the previous one, in this case, the singular values corresponding to the index number 250 to 500 was mainly associated with the noise.

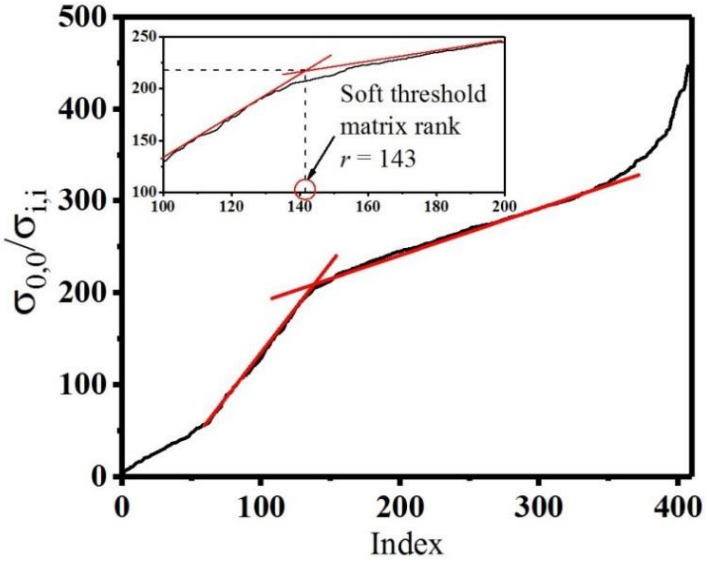

Figure 46. The singular value ratio plot used for soft threshold matrix rank determination. Linear functions (red lines) were fitted to the initial steepest linear region and the following linear region. The index value corresponding to the intercept of the two lines of best fit was found to be 143 (i.e. the soft threshold matrix rank was 143).

The index value corresponding to the intercept of two lines of the best fit provided the soft threshold matrix rank (r). This estimated soft threshold matrix rank(i.e. r = 143) was tested by replacing all the following singular values (i.e. all the singular values with an index number > 143) in the Σ matrix to zero and then reconstructing the FID. As expected, the noise reduced spectrum reconstructed with the matrix rank = 143 still contained some noise existing as dispersion peaks (Figure 47b circled in red). However, dramatic noise reduction was observed by comparing

the full rank (noisy) original data (Figure 47c) and noise reduced spectrum at r = 143 (Figure 47b). Further matrix rank reduction was performed through an iterative procedure until a minimum matrix rank of r = 128 was found (Figure 47a). The total computational time including the iterations was less than 4 minutes.

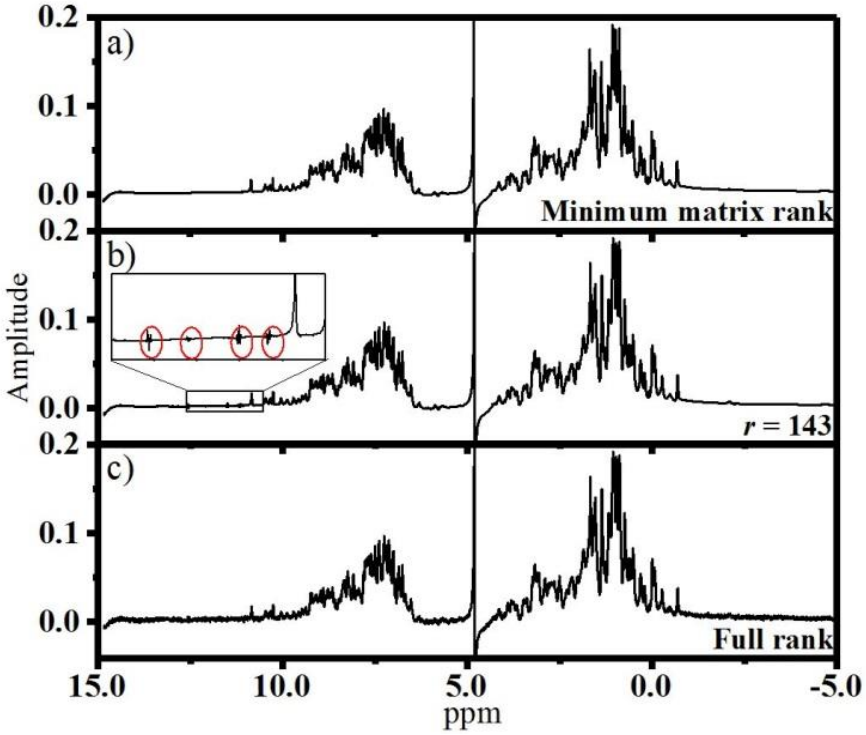

Figure 47. The noise reduced lysozyme spectrum with minimum matrix rank of 128 a), the partially noise reduced spectrum with estimated soft threshold matrix rank of 143 b), and the original full rank (noisy) experimentally measured spectrum c).

To compare the sensitivity enhancement before and after noise reduction, the same signal and chemical shift range (i.e., -0.6 to -0.8 ppm for signal amplitude, 14.6 to 12.1 ppm for baseline noise) used previously in Figure 44 was applied to calculate the SNR in Figure 48b. The SNR values for the spectra in Figure 48a and b were calculated as 15.58 and 36.37, showcasing a significant SNR enhancement achieved by the noise reduction using the singular value ratio method followed by further matrix rank reduction. A detailed comparison between Figure 48a and Figure 48b also showed minimal changes caused by noise reduction in terms of a line shape, line width, and signal amplitude.

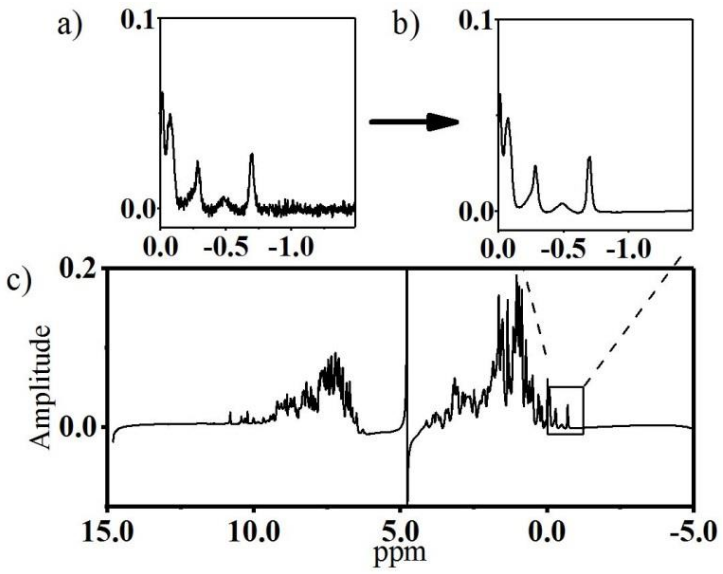

Figure 48. Comparison of the spectral properties of the selected chemical shift range (i.e., 0.0 to -1.5 ppm) before a) and after b) signal processing and the full noise reduced ^{1}H 400 MHz spectrum of the lysozyme sample c).

7.3.4 Wavelet shrinkage method

For comparison, the wavelet shrinkage method (see Section 3.4.4), as contained in MathCad was applied using the same (noisy) lysozyme ^{1}H NMR spectrum used for testing the singular value ratio method. Figure 49 shows the spectra processed with the Daubechies 4 filter (Figure 49a), Daubechies 8 filter (Figure 49b), and the original spectrum (Figure 49c) for comparison. Each inset is presented to emphasise the effects of wavelet shrinkage denoising technique on spectral properties.

``

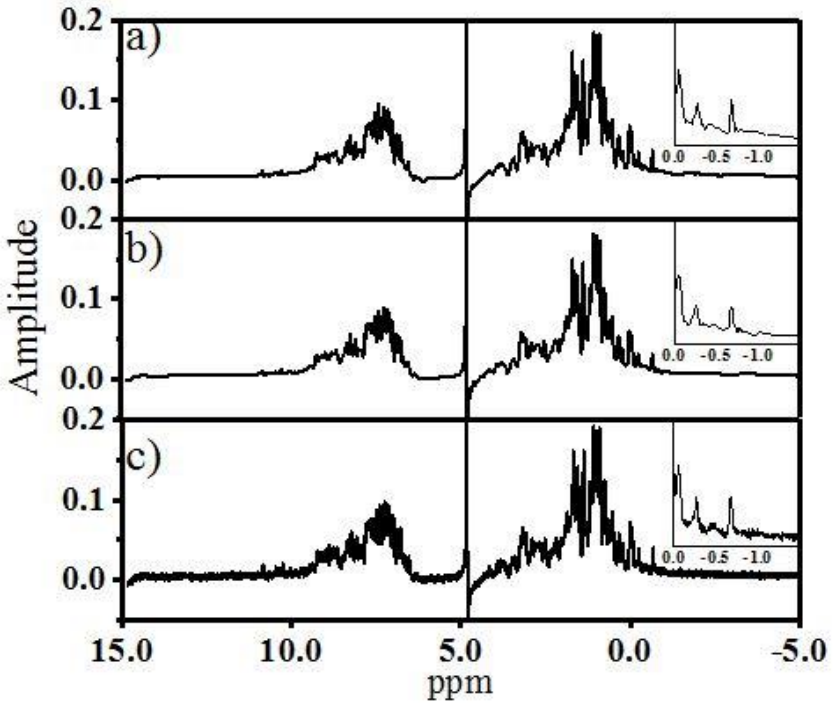

Figure 49. The noise reduced ^{1}H 400 MHz spectrum of the lysozyme sample obtained with the wavelet shrinkage method. using a) the Daubechies 4 filter, b) the Daubechies 8 filter, and. c) the original ^{1}H lysozyme spectrum. The insets indicate the frequency range including the resonance at -0.75 ppm used as a reference signal for SNR calculation.

Compared to the original spectrum (Figure 49c), denoising with the Daubechies 4 and 8 filters both reduced the noise dramatically with the SNR values being calculated as 16.41 and 12.83 respectively with the same SNR calculation used in Section 7.3.1. This reduction in SNR can be attributed to the significant decline in the signal amplitude after noise reduction. However, as a segment of the resonances shown in the inset of Figure 49a and b, the spectral lineshape is far from being Lorentzian after noise reduction, which is in contrast with the Lorentzian lineshape presented in Figure 48b. Furthermore, the signal amplitude and the spectral resolution were reduced dramatically after the increase of the vanishing moment from 4 to 8 (Figure 49 a and b).

7.3.5 Simulation study with singular value ratio method

The singular value ratio method proposed in Section 7.2.3 was tested with a simulated noisy FID data set as described in Section 7.2.4. This study was conducted to determine the efficiency of the initial matrix rank determination process using the singular value ratio method. Figure 50a is the simulated noiseless multiple-resonance spectrum. A simulated spectrum with additive noise of SNR 106.24 and 37.88 are also shown in Figure 50b and c, respectively. The singular value ratio plot of Figure 50c data with insets demonstrating the threshold rank determination process is found in Figure 50d.

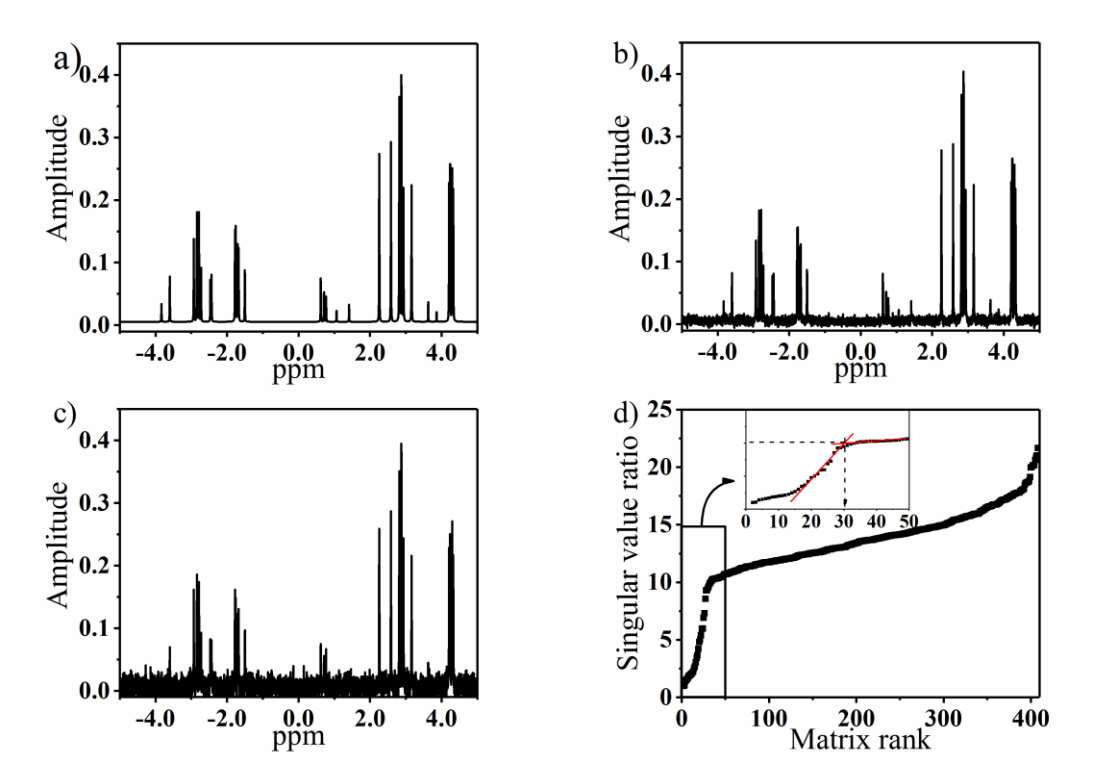

Figure 50. Simulated spectrum and its singular value ratio plot. a) Noiseless simulated spectrum. b) Noisy simulated spectrum with SNR of 106.24. c) Noisy simulated spectrum with SNR of 37.88. d) Singular value ratio plot of c) where the inset is an expansion of the region where the two linearly fitted functions intersect.

The ideal outcome of this method is to predict the initial threshold matrix rank to be equal to or slightly larger than the actual minimum rank of the matrix which is 30. Figure 50d shows the determined threshold matrix rank to be 32 after the singular value ratio method is applied to the noisy FID data set with SNR of 37.88. The

threshold rank of the matrix is determined by finding the intercept of the two linear fits as shown in the inset of Figure 50d where the intercept value was rounded up to an integer. The outcome of the simulation study with the proposed singular value ratio method is summarised in Table 7.

Table 7. Summary of matrix threshold rank determination with the proposed singular value ratio method. Average SNR, Minimum, Maximum and Average rank were calculated from two hundred simulated data sets.

Data Set	Average SNR	Min Rank	Max Rank	Average Rank
1	106.24	30.1 ≅ 30	31.7 ≅ 32	30.4 ≅ 30
2	90.61	29.7 ≅ 30	31.5 ≅ 32	30.6 ≅ 31
3	78.11	29.4 ≅ 29	31.3 ≅ 31	30.4 ≅ 30
4	77.23	29.4 ≅ 29	31.4 ≅ 31	30.3 ≅ 30
5	65.77	29.3 ≅ 29	31.7 ≅ 32	30.2 ≅ 30
6	57.83	29.1 ≅ 29	32.0 ≅ 32	30.2 ≅ 30
7	52.89	28.7 ≅ 29	33.3 ≅ 33	30.4 ≅ 30
8	51.23	28.7 ≅ 29	33.3 ≅ 33	30.4 ≅ 30
9	48.10	28.4 ≅ 28	34.8 ≅ 35	30.6 ≅ 31
10	48.15	28.5 ≅ 29	37.3 ≅ 37	31.0 ≅ 31
11	41.95	28.8 ≅ 29	51.3 ≅ 51	31.9 ≅ 32
12	42.36	28.2 ≅ 28	52.3 ≅ 52	32.3 ≅ 32
13	37.88	28.2 ≅ 28	52.3 ≅ 52	32.3 ≅ 32

The results in Table 7 suggests that this singular value ratio method is capable of determining the threshold matrix rank close to the minimum matrix rank for a wide range of SNR levels from 37.88 to 106.24. There were a few underdetermined ranks collected from this simulation study, however, the maximum difference between the minimum matrix rank and the underdetermined rank was only two. The singular value ratio method decreases the accuracy of matrix rank determination as the SNR levels decrease. However, the overall threshold matrix rank determined by this singular value

ratio method satisfies the aim of determining the matrix rank close to the minimum matrix rank.

7.3.6 A simulation study with the minimum description length method

The simulated FID data sets from Section 7.2.4 were also processed with the MDL method (see Section 7.2.5). The MDL method is an autonomous method which does not require any prior knowledge nor parameter settings to operate. The estimated minimum matrix rank is equal to the k value where the minimum MDL value is obtained from Eq. (147). A plot of the matrix estimation process with the MDL method is shown in Figure 51.

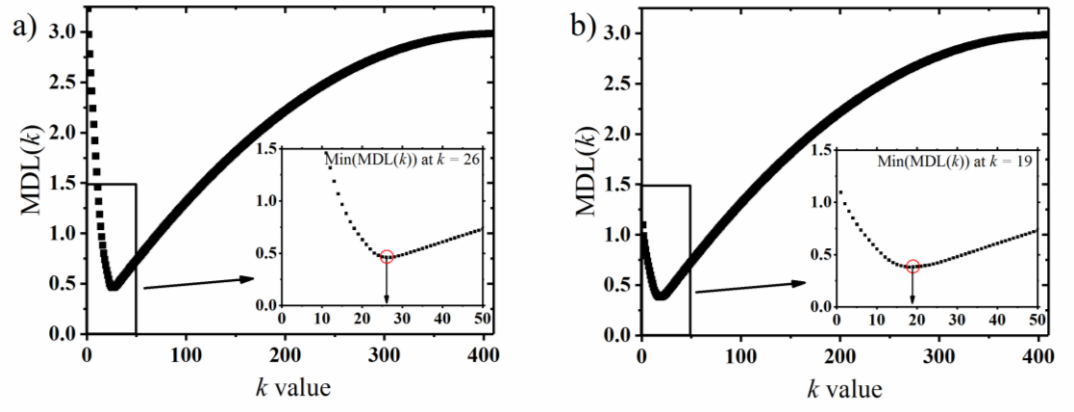

Figure 51. MDL method rank estimation plot. a) MDL rank estimation of SNR 106.24 data giving the estimated minimum matrix rank of 26. b) MDL rank estimation of SNR 37.88 data giving the estimated minimum matrix rank of 19.

Figure 51 illustrates the capability of the MDL method which can provide an estimated minimum matrix rank automatically by finding the k value where the value of the MDL function is a minimum. However, knowing that the exact minimum matrix rank was 30 for this simulated data, all of the obtained estimate rank values were underdetermined by more than 3 ranks. Table 8 summarises the outcome of matrix rank estimation by the MDL method.

Table 8. Summary of the matrix threshold rank determination with the minimum description length method. The average SNR, Minimum, Maximum and Average rank were calculated from two hundred simulated data sets.

Data Set	Average SNR	Min Rank	Max Rank	Average Rank
1	106.24	26	27	26.3 ≅ 26
2	90.61	24	25	24.5 ≅ 25
3	78.11	24	25	24.3 ≅ 24
4	77.23	23	24	23.5 ≅ 24
5	65.77	23	23	23
6	57.83	22	23	22.5 ≅ 23
7	52.89	22	22	22
8	51.23	22	22	22
9	48.10	21	22	21.5 ≅ 22
10	48.15	21	21	21
11	41.95	20	21	21.3 ≅ 21
12	42.36	17	20	18.5 ≅ 19
13	37.88	17	20	18.5 ≅ 19

The consistency of the MDL method having a very narrow range of estimated minimum matrix rank is illustrated in Table 8. However, all of the estimated ranks were significantly underdetermined especially when the result is compared to the proposed singular value ratio method. Noise reduced signal reconstruction using the MDL method then results in an incorrect spectrum due to missing resonances.

7.4 CONCLUSION

The new soft matrix rank threshold determination process using the singular value ratio method affords much higher accuracy than the conventional threshold determination process and also the MDL method. The singular value ratio method not only required just 15 iterations to reach the minimum matrix rank on noisy lysozyme spectrum but also preserved all the singular values corresponding to the solute resonances.

The advantage of applying the composite property mapping algorithm to a biomolecular spectrum is that when the estimated matrix rank is above the minimum rank of the matrix, the non-zero singular values beyond the minimum rank results in dispersion peaks in the noise reduced spectrum. In this study, all the resonances were recovered after the noise reduction using a minimum matrix rank close to the prespecified matrix rank obtained using the singular value ratio method. However, it is important to state that the composite property mapping has its own limitations. As one example, the composite property mapping algorithm cannot be used to recover hidden resonances whose amplitude is equal to or lower than the noise level. This is simply because it is impossible to differentiate between the singular values corresponding to these resonances and the ones corresponding to noise. Therefore, in order to utilise this new threshold determination method in biomolecular NMR, all the resonances of interest are expected to have sufficient SNR values to allow differentiation between the resonances and the noise.

Despite the wavelet shrinkage method being fast, generally applicable, and easy to set up, significant changes in a line shape and signal intensity were observed when the lysozyme spectrum was processed using the wavelet shrinkage method. These changes were absent in the noise reduced spectrum obtained using the singular value ratio method. Compared with the MDL method, the singular value ratio method has a higher accuracy of finding the threshold matrix rank close to the minimum matrix rank. Underdetermination of the matrix rank rarely results with the singular value ratio method while the simulated study showed larger matrix rank underdetermination with the MDL method. These results indicate the potential of the proposed method to become a standard noise reduction procedure.

CHAPTER 8. GENERAL CONCLUSIONS AND FUTURE RESEARCH

8.1 GENERAL CONCLUSIONS

The overall aim of the work contained in this thesis was to implement and develop MR signal processing strategies to enable more efficient use of experimental time and thus expand the possible range of applications. Various strategies were attempted: (i) **The Normalisation Approach** for arrayed experiments in which the required number of signal averages for each element of the array was tailored carefully based on a fundamental understanding of how the SNR changes with the arrayed experimental parameter. NMR diffusion and inversion recovery experiments were used to illustrate the approach and it was experimentally verified that the method significantly reduced the experimental time required for such experiments but with no loss of accuracy in the final result. (ii) **The Composite Property Mapping Algorithm** was studied extensively and applied to liquid state diffusion measurements of quadrupolar nuclei. The spectra of quadrupolar nuclei in solution make almost ideal candidates for this type of noise reduction signal processing and facilitate it being implemented in an almost automated fashion. The sensitivity limitation of the composite property mapping algorithm for reconstructing noise reduced spectra with highly accurate resonance intensities and line shapes was also investigated. The experiments revealed that the minimum workable SNR of the noisy spectrum prior to processing was 11.8. Comparison between the composite property mapping algorithm and the SG filtering method highlighted the superiority of the composite property mapping algorithm in signal enhancement without line shape distortion or broadening. Application of the composite property mapping algorithm afforded a 32 fold reduction in experimental time in ^{23}Na NMR diffusion measurements. (iii) **The Frequency Selective Noise Reduction Method** an adaptation of the composite property mapping algorithm, was applied to noise reduction in biomolecular NMR spectra. In this approach, frequency selection was combined with the composite property mapping algorithm to process a resonance of interest from a spectrum containing multiple peaks. If the resonance/solute of interest is well-defined and separated from other solute resonances then replacing the frequency domain data apart from the resonance of interest with the mean noise baseline transforms this complex spectrum into a simpler spectrum similar to that of the liquid state quadrupolar nuclei. The resonance of interest could then be with the composite property mapping algorithm. (iv) **The Singular Value Ratio**

Method was developed to determine the optimal threshold matrix rank for noise reduction using the composite property mapping algorithm. The difficulty in defining the initial matrix rank to reduce noise in biomolecular spectra was investigated. This singular value ratio method was developed to solve the threshold matrix rank determination in spectra containing multiple resonances such as those containing biomolecules. This new method defines the initial matrix threshold rank using singular value ratios and linear fitting functions successfully preserved all the singular values corresponding to the solute resonances while the estimated matrix rank was close to the minimum matrix rank. A simulation study was also conducted to verify the reliability and superiority of the singular value ratio method compared to another available rank determination method (i.e., MDL). The results revealed that the singular value ratio method accurately determined the minimum rank, while the MDL method significantly underdetermined the minimum matrix rank on every tested data set.

The importance of the results presented in this thesis lies in the ability to make better and more efficient use of expensive magnetic resonance infrastructure. The methods presented are quite general in application and can be performed quickly on commonly available computing platforms. Use of these approaches expands the range of applications since some experiments previously deemed too time consuming now become practicable.

8.2 FUTURE RESEARCH

Although the results obtained in this thesis answered many questions, they also resulted in new questions and ideas for future research. For example, the combination of the normalisation method presented in Chapter 4 and the composite property mapping algorithm could be investigated as a means of providing an even more time-efficient approach of performing arrayed NMR experiments than when one of these two methods is used individually.

It would be interesting to investigate frequency selective noise reduction (Chapter 6) in conjunction with the singular value ratio method (Chapter 7) for obtaining the minimum matrix rank more accurately when used on (noisy) biomolecular NMR spectra.

REFERENCES

[1] P.A. Bottomley, Sodium MRI in human heart, NMR Biomed, 29 (2016) 187-196.
[2] P. Nikolaou, B.M. Goodson, E.Y. Chekmenev, NMR hyperpolarization techniques for biomedicine, Chemistry (Weinheim an der Bergstrasse, Germany), 21 (2015) 3156-3166.
[3] R.A. Komoroski, Applications of ^{7}Li NMR in biomedicine, Magnetic Resonance Imaging, 18 (2000) 103-116.
[4] M.D. Meadows, K.A. Smith, R.A. Kinsey, T.M. Rothgeb, R.P. Skarjune, E. Oldfield, High-resolution solid-state NMR of quadrupolar nuclei, Proceedings of the National Academy of Sciences of the United States of America, 79 (1982) 1351-1355.
[5] F.A. Bovey, P.A. Mirau, The solid-state NMR of polymers, in: F.A. Bovey, P.A. Mirau (Eds.) NMR of Polymers, Academic Press, San Diego, 1996, pp. 243-352.
[6] S.A. Willis, G.R. Dennis, G. Zheng, W.S. Price, Averaging effects in PGSE NMR attenuations observed in bimodal molecular weight PMMA solutions, Macromolecules, 43 (2010) 7351-7356.
[7] J.P. Hindmarsh, K.G. Hollingsworth, D.I. Wilson, M.L. Johns, An NMR study of the freezing of emulsion-containing drops, Journal of Colloid and Interface Science, 275 (2004) 165-171.
[8] J. Wu, N. Kim, J.F. Stebbins, Temperature calibration for high-temperature MAS NMR to 913K: ^{63}Cu MAS NMR of CuBr and CuI, and ^{23}Na MAS NMR of $NaNbO_3$, Solid State Nuclear Magnetic Resonance, 40 (2011) 45-50.
[9] D. Mallamace, S. Longo, C. Corsaro, Proton NMR study of extra virgin olive oil with temperature: Freezing and melting kinetics, Physica A, 499 (2018) 20-27.
[10] M.G. Kubinec, P.G. Williams, Tritium NMR, in, Wiley, New York, 2007.
[11] J.R. Jones, Tritium NMR, applications, in: J.C. Lindon (Ed.) Encyclopedia of spectroscopy and spectrometry, Elsevier, Oxford, 1999, pp. 2366-2369.
[12] R.J. Ouellette, J.D. Rawn, Spectroscopy, in: R.J. Ouellette, J.D. Rawn (Eds.) Principles of organic chemistry, Elsevier, Boston, 2015, pp. 421-446.
[13] J.S. Waugh, Sensitivity in Fourier transform NMR spectroscopy of slowly relaxing systems, Journal of Molecular Spectroscopy, 35 (1970) 298-305.
[14] J.L. Allis, R.M. Dixon, A.M. Till, G.K. Radda, ^{87}Rb NMR studies for evaluation of K^+ fluxes in human erythrocytes, Journal of Magnetic Resonance (1969), 85 (1989) 524-529.
[15] T. Ogino, G.I. Shulman, M.J. Avison, S.R. Gullans, J.A. den Hollander, R.G. Shulman, ^{23}Na and ^{39}K NMR studies of ion transport in human erythrocytes, Proceedings of the National Academy of Sciences of the United States of America, 82 (1985) 1099-1103.
[16] P.J. Brophy, M.K. Hayer, F.G. Riddell, Measurement of intracellular potassium ion concentrations by n.m.r, Biochemical Journal, 210 (1983) 961-963.
[17] L.G. Werbelow, Relaxation theory for quadrupolar nuclei, in: eMagRes, Wiley, New York, 2007.
[18] J.F. Hinton, Sulphur-33 NMR spectroscopy, Annual Reports on NMR Spectroscopy, 19 (1987) 1-34.

[19] R. Siegel, J. Hirschinger, D. Carlier, S. Matar, M. Ménétrier, C. Delmas, ^{59}Co and ^{6,7}Li MAS NMR in polytypes O2 and O3 of $LiCoO_2$, The Journal of Physical Chemistry B, 105 (2001) 4166-4174.
[20] R.A. de Graaf, H. Prinsen, C. Giannini, S. Caprio, R.I. Herzog, Quantification of ^{1}H NMR spectra from human plasma, Metabolomics 11 (2015) 1702-1707.
[21] W.S. Price, L.P. Hwang, Some recent developments in NMR approaches for studying liquid molecular dynamics and their biological applications, Journal of the Chinese Chemical Society, 39 (1992) 479-496.
[22] P. Galvosas, P.T. Callaghan, Multi-dimensional inverse Laplace spectroscopy in the NMR of porous media, Comptes Rendus Physique, 11 (2010) 172-180.
[23] B. Ghadirian, A.M. Torres, N.N. Yadav, W.S. Price, Restricted diffusion in annular geometrical pores, The Journal of Chemical Physics, 138 (2013) 094202-094201-094211.
[24] W.S. Price, F. Tsuchiya, Y. Arata, Time dependence of aggregation in crystallizing lysozyme solutions probed using NMR self-diffusion measurements, Biophysical Journal, 80 (2001) 1585-1590.
[25] H. Weingartner, M. Holz, NMR studies of self-diffusion in liquids, Annual Reports Section "C" (Physical Chemistry), 98 (2002) 121-156.
[26] J.A. Akai, J. Jonas, The effect of pressure and temperature of self-diffusion coefficients in several concentrated deuterium oxide diamagnetic electrolyte solutions, Journal of Solution Chemistry, 5 (1976) 563-574.
[27] W.S. Price, Pulsed-field gradient nuclear magnetic resonance as a tool for studying translational diffusion: part 1. basic theory, Concepts in Magnetic Resonance, 9 (1997) 299-336.
[28] E.O. Stejskal, J.E. Tanner, Spin diffusion measurements: spin echoes in the presence of a time‐dependent field gradient, The Journal of Chemical Physics, 42 (1965) 288-292.
[29] L.E. Kay, G.Y. Xu, A.U. Singer, D.R. Muhandiram, J.D. Formankay, A gradient-enhanced HCCH-TOCSY experiment for recording side-chain ^{1}H and ^{13}C correlations in H_2O samples of proteins, Journal of Magnetic Resonance Series B, 101 (1993) 333-337.
[30] E.T. Olejniczak, R.X. Xu, S.W. Fesik, A 4D HCCH-TOCSY experiment for assigning the side chain ^{1}H and ^{13}C resonances of proteins, Journal of Biomolecular NMR, 2 (1992) 655-659.
[31] M. Balci, Spin–spin coupling, in: M. Balci (Ed.) Basic ^{1}H- and ^{13}C-NMR Spectroscopy, Elsevier, Amsterdam, 2005, pp. 325-337.
[32] M. Balci, Two-dimensional (2D) NMR spectroscopy, in: M. Balci (Ed.) Basic ^{1}H- and ^{13}C-NMR Spectroscopy, Elsevier Amsterdam, 2005, pp. 379-406.
[33] A. Bax, R. Freeman, S.P. Kempsell, Natural abundance ^{13}C - ^{13}C coupling observed via double-quantum coherence, Journal of the American Chemical Society, 102 (1980) 4849-4851.
[34] L.E. Kay, D.A. Torchia, A. Bax, Backbone dynamics of proteins as studied by ^{15}N inverse detected heteronuclear NMR spectroscopy: application to staphylococcal nuclease, Biochemistry, 28 (1989) 8972-8979.
[35] T. Nakai, C.A. McDowell, INADEQUATE NMR spectra of extremely strongly coupled spin systems, Molecular Physics, 79 (1993) 965-983.
[36] A.D. Bain, D.W. Hughes, C.K. Anand, Z. Nie, V.J. Robertson, Problems, artifacts and solutions in the INADEQUATE NMR experiment, Magnetic Resonance in Chemistry, 48 (2010) 630-641.

[37] J. Lambert, J. Buddrus, Sensitivity enhancement of two-dimensional ^{13}C, ^{13}C-INADEQUATE spectroscopy by considering symmetry and isotopic shifts, Journal of Magnetic Resonance, Series A, 101 (1993) 307-312.
[38] J. Lambert, Enhancement of 2D INADEQUATE spectra by means of singular-value decomposition, Journal of Magnetic Resonance, Series A, 123 (1996) 211-214.
[39] G.E. Martin, Small-volume and high-sensitivity NMR probes, Annual Reports on NMR Spectroscopy, 56 (2005) 1-96.
[40] R. Gruetter, S.A. Weisdorf, V. Rajanayagan, M. Terpstra, H. Merkle, C.L. Truwit, M. Garwood, S.L. Nyberg, K. Ugurbil, Resolution improvements in *in Vivo*^{1}H NMR spectra with increased magnetic field strength, Journal of Magnetic Resonance, 135 (1998) 260-264.
[41] P. Styles, N.F. Soffe, C.A. Scott, D.A. Cragg, F. Row, D.J. White, P.C.J. White, A high-resolution NMR probe in which the coil and preamplifier are cooled with liquid helium, Journal of Magnetic Resonance, 213 (2011) 347-354.
[42] J.K. Rainey, J.S. DeVries, B.D. Sykes, Estimation and measurement of flat or solenoidal coil inductance for radiofrequency NMR coil design, Journal of Magnetic Resonance, 187 (2007) 27-37.
[43] A. Neufeld, N. Landsberg, A. Boag, Dielectric inserts for sensitivity and RF magnetic field enhancement in NMR volume coils, Journal of Magnetic Resonance, 200 (2009) 49-55.
[44] T. M. Logan, Nagarajan Murali, Guangshun Wang, Catherine Jolivet, Application of a high-resolution superconducting NMR probe in natural product structure determination, Magnetic Resonance in Chemistry, 37 (1999) 762-765.
[45] A. Brian, Using pulsed gradient spin echo NMR for chemical mixture analysis: How to obtain optimum results, Concepts in Magnetic Resonance, 14 (2002) 225-258.
[46] A. Bax, A spatially selective composite 90° radiofrequency pulse, Journal of Magnetic Resonance (1969), 65 (1985) 142-145.
[47] A. Schwenk, NMR pulse technique with high sensitivity for slowly relaxing systems, Journal of Magnetic Resonance (1969), 5 (1971) 376-389.
[48] K. Horst, M. Siggi, G. Gerd, Multi‐dimensional NMR experiments using selective pulses, Magnetic Resonance in Chemistry, 29 (1991) 527-557.
[49] C. Brissac, T. Malliavin, M.-A. Delsuc, Use of the Cadzow procedure in 2D NMR for the reduction of t_1 noise, Journal of Biomolecular NMR, 6 (1995) 361-365.
[50] J.A. Cadzow, Total least squares, matrix enhancement, and signal processing, Digital Signal Processing, 4 (1994) 21-39.
[51] H. Hassanpour, A. Zehtabian, S.J. Sadati, Time domain signal enhancement based on an optimized singular vector denoising algorithm, Digital Signal Processing, 22 (2012) 786-794.
[52] J.A. Cadzow, Signal enhancement-a composite property mapping algorithm, IEEE Transactions on Acoustics, Speech, and Signal Processing, 36 (1988) 49-62.
[53] G.A. Morris, Reference deconvolution in NMR, in: D.N. Rutledge (Ed.) Data handling in science and technology, Elsevier, Netherlands, 1996, pp. 346.
[54] M.R. Palmer, B.R. Wenrich, P. Stahlfeld, D. Rovnyak, Performance tuning non-uniform sampling for sensitivity enhancement of signal-limited biological NMR, Journal of Biomolecular NMR, 58 (2014) 303-314.
[55] M. Srivastava, E.R. Georgieva, J.H. Freed, A new wavelet denoising method for experimental time-domain signals: pulsed dipolar electron spin resonance, The Journal of Physical Chemistry A, 121 (2017) 2452-2465.

[56] O.A. Ahmed, M.M. Fahmy, NMR signal enhancement via a new time-frequency transform, IEEE Transactions on Medical Imaging 20 (2001) 1018-1025.
[57] A.S. Stern, D.L. Donoho, J.C. Hoch, NMR data processing using iterative thresholding and minimum l_1-norm reconstruction, Journal of Magnetic Resonance, 188 (2007) 295-300.
[58] C.E. Yarman, L. Monzon, M. Reynolds, N. Heaton, A new inversion method for NMR signal processing, in: Computational advances in multi-sensor adaptive processing (CAMSAP), Saint Martin, France, 2013, pp. 260-263.
[59] R.H. Newman, Maximization of entropy and minimization of area as criteria for NMR signal processing, Journal of Magnetic Resonance (1969), 79 (1988) 448-460.
[60] F. Jiru, Introduction to post-processing techniques, European Journal of Radiology, 67 (2008) 202-217.
[61] A. Webb, Increasing the sensitivity of magnetic resonance spectroscopy and imaging, Analytical Chemistry, 84 (2012) 9-16.
[62] M.A. Delsuc, F. Ni, G.C. Levy, Improvement of linear prediction processing of NMR spectra having very low signal-to-noise, Journal of Magnetic Resonance (1969), 73 (1987) 548-552.
[63] Y.Y. Lin, I. advances in NMR signal processing. II. spin dynamics in quantum dissipative systems, in, University of California, Berkeley, CA, 1998, pp. 258.
[64] P.P. Man, C. Bonhomme, F. Babonneau, Denoising NMR time-domain signal by singular-value decomposition accelerated by graphics processing units, Solid State Nuclear Magnetic Resonance, 61–62 (2014) 28-34.
[65] S.D. Kunikeev, H.S. Taylor, Saving measurement time in ^{13}C NMR spectroscopy, The Journal of Physical Chemistry A, 108 (2004) 743-753.
[66] K.M. Wright, Maximum entropy methods in nmr data processing, in: D.N. Rutledge (Ed.) Data handling in science and technology, Elsevier, Netherlands, 1996, pp. 25.
[67] E.D. Lade, J. Skilling, J. Staunton, S. Sibisi, R.G. Brereton, Maximum entropy method in nuclear magnetic resonance spectroscopy, Journal of Magnetic Resonance (1969), 62 (1985) 437-452.
[68] J.F. Martin, The maximum entropy method in NMR, Journal of Magnetic Resonance (1969), 65 (1985) 291-297.
[69] V.A. Mandelshtam, H.S. Taylor, Harmonic inversion of time signals and its applications, The Journal of Chemical Physics, 107 (1997) 6756-6769.
[70] S.D. Kunikeev, H.S. Taylor, J.-J. Pan, A. Kershaw, C.E. McKenna, A new signal processing method to observe weak ^{31}P and ^{17}O NMR peaks, Journal of Organometallic Chemistry, 690 (2005) 2644-2650.
[71] S.D. Kunikeev, H.S. Taylor, T. Schroer, R. Haiges, C.J. Bigler Jones, K.O. Christe, New signalpProcessing method for the faster observation of natural-abundance ^{15}N NMR spectra and its application to N_5^+, Inorganic Chemistry, 45 (2006) 437-442.
[72] J. Chen, V.A. Mandelshtam, A.J. Shaka, Regularization of the two-dimensional filter diagonalization method: FDM2K, Journal of Magnetic Resonance, 146 (2000) 363-368.
[73] V.A. Mandelshtam, FDM: the filter diagonalization method for data processing in NMR experiments, Progress in Nuclear Magnetic Resonance Spectroscopy, 38 (2001) 159-196.
[74] D.L. Donoho, J.M. Johnstone, Ideal spatial adaptation by wavelet shrinkage, Biometrika, 81 (1994) 425-455.

[75] J.C. Hoch, Maximum entropy reconstruction, in: G.C.K. Roberts (Ed.) Encyclopedia of biophysics, Springer Berlin, 2013, pp. 1431-1433.
[76] Y.-Y. Lin, P. Hodgkinson, M. Ernst, A. Pines, A novel detection–estimation scheme for noisy NMR signals: applications to delayed acquisition data, Journal of Magnetic Resonance, 128 (1997) 30-41.
[77] P. Koehl, Linear prediction spectral analysis of NMR data, Progress in Nuclear Magnetic Resonance Spectroscopy, 34 (1999) 257-299.
[78] W.W.F. Pijnappel, A. van den Boogaart, R. de Beer, D. van Ormondt, SVD-based quantification of magnetic resonance signals, Journal of Magnetic Resonance (1969), 97 (1992) 122-134.
[79] H. Yan, J.C. Gore, The relation of HSVD to LPSVD for fitting time-domain signals, Journal of Magnetic Resonance (1969), 80 (1988) 324-327.
[80] Y.-M. Wang, H. Lee, D.V. Apte, Quantitative NMR spectroscopy by matrix pencil methods, International Journal of Imaging Systems and Technology, 4 (1992) 201-206.
[81] Y. Hua, T.K. Sarkar, Matrix pencil method for estimating parameters of exponentially damped/undamped sinusoids in noise, IEEE Transactions on Acoustics, Speech, and Signal Processing, 38 (1990) 814-824.
[82] Y. Hua, T.K. Sarkar, On SVD for estimating generalized eigenvalues of singular matrix pencil in noise, IEEE Transactions on Signal Processing, 39 (1991) 892-900.
[83] M.H. Levitt, Spin dynamics, Wiley, Chichester, England, 2001.
[84] V. Kuperman, Basic principles of nuclear magnetic resonance, Academic Press, San Diego, 2000.
[85] J.H. Lee, Y. Okuno, S. Cavagnero, Sensitivity enhancement in solution NMR: emerging ideas and new frontiers, Journal of Magnetic Resonance, 241 (2014) 18-31.
[86] J. Cavanagh, W.J. Fairbrother, A.G. Palmer Iii, M. Rance, N.J. Skelton, Protein NMR spectroscopy: principles and practice, 2 ed., Academic Press, Burlington, 2007.
[87] P. Atkins, J. de Paula, Atkins' physical chemistry, Oxford University Press, New York, 2010.
[88] J. Keeler, Understanding NMR spectroscopy, 2 ed., Wiley, Oxford, 2011.
[89] J. Kowalewski, L. Mäler, Nuclear spin relaxation in liquids : Theory, experiments, and applications, Taylor & Francis, New York 2006.
[90] J. Cavanagh, W.J. Fairbrother, A.G. Palmer Iii, M. Rance, N.J. Skelton, Relaxation and dynamic processes, in: J. Cavanagh, W.J. Fairbrother, A.G. Palmer, M. Rance, N.J. Skelton (Eds.) Protein NMR spectroscopy, Academic Press, Burlington, 2007, pp. 333-404.
[91] B. Cowan, Nuclear magnetic resonance and relaxation, Cambridge University Press, Cambridge, 1997.
[92] L. Axel, Relaxation times and NMR signals, Magnetic Resonance Imaging, 2 (1984) 121-128.
[93] R.L. Vold, J.S. Waugh, M.P. Klein, D.E. Phelps, Measurement of spin relaxation in complex systems, The Journal of Chemical Physics, 48 (1968) 3831-3832.
[94] E.L. Hahn, Spin echoes, Physical Review, 80 (1950) 580-594.
[95] M.D. Mann, B.F. Chmelka, Measurement of dilute ^{29}Si species in solution using a large volume coil and DEFT NMR, Analytical Chemistry, 72 (2000) 5131-5135.
[96] E.D. Becker, R.R. Shoup, ^{13}C NMR spectroscopy: relaxation times of ^{13}C and methods for sensitivity enhancement, pac, 32 (1972) 51-66.

[97] J.-M. Bernassau, F. Hyafil, Choice of delay time sequence in spin-lattice relaxation time measurements by inversion-recovery, Journal of Magnetic Resonance (1969), 40 (1980) 245-258.
[98] R.J. Ogg, P.B. Kingsley, Optimized precision of inversion-recovery T_1 measurements for constrained scan time, Magnetic Resonance in Medicine, 51 (2004) 625-630.
[99] E.H. Rhoderick, Definition of nuclear quadrupole moments, Nature, 160 (1947) 255-256.
[100] J.A.S. Smith, Nuclear quadrupole resonance spectroscopy. general principles, Journal of Chemical Education, 48 (1971) 39.
[101] E. Oldfield, H.K.C. Timken, B. Montez, R. Ramachandran, High-resolution solid-state NMR of quadrupolar nuclei, Nature, 318 (1985) 163-165.
[102] F.W. Wehrli, Temperature-dependent spin-lattice relaxation of ^{6}Li in aqueous lithium chloride, Journal of Magnetic Resonance (1969), 23 (1976) 527-532.
[103] S. Forsén, T. Drakenberg, H. Wennerström, NMR studies of ion binding in biological systems, Quarterly Reviews of Biophysics, 19 (2009) 83-114.
[104] D.W. Urry, T.L. Trapane, C.M. Venkatachalam, Potassium-39 NMR of K^+ interaction with the gramicidin channel and NMR-derived conductance ratios for Na^+, K^+ and Rb^+, The Journal of Membrane Biology, 89 (1986) 107-111.
[105] S. Forsén, T. Andersson, T. Drakenberg, E. Thulin, T. Wieloch, NMR studies of calcium and magnesium in biological systems, in: I. Bertini, L. Lunazzi, A. Dei (Eds.) Advances in solution chemistry, Springer, Boston, MA, 1981, pp. 191-208.
[106] T.D.W. Claridge, Introducing high-resolution NMR, in: High-resolution NMR techniques in organic chemistry Elsevier, Boston, 2016, pp. 11-59.
[107] D. Sundholm, P. Pyykkö, L. Laaksonen, A.J. Sadlej, Nuclear quadrupole moment of lithium from combined fully numerical and discrete basis-set calculations on LiH, Chemical Physics Letters, 112 (1984) 1-9.
[108] F.W. Wehrli, Spin-lattice relaxation of some less common weakly quadrupolar nuclei, Journal of Magnetic Resonance (1969), 30 (1978) 193-209.
[109] P.P. Man, Quadrupole couplings in nuclear magnetic resonance, general, in: R.A. Meyers (Ed.) Encyclopedia of Analytical Chemistry, Wiley, Chichester, 2000, pp. 12224-12265.
[110] R. Bhattacharyya, L. Frydman, Quadrupolar nuclear magnetic resonance spectroscopy in solids using frequency-swept echoing pulses, The Journal of Chemical Physics, 127 (2007) 194503-194501-194508.
[111] W.S. Price, NMR studies of translational motion: Principles and applications, Cambridge University Press, Cambridge, 2009.
[112] W. Jost, Diffusion in solids, liquids, gases, Academic Press, New York, 1960.
[113] H.C. Berg, Random walks in biology, Princeton University Press, Princeton, 1983.
[114] W. Jost, Diffusion in solids, liquids, gases, 1 ed., Academic Press, New York, 1960.
[115] G.A. Truskey, F. Yuan, D.F. Katz, Transport phenomena in biological systems, Pearson Prentice Hall, Upper Saddle River, 2004.
[116] K.F. Morris, C.S. Johnson, Resolution of discrete and continuous molecular size distributions by means of diffusion-ordered 2D NMR spectroscopy, Journal of the American Chemical Society, 115 (1993) 4291-4299.
[117] L. Avram, Y. Cohen, Diffusion NMR of molecular cages and capsules, Chemical Society Reviews, 44 (2015) 586-602.

[118] M. Nilsson, M. Khajeh, A. Botana, M. Bernstein, G. A Morris, Diffusion NMR and trilinear analysis in the study of reaction kinetics, Chemical Communications (Cambridge), (2009) 1252-1254.
[119] L.H. Lucas, C.K. Larive, Measuring ligand-protein binding using NMR diffusion experiments, Concepts in Magnetic Resonance Part A, 20A (2004) 24-41.
[120] M. Lin, M.J. Shapiro, J.R. Wareing, Diffusion-edited NMR−affinity NMR for direct observation of molecular interactions, Journal of the American Chemical Society, 119 (1997) 5249-5250.
[121] S. A. Willis, T. Stait-Gardner, A. S. Virk, R. Masuda, M. Zubkov, G. Zheng, W. S. Price, Diffusion: denition, description and measurement, in: J. Fisher (Ed.) Modern NMR techniques for synthetic chemistry, CRC Press, Boca Raton, FL, 2014, pp. 125.
[122] M.R. Riazi, A new method for experimental measurement of diffusion coefficients in reservoir fluids, Journal of Petroleum Science and Engineering, 14 (1996) 235-250.
[123] J.H. Wang, C.V. Robinson, I.S. Edelman, Self-diffusion and structure of liquid water. III. measurement of the self-diffusion of liquid water with H^2, H^3 and O^{18} as Tracers, Journal of the American Chemical Society, 75 (1953) 466-470.
[124] A.J.W.G. Visser, M.A. Hink, New perspectives of fluorescence correlation spectroscopy, Journal of Fluorescence, 9 (1999) 81-87.
[125] D. Bernin, D. Topgaard, NMR diffusion and relaxation correlation methods: New insights in heterogeneous materials, Current Opinion in Colloid & Interface Science, 18 (2013) 166-172.
[126] C.K. Larive, M. Lin, B.J. Piersma, W.R. Carper, Diffusion ordered spectroscopy of room temperature chloroaluminate melts, The Journal of Physical Chemistry, 99 (1995) 12409-12412.
[127] W.R. Carper, G.J. Mains, B.J. Piersma, S.L. Mansfield, C.K. Larive, ^{13}C NMR relaxation and ^{1}H diffusion (DOSY) studies of an acidic chloroaluminate melt, The Journal of Physical Chemistry, 100 (1996) 4724-4728.
[128] W.R. Carper, C.E. Keller, Direct determination of NMR correlation times from spin−lattice and spin−spin relaxation times, The Journal of Physical Chemistry A, 101 (1997) 3246-3250.
[129] W.D. E., Brownian motion and its effects in NMR chemical exchange and relaxation in liquids, Concepts in Magnetic Resonance, 8 (1996) 397-421.
[130] R.E. Gordon, J.H. Strange, Self-diffusion studies in solids using nuclear magnetic resonance techniques, Faraday Symposia of the Chemical Society, 13 (1978) 153-160.
[131] B.M. Fung, T.W. McGaughy, Study of spin-lattice and spin-spin relaxation times of ^{1}H, ^{2}H, and ^{17}O in muscular water, Biophysical Journal, 28 (1979) 293-303.
[132] A.L. Lee, A.J. Wand, Assessing potential bias in the determination of rotational correlation times of proteins by NMR relaxation, Journal of Biomolecular NMR, 13 (1999) 101-112.
[133] D.S. Korchuganov, I.E. Gagnidze, E.N. Tkach, A.A. Schulga, M.P. Kirpichnikov, A.S. Arseniev, Determination of protein rotational correlation time from NMR relaxation data at various solvent viscosities, Journal of Biomolecular NMR, 30 (2004) 431-442.
[134] D. Lee, C. Hilty, G. Wider, K. Wüthrich, Effective rotational correlation times of proteins from NMR relaxation interference, Journal of Magnetic Resonance, 178 (2006) 72-76.
[135] P. Debye, Polar molecules, Dover Publication, New York, 1945.

[136] A. Einstein, On the motion of small particles suspended in liquids at rest required by the molecular-kinetic theory of heat, Annalen der Physik, 322 (1905) 549-560.
[137] W. Sutherland, A dynamical theory of diffusion for non-electrolytes and the molecular mass of albumin, The London, Edinburgh, and Dublin Philosophical Magazine and Journal of Science, 9 (1905) 781-785.
[138] G.G. Stokes, On the effect of the internal friction of fluids on the motion of pendulums, Transactions of the Cambridge Philosophical Society, 9 (1856) 8 - 106.
[139] T. Brand, E. Cabrita, S. Berger, Theory and application of NMR diffusion studies, in: Graham A. Webb (Ed.) Modern magnetic resonance, Springer, Netherlands, 2006, pp. 131-139.
[140] W.S. Price, NMR studies of translational motion, Cambridge University Press, Cambridge, 2009.
[141] J.E. Tanner, Use of the stimulated echo in NMR diffusion studies, The Journal of Chemical Physics, 52 (1970) 2523-2526.
[142] S. W. Englander, N. W. Downer, H. Teitelbaum, Hydrogen exchange, Annual Review of Biochemistry, 41 (1972) 903-924.
[143] C. Redfield, Using nuclear magnetic resonance spectroscopy to study molten globule states of proteins, Methods, 34 (2004) 121-132.
[144] T.D.W. Claridge, Practical aspects of high-resolution NMR, in: High-resolution NMR techniques in organic chemistry, Elsevier, Netherland, 1999, pp. 45-110.
[145] H. Mo, J.S. Harwood, D. Raftery, Receiver gain function: the actual NMR receiver gain, Magnetic resonance in chemistry 48 (2010) 235-238.
[146] N.E. Jacobsen, NMR spectroscopy explained: Simplified theory, applications and examples for organic chemistry and structural biology, Wiley, New Jersey, 2007.
[147] W.S. Price, Water signal suppression in NMR spectroscopy, Annual Reports on NMR Spectroscopy, 38 (1999) 289-354.
[148] A.M. Torres, W.S. Price, Common problems and artifacts encountered in solution-state NMR experiments, Concepts in Magnetic Resonance Part A, 45A (2016) e21387-21381-21316.
[149] A.J. Simpson, S.A. Brown, Purge NMR: effective and easy solvent suppression, Journal of Magnetic Resonance, 175 (2005) 340-346.
[150] S.H. Smallcombe, S.L. Patt, P.A. Keifer, WET solvent suppression and its applications to LC NMR and high-resolution NMR spectroscopy, Journal of Magnetic Resonance Series A, 117 (1995) 295-303.
[151] M. Piotto, V. Saudek, V. Sklenář, Gradient-tailored excitation for single-quantum NMR spectroscopy of aqueous solutions, Journal of Biomolecular NMR, 2 (1992) 661-665.
[152] V. Sklenar, M. Piotto, R. Leppik, V. Saudek, Gradient-tailored water suppression for ^{1}H-^{15}N HSQC experiments optimized to retain full sensitivity, Journal of Magnetic Resonance Series A, 102 (1993) 241-245.
[153] U.L. Günther, C. Ludwig, H. Rüterjans, WAVEWAT—improved solvent suppression in NMR spectra employing wavelet transforms, Journal of Magnetic Resonance, 156 (2002) 19-25.
[154] G. Zhu, D. Smith, Y. Hua, Post-acquisition solvent suppression by singular-value decomposition, Journal of Magnetic Resonance, 124 (1997) 286-289.
[155] K.J. Cross, Improved digital filtering technique for solvent suppression, Journal of Magnetic Resonance, Series A, 101 (1993) 220-224.

[156] Y. Kuroda, A. Wada, T. Yamazaki, K. Nagayama, Postacquisition data processing method for suppression of the solvent signal, Journal of Magnetic Resonance (1969), 84 (1989) 604-610.
[157] W.S. Price, F. Elwinger, C. Vigouroux, P. Stilbs, PGSE-WATERGATE, a new tool for NMR diffusion-based studies of ligand–macromolecule binding, Magnetic Resonance in Chemistry, 40 (2002) 391-395.
[158] G. Zheng, T. Stait-Gardner, P.G. Anil Kumar, A.M. Torres, W.S. Price, PGSTE-WATERGATE: An STE-based PGSE NMR sequence with excellent solvent suppression, Journal of Magnetic Resonance, 191 (2008) 159-163.
[159] D.I. Hoult, The NMR receiver: a description and analysis of design, Progress in Nuclear Magnetic Resonance Spectroscopy, 12 (1978) 41-77.
[160] D. Moskau, Application of real time digital filters in NMR spectroscopy, Concepts in Magnetic Resonance, 15 (2002) 164-176.
[161] K. Roth, B.J. Kimber, J. Feeney, Data shift accumulation and alternate delay accumulation techniques for overcoming the dynamic range problem, Journal of Magnetic Resonance (1969), 41 (1980) 302-309.
[162] S. Davies, C. Bauer, P. Barker, R. Freeman, The dynamic range problem in NMR, Journal of Magnetic Resonance (1969), 64 (1985) 155-159.
[163] M. Martin, B. Legat, J. Leenders, J. Vanwinsberghe, R. Rousseau, B. Boulanger, P.H.C. Eilers, P. De Tullio, B. Govaerts, PepsNMR for 1H NMR metabolomic data pre-processing, Analytica Chimica Acta, 1019 (2018) 1-13.
[164] L. Vanhamme, T. Sundin, P.V. Hecke, S.V. Huffel, MR spectroscopy quantitation: a review of time-domain methods, NMR Biomed, 14 (2001) 233-246.
[165] D.W. Tufts, R. Kumaresan, Singular value decomposition and improved frequency estimation using linear prediction, IEEE Transactions on Acoustics, Speech, and Signal Processing, 30 (1982) 671-675.
[166] H. Barkhuijsen, R. de Beer, W.M.M.J. Bovée, D. van Ormondt, Retrieval of frequencies, amplitudes, damping factors, and phases from time-domain signals using a linear least-squares procedure, Journal of Magnetic Resonance (1969), 61 (1985) 465-481.
[167] D.I. Hoult, R.E. Richards, The signal-to-noise ratio of the nuclear magnetic resonance experiment, Journal of Magnetic Resonance (1969), 24 (1976) 71-85.
[168] H. Mo, D. Raftery, Solvent signal as an NMR concentration reference, Analytical Chemistry, 80 (2008) 9835-9839.
[169] H. Mo, J.S. Harwood, D. Raftery, A quick diagnostic test for NMR receiver gain compression, Magnetic Resonance in Chemistry, 48 (2010) 782-786.
[170] R.R. Ernst, W.A. Anderson, Application of fourier transform spectroscopy to magnetic resonance, Review of Scientific Instruments, 37 (1966) 93-102.
[171] J.W. Cooley, J.W. Tukey, An algorithm for the machine calculation of complex fourier series, Mathematics of Computation, 19 (1965) 297-301.
[172] K.C. Brown, Essential mathematics for NMR and MRI spectroscopists, Royal Society of Chemistry, Chembridge, 2016.
[173] J.L. Brown, On the uniform sampling of a sinusoidal signal, IEEE Transactions on Aerospace and Electronic Systems, 24 (1988) 103-106.
[174] J.C. Lindon, A.G. Ferrige, Digitisation and data processing in Fourier transform NMR, Progress in Nuclear Magnetic Resonance Spectroscopy, 14 (1980) 27-66.
[175] M.R. Palmer, C.L. Suiter, G.E. Henry, J. Rovnyak, J.C. Hoch, T. Polenova, D. Rovnyak, Sensitivity of nonuniform sampling NMR, The Journal of Physical Chemistry B, 119 (2015) 6502-6515.

[176] Y. Manassen, G. Navon, Nonuniform sampling in NMR experiments, Journal of Magnetic Resonance (1969), 79 (1988) 291-298.
[177] I.S. Mackenzie, Nuclear magnetic resonance for measurement, Journal of Physics E: Scientific Instruments, 19 (1986) 324.
[178] G.B. Matson, Signal integration and the signal-to-noise ratio in pulsed NMR relaxation measurements, Journal of Magnetic Resonance (1969), 25 (1977) 477-480.
[179] D. Rovnyak, M. Sarcone, Z. Jiang, Sensitivity enhancement for maximally resolved two‐dimensional NMR by nonuniform sampling, Magnetic Resonance in Chemistry, 49 (2011) 483-491.
[180] K. Kazimierczuk, V. Orekhov, Non-uniform sampling: post-Fourier era of NMR data collection and processing, Magnetic Resonance in Chemistry, 53 (2015) 921-926.
[181] M. Mobli, J.C. Hoch, Nonuniform sampling and non-Fourier signal processing methods in multidimensional NMR, Progress in Nuclear Magnetic Resonance Spectroscopy, 83 (2014) 21-41.
[182] J.C. Hoch, M.W. Maciejewski, M. Mobli, A.D. Schuyler, A.S. Stern, Nonuniform sampling in multidimensional NMR, in: eMagRes, Wiley, New York, 2012, pp. 181-196.
[183] M. Mobli, J.C. Hoch, Fast NMR Data Acquisition: Beyond the Fourier Transform, Royal Society of Chemistry, 2017.
[184] H.M. Nguyen, X. Peng, M.N. Do, Z. Liang, Denoising MR spectroscopic imaging data with low-rank approximations, IEEE Transactions on Biomedical Engineering, 60 (2013) 78-89.
[185] D. Rovnyak, D.P. Frueh, M. Sastry, Z.-Y.J. Sun, A.S. Stern, J.C. Hoch, G. Wagner, Accelerated acquisition of high resolution triple-resonance spectra using non-uniform sampling and maximum entropy reconstruction, Journal of Magnetic Resonance, 170 (2004) 15-21.
[186] S.G. Hyberts, H. Arthanari, S.A. Robson, G. Wagner, Perspectives in magnetic resonance: NMR in the post-FFT era, Journal of Magnetic Resonance, 241 (2014) 60-73.
[187] M. Mobli, M.W. Maciejewski, A.D. Schuyler, A.S. Stern, J.C. Hoch, Sparse sampling methods in multidimensional NMR, Physical chemistry chemical physics : PCCP, 14 (2012) 10835-10843.
[188] M.W. Maciejewski, M. Mobli, A.D. Schuyler, A.S. Stern, J.C. Hoch, Data sampling in multidimensional NMR: fundamentals and strategies, Topics in current chemistry, 316 (2012) 49-77.
[189] K. Kazimierczuk, M. Misiak, J. Stanek, A. Zawadzka-Kazimierczuk, W. Koźmiński, Generalized Fourier Transform for Non-Uniform Sampled Data, in: M. Billeter, V. Orekhov (Eds.) Novel Sampling Approaches in Higher Dimensional NMR, Springer Berlin Heidelberg, Berlin, Heidelberg, 2012, pp. 79-124.
[190] S.J. Wernecke, L.R. D'Addario, Maximum entropy image reconstruction, IEEE Trans. Comput., 26 (1977) 351-364.
[191] S.G. Hyberts, A.G. Milbradt, A.B. Wagner, H. Arthanari, G. Wagner, Application of iterative soft thresholding for fast reconstruction of NMR data non-uniformly sampled with multidimensional poisson gap scheduling, Journal of biomolecular NMR, 52 (2012) 315-327.
[192] I. Drori, Fast l_1 minimization by iterative thresholding for multidimensional NMR spectroscopy, EURASIP Journal on Advances in Signal Processing, 2007 (2007) 020248.

[193] L. Petrakis, Spectral line shapes: Gaussian and Lorentzian functions in magnetic resonance, Journal of Chemical Education, 44 (1967) 432.
[194] Y. Hiltunen, M. Ala-Korpela, J. Jokisaari, S. Eskelinen, K. Kiviniitty, M. Savolainen, Y.A. Kesäniemi, A lineshape fitting model for 1H NMR spectra of human blood plasma, Magnetic Resonance in Medicine, 21 (1991) 222-232.
[195] J. Higinbotham, I. Marshall, NMR lineshapes and lineshape fitting procedures, in: Annual Reports on NMR Spectroscopy, Academic Press, 2001, pp. 59-120.
[196] J.-B. Poullet, D.M. Sima, S. Van Huffel, MRS signal quantitation: A review of time- and frequency-domain methods, Journal of Magnetic Resonance, 195 (2008) 134-144.
[197] C.H. Sotak, C.L. Dumoulin, M.D. Newsham, Automatic phase correction of fourier transform NMR spectra based on the dispersion versus absorption (DISPA) lineshape analysis, Journal of Magnetic Resonance (1969), 57 (1984) 453-462.
[198] F. Montigny, K. Elbayed, J. Brondeau, D. Canet, Automatic phase correction of Fourier-transform NMR data and estimation of peak area by fitting to a Lorentzian shape, Analytical Chemistry, 62 (1990) 864-867.
[199] L. Chen, Z. Weng, L. Goh, M. Garland, An efficient algorithm for automatic phase correction of NMR spectra based on entropy minimization, Journal of Magnetic Resonance, 158 (2002) 164-168.
[200] J.J. van Vaals, P.H.J. van Gerwen, Novel methods for automatic phase correction of NMR spectra, Journal of Magnetic Resonance (1969), 86 (1990) 127-147.
[201] R.R. Ernst, Numerical Hilbert transform and automatic phase correction in magnetic resonance spectroscopy, Journal of Magnetic Resonance (1969), 1 (1969) 7-26.
[202] Q. Bao, J. Feng, L. Chen, F. Chen, Z. Liu, B. Jiang, C. Liu, A robust automatic phase correction method for signal dense spectra, Journal of Magnetic Resonance, 234 (2013) 82-89.
[203] G.N. Chmurny, D.I. Hoult, The ancient and honourable art of shimming, Concepts in Magnetic Resonance, 2 (1990) 131-149.
[204] R.R. Ernst, Measurement and control of magnetic field homogeneity, Review of Scientific Instruments, 39 (1968) 998-1012.
[205] M. Weiger, T. Speck, M. Fey, Gradient shimming with spectrum optimisation, Journal of Magnetic Resonance, 182 (2006) 38-48.
[206] C.G. Tang, An analysis of baseline distortion and offset in NMR spectra, Journal of Magnetic Resonance, Series A, 109 (1994) 232-240.
[207] J. Near, R. Edden, C.J. Evans, R. Paquin, A. Harris, P. Jezzard, Frequency and phase drift correction of magnetic resonance spectroscopy data by spectral registration in the time domain, Magnetic resonance in medicine, 73 (2015) 44-50.
[208] G.A. Pearson, A general baseline-recognition and baseline-flattening algorithm, Journal of Magnetic Resonance (1969), 27 (1977) 265-272.
[209] D. Barache, J.P. Antoine, J.M. Dereppe, The continuous wavelet transform, an analysis tool for NMR spectroscopy, Journal of Magnetic Resonance, 128 (1997) 1-11.
[210] A. Graps, An introduction to wavelets, IEEE Computational Science and Engineering, 2 (1995) 50-61.
[211] T. Coor, Signal to noise optimization in chemistry - Part one, Journal of Chemical Education, 45 (1968) A533.
[212] G.M. Hieftje, Signal-to-noise enhancement through instrumental techniques. 1. signals, noise, and S/N enhancement in the frequency domain, Analytical Chemistry, 44 (1972) 81A-88a.

[213] F.R. Connor, Noise: Introductory topics in electronics and telecommunication, Edward Arnold, London, 1973.
[214] F.N. Hooge, 1/f noise, Physica B, 83 (1976) 14-23.
[215] W.B. Davenport, W.L. Root, An Introduction to the Theory of Random Signals and Noise, 1 ed., Wiley, 1987.
[216] D.D. Traficante, Time averaging. does the noise really average toward zero?, Concepts in Magnetic Resonance, 3 (1991) 83-87.
[217] F.N. Hooge, 1/f noise sources, IEEE Transactions on Electron Devices, 41 (1994) 1926-1935.
[218] K. Chandra, Noise detected NMR spectroscopy, Journal of the Indian Institute of Science, 94 (2014) 517-526.
[219] W. Hartmann, Acoustic signal processing, in: T.D. Rossing (Ed.) Springer handbook of acoustics, Springer, New York, 2007, pp. 503.
[220] J.A. Cadzow, M.M. Wu, Analysis of transient data in noise, IEE Proceedings F (Radar and Signal Processing), 134 (1987) 69-78.
[221] M. Pachter, M.M. Briggs, Simulation of white noise in dynamical systems, Simulation, 56 (1991) 19-25.
[222] B. Blümich, White noise nonlinear system analysis in nuclear magnetic resonance spectroscopy, Progress in Nuclear Magnetic Resonance Spectroscopy, 19 (1987) 331-417.
[223] H. Grage, M. Akke, A statistical analysis of NMR spectrometer noise, Journal of Magnetic Resonance, 162 (2003) 176-188.
[224] J.B. Johnson, Thermal agitation of electricity in conductors, Physical Review, 32 (1928) 97-109.
[225] H. Nyquist, Thermal agitation of electric charge in conductors, Physical Review, 32 (1928) 110-113.
[226] W. Schottky, Small-shot effect and flicker effect, Physical Review, 28 (1926) 74-103.
[227] K. Chida, M. Hashisaka, Y. Yamauchi, S. Nakamura, T. Arakawa, T. Machida, K. Kobayashi, T. Ono, Shot noise induced by electron-nuclear spin-flip scattering in a nonequilibrium quantum wire, Physical Review B, 85 (2012) 041309.
[228] J.B. Johnson, The Schottky effect in low frequency circuits, Physical Review, 26 (1925) 71-85.
[229] E. Burstein, R.H. Kingston, A.L. McWhorter, Semiconductor surface physics, University of Pennsylvania press, Philadelphia, 1957.
[230] G. Reimbold, Modified 1/*f* trapping noise theory and experiments in MOS transistors biased from weak to strong inversion influence of interface states, IEEE Transactions on Electron Devices, 31 (1984) 1190-1198.
[231] G. Ghibaudo, A simple derivation of Reimbold's drain current spectrum formula for flicker noise in MOSFETs, Solid-State Electronics, 30 (1987) 1037-1038.
[232] R.P. Jindal, A. Van Der Ziel, Phonon fluctuation model for flicker noise in elemental semiconductors, Journal of Applied Physics, 52 (1981) 2884-2888.
[233] P.H. Handel, Quantum approach to 1/*f* noise, Physical Review A, 22 (1980) 745-757.
[234] H. Senn, H.-R. Loosli, Influence of vibration on NMR experiments, Journal of Magnetic Resonance (1969), 86 (1990) 394-399.
[235] J.W. Britton, J.G. Bohnet, B.C. Sawyer, H. Uys, M.J. Biercuk, J.J. Bollinger, Vibration-induced field fluctuations in a superconducting magnet, Physical Review A, 93 (2016) 062511-062517.

[236] Y. Ben‐Dov, NMR sensitivity to floor vibration, The Journal of the Acoustical Society of America, 123 (2008) 3813.
[237] F. Bloch, Nuclear induction, Physical Review, 70 (1946) 460-474.
[238] T. Sleator, E.L. Hahn, C. Hilbert, J. Clarke, Nuclear-spin noise, Physical Review Letters, 55 (1985) 1742-1745.
[239] D.I. Hoult, B. Bhakar, NMR signal reception: virtual photons and coherent spontaneous emission, Magn. Reson.: Educ. J., 9 (1997) 277-297.
[240] M.A. McCoy, R.R. Ernst, Nuclear spin noise at room temperature, Chemical Physics Letters, 159 (1989) 587-593.
[241] M. Guéron, J.L. Leroy, NMR of water protons. the detection of their nuclear-spin noise, and a simple determination of absolute probe sensitivity based on radiation damping, Journal of Magnetic Resonance (1969), 85 (1989) 209-215.
[242] D.J.Y. Marion, H. Desvaux, An alternative tuning approach to enhance NMR signals, Journal of Magnetic Resonance, 193 (2008) 153-157.
[243] M. Nausner, M. Goger, E. Bendet-Taicher, J. Schlagnitweit, A. Jerschow, N. Müller, Signal enhancement in protein NMR using the spin-noise tuning optimum, Journal of Biomolecular NMR, 48 (2010) 157-167.
[244] E. Bendet-Taicher, N. Müller, A. Jerschow, Dependence of NMR noise line shapes on tuning, matching, and transmission line properties, Concepts in Magnetic Resonance B, 44 (2014) 1-11.
[245] A.F. Mehlkopf, D. Korbee, T.A. Tiggelman, R. Freeman, Sources of t_1 noise in two-dimensional NMR, Journal of Magnetic Resonance (1969), 58 (1984) 315-323.
[246] K. Nagayama, P. Bachmann, K. Wuthrich, R.R. Ernst, The use of cross-sections and of projections in two-dimensional NMR spectroscopy, Journal of Magnetic Resonance (1969), 31 (1978) 133-148.
[247] A. Gibbs, G.A. Morris, A.G. Swanson, D. Cowburn, Suppression of t1 noise in 2D NMR spectroscopy by reference deconvolution, Journal of Magnetic Resonance, Series A, 101 (1993) 351-356.
[248] S. Eroglu, G. Friedman, R.L. Magin, Estimate of losses and signal-to-noise ratio in planar inductive micro-coil detectors used for NMR, IEEE Transactions on Magnetics, 37 (2001) 2787-2789.
[249] D. Erdogmus, E. G. Larsson, R. Yan, J. C. Principe, J. R. Fitzsimmons, Measuring the signal-to-noise ratio in magnetic resonance imaging: a caveat, Signal Processing, 84 (2004) 1035-1040.
[250] S.G. Hyberts, S.A. Robson, G. Wagner, Exploring signal-to-noise ratio and sensitivity in non-uniformly sampled multi-dimensional NMR spectra, Journal of biomolecular NMR, 55 (2013) 167-178.
[251] S.O. Rice, Mathematical analysis of random noise, Bell System Technical Journal, 24 (1945) 46-156.
[252] P. Styles, N.F. Soffe, C.A. Scott, The first cryoprobe – some recollections, Journal of Magnetic Resonance, 213 (2011) 355-356.
[253] H. Kovacs, D. Moskau, Cryogenic NMR probes, in: G.C.K. Roberts (Ed.) Encyclopedia of Biophysics, Springer, Heidelberg, 2013, pp. 392-396.
[254] P. Styles, N.F. Soffe, C.A. Scott, An improved cryogenically cooled probe for high-resolution NMR, Journal of Magnetic Resonance (1969), 84 (1989) 376-378.
[255] R.R. Ernst, Sensitivity enhancement in magnetic resonance. I. analysis of the method of time averaging, Review of Scientific Instruments, 36 (1965) 1689-1695.
[256] D.I. Hoult, Sensitivity of the NMR experiment, eMagRes, (2007).

[257] V.M.M. Lobo, A.C.F. Ribeiro, L.M.P. Verissimo, Diffusion coefficients in aqueous solutions of potassium chloride at high and low concentrations, Journal of Molecular Liquids, 78 (1998) 139-149.
[258] A.M. Kusova, A.E. Sitnitsky, B.Z. Idiyatullin, D.R. Bakirova, Y.F. Zuev, The effect of shape and concentration on translational diffusion of proteins measured by PFG NMR, Applied Magnetic Resonance, 49 (2018) 35-51.
[259] F. Susanne, D.S. Smith, A. Codina, Kinetic understanding using NMR reaction profiling, Organic Process Research and Development, 16 (2012) 61-64.
[260] T.K. Karamanos, A.P. Kalverda, G.S. Thompson, S.E. Radford, Mechanisms of amyloid formation revealed by solution NMR, Progress in nuclear magnetic resonance spectroscopy, 0 (2015) 86-104.
[261] A. Ross, G. Schlotterbeck, F. Dieterle, H. Senn, NMR spectroscopy techniques for application to metabonomics, in: J.C. Lindon, J.K. Nicholson, E. Holmes (Eds.) The handbook of metabonomics and metabolomics, Elsevier Science B.V., Amsterdam, 2007, pp. 55-112.
[262] G. Schlotterbeck, A. Ross, R. Hochstrasser, H. Senn, T. Kühn, D. Marek, O. Schett, High-resolution capillary tube NMR. a miniaturized 5-μL high-sensitivity TXI probe for mass-limited samples, off-line LC NMR, and HT NMR, Analytical Chemistry, 74 (2002) 4464-4471.
[263] G.E. Martin, C.E. Hadden, Comparison of 1.7 mm submicro and 3 mm micro gradient NMR probes for the acquisition of ^{1}H-^{13}C and ^{1}H-^{15}N heteronuclear shift correlation data, Magnetic Resonance in Chemistry, 37 (1999) 721-729.
[264] R.W. Dykstra, The use of a symmetrical microtube for increased sensitivity in carbon-13 NMR measurements, Journal of Magnetic Resonance, Series A, 112 (1995) 255-257.
[265] A. Krunić, J. Orjala, Application of high-field NMR spectroscopy for characterization and quantitation of submilligram quantities of isolated natural products, Magnetic Resonance in Chemistry, 53 (2015) 1043-1050.
[266] F. D. Doty, Probe design and construction, in: D. M. Grant, R. K. Harris (Eds.) Encyclopedia of NMR, Wiley, New York, 1996, pp. 3753-3762.
[267] A.G. Webb, Advances in Probe Design for Protein NMR, Annual Reports on NMR Spectroscopy, 58 (2006) 1-50.
[268] D.I. Hoult, R.E. Richards, The signal-to-noise ratio of the nuclear magnetic resonance experiment, Journal of Magnetic Resonance, 213 (2011) 329-343.
[269] H.C. Bertram, A. Malmendal, B.O. Petersen, J.C. Madsen, H. Pedersen, N.C. Nielsen, C. Hoppe, C. Mølgaard, K.F. Michaelsen, J.Ø. Duus, Effect of magnetic field strength on NMR-based metabonomic human urine data. comparative study of 250, 400, 500, and 800 MHz, Analytical Chemistry, 79 (2007) 7110-7115.
[270] E.D. Becker, A brief history of nuclear magnetic resonance, Analytical Chemistry, 65 (1993) 295-302.
[271] R. Freeman, G.A. Morris, The Varian story, Journal of Magnetic Resonance, 250 (2015) 80-84.
[272] K. Hashi, S. Ohki, S. Matsumoto, G. Nishijima, A. Goto, K. Deguchi, K. Yamada, T. Noguchi, S. Sakai, M. Takahashi, Y. Yanagisawa, S. Iguchi, T. Yamazaki, H. Maeda, R. Tanaka, T. Nemoto, H. Suematsu, T. Miki, K. Saito, T. Shimizu, Achievement of 1020MHz NMR, Journal of Magnetic Resonance, 256 (2015) 30-33.
[273] U.L. Günther, Dynamic nuclear hyperpolarization in liquids, in: H. Heise, S. Matthews (Eds.) Modern NMR methodology, Springer, Berlin, 2013, pp. 23.

[274] S. Odedra, S. Wimperis, Spin-locking of half-integer quadrupolar nuclei in NMR of solids: The far off-resonance case, Solid State Nuclear Magnetic Resonance, 84 (2017) 4-13.
[275] W.C. Liao, B. Ghaffari, C.P. Gordon, J. Xu, C. Copéret, Dynamic nuclear polarization surface enhanced NMR spectroscopy (DNP SENS): principles, protocols, and practice, Current Opinion in Colloid & Interface Science, 33 (2018) 63-71.
[276] J. van Bentum, B. van Meerten, M. Sharma, A. Kentgens, Perspectives on DNP-enhanced NMR spectroscopy in solutions, Journal of Magnetic Resonance, 264 (2016) 59-67.
[277] M. Mishkovsky, U. Eliav, G. Navon, L. Frydman, Nearly 10^6-fold enhancements in intermolecular ^{1}H double-quantum NMR experiments by nuclear hyperpolarization, Journal of Magnetic Resonance, 200 (2009) 142-146.
[278] T.D.W. Claridge, One-dimensional techniques, in: High-resolution NMR techniques in organic chemistry, Elsevier, Boston, 2016, pp. 133.
[279] N.K. Goto, K.H. Gardner, G.A. Mueller, R.C. Willis, L.E. Kay, A robust and cost-effective method for the production of Val, Leu, Ile (δ1) methyl-protonated ^{15}N-, ^{13}C-, ^{2}H-labeled proteins, Journal of Biomolecular NMR, 13 (1999) 369-374.
[280] M. Kainosho, T. Torizawa, Y. Iwashita, T. Terauchi, A. Mei Ono, P. Güntert, Optimal isotope labelling for NMR protein structure determinations, Nature, 440 (2006) 52-57.
[281] I. Solomon, Relaxation processes in a system of two spins, Physical Review, 99 (1955) 559-565.
[282] J.H. Ardenkjær-Larsen, B. Fridlund, A. Gram, G. Hansson, L. Hansson, M.H. Lerche, R. Servin, M. Thaning, K. Golman, Increase in signal-to-noise ratio of > 10,000 times in liquid-state NMR, Proceedings of the National Academy of Sciences, 100 (2003) 10158-10163.
[283] B. Wrackmeyer, O.L. Tok, M. Herberhold, ^{57}Fe NMR of ferrocenes by ^{1}H–^{57}Fe INEPT techniques, Organometallics, 20 (2001) 5774-5776.
[284] A. Tokatlı, A. Gençten, M. Şahin, Ö. Tezel, S. Bahçeli, Product operator descriptions of INEPT and RINEPT NMR spectroscopies for IS_n (I=1/2, S=3/2) spin systems, Journal of Magnetic Resonance, 169 (2004) 68-72.
[285] P. Nikolaou, A.M. Coffey, L.L. Walkup, B.M. Gust, N. Whiting, H. Newton, S. Barcus, I. Muradyan, M. Dabaghyan, G.D. Moroz, M.S. Rosen, S. Patz, M.J. Barlow, E.Y. Chekmenev, B.M. Goodson, Near-unity nuclear polarization with an open-source ^{129}Xe hyperpolarizer for NMR and MRI, Proceedings of the National Academy of Sciences, 110 (2013) 14150-14155.
[286] H.G. Fijolek, T.A. Oriskovich, A.J. Benesi, P. González-Duarte, M.J. Natan, Solid-state ^{109}Ag NMR: a sensitive environmental probe for silver thiolates, Inorganic Chemistry, 35 (1996) 797-799.
[287] A. Abragam, M. Goldman, Principles of dynamic nuclear polarisation, Reports on Progress in Physics, 41 (1978) 395-467.
[288] A.W. Overhauser, Polarization of nuclei in metals, Physical Review, 92 (1953) 411-415.
[289] T.R. Carver, C.P. Slichter, Polarization of nuclear spins in metals, Physical Review, 92 (1953) 212-213.
[290] K.H. Hausser, D. Stehlik, Dynamic nuclear polarization in liquids, Advances in Magnetic Resonance, 3 (1968) 79-139.
[291] C. Griesinger, M. Bennati, H.M. Vieth, C. Luchinat, G. Parigi, P. Höfer, F. Engelke, S.J. Glaser, V. Denysenkov, T.F. Prisner, Dynamic nuclear polarization at

high magnetic fields in liquids, Progress in Nuclear Magnetic Resonance Spectroscopy, 64 (2012) 4-28.
[292] N.M. Loening, M. Rosay, V. Weis, R.G. Griffin, Solution-state dynamic nuclear polarization at high magnetic field, Journal of the American Chemical Society, 124 (2002) 8808-8809.
[293] G. Liu, M. Levien, N. Karschin, G. Parigi, C. Luchinat, M. Bennati, One-thousand-fold enhancement of high field liquid nuclear magnetic resonance signals at room temperature, Nature Chemistry, 9 (2017) 676.
[294] R.G. Lawler, Chemically induced dynamic nuclear polarization, Journal of the American Chemical Society, 89 (1967) 5519-5521.
[295] T. Jonischkeit, K. Woelk, Hydrogen induced polarization–nuclear-spin hyperpolarization in catalytic hydrogenations without the enrichment of para- or orthohydrogen, Advanced Synthesis & Catalysis, 346 (2004) 960-969.
[296] P. György, S. Harald, Unprecedented carbon signal enhancement in liquid-state NMR spectroscopy, Angewandte Chemie International Edition, 56 (2017) 8332-8334.
[297] H.-U. Kauczor, R. Surkau, T. Roberts, MRI using hyperpolarized noble gases, European Radiology, 8 (1998) 820-827.
[298] J. Haupt, A new effect of dynamic polarization in a solid obtained by rapid change of temperature, Physics Letters A, 38 (1972) 389-390.
[299] L.R. Becerra, G.J. Gerfen, R.J. Temkin, D.J. Singel, R.G. Griffin, Dynamic nuclear polarization with a cyclotron resonance maser at 5 T, Physical Review Letters, 71 (1993) 3561-3564.
[300] E.A. Nanni, A.B. Barnes, R.G. Griffin, R.J. Temkin, THz dynamic nuclear polarization NMR, IEEE transactions on terahertz science and technology, 1 (2011) 145-163.
[301] R. Mukhopadhyay, Liquid NMR probes: oh so many choices, Analytical Chemistry, 79 (2007) 7959-7963.
[302] A.F. Privalov, O. Lips, Low-cost high-temperature NMR probe head, Applied Magnetic Resonance, 22 (2002) 597.
[303] D.I. Hoult, Fast recovery, high sensitivity NMR probe and preamplifier for low frequencies, Review of Scientific Instruments, 50 (1979) 193-200.
[304] F. Castiglione, A. Mele, G. Raos, ^{17}O NMR: A “rare and sensitive” probe of molecular interactions and dynamics, Annual reports on NMR spectroscopy, 85 (2015) 143.
[305] T.D.W. Claridge, Practical aspects of high-resolution NMR, in: High-resolution NMR techniques in organic chemistry Elsevier, Boston, 2016, pp. 61.
[306] H. Kovacs, D. Moskau, M. Spraul, Cryogenically cooled probes—a leap in NMR technology, Progress in Nuclear Magnetic Resonance Spectroscopy, 46 (2005) 131-155.
[307] P.F. Flynn, D.L. Mattiello, H.D.W. Hill, A.J. Wand, Optimal use of cryogenic probe technology in NMR studies of proteins, Journal of the American Chemical Society, 122 (2000) 4823-4824.
[308] D.J. Russell, C.E. Hadden, G.E. Martin, A.A. Gibson, A.P. Zens, J.L. Carolan, A comparison of inverse-detected heteronuclear NMR performance: conventional vs cryogenic microprobe performance, Journal of Natural Products, 63 (2000) 1047-1049.
[309] D. Rovnyak, J.C. Hoch, A.S. Stern, G. Wagner, Resolution and sensitivity of high field nuclear magnetic resonance spectroscopy, Journal of Biomolecular NMR, 30 (2004) 1-10.

[310] A.J. Charlton, J.A. Donarski, S.A. Jones, B.D. May, K.C. Thompson, The development of cryoprobe nuclear magnetic resonance spectroscopy for the rapid detection of organic contaminants in potable water, Journal of Environmental Monitoring, 8 (2006) 1106-1110.
[311] M. Sack, F. Wetterling, A. Sartorius, G. Ende, W. Weber-Fahr, Signal-to-noise ratio of a mouse brain ^{13}C cryoprobe system in comparison with room temperature coils: spectroscopic phantom and in vivo results, NMR Biomed, 27 (2014) 709-715.
[312] T.W.M. Fan, A.N. Lane, Applications of NMR spectroscopy to systems biochemistry, Progress in Nuclear Magnetic Resonance Spectroscopy, 92–93 (2016) 18-53.
[313] J. Paff, R. Freeman, B. Blumich, Reduction of systematic noise in stochastic-excitation NMR by oversampling, Journal of Magnetic Resonance, Series A, 102 (1993) 332-343.
[314] M.A. Delsuc, J.Y. Lallemand, Improvement of dynamic range in NMR by oversampling, Journal of Magnetic Resonance (1969), 69 (1986) 504-507.
[315] R.A. Beckman, E.R.P. Zuiderweg, Guidelines for the use of oversampling in protein NMR, Journal of Magnetic Resonance, Series A, 113 (1995) 223-231.
[316] J.B. Poullet, D.M. Sima, S. Van Huffel, MRS signal quantitation: a review of time- and frequency-domain methods, Journal of Magnetic Resonance, 195 (2008) 134-144.
[317] P. Stoica, T. Sundin, Nonparametric NMR spectroscopy, Journal of Magnetic Resonance, 152 (2001) 57-69.
[318] N. Sandgren, Y. Selén, P. Stoica, J. Li, Parametric methods for frequency-selective MR spectroscopy—a review, Journal of Magnetic Resonance, 168 (2004) 259-272.
[319] J.J. Led, H. Gesmar, Application of the linear prediction method to NMR spectroscopy, Chemical Reviews, 91 (1991) 1413-1426.
[320] D.W. Tufts, R.J. Vacarro, A.C. Kot, Analysis of Estimation of Signal Parameters by Linear-Prediction at High SNR Using Matrix Approximation, 4 (1989) 2194-2197.
[321] E. Bartholdi, R.R. Ernst, Fourier spectroscopy and the causality principle, Journal of Magnetic Resonance (1969), 11 (1973) 9-19.
[322] A. Ebel, W. Dreher, D. Leibfritz, Effects of zero-filling and apodization on spectral integrals in discrete Fourier-transform spectroscopy of noisy data, Journal of Magnetic Resonance, 182 (2006) 330-338.
[323] D.D. Traficante, M. Rajabzadeh, Optimum window function for sensitivity enhancement of NMR signals, Concepts in Magnetic Resonance, 12 (2000) 83-101.
[324] D.D. Traficante, D. Ziessow, A new apodization function for resolution enhancement with a minimum loss of sensitivity, Journal of Magnetic Resonance (1969), 66 (1986) 182-186.
[325] Y.Y. Lin, L.P. Hwang, NMR signal enhancement based on matrix property mappings, Journal of Magnetic Resonance Series A, 103 (1993) 109-114.
[326] W. Dreher, P. Börnert, D. Leibfritz, Signal-dependent preprocessing of NMR data using the constrained least-square method, Journal of Magnetic Resonance (1969), 97 (1992) 376-381.
[327] R.G. Spencer, The time-domain matched filter and the spectral-domain matched filter in 1-dimensional NMR spectroscopy, Concepts in magnetic resonance. Part A, Bridging education and research, 36A (2010) 255-264.
[328] W.D. Van Horn, A.J. Beel, C. Kang, C.R. Sanders, The impact of window functions on NMR-based paramagnetic relaxation enhancement measurements in

membrane proteins, Biochimica et Biophysica Acta (BBA) - Bioenergetics, 1798 (2010) 140-149.
[329] S. Tiziani, A. Lodi, C. Ludwig, H.M. Parsons, M.R. Viant, Effects of the application of different window functions and projection methods on processing of ^{1}H *J*-resolved nuclear magnetic resonance spectra for metabolomics, Analytica Chimica Acta, 610 (2008) 80-88.
[330] W.D. Keller, T.R. Lusebrink, C.H. Sederholm, NMR spectrum of 3‐chlorothietane, an example of complete NMR spectral analysis by computer techniques, The Journal of Chemical Physics, 44 (1966) 782-793.
[331] R.R. Ernst, R. Freeman, B. Gestblom, T.R. Lusebrink, Detection of very small N.M.R. spin coupling constants by resolution enhancement, Molecular Physics, 13 (1967) 283-285.
[332] E. Parvaneh, N. Mathias, M.G. A., J.H. M., E.S. B., Cleaning up NMR spectra with reference deconvolution for improving multivariate analysis of complex mixture spectra, Journal of Chemometrics, 28 (2014) 656-662.
[333] G.A. Morris, H. Barjat, T.J. Home, Reference deconvolution methods, Progress in Nuclear Magnetic Resonance Spectroscopy, 31 (1997) 197-257.
[334] M. Goez, R. Heun, Reference deconvolution in the frequency domain, Journal of Magnetic Resonance, 136 (1999) 69-75.
[335] R. Huo, R. Wehrens, L.M.C. Buydens, Improved DOSY NMR data processing by data enhancement and combination of multivariate curve resolution with non-linear least square fitting, Journal of Magnetic Resonance, 169 (2004) 257-269.
[336] H. Barjat, G.A. Morris, A.G. Swanson, S. Smart, S.C.R. Williams, Reference deconvolution using multiplet reference signals, Journal of Magnetic Resonance, Series A, 116 (1995) 206-214.
[337] A. Gibbs, G.A. Morris, Reference deconvolution. Elimination of distortions arising from reference line truncation, Journal of Magnetic Resonance (1969), 91 (1991) 77-83.
[338] C. He, J. Xing, J. Li, Q. Yang, R. Wang, A new wavelet threshold determination method considering interscale correlation in signal denoising, Mathematical Problems in Engineering, 2015 (2015) 9.
[339] X. Ge, Y. Fan, J. Li, Y. Wang, S. Deng, Noise reduction of nuclear magnetic resonance (NMR) transversal data using improved wavelet transform and exponentially weighted moving average (EWMA), Journal of Magnetic Resonance, 251 (2015) 71-83.
[340] Z. Liu, A. Abbas, B.-Y. Jing, X. Gao, WaVPeak: picking NMR peaks through wavelet-based smoothing and volume-based filtering, Bioinformatics, 28 (2012) 914-920.
[341] D.L. Donoho, I.M. Johnstone, G. Kerkyacharian, D. Picard, Wavelet shrinkage: asymptopia?, Journal of the Royal Statistical Society. Series B (Methodological), 57 (1995) 301-369.
[342] L. Castañar, G.D. Poggetto, A.A. Colbourne, G.A. Morris, M. Nilsson, The GNAT: A new tool for processing NMR data, Magnetic Resonance in Chemistry, 56 (2018) 546-558.
[343] M. Urbańczyk, D. Bernin, W. Koźmiński, K. Kazimierczuk, Iterative thresholding algorithm for multiexponential decay applied to PGSE NMR data, Analytical Chemistry, 85 (2013) 1828-1833.
[344] G. Zhu, Y. Hua, Quantitative NMR signal analysis by an iterative quadratic maximum likelihood method, Chemical Physics Letters, 264 (1997) 424-428.

[345] J.C. Hoch, A.S. Stern, Maximum entropy reconstruction, eMagRes, (2007) 1-9.
[346] L.C.M. Van Gorkom, T.M. Hancewicz, Analysis of DOSY and GPC-NMR experiments on polymers by multivariate curve resolution, Journal of Magnetic Resonance, 130 (1998) 125-130.
[347] A. Chen, D. Wu, C.S. Johnson, Determination of molecular weight distributions for polymers by diffusion-ordered NMR, Journal of the American Chemical Society, 117 (1995) 7965-7970.
[348] J. Viéville, M. Tanty, M.-A. Delsuc, Polydispersity index of polymers revealed by DOSY NMR, Journal of Magnetic Resonance, 212 (2011) 169-173.
[349] A. Jerschow, N. Müller, Diffusion-separated nuclear magnetic resonance spectroscopy of polymer mixtures, Macromolecules, 31 (1998) 6573-6578.
[350] P. Groves, Diffusion ordered spectroscopy (DOSY) as applied to polymers, Polymer Chemistry, 8 (2017) 6700-6708.
[351] C.S. Johnson, Diffusion ordered nuclear magnetic resonance spectroscopy: principles and applications, Progress in Nuclear Magnetic Resonance Spectroscopy, 34 (1999) 203-256.
[352] S.W. Provencher, CONTIN: A general purpose constrained regularization program for inverting noisy linear algebraic and integral equations, Computer Physics Communications, 27 (1982) 229-242.
[353] S.W. Provencher, A constrained regularization method for inverting data represented by linear algebraic or integral equations, Computer Physics Communications, 27 (1982) 213-227.
[354] W. Windig, B. Antalek, Direct exponential curve resolution algorithm (DECRA): a novel application of the generalized rank annihilation method for a single spectral mixture data set with exponentially decaying contribution profiles, Chemometrics and Intelligent Laboratory Systems, 37 (1997) 241-254.
[355] R. Huo, R. Wehrens, J.v. Duynhoven, L.M.C. Buydens, Assessment of techniques for DOSY NMR data processing, Analytica Chimica Acta, 490 (2003) 231-251.
[356] M. Nilsson, The DOSY Toolbox: A new tool for processing PFG NMR diffusion data, Journal of Magnetic Resonance, 200 (2009) 296-302.
[357] B. Antalek, W. Windig, Generalized rank annihilation method applied to a single multicomponentpPulsed gradient spin echo NMR data set, Journal of the American Chemical Society, 118 (1996) 10331-10332.
[358] N.M. Faber, L.M.C. Buydens, G. Kateman, Generalized rank annihilation method. I: Derivation of eigenvalue problems, Journal of Chemometrics, 8 (1994) 147-154.
[359] B. Antalek, J.M. Hewitt, W. Windig, P.D. Yacobucci, T. Mourey, K. Le, The use of PGSE NMR and DECRA for determining polymer composition, Magnetic Resonance in Chemistry, 40 (2002) S60-S71.
[360] T.M. Alam, M.K. Alam, Effect of non-exponential and multi-exponential decay behavior on the performance of the direct exponential curve resolution algorithm (DECRA) in NMR investigations, Journal of Chemometrics, 17 (2003) 583-593.
[361] D.A. Bini, F. Di Benedetto, Toeplitz matrices: Structures, algorithms and applications, CALCOLO, 33 (1996) 1-10.
[362] U. Grenander, G. Szegö, Toeplitz forms and their applications, University of California Press, Berkeley, 1958.
[363] L.D. Pustyl'nikov, Toeplitz and Hankel matrices and their applications, Russian Matematical Surveys, 39 (1984) 63-98.

[364] G. Strang, A proposal for toeplitz matrix calculations, Studies in Applied Mathematics, 74 (1986) 171-176.
[365] B. Silbermann, On the limiting set of singular values of Toeplitz matrices, Linear Algebra and its Applications, 182 (1993) 35-43.
[366] G.H. Golub, C. Reinsch, Singular value decomposition and least squares solutions, Numerische Mathematik, 14 (1970) 403-420.
[367] G.H. Golub, C.F.V. Loan, Matrix computations, 3 ed., Johns Hopkins University Press, Baltimore, 1996.
[368] S. Weiland, F. van Belzen, Singular value decompositions and low rank approximations of tensors, IEEE Transactions on Signal Processing, 58 (2010) 1171-1182.
[369] T. Oh, Y. Matsushita, Y. Tai, I.S. Kweon, Fast randomized singular value thresholding for low-rank optimization, IEEE Transactions on Pattern Analysis and Machine Intelligence, 40 (2018) 376-391.
[370] K. Shin, S.A. Feraday, C.J. Harris, M.J. Brennan, J.E. Oh, Optimal autoregressive modelling of a measured noisy deterministic signal using singular-value decomposition, Mechanical Systems and Signal Processing, 17 (2003) 423-432.
[371] G. Zeng, Facial recognition with singular value decomposition, in: K. Elleithy (Ed.) Advances and innovations in systems, computing sciences and software engineering, Springer Dordrecht, Netherlands, 2007, pp. 145-148.
[372] F.W. Mauldin, D. Lin, J.A. Hossack, The singular value filter: A general filter design strategy for PCA-based signal separation in medical ultrasound imaging, Ieee Transactions on Medical Imaging, 30 (2011) 1951-1964.
[373] S. Padhy, L.N. Sharma, S. Dandapat, Multilead ECG data compression using SVD in multiresolution domain, Biomedical Signal Processing and Control, 23 (2016) 10-18.
[374] A.G. Akritas, G.I. Malaschonok, Applications of singular-value decomposition (SVD), Mathematics and Computers in Simulation, 67 (2004) 15-31.
[375] S. Majumder, C.M. DeMott, D.S. Burz, A. Shekhtman, Using singular value decomposition to characterize protein–protein interactions by in-cell NMR spectroscopy, A European Journal of Chemical Biology, 15 (2014) 929-933.
[376] S.E. Fotinea, I. Dologlou, G. Carayannis, Decimation and SVD to estimate exponentially damped sinusoids in the presence of noise, in: Acoustics, Speech, and Signal Processing, 2001. Proceedings. (ICASSP '01). 2001 IEEE International Conference on, 2001, pp. 3073-3076 vol.3075.
[377] G.W. Stewart, On the early history of the singular value decomposition, SIAM Review, 35 (1993) 551-566.
[378] H. Barkhuijsen, R. de Beer, D. van Ormondt, Error theory for time-domain signal analysis with linear prediction and singular value decomposition, Journal of Magnetic Resonance (1969), 67 (1986) 371-375.
[379] S.Y. Kung, K.S. Arun, D.V.B. Rao, State-space and singular-value decomposition-based approximation methods for the harmonic retrieval problem, J. Opt. Soc. Am., 73 (1983) 1799-1811.
[380] H.V. Henderson, S.R. Searle, On deriving the inverse of a sum of matrices, SIAM Review, 23 (1981) 53-60.
[381] H. Barkhuijsen, R. de Beer, D. van Ormondt, Improved algorithm for noniterative time-domain model fitting to exponentially damped magnetic resonance signals, Journal of Magnetic Resonance (1969), 73 (1987) 553-557.

[382] H. Yan, Signal Processing for Magnetic Resonance Imaging and Spectroscopy, CRC Press, New York, 2002.
[383] V.A. Mandelshtam, H.S. Taylor, A.J. Shaka, Application of the filter diagonalization method to one- and two-dimensional NMR spectra, Journal of Magnetic Resonance, 133 (1998) 304-312.
[384] J.W. Pang, T. Dieckmann, J. Feigon, D. Neuhauser, Extraction of spectral information from a short-time signal using filter-diagonalization: Recent developments and applications to semiclassical reaction dynamics and nuclear magnetic resonance signals, The Journal of Chemical Physics, 108 (1998) 8360-8368.
[385] V.A. Mandelshtam, The multidimensional filter diagonalization method: I. theory and numerical implementation, Journal of Magnetic Resonance, 144 (2000) 343-356.
[386] C.D. Ridge, A.J. Shaka, "Ersatz" and "Hybrid" NMR spectral estimates using the filter diagonalization method, The Journal of Physical Chemistry A, 113 (2009) 2036-2045.
[387] V. A. Mandelshtam, H. Taylor, Multidimensional harmonic inversion by filter-diagonalization, 1998.
[388] C. Eckart, G. Young, The approximation of one matrix by another of lower rank, Psychometrika, 1 (1936) 211-218.
[389] B.N. Mukherjee, S.S. Maiti, On some properties of positive definite toeplitz matrices and their possible applications, Linear Algebra and its Applications, 102 (1988) 211-240.
[390] W.F. Trench, On the eigenvalue problem for Toeplitz band matrices, Linear Algebra and its Applications, 64 (1985) 199-214.
[391] J. Makhoul, On the eigenvectors of symmetric Toeplitz matrices, IEEE Transactions on Acoustics, Speech, and Signal Processing, 29 (1981) 868-872.
[392] A. A. Shah, D. W. Tufts, Estimation of the signal component of a data vector, in: Proc. IEEE Int. Conf. Acoust. Speech. Signal Process., IEEE, San Francisco, 1992, pp. 393-396.
[393] E. Biglieri, K. Yao, Some properties of singular value decomposition and their applications to digital signal processing, Signal Processing, 18 (1989) 277-289.
[394] V.A. Mandelshtam, H.S. Taylor, Erratum: "Harmonic inversion of time signals and its applications" [J. Chem. Phys. 107, 6756 (1997)], The Journal of Chemical Physics, 109 (1998) 4128-4128.
[395] A. Zhigljavsky, Singular spectrum analysis for time series: introduction to this special issue, Statistics and Its Interface, 3 (2010) 255-258.
[396] N. Golyandina, V. Viktorovich Nekrutkin, A. Zhigljavsky, Analysis of Time Series Structure: SSA and Related Techniques, 1st ed., Taylor & Francis New York, 2001.
[397] I. Markovsky, Bibliography on total least squares and related methods, Statistics and Its Interface, 3 (2010) 329-334.
[398] R. Ghanati, M. Kazem Hafizi, R. Mahmoudvand, M. Fallahsafari, Filtering and parameter estimation of surface-NMR data using singular spectrum analysis, Journal of Applied Geophysics, 130 (2016) 118-130.
[399] N. Golyandina, On the choice of parameters in singular spectrum analysis and related subspace-based methods, Statistics and Its Interface, 3 (2010) 259-279.
[400] G. Golub, Numerical methods for solving linear least squares problems, Numerische Mathematik, 7 (1965) 206-216.

[401] G.H. Golub, C.F. Van Loan, Matrix Computations, 3rd ed., Johns Hopkins University Press, 2013.
[402] V. Rokhlin, A. Szlam, M. Tygert, A randomized algorithm for principal component analysis, SIAM Journal on Matrix Analysis and Applications, 31 (2009) 1100-1124.
[403] H. Gillard, Cadzow's basic algorithm, alternating projections and singular spectrum analysis, Statistics and Its Interface, 3 (2010) 335-343.
[404] M.P. Nicholas, E. Eryilmaz, F. Ferrage, D. Cowburn, R. Ghose, Nuclear spin relaxation in isotropic and anisotropic media, Progress in Nuclear Magnetic Resonance Spectroscopy, 57 (2010) 111-158.
[405] C. Cobas, Applications of the Whittaker smoother in NMR spectroscopy, Magn Reson Chem, 56 (2018) 1140-1148.
[406] H. Azami, M. Saraf, K. Mohammadi, A new signal segmentation approach based on singular value decomposition and intelligent Savitzky-Golay filter, in, Springer International Publishing, Cham, 2014, pp. 212-224.
[407] A. Savitzky, M.J.E. Golay, Smoothing and differentiation of data by simplified least squares procedures, Analytical Chemistry, 36 (1964) 1627-1639.
[408] J. Carlos Cobas, M.A. Bernstein, M. Martín-Pastor, P.G. Tahoces, A new general-purpose fully automatic baseline-correction procedure for 1D and 2D NMR data, Journal of Magnetic Resonance, 183 (2006) 145-151.
[409] W.H. Press, S.A. Teukolsky, Savitzky‐Golay smoothing filters, Computers in Physics, 4 (1990) 669-672.
[410] G. Vivó-Truyols, P.J. Schoenmakers, Automatic Selection of Optimal Savitzky−Golay Smoothing, Analytical Chemistry, 78 (2006) 4598-4608.
[411] M.U.A. Bromba, H. Ziegler, Application hints for Savitzky-Golay digital smoothing filters, Analytical Chemistry, 53 (1981) 1583-1586.
[412] B.C.H. Turton, A novel variant of the Savitzky-Golay filter for spectroscopic applications, Measurement Science and Technology, 3 (1992) 858-863.
[413] S.J. Orfanidis, Introduction to Signal Processing, Prentice Hall, Englewood Cliffs, NJ, 1996.
[414] J. Guiñón, E. Ortega, J. García-Antón, V. Pérez-Herranz, Moving average and Savitzki-Golay smoothing filters using Mathcad, 2007.
[415] S.J. Opella, F.M. Marassi, Applications of NMR to membrane proteins, Archives of Biochemistry and Biophysics, 628 (2017) 92-101.
[416] T.S. Derrick, E.F. McCord, C.K. Larive, Analysis of protein/ligand interactions with NMR diffusion measurements: the importance of eliminating the protein background, Journal of Magnetic Resonance, 155 (2002) 217-225.
[417] A.-H.M. Emwas, J.S. Merzaban, H. Serrai, Theory and applications of NMR-based metabolomics in human disease diagnosis, in: A. ur-Rahman, M.I. Choudhary (Eds.) Applications of NMR spectroscopy, Bentham Science Publishers, London, 2015, pp. 93-130.
[418] A.H. Kwan, M. Mobli, P.R. Gooley, G.F. King, J.P. Mackay, Macromolecular NMR spectroscopy for the non-spectroscopist, The FEBS Journal, 278 (2011) 687-703.
[419] F. Rastrelli, S. Jha, F. Mancin, Seeing through macromolecules: T_2-filtered NMR for the purity assay of functionalized nanosystems and the screening of biofluids, Journal of the American Chemical Society, 131 (2009) 14222-14224.
[420] G. Zheng, W.S. Price, Solvent signal suppression in NMR, Progress in Nuclear Magnetic Resonance Spectroscopy, 56 (2010) 267-288.

[421] W.S. Price, NMR gradient methods in the study of proteins, Annual Reports Section "C" (Physical Chemistry), 96 (2000) 3-53.
[422] D.L. Rabenstein, T. Nakashima, G. Bigam, A pulse sequence for the measurement of spin-lattice relaxation times of small molecules in protein solutions, Journal of Magnetic Resonance (1969), 34 (1979) 669-674.
[423] L.F. Pinto, J. Correa, L. Zhao, R. Riguera, E. Fernandez-Megia, Fast NMR screening of macromolecular complexes by a paramagnetic spin relaxation filter, ACS Omega, 3 (2018) 2974-2983.
[424] Emmanuel J. Candes, Carlos A. Sing-Long, Joshua D. Trzasko, Unbiased risk estimates for singular value thresholding and spectral estimators, IEEE Transactions on Signal Processing, 61 (2013) 4643-4657.
[425] H. Hu, Q.N. Van, V.A. Mandelshtam, A.J. Shaka, Reference deconvolution, phase correction, and line listing of NMR spectra by the 1D filter diagonalization method, Journal of Magnetic Resonance, 134 (1998) 76-87.
[426] B.I. Ionin, B.A. Ershov, NMR spectroscopy in organic chemistry, Springer, Boston, MA, 1970.
[427] A.-H. Emwas, E. Saccenti, X. Gao, R.T. McKay, V.A.P.M. Dos Santos, R. Roy, D.S. Wishart, Recommended strategies for spectral processing and post-processing of 1D ^{1}H-NMR data of biofluids with a particular focus on urine, Metabolomics, 14 (2018) 31-31.
[428] Y. Selen, P. Stoica, N. Sandgren, S.v. Huffel, Using prior knowledge in SVD-based NMR spectroscopy - the ATP example, in: Seventh International Symposium on Signal Processing and Its Applications, 2003. Proceedings., 2003, pp. 33-36 vol.32.
[429] S. Van Huffel, R. de Beer, D. van Ormondt, Advanced time-domain quantitation methods for MR spectroscopy and metabolite imaging, in: Engineering in Medicine and Biology Society, 1996. Bridging Disciplines for Biomedicine. Proceedings of the 18th Annual International Conference of the IEEE, 1996, pp. 2124-2126 vol.2125.
[430] C. Decanniere, P. Vanhecke, F. Vanstapel, H. Chen, S. Vanhuffel, C. Vandervoort, B. Vantongeren, D. Vanormondt, Evaluation of signal processing methods for the quantification of strongly overlapping peaks in ^{31}P NMR spectra, Journal of Magnetic Resonance, Series B, 105 (1994) 31-37.
[431] A.A. De Graaf, W.M.M.J. Bovée, Improved quantification of in vivo1H NMR spectra by optimization of signal acquisition and processing and by incorporation of prior knowledge into the spectral fitting, Magnetic Resonance in Medicine, 15 (1990) 305-319.
[432] E. Aboutanios, D.S. Thomas, J.M. Hook, C. Cobas, LocMAP: A new localization method for the parametric processing of high resolution NMR data, Journal of Magnetic Resonance, 282 (2017) 62-70.
[433] G. Schwarz, Estimating the dimension of a model, The Annals of Statistics, 6 (1978) 461-464.
[434] J. Rissanen, Modeling by shortest data description, Automatica, 14 (1978) 465-471.
[435] H. Akaike, A new look at the statistical model identification, IEEE Transactions on Automatic Control, 19 (1974) 716-723.
[436] M. Wax, T. Kailath, Detection of signals by information theoretic criteria, IEEE Transactions on Acoustics, Speech, and Signal Processing, 33 (1985) 387-392.

APPENDICES

APPENDIX A: THRESHOLD DETERMINATION MATHCAD PROGRAM

Import spectral data from the txt file as data:

$$data := \blacksquare$$

Define the frequency range (min_w, max_w) and a number of data points (N) from the data:

$$min\_w := \blacksquare$$

$$max\_w := \blacksquare$$

$$N := rows(data) - 10$$

Note: Exported Topspin data in the text file is formatted in a way that first 9 rows are filled with the information of the data set.

Extract spectral data:

$$Original\_Spec := submatrix(data, 10, rows(data) - 1, 0, 0)$$

Create a frequency scale:

$$\text{original\_ppm} := \left| \begin{array}{l} \text{for } i \in 0..N-1 \\ \quad \text{original\_ppm}_{i,0} \leftarrow \text{min\_w} - \frac{\text{min\_w} - \text{max\_w}}{N-1} i \\ \text{original\_ppm} \end{array} \right.$$

Take inverse Fourier transform to obtain FID:

$$\text{Original\_FID} := \text{ICFFT}(\text{Original\_Spec})$$

Creating the time scale in second:

$$AQ := \blacksquare$$

$$\text{original\_time} := \left| \begin{array}{l} \text{for } i \in 0..N-1 \\ \quad \text{original\_time}_{i,0} \leftarrow \frac{AQ}{N-1} i \\ \text{original\_time} \end{array} \right.$$

Plot both spectrum and FID

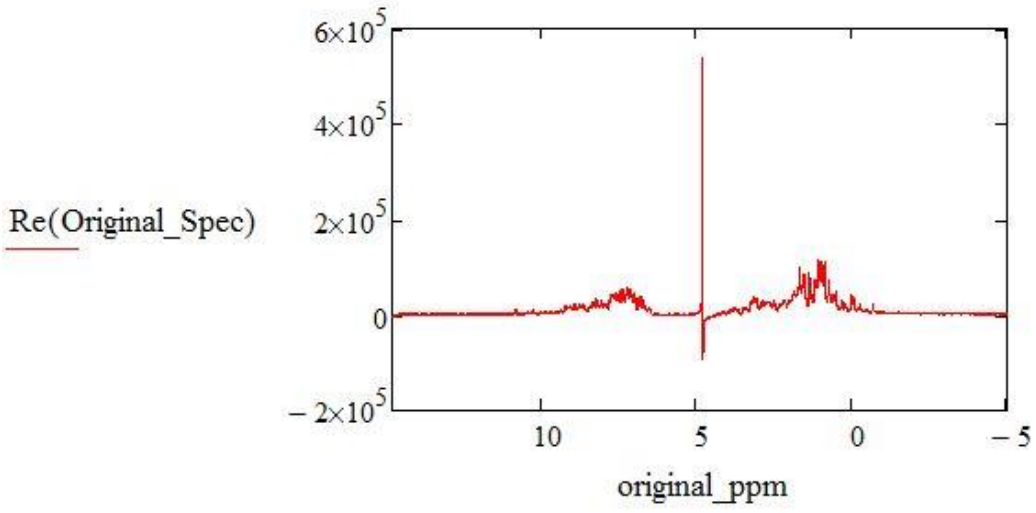

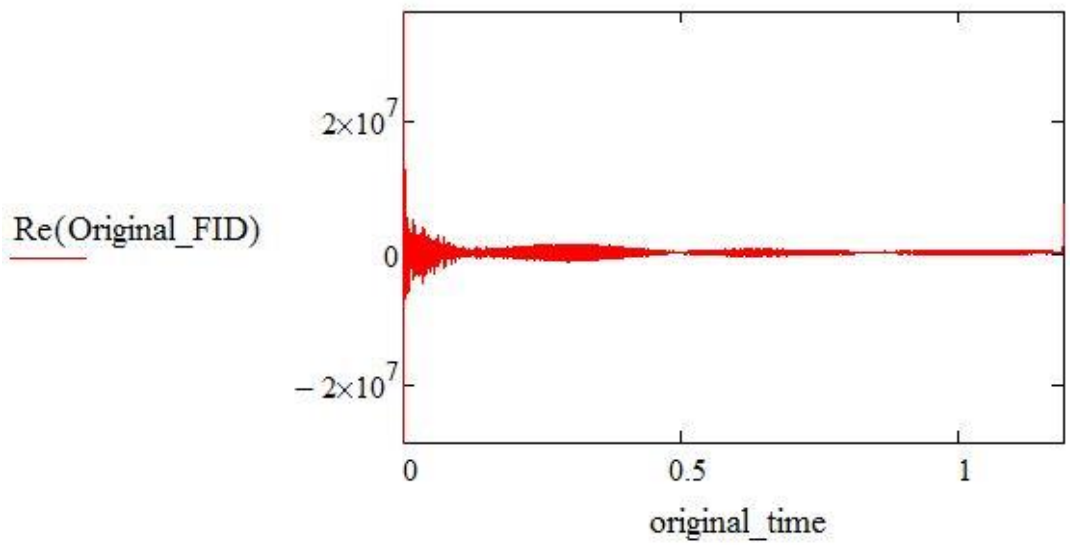

Define Toeplitz matrix size

$$Matrix\_size := 10$$

Column number (L1)

$$L1 := floor\left[\frac{(N)}{Matrix\_size}\right] - 1$$

Row number (M1)

$$M1 := N - L1 + 1$$

Formatting FID into Toeplitz matrix

$$\text{Toeplitz\_FID} := \left| \begin{array}{l} \text{for } i0 \in 0..L1-1 \\ \quad \text{for } j0 \in 0..M1-1 \\ \quad\quad X_{i0,j0} \leftarrow \text{Original\_FID}_{j0+i0} \\ \text{if } L1 \le M1 \\ \quad \left| \begin{array}{l} X1 \leftarrow X^T \\ \text{for } i \in 0..M1-1 \\ \quad \text{for } j \in 0..L1-1 \\ \quad\quad X2_{i,j} \leftarrow X1_{i,L1-1-j} \end{array} \right. \\ \text{otherwise} \\ \quad \left| \begin{array}{l} X1 \leftarrow X \\ \text{for } i \in 0..L1-1 \\ \quad \text{for } j \in 0..M1-1 \\ \quad\quad X2_{i,j} \leftarrow X1_{i,M1-1-j} \end{array} \right. \\ \text{Toeplitz\_FID} \leftarrow X2 \end{array} \right.$$

Singular value decomposition of Toeplitz_FID

$$SVD := \text{svd2}(\text{Toeplitz\_FID})$$

Define each submatrix

$$U := SVD_{1,} \qquad \Sigma := SVD_{0,} \qquad Vt := SVD_2$$

Create singular_value_index in order to plot singular values

$$\text{singular\_value\_index} := \left| \begin{array}{l} \text{for } i \in 0..L1-1 \\ \quad \text{singular\_value\_index}_{i,0} \leftarrow i \\ \text{singular\_value\_index} \end{array} \right.$$

Plot the singular values

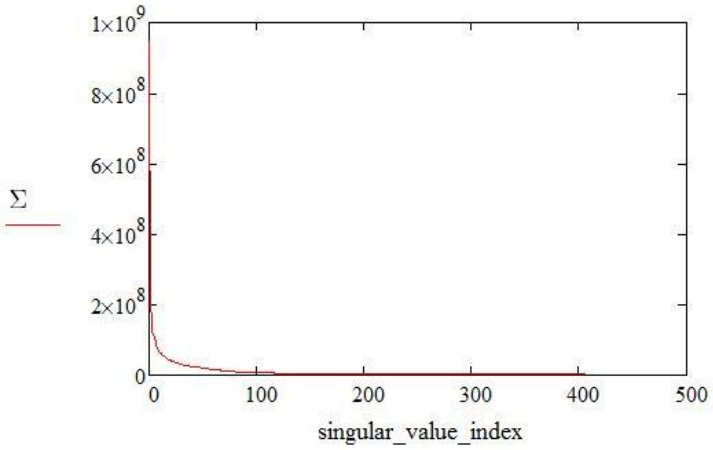

Create a singular value ratio

$$\text{singular\_value\_ratio} := \left| \begin{array}{l} \text{for } i \in 0 .. L1 - 1 \\ \quad \text{singular\_value\_ratio}_{i,0} \leftarrow \dfrac{\Sigma_{0,0}}{\Sigma_{i,0}} \\ \text{singular\_value\_ratio} \end{array} \right.$$

Plot the singular value ratio

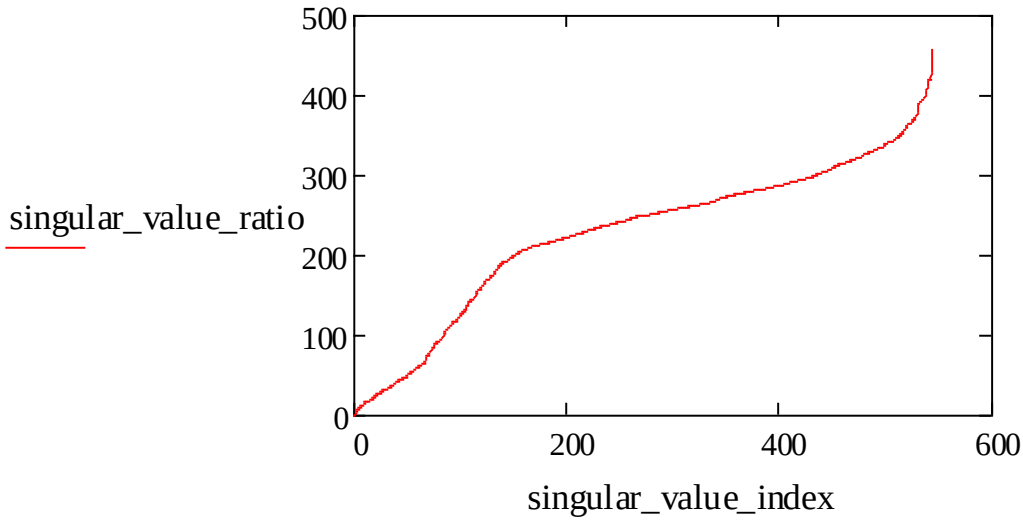

Select the region for the steepest slope:

region_1_start := region_1_end :=

Select the region for the following slope:

region_2_start := region_2_end :=

Extract the data of the steepest slope region 1 (R1) and the following slope region 2 (R2)

$$R1 := \text{submatrix}(\text{singular\_value\_ratio}, \text{region\_1\_start}, \text{region\_1\_end}, 0, 0)$$

$$R2 := \text{submatrix}(\text{singular\_value\_ratio}, \text{region\_2\_start}, \text{region\_2\_end}, 0, 0)$$

Format each region data set into a column vector R1, R2 and create the corresponding index column vector X1, X2 respectively.

$$
\begin{aligned}
R1 := \;& r1s \leftarrow region\_1\_start \\
& r1e \leftarrow region\_1\_end \\
& \text{for } i \in 0..(r1e - r1s) \\
& \quad R1_{i,0} \leftarrow singular\_value\_ratio_{r1s+i,0} \\
& R1
\end{aligned}
$$

$$
\begin{aligned}
X1 := \;& \text{for } i \in 0..(region\_1\_end - region\_1\_start) \\
& \quad X1_{i,0} \leftarrow i + region\_1\_start \\
& X1
\end{aligned}
$$

$$
\begin{aligned}
R2 := \;& r2s \leftarrow region\_2\_start \\
& r2e \leftarrow region\_2\_end \\
& \text{for } i \in 0..(r2e - r2s) \\
& \quad R2_{i,0} \leftarrow singular\_value\_ratio_{r2s+i,0} \\
& R2
\end{aligned}
$$

$$
\begin{aligned}
X2 := \;& \text{for } i \in 0..(region\_2\_end - region\_2\_start) \\
& \quad X2_{i,0} \leftarrow i + region\_2\_start \\
& X2
\end{aligned}
$$

Create a new fitted linear function F(r)and finding the parameter for the new fitted linear function $\mathbf{F(r)} = \boldsymbol{a} \times \boldsymbol{r} + \boldsymbol{b}$. Solving the equation below to find the value r:

$$F(r) := \begin{pmatrix} r \\ 1 \end{pmatrix} \qquad S1 := linfit(X1, R1, F)$$

$$S2 := linfit(X2, R2, F)$$

$$S1 = \begin{pmatrix} a1 \\ b1 \end{pmatrix}, \qquad S2 = \begin{pmatrix} a2 \\ b2 \end{pmatrix}$$

$$a1 \times r + b1 = a2 \times r + b2$$

The value r is the soft threshold value for the Toeplitz_ FID. Let r ≔ initial_peak, reduced ranked new_Σ will be formed as

$$
\begin{aligned}
\text{new\_}\Sigma \;:=\; & \text{for } i \in 0 .. \text{initial\_peak} \\
& \quad \text{for } j \in \text{initial\_peak} + 1 .. L1 - 1 \\
& \qquad \text{new\_}\Sigma_{i,0} \leftarrow \Sigma_{i,0} \\
& \qquad \text{new\_}\Sigma_{j,0} \leftarrow 0 \\
& \text{new\_}\Sigma
\end{aligned}
$$

Re-assemble together with U and Vt submatrices.

$$\text{new\_matrix} := U \cdot \text{diag}(\text{new\_}\Sigma) \cdot Vt$$

Since_new_matrix is not in the Toeplitz form, average of the subdiagonal elements are taken then reformatted into a one column vector (new_FID).

new_FID :=

$r \leftarrow rows(new\_matrix)$

$c \leftarrow cols(new\_matrix)$

$rc \leftarrow r - c$

for $i \in 0 .. c - 1$

$C_{0,i} \leftarrow submatrix(new\_matrix, 0, i, c - 1 - i, c - 1)$

$C2_{0,i} \leftarrow \frac{tr(C_{0,i})}{cols(C_{0,i})}$

$C2$

for $j \in 1 .. rc$

$D_{j,0} \leftarrow (submatrix(new\_matrix, j, j + c - 1, 0, c - 1))$

$D2_{j,0} \leftarrow \frac{tr(D_{j,0})}{c}$

$D2 \leftarrow submatrix(D2, 1, last(D2), 0, 0)$

for $k \in 0 .. c - 1$

$E_{k,k} \leftarrow submatrix(new\_matrix, rc, rc + k, c - 1 - k, c - 1)$

$E1 \leftarrow E_{k,k}^{T}$

$e \leftarrow cols(E1) - 1$

for $m \in 0 .. e$

$E2_{0,m} \leftarrow submatrix(E1, 0, m, e - m, e)$

$E3_{0,m} \leftarrow \frac{tr(E2_{0,m})}{cols(E2_{0,m})}$

$E4 \leftarrow E3^{T}$

for $n \in 0 .. rows(E4) - 1$

$E5_{n,0} \leftarrow E4_{rows(E4)-1-n,0}$

$E5 \leftarrow submatrix(E5, 1, last(E5), 0, 0)$

$new\_FID \leftarrow stack(C2^{T}, D2, E5)$

Take an FT of the new_FID to observe the results

new_FT := Re(CFFT(new_FID))

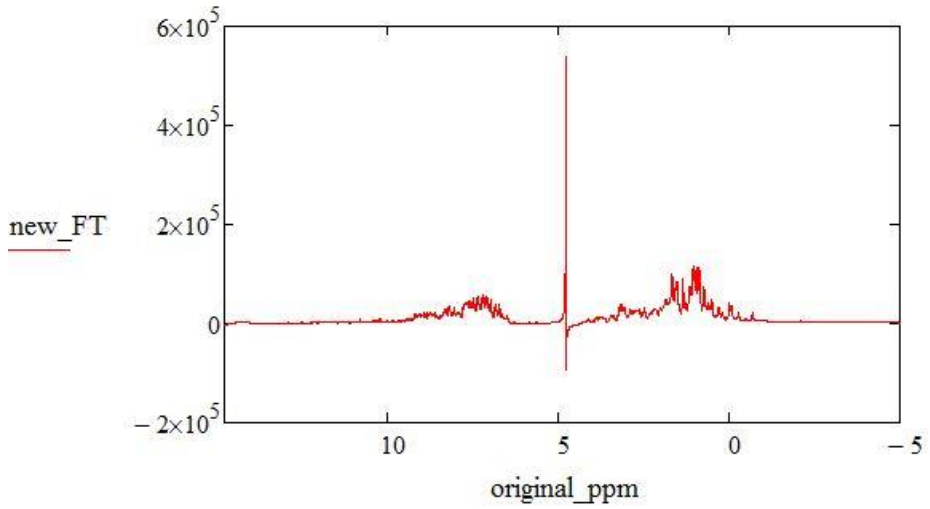

Iterate the process reducing the rank of the matrix until reach minimum = no dispersion noise peaks to be observed.

■

APPENDIX B: MATRIX SIZE, COMPUTATIONAL TIME, AND PROCESSED RESULTS

Throughout this thesis, the column length of the Toeplitz matrix used for composite property mapping was equal to one-tenth of the total data points. In this appendix, the reason why this ratio was chosen is presented using simulated data. Since the matrix dimension has to be overdetermined (rows > columns) in the matrix decomposition for signal processing, the length of the columns are defined first. To define the length of the column, the floor of the total number of data points divided by the term named "matrix size" was calculated. For example, if the matrix size is equal to 2 then the constructed matrix has a square or almost square matrix. The computational time of the SVD was the major problem in the past especially the majority of the matrix used was a square matrix.

For quadrupolar nuclei, in a liquid state, there is only one resonance in the spectrum thus only a few as 926 data points were selected to process in Chapter 5. ^{1}H NMR multiple-resonance of the lysozyme spectrum in Chapter 7, on the other hand containing numerous resonances that 4096 data points were used for spectral digitization. For this reason, the relationships between the matrix size and computational time were studied using a total data points of 4000 and 5000 with various matrix size. The matrix size of 2, 4, 5, 10, 20 and 25 was chosen to construct the overdetermined Toeplitz matrix with 4000 and 5000 random numbers.

Those 4000 and 5000 random numbers were processed in a similar way as reduced rank matrix problem. Matrix rank was reduced from full to one. The time required from the formation of the specified Toeplitz matrix size from a column vector with 4000 and/or 5000 data points, until reconstructed data with one rank which are reformatted back to a column vector of the same length was measured. B-1 shows the relationships between Computational time versus matrix size.

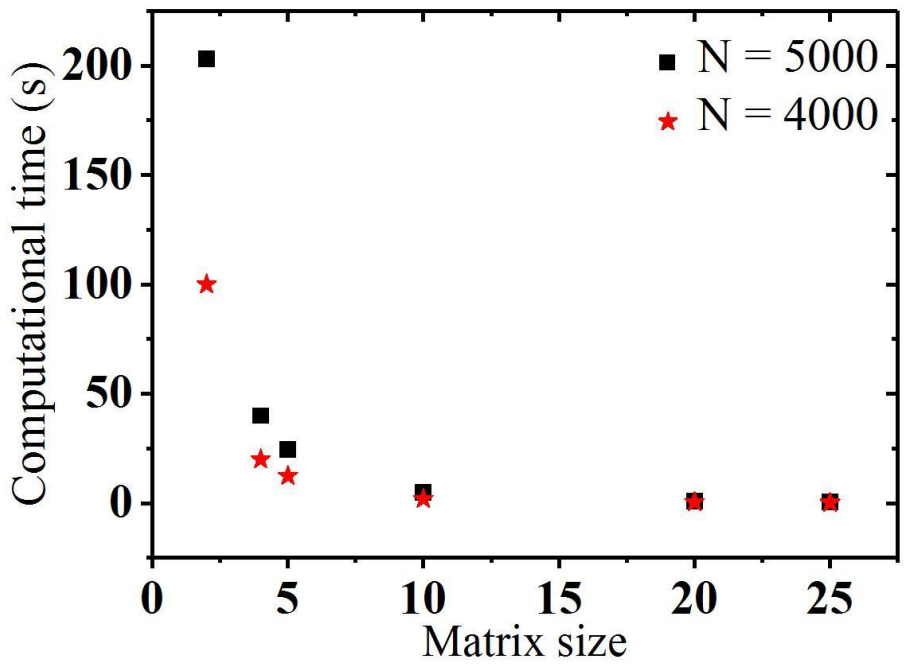

B-1. Matrix size versus computational time measurements for reduced rank data reconstruction with a total number of data points N = 4000 (in a red star) and N = 5000 (in a black square).

At the matrix size of 10, the column length of the matrix of N = 4000 and 5000 are equal to 400 and 500, the processing time of 2 and 5 seconds respectively. From B - 1, the matrix size of 10 or higher seems to be able to process a large volume of data points within the reasonable timeframe. The next question is how big the matrix size can be, in other words, how skinny the decomposing Toeplitz matrix can be to reconstruct spectral data correctly. To investigate, noiseless FID with one resonance was simulated with N = 4096 (B-2a). With additive white Gaussian, the noisy spectrum (i.e., B-2b) with SNR = 7.07 was processed with various matrix size (i.e., matrix size = 5, 10, 15, 20, 30). Reducing the matrix rank to $k = 1$.

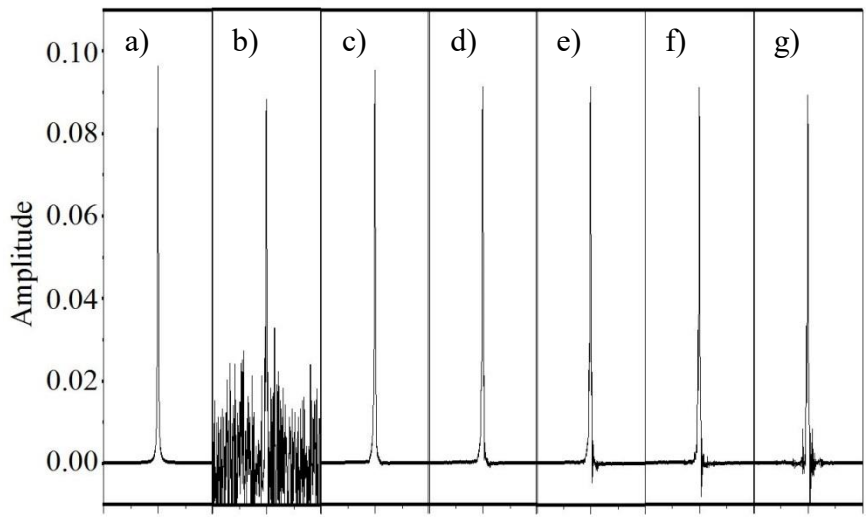

B-2. Simulated spectrum processing with different matrix size: a) noiseless reference data; b) noisy data with SNR = 7.07; c) processed spectrum with matrix size 5; d) processed spectrum with matrix size 10; e) processed spectrum with matrix size 15; f) processed spectrum with matrix size 20; g) processed spectrum with matrix size 30.

The result shows the impeccable signal reconstruction by the matrix size 5 and 10 is observed. The slight spectral intensity decline in B-2d with matrix size 10 is due to the phase distortion due to the matrix size. As the matrix size increases, the matrix becomes skinner and by the matrix size 30, the processed spectrum (B-2g) is similar to the heavily truncated spectrum having a frequency ripple. From these results, the entire signal processing using a composite property mapping algorithm in this thesis was processed with the matrix size of 10 to have sufficient processing speed and spectral resolution.